ANNUAL REPORT ON

APPLICATION OF MODEL-BASED SIGNAL PROCESSING METHODS TO COMPUTATIONAL ELECTROMAGNETICS SIMULATORS

Submitted by

Professor Hao Ling

Department of Electrical and Computer Engineering
The University of Texas at Austin
Austin, TX 78712-1084

December 30, 1999

20000114 034

REPORT DOCUMENTATION PAGE

Public reporting burden for this collection of information is estimated to average 1 hour per response, including the time for reviewing instructions, searching existing data sources, gathering and maintaining the data needed, and completing and reviewing the collection of information. Send comments regarding this burden estimate or any other aspect of this collection of information, including suggestions for reducing this burden to Washington Headquarters Services, Directorate for Information Operations and Reports, 1215 Jefferson Davis Highway, Suite 1204, Arlington, VA 22202-4302, and to the Office of Management and Budget, Paperwork Reduction Project (0704-0188), Washington, DC 20503.

1. AGENCY USE ONLY *(Leave blank)*	2. REPORT DATE Dec. 30, 1999	3. REPORT TYPE AND DATES COVERED Annual Report 1 Dec. 98 – 30 Nov. 99

4. TITLE AND SUBTITLE Annual Report on Application of Model-Based Signal Processing Methods to CEM Simulators	5. FUNDING NUMBERS Research Grant ONR N00014-98-1-0178
6. AUTHOR(S) Hao Ling	

7. PERFORMING ORGANIZATION NAMES(S) AND ADDRESS(ES) The University of Texas at Austin Department of Electrical and Computer Engineering Austin, TX 78712-1084	8. PERFORMING ORGANIZATION REPORT NUMBER No. 2

9. SPONSORING / MONITORING AGENCY NAMES(S) AND ADDRESS(ES) Office of Naval Research Program Officer Ballston Centre Tower One Wen Masters 800 North Quincy Street ONR 311 Arlington, VA 22217-5660	10. SPONSORING / MONITORING AGENCY REPORT NUMBER

11. SUPPLEMENTARY NOTES

a. DISTRIBUTION / AVAILABILITY STATEMENT Approved for Public Release Distribution Unlimited	12. DISTRIBUTION CODE

13. ABSTRACT *(Maximum 200 words)*

This report summarizes the scientific progress on the research grant "Application of Model-Based Signal Processing Methods to Computational Electromagnetics Simulators" during the period 1 December 1998 – 30 November 1999. Progress on model-based extrapolation and interpolation of complex radiation and scattering data in frequency and aspect is described.

14. SUBJECT TERMS Computational electromagnetics Model-based signal processing	15. NUMBER OF PAGES 213
	16. PRICE CODE

17. SECURITY CLASSIFICATION OF REPORT Unclassified	18. SECURITY CLASSIFICATION OF THIS PAGE Unclassified	19. SECURITY CLASSIFICATION OF ABSTRACT Unclassified	20. LIMITATION OF ABSTRACT

ANNUAL REPORT ON

APPLICATION OF MODEL-BASED SIGNAL PROCESSING METHODS TO COMPUTATIONAL ELECTROMAGNETICS SIMULATORS

Submitted by

Professor Hao Ling

Department of Electrical and Computer Engineering
The University of Texas at Austin
Austin, TX 78712-1084

December 30, 1999

APPLICATION OF MODEL-BASED SIGNAL PROCESSING METHODS TO COMPUTATIONAL ELECTROMAGNETICS SIMULATORS

Principal Investigator: Professor Hao Ling
                       (512) 471-1710
                       ling@ece.utexas.edu

Graduate Students: Tao Su, Yuanxun Wang, Bin Jiang

A. SCIENTIFIC OBJECTIVES: The objective of this research program is to apply model-based signal processing methods to enhance the performance of computation electromagnetics (CEM) simulators for shipboard antenna design. While recent advances in CEM algorithms has significantly reduced the simulation cost of modeling complex radiation and scattering phenomena, real-world engineering design and optimization often require that calculations be carried out repeatedly over large parameter spaces such as frequency and aspect angle, making the computation cost still exceedingly high. The goal of this research is to apply model-based signal processing algorithms to CEM simulators to overcome such computational bottleneck and achieve higher design throughput. In particular, we shall address the issue of how to interpolate and extrapolate the frequency and angular behaviors of antenna characteristics based on a sparse set of computed data. We shall develop algorithms to extract sparse and physical models of the relevant physics embedded in CEM data to facilitate design and synthesis. Finally, we shall explore the transportability of the methodology to other applications such as radar signatures and wireless channel characteristics.

B. SUMMARY OF RESULTS AND SIGNIFICANT ACCOMPLISHMENTS: Our research during the second year of this program has been focused on three topics. First, we continue our research to develop an effective algorithm to extrapolate the frequency behavior of antenna radiation characteristics on a complex platform from a limited set of computed data. A frequency-dependent time-of-arrival model is utilized to more

accurately describe the scattering physics of the induced current on the platform. We have devised and implemented a robust algorithm to estimate the model parameters, including the additional frequency-dependent factors. Second, we have developed an algorithm based on the adaptive feature extraction approach to address the frequency interpolation problem. This algorithm has also been extended to the angular domain to achieve two-dimensional interpolation. It was used in conjunction with the fast multipole code FISC to predict the radar image of the benchmark VFY-218 airplane at UHF band with excellent results. Third, we have developed a methodology to parameterize complex antenna radiation patterns using a sparse point radiator model. Our approach is based on a matching pursuit algorithm and the concept has been demonstrated on FISC-generated data for a ship-like platform. The detailed descriptions of these three topics are described below. They are followed by discussions on some exploratory efforts related to this program.

Model-based frequency extrapolation of antenna radiation patterns on complex platforms. In antenna design and analysis, the mounting platform can have a significant effect on the antenna radiation characteristics. However, rigorous solution of the radiation problem over a complex platform is very time consuming, and the computation complexity increases dramatically as the frequency increases. During the first year of this program, we developed a model-based frequency extrapolation technique with which the radiated field over a broad band of frequencies can be obtained using rigorously computed results at low frequencies. Our approach entailed fitting the currents computed at low frequencies to a time-of-arrival model and determining the model coefficients using the superresolution algorithm ESPRIT [1]. The currents and the radiation characteristics were then extrapolated from the resulting model. Some initial results were obtained during the first year but the accuracy of the extrapolated results was not satisfactory.

During this past year, we have significantly improved the algorithm by adopting an improved frequency-dependent model:

$$J(\omega) = \sum_n a_n \omega^{\alpha_n} e^{-j\omega \tau_n} \tag{1}$$

to parameterize the induced current on the platform. In the above expression, t_n is the arrival time of the nth incident wave and a_n and α_n are its amplitude and frequency dependency, respectively. The different time-of-arrival terms correspond to the different incident wave mechanisms from both the direct antenna radiation and higher-order scattering from other parts of the platform, as illustrated in Fig. 1. These different mechanisms have in general different frequency dependencies. For canonical platform shapes, their exact frequency dependencies are known through the geometrical theory of diffraction (GTD) [2]. However, for more complex structures, they must be determined numerically. To accurately extrapolate the frequency response to a much broader range, the accurate estimation of the frequency factors is critical. A small error in α will result in dramatic difference in amplitude at frequencies in the extrapolated region. However, the existing superresolution algorithms based on eigenspace decomposition (e.g. ESPRIT and MUSIC) cannot be directly apply to this more realistic model. We have devised a pre-multiplication scheme in conjunction with the complex time-of-arrival estimation from ESPRIT to determine the additional frequency-dependent factors [22,24]. The performance of the algorithm in the presence of noise has been evaluated based on simulated data and errors in the estimation of model parameters have been quantified. Our results show that the method is quite robust. The algorithm has been applied to extrapolate the induced currents and radiation patterns in both 2D and 3D antenna-platform radiation problems.

As an example, a 2D structure shown in Fig. 2(a) is considered. The platform is 14m in length and 3m in height. The antenna is a horizontal line source placed at 5m above the platform. The induced current on the platform is computed from 0.1 to 0.5 GHz at 21 frequency points using 2D method of moments (MoM). The current is extrapolated to 1.3 GHz and radiated field is then computed based on the extrapolated current. Both the frequency-independent and frequency-dependent time-of-arrival models are used to perform the extrapolation, and the resulting radiated fields at the observation angle of $\theta = 40°$ are plotted in Figs. 2(b) and 2(c), respectively. Also plotted is the reference MoM result obtained via brute force computation. The primary radiation of the dipole antenna is not included in the plots so that we can better observe the secondary radiation from the platform. It is apparent that the frequency dependency in the field response is not
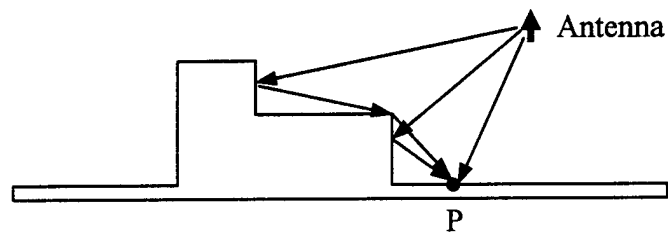
Fig. 1. Time-of-arrival model for the induced current at point P accounts for the direct incident radiation from the antenna and the multiple scattered waves from other parts of the platform.
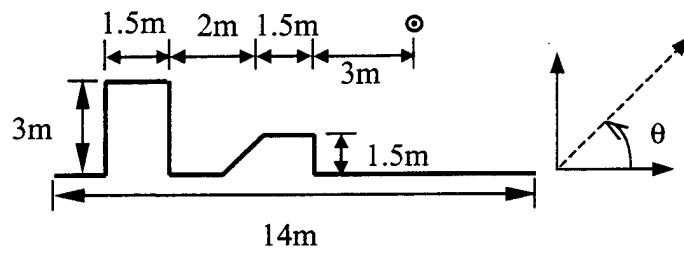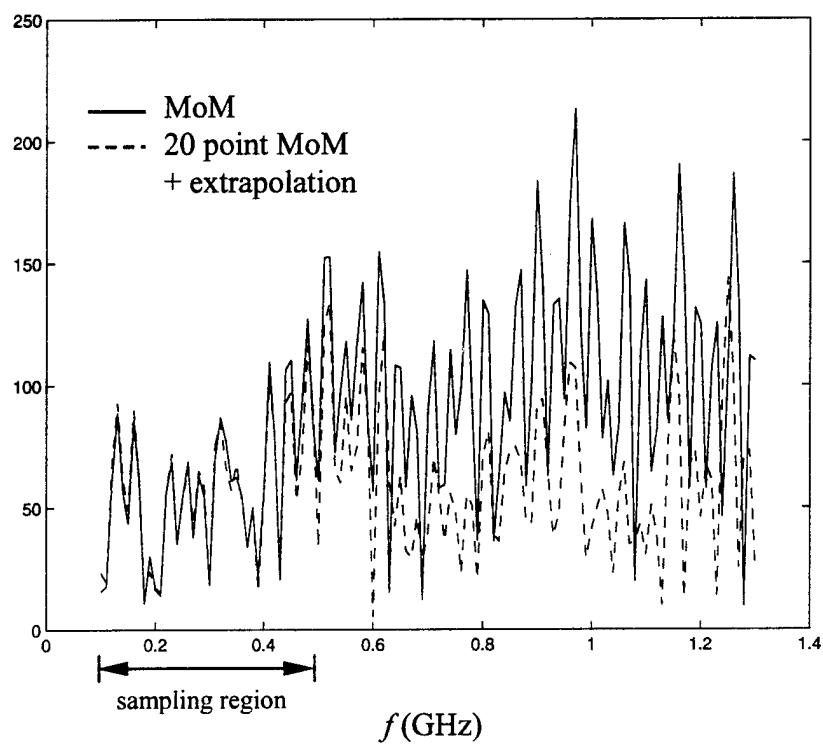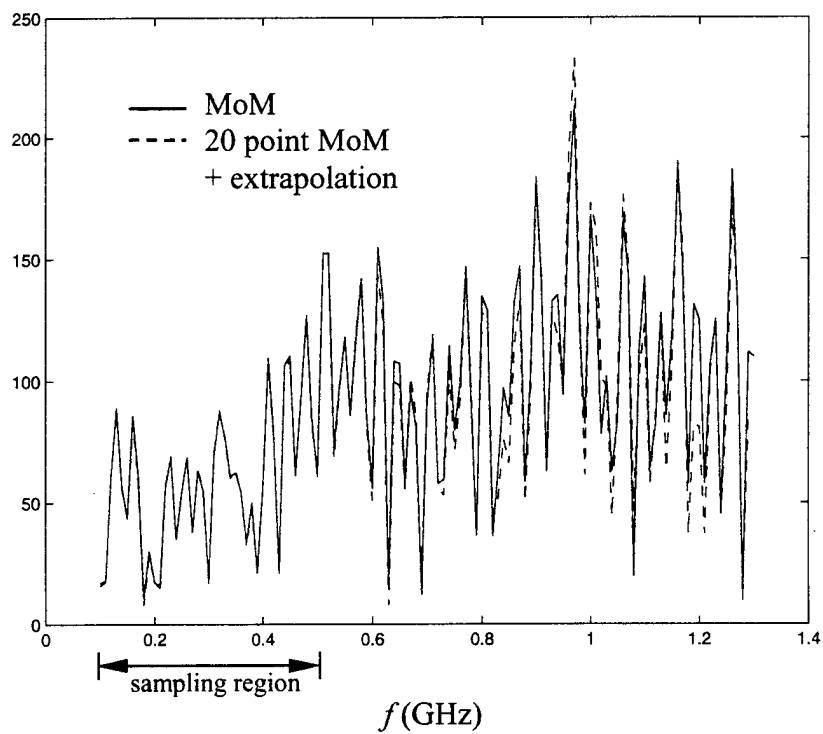

Fig. 2(a). 2D platform geometry

Fig. 2(b) Frequency response predicted by the frequency-independent time-of-arrival model at $\theta = 40°$.

2(c) Frequency response predicted by the frequency dependent model at $\theta = 40°$.

captured by the frequency-independent time-of-arrival model, while the field predicted by the frequency dependent model is in good agreement with the computed result.

Next, we look at a 3D platform shown in Fig. 3(a). The antenna is a horizontal dipole oriented in the x direction. The induced current is computed from 0.1 to 0.36 GHz at 13 frequencies and extrapolated to 0.7GHz. The computation is carried out using FISC, a 3D MoM code based on the fast multipole method [3]. The extrapolated frequency response at the observation angle ϕ_{el} = 30°, ϕ_{az} = -60° is plotted in Fig. 3(b). Also plotted for comparison is the reference response computed by FISC via brute force. The major radiation features are captured by the extrapolation. Figs. 3(c) and 3(d) show the reference and extrapolated radiation patterns as functions of frequency and azimuth angle when the elevation angle is fixed at 50°. Good qualitative agreement is observed. The correlation index between the two figures is found to be 0.9980 in the sampled region and 0.9742 in the extrapolated region, respectively. The computation time of the brute force reference results is about 50 hours on a PentiumII 400MHz PC, while the total computation time to carry out the electromagnetic computation in the sampled region and the extrapolation process is 7 hours.

Although the determination of model parameters is more complicated, the frequency dependent model show significant performance improvement over the frequency independent model. This is due to the improved modeling of the scattering physics. Since the current required for the extrapolation is only computed at lower frequencies, large savings in computation time and memory can be achieved. We hope to further extend this methodology to model the near fields of complex platforms for problems related to antenna coupling and radiation hazard evaluation [17]. We also plan to investigate extrapolation issues related to non-perfect conducting structures.

Model-based frequency interpolation using adaptive feature extraction. We have begun to investigate the interpolation problem for CEM data. Although the potential payoff of an interpolation algorithm is not as great as extrapolation, it may provide a more robust way to achieve computational savings. To achieve the parameterization in the frequency dimension, we again utilize the multiple-arrival model for the induced current. To obtain the model parameters from the computed data, we adopt an algorithm
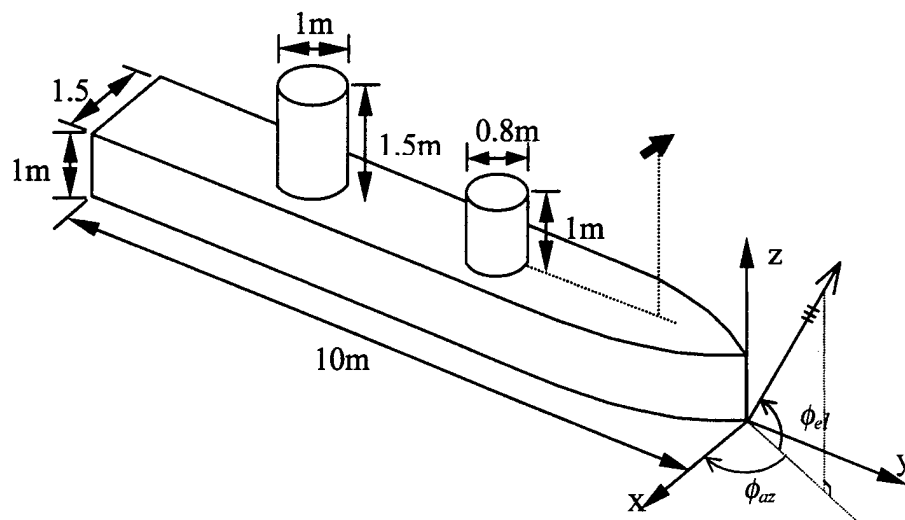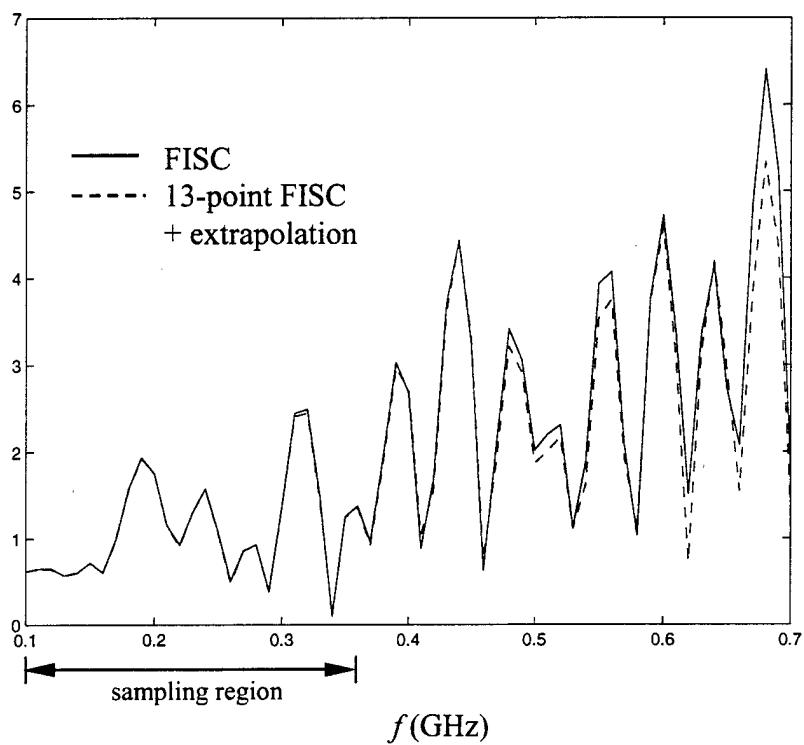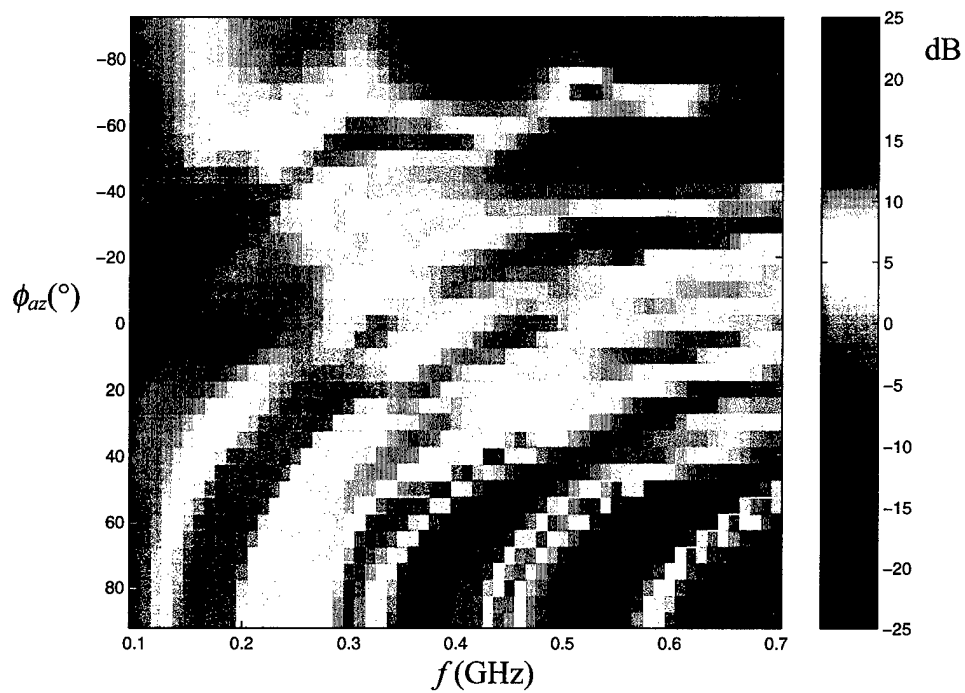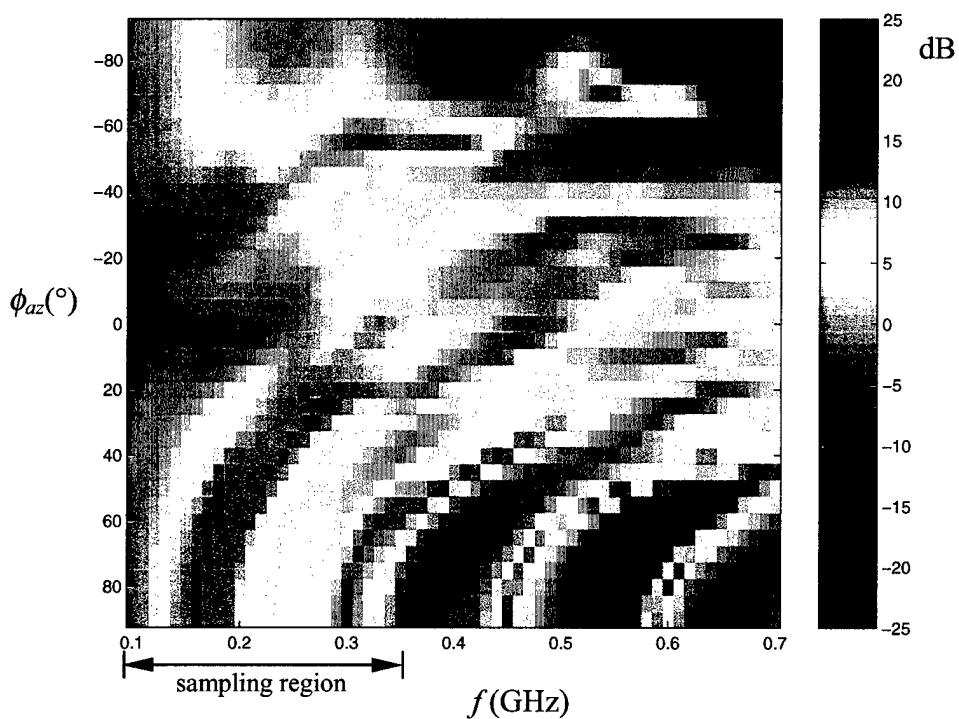
Fig. 3(a). 3D platform geometry

Fig 3. (b) Frequency response predicted by the frequency dependent model at $\phi_{el} = 30°$, $\phi_{az} = -60°$.

(c) Computed by FISC

(d) Computed through extrapolation

Fig. 3(c), (d). Comparison of the radiated field generated from brute force FISC computation and frequency extrapolation as a function of frequency and azimuth angle at the elevation angle of $\phi_{el} = 50°$.

termed adaptive feature extraction (AFE). AFE can be considered as a generalization of the CLEAN algorithm [4], and is similar to the adaptive joint time-frequency technique [5-7] and the matching pursuit algorithm [8] in the iterative manner it performs the parameterization. We have previously applied it to construct the inverse synthetic aperture radar (ISAR) image from radar measurement data that was undersampled in the aspect dimension [18]. The essential idea of the AFE algorithm is to search and extract out individual scattering features from the data set one at a time. During each iteration the strongest feature is identified and removed from the original data. The procedure is then iterated until the data is well parameterized by the feature set. In this manner, the interference between different scattering features, which is significant for undersampled data, can be largely avoided. Since the features in our model are exponential functions of frequency and aspect, we use random sampling during the collection of the original computation data in order to avoid the ambiguity in selecting the strongest feature. This approach is similar to the random array concept that uses highly thinned but randomly spaced elements to avoid grating lobes [9].

We have also extended this algorithm to interpolate 2-dimensional frequency and angle data [20, 26]. In this case, a more generalized time-of-arrival and angle-of-arrival model is used to parameterize the current. We have applied the 2D algorithm to predict the ISAR image of the benchmark VFY218 airplane [10]. The fuselage length of the airplane is 15.33 meters and the maximum width measured from the wing tips is 8.90 meters. To generate its ISAR image at a center frequency of 400 MHz with bandwidth 267 MHz, we use the fast solver FISC on a Pentium II 450MHz computer. The total number of sampling points must be at least 40 frequency points by 40 aspect points within the 40-degree aperture to satisfy the Nyquist sampling criterion. The resulting range and cross range resolution is about half a meter. Since the calculation for one single frequency-aspect point takes about 3 hours (with about 80,000 unknowns in the moment equation), the total computation time would be 200 days if we use brute-force calculation to generate the data. Based on a 5:1 undersampling rate, we only compute the scattering problem at 62 randomly sampled points and use the AFE interpolation scheme to interpolate the data to all 40x40=1600 points. The computation time is about 8 days. The resulting ISAR image at the 130-degree (from nose-on) look angle is plotted in Fig.

4(a). For comparison, Fig. 4(b) shows the ISAR image constructed from the chamber measurement data for the same look angle. The target outline is overlaid on the measurement image. The measurement was carried out at the US Navy China Lake facility on a 1:30 scaled model at the frequency band of 8 to 16 GHz. Comparing Fig. 4(a) to Fig. 4(b), we find that all the features in the measurement image are well predicted in the simulated image from using FISC and interpolation.

The AFE approach has been found to be stable and robust. Sufficient accuracy in the predicted image features can be achieved even when the original computed data is sampled at 5:1 below the Nyquist criterion in either frequency or aspect. Therefore, the expected time savings in using this approach is about 25:1 in comparison to the brute-force computation. The AFE algorithm does involve exhaustive search and must be carried out for every current element on the target. However, the time consumed in the interpolation is still relatively insignificant when compared to the electromagnetic computation time. This error sources that limit the dynamic range of the final interpolated data are currently being investigated. The approach will also be further explored for application in the antenna placement problem.

Extraction of sparse representation of antenna radiation data. The previous topics are focused on the utilization of model-based processing to extrapolate or interpolate CEM data for the "forward" solution of electromagnetic radiation and scattering problems involving complex platforms. An equally important problem from the design perspective is the "inverse" algorithm of spatially pinpointing the locations of platform scattering based on CEM data. Toward this end, we had previously developed a method to extract sparse model of the antenna radiation pattern on a complex platform [11],[12]. This representation is based on a point radiator model that describes the radiation pattern by a collection of "radiation centers" on the platform. The methodology for obtaining the radiation center model entails first generating the 3-D antenna synthetic aperture radar (ASAR) imagery of the platform, and then parameterizing the resulting image by a collection of point radiators via the CLEAN algorithm [27]. Once such a representation is obtained, we can rapidly reconstruct antenna radiation patterns over frequencies and aspects with good fidelity. Thus such a model can be used for real-time
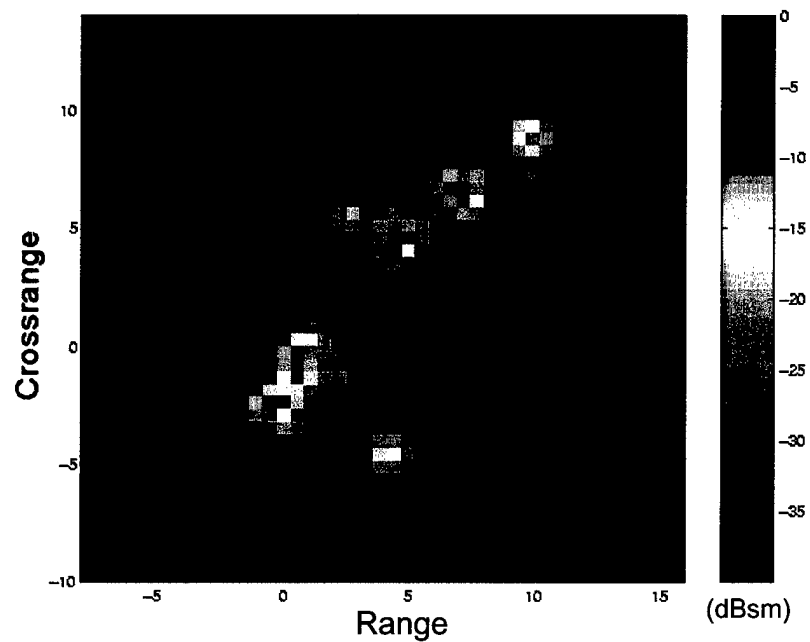
Fig.4(a) ISAR image of VFY-218 at 130 degrees from nose-on
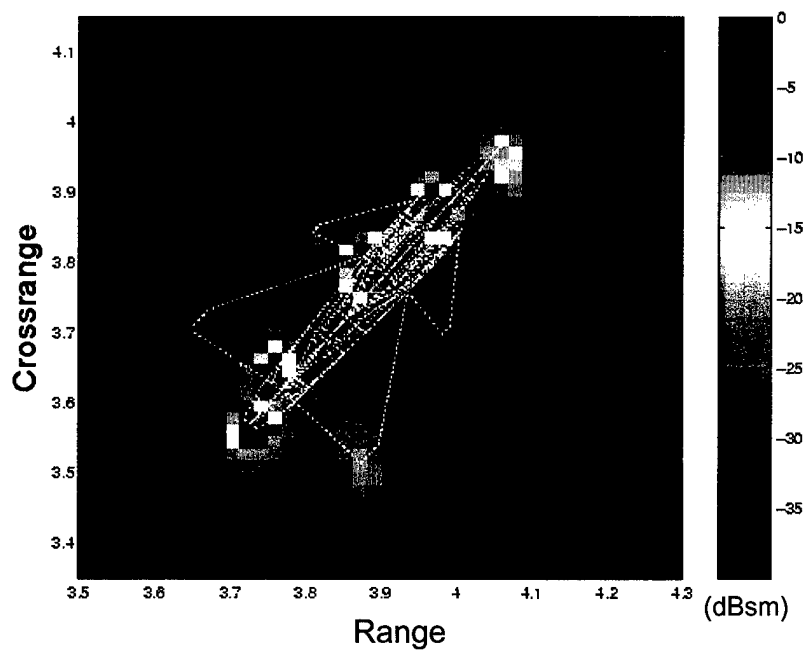generated from interpolated result using AFE with 62
FISC-computed points.

Fig.4(b) ISAR image of VFY-218 at 130 degrees from nose-on
generated from chamber measurement data.

reconstruction of complex antenna patterns in high-level system simulations. Furthermore, the resulting radiation center information can be used to pinpoint cause-and-effect in platform scattering and provide important design guidelines for antenna placement and optimization. However, the method was based on a Fourier-based algorithm that relied on a number of small-angle, small-bandwidth approximations. Furthermore, the concept was only demonstrated using high-frequency ray-tracing simulations and not more rigorous CEM data.

During the past year, we have overcome the above deficiencies by developing a more generalized matching pursuit algorithm in the frequency-aspect domain based on a point radiator basis [25]. We have also demonstrated the feasibility of extracting a sparse model of the antenna-platform interaction using CEM data from FISC. The matching pursuit algorithm is implemented based on the following radiation center basis:

$$E^s(k, \theta, \phi) = Ae^{-jkr_0}e^{jk(x_0 \sin\theta \cos\phi + y_0 \sin\theta \sin\phi + z_0 \cos\theta)} = Ae^{-jkr_0}e^{j(k_x x_0 + k_y y_0 + k_z z_0)}$$

(2)

where k is the wave number, (x_0, y_0, z_0) is the location of the radiation center. The origin of the above basis is illustrated in Fig. 5. Note that the phase factor in (2) accounts for the path delay from the antenna to the point scatterer on the platform, and then to the observation direction in the far field. To speed up the parameterization time of the matching pursuit algorithm, we estimate the location of the radiation centers by utilizing the Fourier-based ASAR algorithm. The point with the highest intensity is first located in the ASAR image and its amplitude and coordinates are determined to serve as an estimate of the strongest radiation center. We next zoom in on the precise location of the radiation center via a fine search. We then subtract the contribution of this radiation center from the total radiated field and iterate the process until the energy in the residual signal has reached a sufficiently small level.

As an example, the radiation center model is extracted from the computed radiation data from FISC for the ship-like structure shown earlier in Fig. 3(a). The radiated field is computed at a center frequency of 1.0 GHz and a bandwidth of 500 MHz. The center observation angle is $\phi_{el} = 40°$, $\phi_{az} = 50°$ and the angular range is about 23° in both azimuth and elevation angles. The first 20 extracted radiation centers are plotted in Fig. 6(a). The
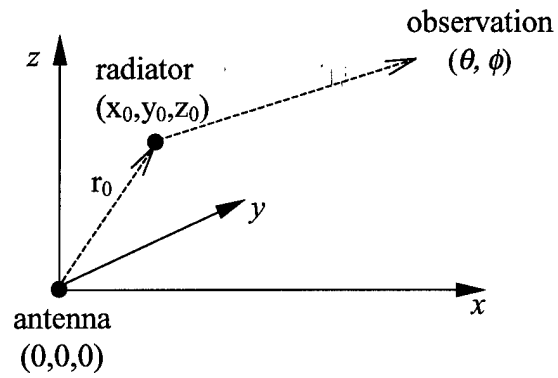
Fig. 5. Radiation center model

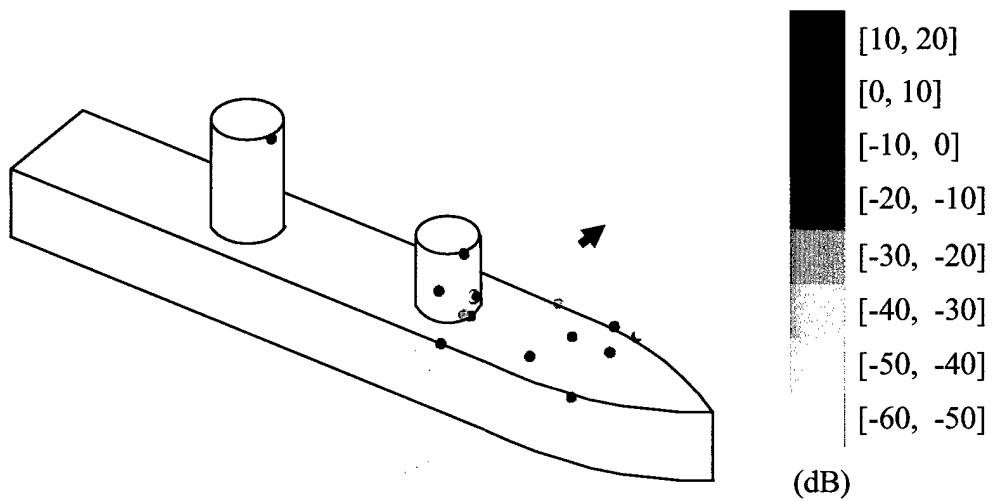|	
	[10, 20]
	[0, 10]
	[-10, 0]
	[-20, -10]
	[-30, -20]
	[-40, -30]
	[-50, -40]
	[-60, -50]
(dB)	

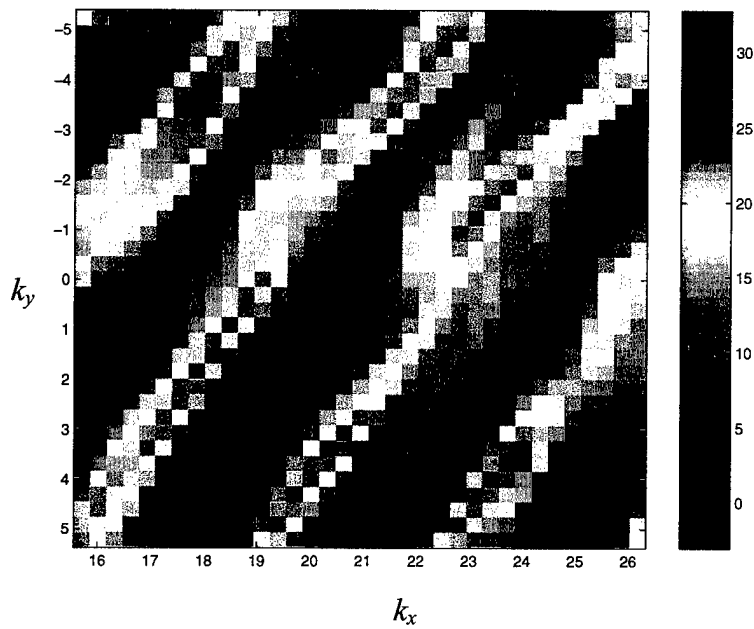Fig. 6(a). First 20 radiation centers extracted using the matching
pursuit algorithm

Fig. 6(b) Original radiated field computed by FISC over a
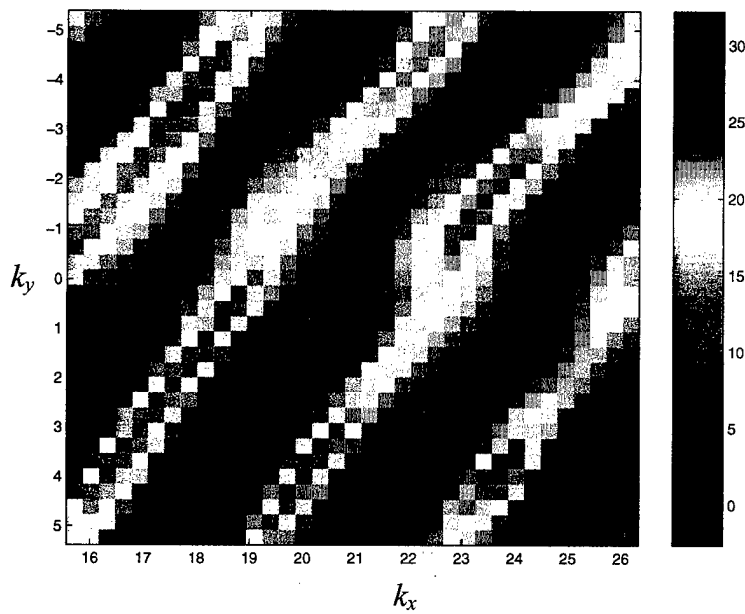bandwidth of 500 MHz and 23° azimuth angle.

Fig. 6(c) The radiated field reconstructed from the first 20
extracted radiation centers

strength of the radiation centers is represented by different colors. We observe that the dominant platform scattering comes from the edge diffraction from the bow of the ship platform and the corner structure formed by the cylinder and plate. Note that a few radiation centers due to the edge diffraction are slightly off the platform. This is due to the limited resolution of the matching pursuit algorithm. Once the sparse representation is generated, the radiated field can be easily reconstructed using the radiation centers. The original radiated field at $k_z = 0$ is plotted in Fig. 6(b) as a function of the k_x and k_y, where the wave numbers k_x, k_y and k_z are defined in (2). The field reconstructed from the first 20 radiation centers is shown in Fig. 6(c). The two patterns match well over both frequency and angle. The correlation index between the two figures is found to be 0.958.

We have demonstrated that radiation patterns from complex platforms can be well represented by a very sparse set of radiation centers. The resulting model can be used to spatially pinpoint cause-and-effect on the platform and could play an important role in antenna placement and optimization. We shall continue to refine this algorithm and examine more complex topside structures. We also plan to utilize this model for addressing the antenna coupling issue once the CEM capability for simulating antenna coupling characteristics is in place.

Other exploratory topics. Several additional studies have been carried out during the past year and are described below. They serve as possible launching points into more relevant and focused efforts for the present program in the next year. First, we have begun to investigate the resonant behaviors of antenna-platform configurations. This topic is motivated by the interest of the Navy SPAWAR Center in HF antennas where ship body resonances can dominate the antenna frequency characteristics. In the lower frequency regime, the scattering phenomenology differs from ray-optical characteristics. Consequently, the time-of-arrival model we have utilized successfully may no longer be efficient in this regime. We have carried out a preliminary study to understand the scattering phenomenology in these configurations. Furthermore, we are exploring a hybrid scheme to achieve a sparse parameterization of the data using a combination of (i) a rational function model for those regions on the structure dominated by resonant effects, and (ii) a exponential model for those regions on the structure dominated by ray

optical phenomena. We hope to devise a robust parameterization procedure so that both types of physical mechanisms can be accurately described.

An important issue related to the study of resonant region using an iterative CEM solver like FISC is that when the platform exhibits strong resonance effect, the iteration number required for an accurate solution can become large. A good preconditioner for the moment matrix is needed to alleviate this problem. We have been investigating the use of wavelet packet basis for the sparsification of moment matrix [13,14]. We have recently extended this work by devising an approximate-inverse preconditioner to the moment equation using the wavelet representation [15,23]. We plan to further investigate this topic, which may become important for simulating near-resonant structures.

C. FOLLOW-UP STATEMENT:

In the coming year, we will continue our research along the three research topics outlined above by: (i) extending our work on frequency extrapolation to near-field radiation characteristics, (ii) extending the frequency-aspect interpolation algorithm for multiple frequency-antenna position study, and (iii) refining the radiation center extraction algorithm. In addition, we plan to initiate several new research topics in: (i) applying the new FISC code for mixed wire-facet bases for antenna self-impedance study, (ii) investigating antenna mutual coupling issues and exploring the usage of CEM data in array calibration, and (iii) devising an improved model for describing both ray-optical and resonance phenomena in antenna-platform interactions.

D. REFERENCES:

1. R. Roy, A. Paulraj and T. Kailath, "ESPRIT – a subspace rotation approach to estimation of parameters of cisoids in noise," *IEEE Trans. Acoust., Speech, Signal Processing*, vol. ASSP-34, pp. 1340-1342, Oct. 1986.

2. L. C. Potter, D. Chiang, R. Carriere and M. J. Gerry, "A GTD-based parametric model for radar scattering," *IEEE Trans. Antennas Propagat.*, vol. 43, pp. 1058-1067, Oct. 1995.

3. J. Song, C. C. Lu and W. C. Chew, "Multilevel fast multipole algorithm for electromagnetic scattering by large complex objects," *IEEE Trans. Antennas Propagat.*, vol. 45, no. 10, pp. 1488-1493, Oct. 1997.

4. J. Tsao and B.D. Steinberg, "Reduction of sidelobe and speckle artifacts in microwave imaging: the CLEAN technique," *IEEE Trans. Antennas Propagat.,* vol. AP-36, pp. 543-556, Apr. 1988.

5. S. Qian and D. Chen, "Signal representation using adaptive normalized Gaussian functions," *Signal Processing,* vol. 36, no. 1, pp. 1-11, Mar. 1994.

6. L. C. Trintinalia, and H. Ling, "Joint time-frequency ISAR using adaptive processing," *IEEE Trans. Antennas Propagat.,* vol. AP-45, pp. 221-227, Feb. 1997.

7. Y. Wang, H. Ling and V. C. Chen, "Application of adaptive joint time-frequency processing to ISAR image enhancement and Doppler feature extraction for targets with rotating parts," *SPIE Proceedings,* vol. 3462, pp.156-163, July 1998.

8. S. G. Mallat and Z. Zhang, "Matching pursuits with time-frequency dictionaries," *IEEE Trans. Signal Processing,* vol. 41, pp. 3397-3415, Dec. 1993.

9. Y. T. Lo, "A mathematical theory of antenna arrays with randomly spaced elements," *IEEE Trans. Antennas Propagat.,* vol. AP-15, pp. 257-268, May 1964.

10. H. T. G. Wang, M. L. Sanders and A. Woo, "Radar cross section measurement data of the VFY 218 configuration," *Tech. Rept. NAWCWPNS TM-7621,* Naval Air Warfare Center, China Lake, CA, Jan. 1994.

11. C. Ozdemir, R. Bhalla, L. C. Trintinalia and H. Ling, "ASAR - antenna synthetic aperture radar imaging," *IEEE Trans. Antennas Propagat.,* vol. AP-46, pp. 1845-1852, Dec. 1998.

12. C. Ozdemir, R. Bhalla and H. Ling, "A radiation center representation of antenna radiation pattern on a complex platform," submitted for publication in *IEEE Trans. Antennas Propagat.,* Sept. 1997.

13. H. Deng and H. Ling, "Fast solution of electromagnetic integral equations using adaptive wavelet packet transform," *IEEE Trans. Antennas Propagat.,* vol. AP-47, pp. 674-682, Apr. 1999.

14. H. Deng and H. Ling, "On a class of pre-defined wavelet packet bases for efficient representation of electromagnetic integral equations," to appear in *IEEE Trans. Antennas Propagat.,* Nov. 1999.

15. H. Deng and H. Ling, "Preconditioning of electromagnetic integral equations using pre-defined wavelet packet basis," *Elect. Lett.,* vol. 35, pp. 1144-1146, July 1999.

E. PUBLICATIONS:

I. LIST OF JOURNAL ARTICLES (ONR supported in whole or in part)

16. Y. Wang and H. Ling, "A model-based angular extrapolation technique for iterative method-of-moments solvers," *Microwave Optical Tech. Lett.*, vol. 20, pp. 229-233, Feb. 1999.

17. C. Ozdemir and H. Ling, "ACSAR - antenna coupling synthetic aperture radar imaging algorithm," *J. Electromag. Waves Applications*, vol. 13, pp. 285-306, Mar. 1999.

18. Y. Wang and H. Ling, "Adaptive ISAR image construction from unevenly undersampled data," to appear in *IEEE Trans. Antennas Propagat.*, Feb. 2000.

19. T. Su and H. Ling, "Determining the equivalent impedance boundary condition for corrugated coatings based on the genetic algorithm," to appear in *IEEE Trans. Antennas Propagat.*, Mar. 2000.

20. Y. Wang and H. Ling, "Efficient radar signature prediction using a frequency-aspect interpolation technique based on adaptive feature extraction," submitted for publication in *IEEE Trans. Antennas Propagat.*, June 1999.

21. Y. Wang and H. Ling, "A frequency-aspect extrapolation algorithm for ISAR image simulation based on two-dimensional ESPRIT," submitted for publication in *IEEE Trans. Geo. Science and Remote Sensing*, Special Issue on Computational Wave Issues in Remote Sensing, Imaging and Target Identification, Aug. 1999.

22. T. Su, Y. Wang and H. Ling, "A frequency extrapolation technique for computing antenna-platform radiation problems," submitted for publication in *IEEE Trans. Antennas Propagat.*, Sept. 1999.

23. H. Deng and H. Ling, "An efficient preconditioner for electromagnetic integral equations using pre-defined wavelet packet basis," submitted for publication in *IEEE Trans. Antennas Propagat.*, Nov. 1999.

II. LIST OF CONFERENCE PROCEEDINGS (ONR supported in whole or in part)

24. T. Su, Y. Wang and H. Ling, "Model-based frequency extrapolation of antenna radiation characteristics on complex platforms," 15th Annual Review of Progress in Applied Computational Electromagnetics, pp. 272-277, Monterey, CA, Mar. 1999.

25. T. Su, Y. Wang and H. Ling, "Frequency extrapolation and model-based parameterization of antenna-platform radiation from CEM data," International IEEE AP-S Symposium, pp. 446-449, Orlando, FL, July 1999.

26. Y. Wang and H. Ling, "RCS interpolation in frequency and angle using adaptive feature extraction," International IEEE AP-S Symposium, pp. 450-453, Orlando, FL, July 1999.

27. C. Ozdemir and H. Ling, "A sparse representation of antenna coupling synthetic aperture radar (ACSAR) imaging using the CLEAN algorithm," 1999 URSI General Assembly, Toronto, Canada, Aug. 1999.

III. LIST OF RELATED PRESENTATIONS

28. "Electromagnetic signature simulation and feature extraction for radar target identification," University of Illinois, Signal Processing Seminar, Champaign, IL, Feb. 3, 1999.

29. "Radar image simulation: solving Maxwell's equations for radar target identification," University of Illinois, ECE Department Graduate Seminar, Champaign, IL, Feb. 4, 1999.

30. "Fast postprocessing algorithms for fast CEM solvers," 1999 Electromagnetics Code Consortium Annual Meeting, Hughes Research Laboratory, Malibu, California, Apr. 20, 1999.

31. "Application of model-based signal processing to computational electromagnetics simulators," Navy H-Infinity Program Workshop, Office of Naval Research, Washington, DC, June 17, 1999.

32. "Evaluation of Apatch – a platform radiation code based on the shooting and bouncing ray technique," Electromagnetic Software Evaluation for Integrated Topside Design Meeting, Navy SPAWAR System Center, San Diego, California, Sept. 27, 1999.

IV. LIST OF THESES AND DISSERTATIONS

Ph.D.
Y. Wang, "Radar signature prediction and feature extraction using advanced signal processing techniques," August 1999.

V. CONTRACTS AND GRANTS

H. Ling, "Advanced research and development for the MSTAR prediction module," Defense Advanced Research Project Agency (via DEMACO, Inc.), June 1, 1995 - January 31, 1999.

H. Ling, "MURI center for computational electromagnetics research," Air Force Office of Scientific Research (via Univ. of Illinois), December 15, 1995 - December 14, 2000.

R. Chen and H. Ling, "Si MOS process-compatible optical interconnects and applications," Texas Advanced Technology Program, January 1, 1998 - December 31, 1999.

H. Ling, "Application of model-based signal processing methods to computational electromagnetics simulators," Office of Naval Research, December 1, 1997 - November 30, 2000.

H. Ling, "Radar image enhancement, feature extraction and motion compensation using joint time-frequency techniques," Office of Naval Research, April 15, 1998 - April 14, 2001.

H. Ling, "Moving target modeling and simulation," Air Force Research Laboratory (via DEMACO, Inc.), October 1, 1998 – April 30, 1999.

H. Ling, "Electromagnetic scattering from periodic surfaces," Lockheed Martin Corporate Grant, November 15, 1998 - December 31, 1999.

D. T. Jaffe and H. Ling, "High index grisms for mid-infrared spectroscopy," NASA, June 1, 1999 – May 31, 2001.

F. INTERACTIONS/COLLABORATIONS WITH NAVY SCIENTISTS:

The second H-infinity workshop was held at the Office of Naval Research on June 17-18, 1999. In addition to reporting our progress and exchanging ideas with the other team members of the H-infinity program, new collaborative opportunities were explored. The PI participated in a panel study organized by Dr. Jeffrey Ho of SPAWAR to evaluate existing antenna codes for the design of large active phased arrays in connection with Navy's next-generation destroyer (DD-21) project. The PI presented an evaluation of the high-frequency code Apatch for characterizing antenna-platform interactions at a panel meeting on Sept. 27, 1999 at SPAWAR. We continue to interact closely with Dr. Victor Chen of Naval Research Lab on a separate ONR program in applying joint time-frequency processing to inverse synthetic aperture radar imagery. We expect to generate cross-fertilization of ideas with the H-infinity program since a good physical

understanding of electromagnetic scattering and radiation phenomena is the basis of our work in both programs.

G. NEW DISCOVERIES, INVENTIONS, OR PATENT DISCLOSURES:

None.

H. HONORS AND AWARDS:

Dr. Ling has been elected to IEEE Fellow for 1999 for his "contribution to the development of radar signature prediction and feature extraction techniques."

APPENDIX

Publications Supported by ONR Grant

A MODEL-BASED ANGULAR EXTRAPOLATION TECHNIQUE FOR ITERATIVE METHOD-OF-MOMENTS SOLVERS

Yuanxun Wang[1] and Hao Ling[1]
[1] Department of Electrical and Computer Engineering
University of Texas at Austin
Austin, Texas 78712-1084

ABSTRACT: *An angular extrapolation technique is proposed to accelerate the multiangle RCS calculation of iterative MoM solvers. Based on high-frequency electromagnetic phenomenology, an exponential model is proposed to parameterize the induced currents on the target. The model parameters are extracted from MoM results at a limited number of angular samples using the superresolution algorithm ESPRIT. The RCSs at a wide extent of angles are then extrapolated. This approach is tested on two numerical examples. Comparison with the bistatic approximation shows the improved accuracy of the algorithm.* © 1999 John Wiley & Sons, Inc. Microwave Opt Technol Lett 20: 229–233, 1999.

Key words: *angular extrapolation; method of moments; superresolution*

I. INTRODUCTION

It is well known that when the method of moments (MoM) equation is solved using direct matrix inversion or LU decomposition, multiple right-hand-side (RHS) solutions can be generated efficiently. Unfortunately, the computation complexity of $O(N^3)$ for such direct solvers is usually too high when the target size is bigger than a few wavelengths. To overcome this difficulty, many iterative MoM solvers have been developed by using iterative matrix–vector multiplication. Among them, the fast multipole method (FMM) [1] and the multilevel fast multipole method (MLFMM) [2] can reduce the computational complexity of the matrix–vector multiply operation from $O(N^2)$ to $O(N^{1.5})$ and $O(N \log N)$, respectively. However, for applications such as generating multiangle radar cross section (RCS) data, these iterative procedures have to be repeated for each RHS or look angle. There are some existing techniques to speed up iterative matrix solvers for multiple RHS problems [3, 4]. Nevertheless, the computational gain usually comes at the expense of more memory requirement. In this paper, we propose an angular extrapolation scheme to extrapolate angular RCS data from the solutions at a few densely sampled angles. These solutions can be obtained by iterative MoM solvers, either with or without the accelerated multiple RHS algorithms.

An often-used angular extrapolation (or interpolation) approach for RCS is the so-called bistatic approximation [5–7], which is based on the physical optics assumption. Under this assumption, the monostatic scattered data are approximated by the bistatic scattered data at nearby angles.

Because bistatic data are relatively inexpensive to compute, additional monostatic data can be readily generated using this approach. However, since physical optics does not take into account multiple interactions among different parts of the target, the bistatic approximation breaks down when applied to scattering data of targets that are dominated by multiple scattering mechanisms.

The angular extrapolation algorithm we will present here is based on a multiple scattering model. We parameterize the current on the target, which is available from the MoM solution, using an exponential, multiple-excitation model. The parameters of this model are extracted from a few angular samples via the ESPRIT superresolution algorithm [8]. Once these parameters are obtained, the angular-dependent model of the induced current at each point on the target is constructed. Thus, the induced current over a wider angular extent can be extrapolated and the multiangle RCS can be calculated. This approach can be considered as a dual of the model-based frequency extrapolation that we have devised earlier [9]. In the following section, the multiple-excitation model will be described in detail. In Section III, numerical examples are presented to illustrate the performance of our extrapolation algorithm, and comparisons are made against the bistatic approximation.

II. MODEL-BASED EXTRAPOLATION

The key to the success of any model-based extrapolation is a good model that coincides with the underlying physical mechanisms [9, 10]. We postulate that in high-frequency scattering, the induced current at each point S on the target is excited by multiple-arriving scattered waves, as shown in Figure 1. If we denote the down-range direction with respect to the incident wave as x and the cross-range direction as y, the current at S can be written as

$$J(S) = \sum_{i=1}^{N} A_i e^{-2jkd_i}, \qquad d_i = x_i + l_i \qquad (1)$$

where N is the number of scattered waves arriving at S and k is the free-space wavenumber. In the above definition of the path length d_i, we let (x_i, y_i) be the first hit point on the target due to the incident wave, and let l_i be the total intermediate path length of the multiple-scattering mechanism. Note that the two mechanisms illustrated in Figure 1 are both two-bounce mechanisms. For a single-bounce physical-optics mechanism, $l_i = 0$ and (x_i, y_i) simply corresponds to the point S.
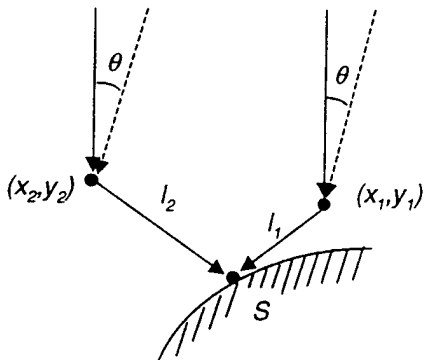

Figure 1 Multiple-arrival model of the scattering mechanisms

We now make a key assumption about the current model as the incident angle is varied. We assume that all intermediate scattering points for each mechanism remain fixed as the incident angle is varied, as illustrated in Figure 1. This assumption has been found to be fairly accurate for ray-optical fields under small angular variation [11], and leads us to the following current model as a function of incident angle:

$$J(\theta, S) = \sum_{i=1}^{N} A_i(\theta) e^{-2jk(x_i \cos \theta + y_i \sin \theta + l_i)}. \qquad (2)$$

If we further use the small-angle approximation $\cos \theta \approx 1$ and $\sin \theta \approx \theta$, and assume that A_i is independent of angle, then

$$J(\theta, S) \approx \sum_{i=1}^{N} A_i e^{-2jky_i\theta_e - 2jk(x_i + l_i)} \qquad (3a)$$

$$\approx \sum_{i=1}^{N} A'_i e^{-2jky_i\theta}. \qquad (3b)$$

We observe that the above equation is in the form of a sum-of-exponential model, with linear phase dependence with respect to the incident angle.

With the above multiple-excitation model in hand, we set out to extract the parameters (A'_i, y_i) at each point on the target from a limited number of angular samples calculated using the MoM. We apply the superresolution algorithm ESPRIT [9] for this purpose due to its robustness in the presence of noise. ESPRIT is based on the data model

$$F(\theta_m) = \sum_{i=1}^{N} A'_i e^{-j2ky_i\theta_m} + n(\theta_m), \qquad \theta_m = \theta_1, \theta_2, \ldots, \theta_M$$

$$(4)$$

where $n(\cdot)$ denotes additive white Gaussian noise and the samples are uniformly spaced. If the data sequence obeys this ideal model exactly and the number of sampling points M is infinite, ESPRIT can estimate N and resolve each A'_i and y_i without any error. For finite-length data, the minimum number of samples to perform the estimation is $M > 2N + 1$, and the accuracy of the estimated parameters will depend on the length of the available data. At frequencies above target resonance, the first few interactions dominate the scattering phenomenon, and only a small N is needed to adequately model the observed data. Therefore, by running ESPRIT using the MoM-generated current at M angles, the angular-dependent current model in (3b) can be obtained. Note that the ESPRIT processing is carried out at each point on the target. Once such a model is found, we can extrapolate the data to determine the current at other angles. The total scattered field versus angle can thus be calculated by integrating the extrapolated current. For large angle extrapolation, we find that it is more accurate to use the original $\sin \theta$ factor in place of the θ term in the phase of the current model in (3b). To both satisfy the Nyquist sampling criterion for ESPRIT and achieve the maximum calculation efficiency, the angular sampling interval is normally chosen as $\pi/2ky_{max}$, where y_{max} is the maximum target dimension in cross range.

III. NUMERICAL RESULTS

To demonstrate the performance of the angular extrapolation algorithm, two numerical examples are presented based on
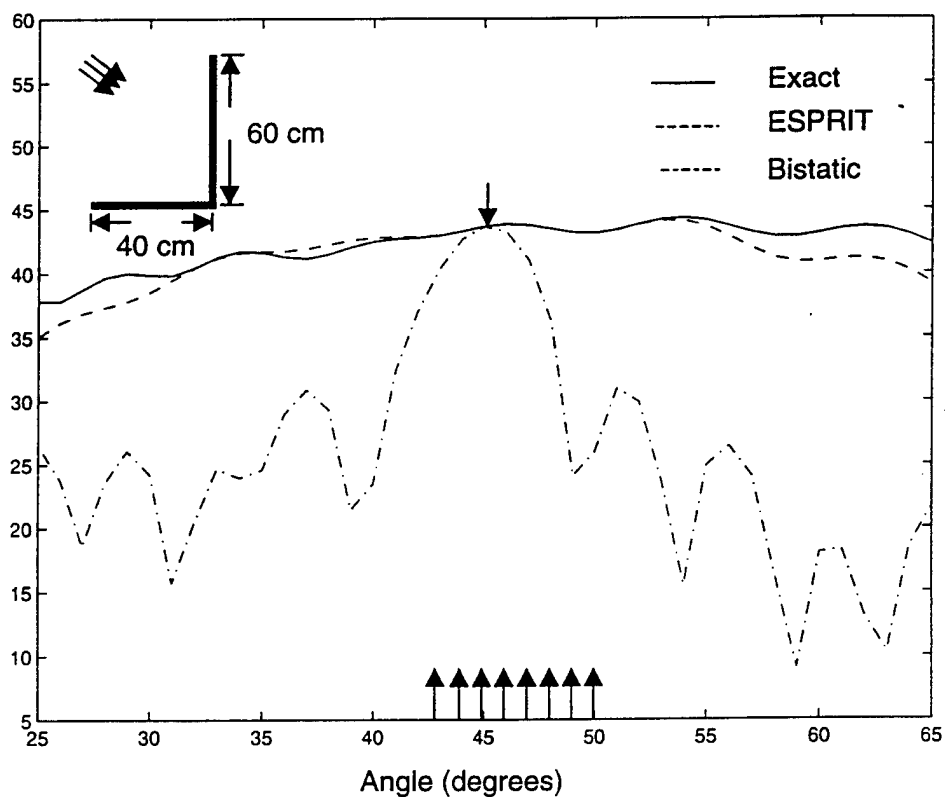
Figure 2 Comparison between the single-point bistatic approximation and the ESPRIT extrapolation results for the dihedral
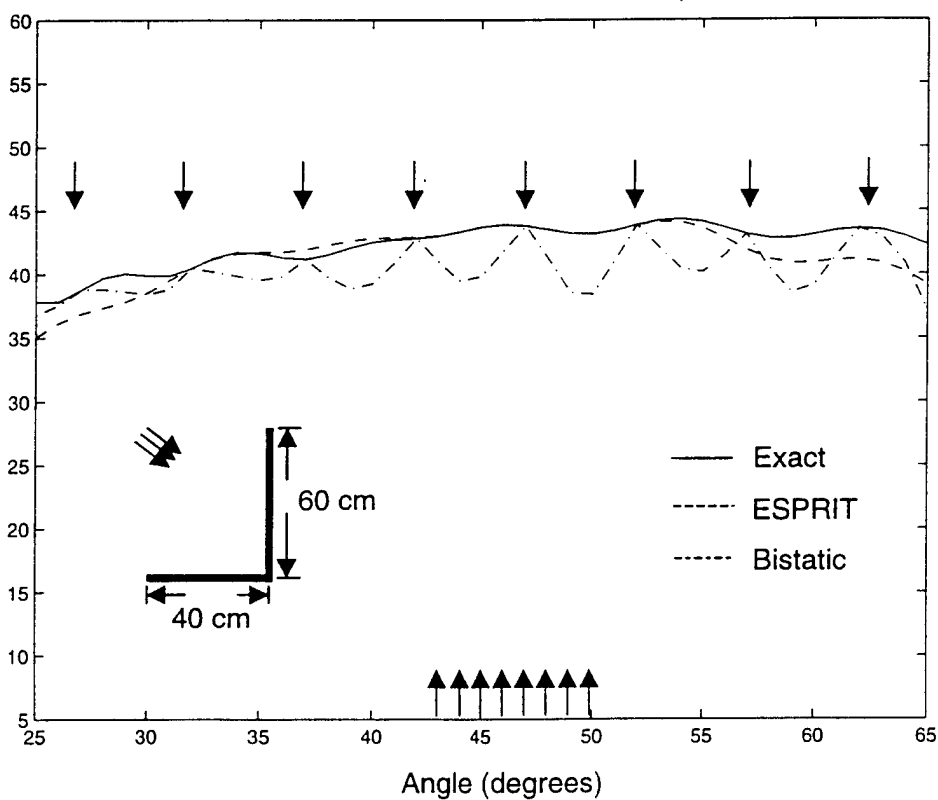
Figure 3 Comparison between the eight-point bistatic interpolation results and the ESPRIT extrapolation results for the dihedral

2-D MoM results. The first example is a 2-D dihedral corner reflector (shown in the inset of Fig. 2) that is 40 cm along the horizontal face and 60 cm along the vertical face. The frequency of the incident wave is 3 GHz. The RCS data versus angle are calculated by the MoM code between 25 and 65° (measured from the horizontal face). The data are plotted as the solid curve in Figure 2. A relatively isotropic scattering pattern is observed within this angular range. Using eight points evenly sampled between 43 and 50°, we carry out our extrapolation algorithm. The model order N used is 3. The extrapolated RCS data are plotted as the dashed curve in Figure 2. The ESPRIT result coincides well with the exact result, unless the extrapolation angles are too far removed. If we use the bistatic approximation with the incident angle at 45° to approximate the monostatic RCS in this range, the RCS data fall apart rapidly away from the center angle, as shown by the dash–dotted line in Figure 2. This is because the dominant double-bounce mechanism is not included in the bistatic model. Even if we calculate the bistatic field at eight points evenly distributed in the angular aperture and linearly interpolate the monostatic RCS in between, the result still deviates from the exact result once the interpolation angle is away from those calculated angles. This is illustrated in Figure 3.

A second example is a (circular cylinder)-(plate) scatterer shown in Figure 4. The diameter of the cylinder is 42 cm, and the length of the plate is 2 m. The distance between the origin of the cylinder and the plate is 62 cm. The calculation frequency is 3 GHz. In this structure, strong multiple-scattering mechanisms between the cylinder and the plate dominate the backscattering. The exact RCS data calculated by the MoM are plotted as the solid curve in both Figures 5 and 6. They consist of a total of 81 points from 25 to 65°. Only eight points between 43.5 and 47° are used for the ESPRIT extrapolation. The model order N used is 3. The result is plotted as the dashed curve in Figure 5, which agrees
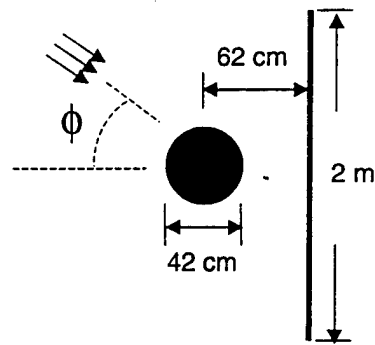

Figure 4 Geometry of the (circular cylinder)-(plate) target

well with the exact result. It is observed that some deviations occur when the extrapolation angle is beyond the range 35–55°. Using eight points evenly distributed in the angular aperture [25°, 65°], the bistatically interpolated result is plotted as the dashed curve in Figure 6. It can be seen that the result deviates significantly from the exact result between any two calculated angles. The beatings in the RCS curve are not well predicted.

IV. CONCLUSION

A model-based extrapolation algorithm has been proposed to generate multiangle RCS for iterative MoM solvers. An exponential model is used to incorporate the multiple-scattering mechanisms. The parameters of the exponential model are extracted using the ESPRIT superresolution algorithm. Once the model is found, it can be extended to predict the RCS at a wider range of angles. Numerical examples show that the extrapolation technique has robust performance for targets dominated by multiple-scattering mechanisms, while the standard bistatic approximation usually gives poor extrapolation/ interpolation results for this type of target. The accuracy of
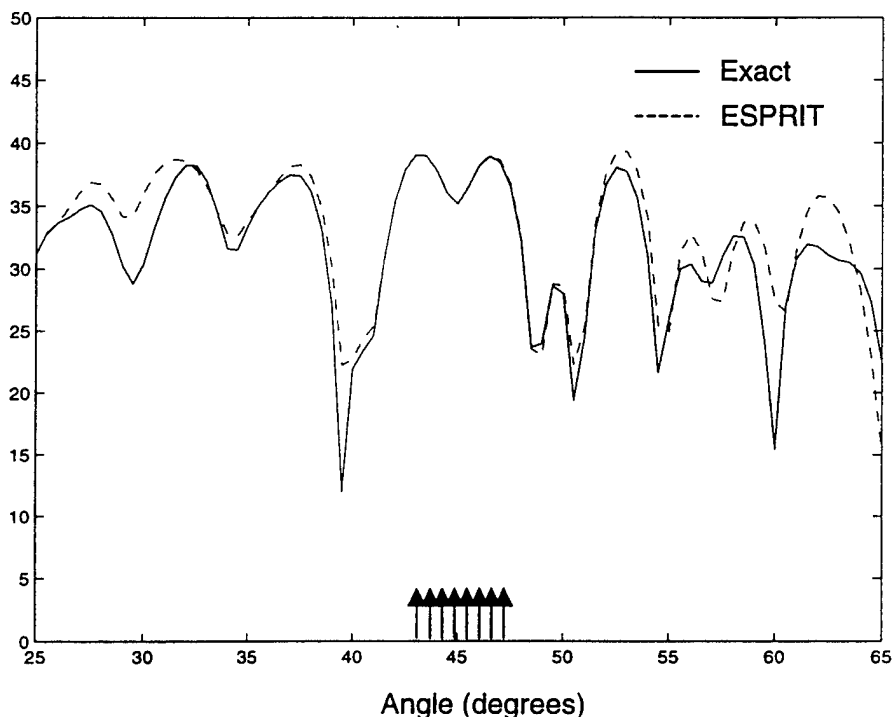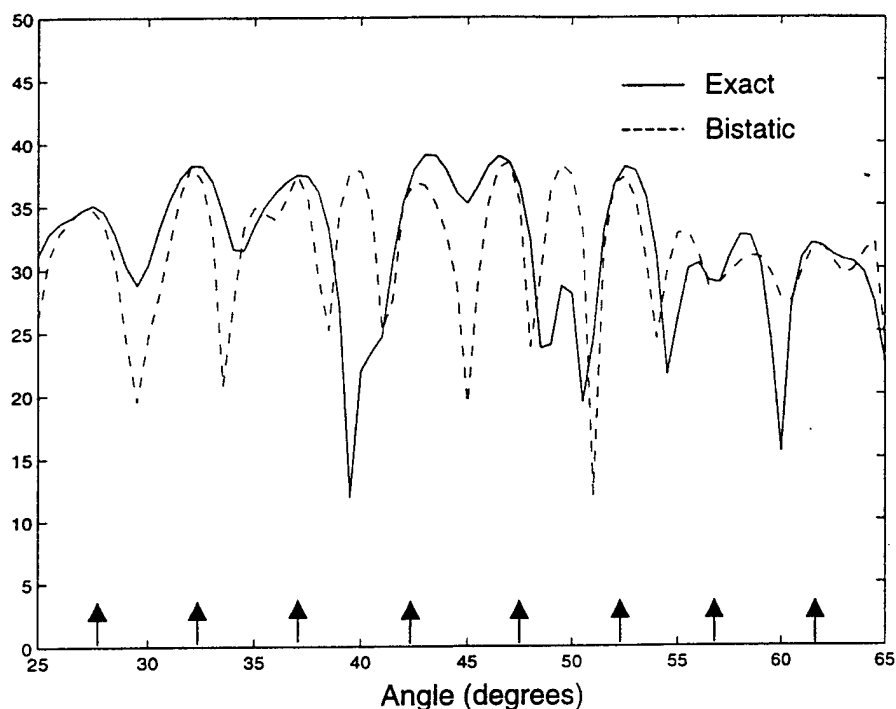

Figure 5 Comparison between the ESPRIT extrapolation result and the exact result for the cylinder plate

Figure 6 Comparison between the bistatic approximation result and the exact result for the cylinder plate

the present extrapolation algorithm is limited by the validity of the model, in which the small-angle approximation is implicitly assumed. It is expected that multiplicative speedup in time can be achieved when this algorithm is combined with the existing acceleration schemes for multiple RHSs [3, 4]. Finally, the angular extrapolation algorithm can be combined with previously proposed frequency extrapolation to generate 2-D frequency-aspect data for radar image formation. These topics are currently under study.

ACKNOWLEDGMENT

REFERENCES

1. R. Coifman, V. Rokhlin, and S. Wandzura, The fast multipole method for the wave equation: A pedestrian prescription, IEEE Antennas Propagat Mag 35 (1993), 7–12.
2. J. Song, C.C. Lu, and W.C. Chew, Multilevel fast multipole algorithm for electromagnetic scattering by large complex objects, IEEE Trans Antennas Propagat 45 (1997), 1488–1493.
3. C.F. Smith, A.F. Peterson, and R. Mittra, A conjugate gradient algorithm for the treatment of multiple incident electromagnetic fields, IEEE Trans Antennas Propagat 37 (1989), 1490–1493.
4. F.L. Ng, B. Shanker, E. Michielssen, J. Song, and W.C. Chew, A block seed biconjugate gradient algorithm for large electromagnetic scattering problems with multiple excitations, Center for Computational Electromagnetics Tech Rep, University of Illinois, July 1998.
5. R.E. Kell, On the derivation of bistatic RCS from monostatic measurements, Proc IEEE 53 (1965), 983–988.
6. R. Bhalla and H. Ling, ISAR image formation using bistatic data computed from the shooting and bouncing ray technique, J Electromag Waves Appl 7 (1993), 1271–1287.
7. M.J. Schuh, A.C. Woo, and M.P. Simon, The monostatic/bistatic approximation, IEEE Antennas Propagat Mag 36 (1994), 76–78.
8. R. Roy, A. Paulraj, and T. Kailath, ESPRIT—A subspace rotation approach to estimation of parameters of cisoids in noise, IEEE Trans Acoust, Speech, Signal Processing ASSP-34 (1986), 1340–1342.
9. Y. Wang, H. Ling, J. Song, and W.C. Chew, A frequency extrapolation algorithm for FISC, IEEE Trans Antennas Propagat 45 (1997), 1891–1893.
10. E.K. Miller, Model-based parameter estimation in electromagnetics: Part I. Background and theoretical development, IEEE Antennas Propagat Mag 40 (1998), 42–52.
11. R. Bhalla, H. Ling, and H. Nussbaum, Multi-aspect range profile extrapolation for the shooting and bouncing ray technique, J Electromag Waves Appl 10 (1996), 249–268.

ACSAR-ANTENNA COUPLING SYNTHETIC APERTURE RADAR IMAGING ALGORITHM

C. Ozdemir and H. Ling

Department of Electrical and Computer Engineering
The University of Texas at Austin
Austin, TX 78712-1084, USA

Abstract–A synthetic aperture radar imaging technique called AC-SAR for antenna coupling scenarios is introduced. It is shown that an ACSAR image of a platform can be formed by inverse-Fourier transforming the multi-frequency, multi-spatial coupling data between two antennas. Furthermore, we present a fast ACSAR imaging algorithm that is specifically tailored to the shooting and bouncing ray (SBR) technique. The fast algorithm is shown to reduce the total simulation time by several orders of magnitude without significant loss of fidelity. Finally, a sparse representation of ACSAR imagery is introduced by extracting the point radiators in the image. By parameterizing the ACSAR image, it is possible to reconstruct the 3-D ACSAR image and the 3-D frequency-spatial data with a very sparse set of radiation centers.

1. INTRODUCTION

The electromagnetic coupling between antennas on a complex platform is an important issue in antenna design. For an antenna designer, it is useful to identify the areas on the platform that cause strong coupling between the antennas. In this work, we set out to develop an imaging algorithm to pinpoint the dominant scattering locations on the platform that give rise to antenna interactions from the coupling data between antennas. Our approach to this problem is based on the Inverse Synthetic Aperture Radar (ISAR) concept. ISAR imaging is a standard technique to map the locations of dominant scattering off a target based on the multi-frequency, multi-aspect backscattered data [1,2]. We have extended this concept previously to the far-field antenna
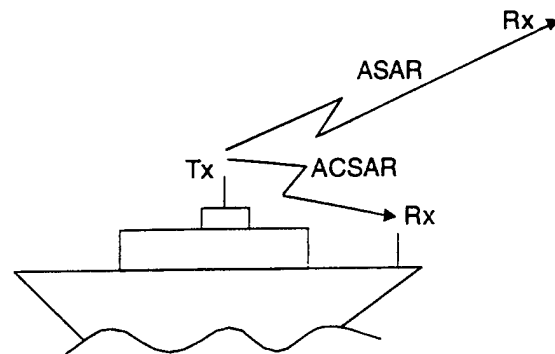
Figure 1. Comparison of the ASAR and the ACSAR scenario.

radiation problem by introducing the Antenna SAR (ASAR) imaging
algorithm [3]. An ASAR image of a platform maps the strong sec-
ondary radiators on the platform from multi-frequency, multi-aspect
radiation data in the far field. Such information can be useful to the
antenna designer in mitigating platform effects. In this paper, we ex-
tend the ASAR concept to the near-field antenna coupling problem by
generating the Antenna Coupling SAR (ACSAR) image of the plat-
form (see Fig. 1). By collecting the multi-frequency, multi-spatial cou-
pling data, it is shown that an ACSAR image of the platform can be
formed to display the dominant scattering locations on the platform.
To achieve the required spatial diversity, the data are collected on a
2-D grid at the receiver site.

   This paper is organized as follows. First, we derive the ACSAR
imaging algorithm. In Sec. 2, it is shown that under the single-bounce
and small-bandwidth approximations, a Fourier transform relationship
exists between the multi-frequency, multi-spatial coupling data and the
3-D locations of antenna-platform interaction. Hence, by 3-D inverse-
Fourier transforming the coupling data, it is possible to image these
scattering locations on the platform. This concept will be demon-
strated by using the computed frequency-spatial data from the Shoot-
ing and Bouncing Ray (SBR) technique [4–6]. In section 3, we present a
fast ACSAR imaging algorithm that is specifically tailored to the SBR
technique. By taking advantage of the ray tracing information within
the SBR engine, we demonstrate that a direct image-domain formation
is possible without resorting to multi-frequency, multi-spatial calcula-
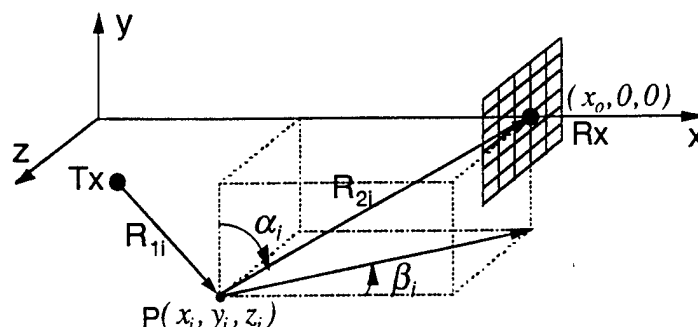tions. The image-domain formation algorithm can be further acceler-

Figure 2. The geometry for ACSAR imaging.

ated by the application of the fast fourier transform (FFT) algorithm. The fast algorithm is compared to the general frequency-aperture algorithm in several numerical examples. It is also shown that the total computation time can be reduced from hundreds of hours to minutes without significant loss of fidelity. In Sec. 4, we further present a sparse model to represent ACSAR imagery. By parameterizing the ACSAR imagery with a set of point radiators on the platform, it is possible to reconstruct the 3-D ACSAR image and the 3-D frequency-spatial data with a very sparse set of radiation centers.

2. ACSAR IMAGING ALGORITHM

2.1 Formulation

We shall first derive the general ACSAR imaging algorithm that utilizes multi-frequency, multi-spatial radiation data in the near-field region of the platform. We assume the transmitter and receiver setup as depicted in Fig. 2. At the receiver site, spatial diversity on a two-dimensional aperture centered at $(x_0, 0, 0)$ is used to achieve resolution in the two cross range dimensions. Similarly, to achieve down range resolution, frequency diversity is used. In addition to the direct radiation from the transmitter to the receiver, there are contributions from the antenna-platform interactions. The scattered electric field at the receiver site due to the scattering from a point $P(x_i, y_i, z_i)$ on the platform can be written as

$$E_s(k) = A_i \cdot e^{-jkR_{1i}} \cdot e^{-jkR_2} \tag{1}$$

where A_i is the strength of the scattered field, R_{1i} is the path length from the transmitter antenna to P, R_2 is the path length from P to the receiver and k is the free-space wave number. Next, we will make two approximations to the above equation to arrive at a Fourier-based imaging algorithm. The first assumption, commonly used in ISAR imaging, is that the radiation data are collected within a certain frequency bandwidth that is small compared to the center frequency of operation. We will further assume that the size of the aperture at the receiver site is small compared to path length R_2. Combining these assumptions, we can approximate the phase lag in the second exponential term as follows:

$$kR_2 \cong kR_{2i} + k_0(y\cos\alpha_i + z\sin\alpha_i\sin\beta_i) \tag{2}$$

where α_i and β_i are defined in Fig. 2, R_{2i} is the distance from P to the center of the 2-D aperture, and the variables y and z refer to spatial locations in the receiver aperture. The scattered electric field can thus be approximated by

$$E_s(k, y, z) = A_i \cdot e^{-jk(R_{1i}+R_{2i})} \cdot e^{-jk_0 \cdot y\cos\alpha_i} \cdot e^{-jk_0 \cdot z\sin\alpha_i\sin\beta_i} \tag{3}$$

In the above formula, a Fourier transform relationship exists between the variables (k, y, z) and $(R_i = R_{1i} + R_{2i}, \ u_i = k_0 \cdot \cos\alpha_i, \ v_i = k_0 \cdot \sin\alpha_i\sin\beta_i)$. By taking the 3-D inverse Fourier transform of the scattered field with respect to k, y, and z, we obtain a 3-D ACSAR image of the platform as follows:

$$
\begin{aligned}
\text{ACSAR}(R, u, v) &= \text{IFT}\left\{ E_s(k, y, z) \right\} \\
&= \text{IFT}\left\{ A_i \cdot e^{-jk \cdot R} \cdot e^{-jk_0 \cdot u} \cdot e^{-jk_0 \cdot v} \right\} \\
&= A_i \cdot \delta(R - R_i) \cdot \delta(u - u_i) \cdot \delta(v - v_i)
\end{aligned}
\tag{4}
$$

Therefore, by inverse Fourier transforming the multi-frequency, multi-spatial coupling data, the point scatterer P will manifest itself as a peak in the image at (R_i, u_i, v_i) with amplitude A_i. In practice, since the frequency bandwidth and the aperture size are not infinite, the actual spot size of the point scatterer will be inversely proportional to the frequency bandwidth and the aperture size. Note that we have not
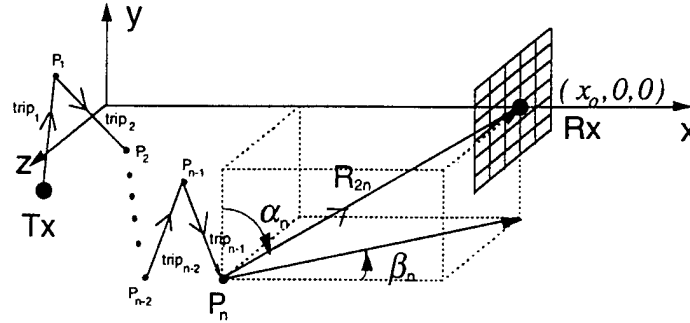
Figure 3. The geometry for a multiple bounce mechanism.

yet constructed the ACSAR image in the original (x, y, z) coordinates. However, it is straightforward to transform the ACSAR image from the (R, u, v) to the (x, y, z) coordinates by the following transformation formulas:

$$x = \frac{x_0^2 + R^2 - 2 \cdot R \cdot x_0 \cdot \sqrt{1 + c}}{2 \cdot (x_0 - R \cdot \sqrt{1 + c})} \tag{5a}$$

$$y = -\frac{(x_0 - x)}{\tan \alpha \cdot \tan \beta} \tag{5b}$$

$$z = \tan \beta \cdot (x_0 - x) \tag{5c}$$

$$c = \tan^2 \beta + \frac{1 + \tan^2 \beta}{\tan^2 \alpha} \tag{5d}$$

Since the transformation is not linear, it is not easy to estimate the distortion effect of the transformation on the ACSAR image. This issue will be addressed in the numerical examples as well in Sec 4.3. To summarize, the ACSAR imaging algorithm consists of three basic steps:

(1) Collect multi-frequency, multi-spatial coupling data $E_s(k, y, z)$,

(2) Take the 3-D inverse Fourier transform of $E_s(k, y, z)$ to form ACSAR(R, u, v),

(3) Use (5) to generate ACSAR(x, y, z), the image in the platform coordinates.

In the resulting ACSAR image, the dominant scattering points on the platform due to platform interactions between the transmitter and the receiver will be manifested as peaks.

Several comments are in order. First, the present Fourier-based imaging algorithm is derived based on small bandwidth and small aperture approximations. Since these assumptions are similar to those made in the ISAR imaging algorithm, no attempts have been made by us in this paper to quantify the errors related to these approximations. Second, the present ACSAR algorithm is based on the single-bounce assumption. Therefore, multiple-bounce mechanisms will not be mapped correctly in the resulting ACSAR image. This situation is similar to the standard ISAR algorithm. We shall discuss how the multi-bounce mechanisms are manifested in the ACSAR image to guide us in image understanding. We consider an n-bounce scattering mechanism as shown in Fig. 3. The corresponding scattered electric field for this mechanism is given by

$$E_s(k, y, z) = A \cdot e^{-jk(\mathrm{trip_{total}}+R_{2n})} \cdot e^{-jk_0 \cdot y \cos \alpha_n} \cdot e^{-jk_0 \cdot z \sin \alpha_n \sin \beta_n} \quad (6)$$

where $\mathrm{trip_{total}} = \mathrm{trip_1} + \ldots + \mathrm{trip_{n-1}}$ corresponds to the path that the wave travels from the transmitter to the last hit point and R_{2n} is the path length from the last hit point to the center of the aperture at the receiver site. By taking the 3-D inverse-Fourier transform of the above equation, we obtain a peak in the ACSAR image at (R_u, u_n, v_n) where $R_n = \mathrm{trip_{total}} + R_{2n}$, $u_n = k_0 \cdot \cos \alpha_n$ and $v_n = k_0 \cdot \sin \alpha_n \cdot \sin \beta_n$. We observe that this corresponds nearly to the last hit point on the platform. The u and v values (and the corresponding α and β angles) correspond exactly to those of the last hit points, while the R value corresponds to the cumulative delay of the mechanism. This means that a multiple-bounce mechanism will be mapped in the AC-SAR image as a point shifted from the last hit point on the platform in a direction opposite to $\hat{R}_{2n}$, the vector from the last hit point to the receiver. This effect will be seen in the example next. Finally, in the ACSAR algorithm derivation only the scattered field is considered. If the total field is applied to the algorithm, the direct radiation from the transmitter to the receiver will be imaged at the transmitter location. Since this peak will likely be the strongest one in the image, it may pose a dynamic range problem as the other scattering mechanisms due to antenna-platform interactions may be overshadowed. For simulation data, the isolation of the scattered field contribution from the direct antenna radiation is straightforward. For measurement data, a separate calibration run to measure the direct antenna radiation may be required to remove its contribution from the total field.
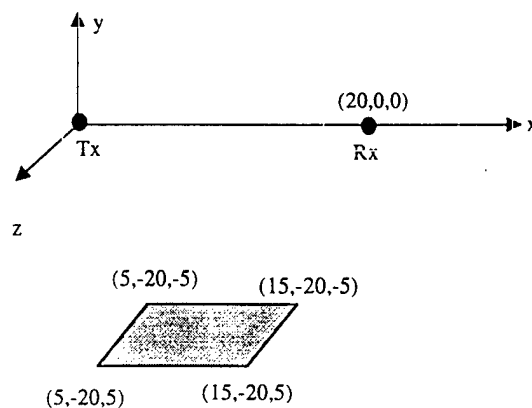
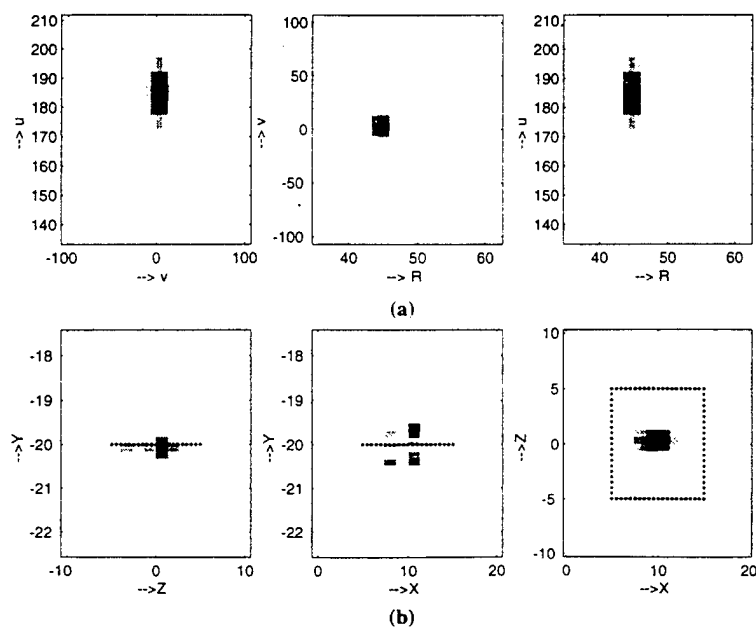**Figure 4.** The geometry of the plate test example.

Figure 5. 2-D projected ACSAR images for the plate. (a) In (R, u, v) coordinates, (b) In (x, y, z) coordinates.

2.2 Numerical Example

The algorithm presented above is first tested using a simple config-
uration shown in Fig. 4. The platform is a perfectly conducting square
plate of size 10m by 10m. The transmitter antenna is a half-wave
dipole (at 10 GHz) and is located 20m above the plate. A total of 32
frequencies are computed within a 0.35 GHz bandwidth at the center
frequency of 10 GHz. The simulation is carried out by a modified ver-
sion of the SBR code Apatch [6]. The scattered field is collected on an
aperture centered at (20m, 0, 0). The collection aperture consists of
$16 \times 32 = 512$ points, which range from -0.66m to 0.56m in 16 steps
along the y direction and from -0.46m to 0.44m in 32 steps along the
z direction. In the computed data only the scattered field from the
platform is considered and the primary radiation due to the antenna is
not included. Using the ACSAR algorithm, we first generate the 3-D
ACSAR images in (R, u, v) domain. While applying the algorithm, a
3-D Hanning window is used prior to the FFT operation to suppress
the sidelobes in the image. For display purpose, the 3-D ACSAR im-
age is projected onto the 2-D R-u, R-v and u-v plane as shown in
Fig. 5(a). To view the ACSAR image in the platform (x, y, z) coordi-
nates, we perform the necessary transformations in (5). The resulting
3-D ACSAR image is then projected onto the 2-D y-z, x-y, and x-z
planes as shown in Fig. 5(b). The dynamic range of the images is cho-
sen to be 35 dB. According to the geometry, we expect a peak in the
(x, y, z) image at (10m, -20m, 0) corresponding to the specular point
on the plate. The corresponding R, u and v values for this point are
(44.72m, 186.4, 0). We observe from Figs. 5(a) and 5(b) that the peak
occurs at the expected location. However, we notice that the specular
peak is not as well focused in the xyz-plane as the Ruv-plane. This
degradation is due to the additional (R, u, v)-to-(x, y, z) transforma-
tion.

As the second example, we used a much more complex test platform
called 'Slicy', whose CAD geometry is shown in Fig. 6. Slicy contains
a number shapes on top of the platform including a closed cylinder,
an open cylinder, a corner reflector and a step region. The platform
is assumed to be perfectly conducting. A half-wave dipole is used as
the transmitter and is placed at the origin. A total of 32 frequencies
are computed within a 0.19 GHz bandwidth at the center frequency
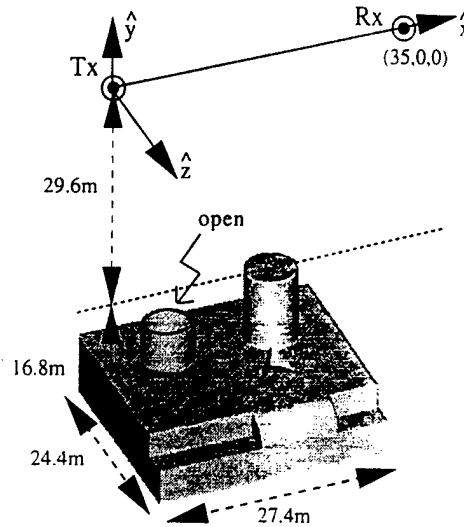of 10 GHz. The scattered field is collected on an aperture centered

Figure 6. The geometry of the test example Slicy.

at $(35m, 0, 0)$. There are $32 \times 32 = 1024$ spatial points on the aperture, ranging from $-1.14\,m$ to $1.14\,m$ along the y direction and from $-0.49\,m$ to $0.49\,m$ along the z direction. The total computation time for the SBR simulation is about 160 hours on an IBM RS6000/590 workstation. Using the ACSAR algorithm, we generate the 3-D ACSAR image for the configuration. Again, a 3-D Hanning window is used to suppress sidelobes. The 3-D ACSAR image projected onto the 2-D R-u, R-v and u-v planes are shown in Fig. 7(a). Fig. 7(b) shows the projected ACSAR image in the platform (x, y, z) coordinates along the y-z, x-y and x-z planes. Also plotted in the images is the platform overlay. The dynamic range of the images is 35dB. We observe that the dominant scattering is from the middle of the platform around the point (17.5m, -40m, 0). This is the expected specular point on the platform (labeled as mechanism (i)). Also apparent is the scattering off the curved region between two steps (mechanism (ii)). This mechanism appears to be quite diffused in the image. We believe this is due to the distortion effect from the transformation in (5). A technique to alleviate this effect will be discussed in Sec. 4.3. We also observe some scattering mechanisms from the open cylinder (mechanism (iii)). Since the open cylinder is expected to create multiple bounces, the contribution in the image is shifted in the direction away from the re-
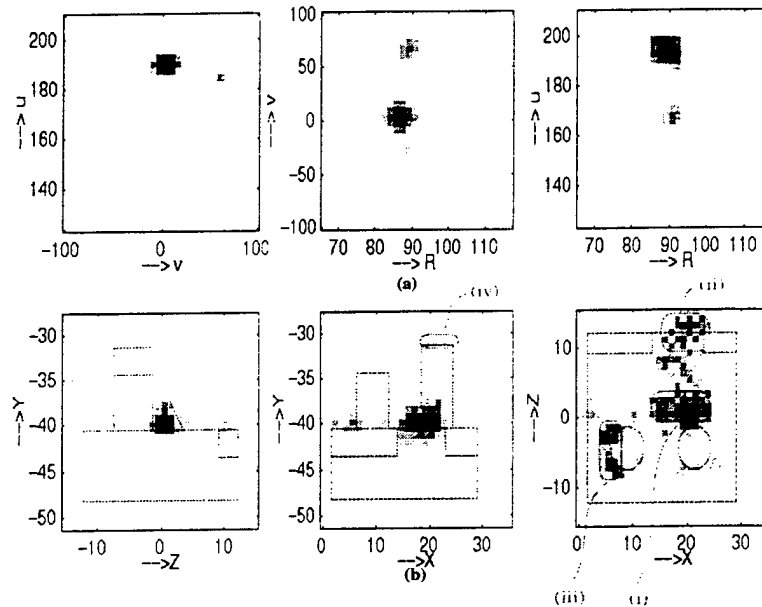
Figure 7. 2-D projected ACSAR images for Slicy   (a) In (R, u, v) coordinates.   (b) In (x, y, z) coordinates.

ceiver as discussed in the last section. As a result, it is located around the outside region of the open cylinder. Finally, the scattering off the top of the closed cylinder is labeled as mechanism (iv), although it is rather weak.

3. FAST ACSAR IMAGE GENERATION USING SBR

The ACSAR image formation algorithm discussed in the last section can be applied to either measurement or simulation data. In this section, we shall derive a fast ACSAR imaging algorithm specially tailored to the SBR technique. This is accomplished by utilizing the ray information within the SBR ray-tracing engine to generate the ACSAR image without resorting to any multi-frequency, multi-spatial calculations. We first derive an image-domain formula of ACSAR imaging [7]. Next, we implement a fast ray summation scheme [8,9] based on the image-domain formulation to reduce the total computation time. It is demonstrated that an ACSAR image can be simulated at a fraction of the time as the brute-force frequency-aperture approach.

3.1 Image-Domain Formulation of ACSAR Imaging

In applying the SBR technique to the antenna-platform interaction problem, rays are first shot from the phase center of the transmitter and traced according to geometrical optics. At the exit point of each ray before they leave the platform altogether, a ray-tube integration is carried out to find the contribution of each ray to the field at the receiver. Under this construct, the scattered near field can be written as:

$$E_s(k, \phi, \theta) = \sum_{i \text{ rays}} \frac{jk}{2\pi} \cdot C_i \cdot (\Delta A)_{\text{exit}} S(\phi, \theta) \cdot e^{-j\mathbf{k}\cdot\mathbf{r_A}} \qquad (7)$$

where $\mathbf{r_A}$ is the position vector from the last hit point A to the receiver, $(\Delta A)_{\text{exit}}$ is the cross section of the exit ray tube, $S(\phi, \theta)$ is the normalized radiation pattern from the ray tube and C_i is the field at the exit ray tube. For sufficiently small ray tubes, $S(\phi, \theta)$ can be assumed to be unity. In the image-domain formulation, we will assume that the frequency bandwidth is small compared to the center frequency and the aperture size at the receiver site is small compared to the path length from the last hit point to the receiver. With these assumptions, we have $\mathbf{k} \cdot \mathbf{r_A} \cong k \cdot R_2 + k_0 \cos\alpha \cdot y + k_0 \cdot \sin\alpha \sin\beta \cdot z$. We further assume that the platform is perfectly conducting. (For non-perfectly conducting platforms, this derivation still applies as long as the frequency bandwidth is small.) Using these assumptions, we can let

$$\frac{jk}{2\pi} \cdot C_i \cdot (\Delta A)_{\text{exit}} \approx \sigma_i \cdot e^{-jk\cdot(\text{trip})_i} \qquad (8)$$

where σ_i is assumed to be independent of frequency and $(\text{trip})_i$ is the total path that the i'th ray traveled from the transmitter to the last hit point. Consequently, the scattered electric field at the receiver can be written as

$$E_s(k, y, z) = \sum_{i \text{ rays}} \sigma_i \cdot e^{-jk(\text{trip}_i + R_{2i})} \cdot e^{-jk_0\cdot\cos\alpha_i\cdot y} \cdot e^{-jk_0\cdot\sin\alpha_i\sin\beta_i\cdot z} \qquad (9a)$$

or by the change of variables similar to that in Sec. 2, we have simply

$$E_s(k, y, z) = \sum_{i \text{ rays}} \sigma_i \cdot e^{-jkR_1} \cdot e^{-ju_i\cdot y} \cdot e^{-jv_i\cdot z} \qquad (9b)$$

Substituting the above equation to our ACSAR imaging formula, we

get

$$\mathrm{ACSAR}(R, u, v) = \mathrm{IFT}_3\{E_s(k, y, z)\}$$
$$= \sum_{i \text{ rays}} \sigma_i \cdot \mathrm{IFT}\{e^{-jkR_i}\} \cdot \mathrm{IFT}\{e^{-jy \cdot u_i}\} \cdot \mathrm{IFT}\{e^{-jz \cdot v_i}\}$$

$$(10)$$

The inverse-Fourier transform operations in (10) can be performed in closed form with the result

$$\mathrm{ACSAR}(R, u. v) = \sum_{i \text{ rays}} \sigma_i \cdot \{2\Delta k \cdot e^{jk_0(R-R_i)} \sin \mathrm{c}(\Delta k(R - R_i))\}$$
$$\cdot \{2k_0 \Delta y \cdot \sin \mathrm{c}(\Delta y(u - u_i))\}$$
$$\cdot \{2k_0 \Delta z \cdot \sin \mathrm{c}(\Delta z(v - v_i))\}$$

$$(11)$$

where Δk is the half bandwidth in frequency, Δy and Δz are the half-lengths of the aperture in y and z, respectively. We observe that the image-domain formulation gives the contribution of each ray to the total ACSAR image explicitly. Since σ_i, (x_i, y_i, z_i) are available from the ray tracing, it is straightforward to calculate the corresponding (R_i, u_i, v_i) values. Therefore, given $(\sigma_i, x_i, y_i, z_i)$ for each ray, we can form the ACSAR image directly by summing up the weighted 3-D sinc functions in (11).

3.2 Fast Algorithm

The image-domain expression of (11) is time consuming to carry out. We next apply a fast ray summation scheme to speed up the calculation in (11).We rewrite the image domain formula as

$$\mathrm{ACSAR}(R, u, v) = \sum_{i \text{ rays}} \rho_i \cdot h(R - R_i, u - u_i, v - v_i) \qquad (12a)$$

where $\rho_i = 8 \cdot \sigma_i \cdot k_0^2 \Delta k \cdot \Delta y \cdot \Delta z$ and $h(R, u, v)$ is the 3-D ray-spread function given by

$$h(R, u, v) = e^{jk_0 R} \sin \mathrm{c}(\Delta k \cdot R) \cdot \sin \mathrm{c}(\Delta y \cdot u) \cdot \sin \mathrm{c}(\Delta z \cdot v) \qquad (12b)$$

We can cast (12a) as a convolution between a 3-D weighted impulse

function and h as shown below:

$$ACSAR(R, u, v) = \left\{ \sum_{i \text{ rays}} \rho_i \cdot \delta(R - R_i, u - u_i, v - v_i) \right\} * h(R, u, v)$$
$$= g * h$$

(13)

To speed up the computation time of the convolution, we use an FFT-based fast scheme proposed by Sullivan [9]. Since the 3-D weighted impulse train g is not uniformly spaced, we first interpolate the function onto a uniformly sampled grid. To ensure the accuracy of computation, we oversample the grid at N times the Nyquist rate. For the interpolation, we use a linear approximation to update the closest eight neighbors depending on their distances from the location of the original impulse. The detail of this scheme can be found in [3] and will not be repeated here. After applying the interpolation scheme, the ACSAR image can be generated by

$$ACSAR(R, u, v) = IFFT_3(FFT_3(g_s(R, u, v)) \cdot FFT_3(h(R, u, v))\} \quad (14)$$

where FFT_3 and $IFFT_3$ are the three-dimensional forward and inverse fast Fourier transforms, respectively. The final $ACSAR(x, y, z)$ image can be generated using the transformations in (5).

3.3 Numerical Example

The fast approach presented above is applied to the same Slicy geometry that was used in the frequency-aperture approach. In the interpolation grid, an over sampling ratio of $N = 4$ is used in all three dimensions to ensure the accuracy of the computation. The results are depicted in Figs. 8(a) and 8(b) as 2-D projected ACSAR images in the three principal planes. Fig. 8(a) shows the images in the (R, u, v) coordinates, while Fig. 8(b) shows the images in the (x, y, z) coordinates. Again, a 3-D Hanning window is applied and the dynamic range of the images is chosen to be 35dB. By comparing these images with the images that are generated by using the frequency-aperture approach (Figs. 7(a) and 7(b)), we observe a fairly good agreement where all the key features are correctly simulated. The rms error between the frequency-aspect result and the image-domain result in the (R, u, v) domain is calculated to be 2.13%. The image-domain results lead to a
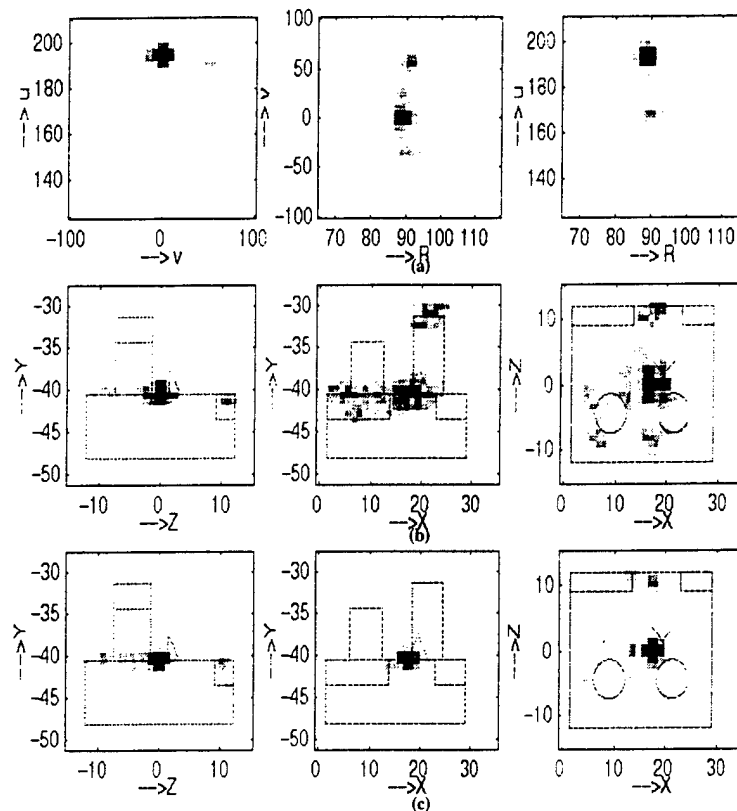
Figure 8. 2-D projected ACSAR images for Slicy using the fast algorithm. (a) Image formed in (R, u, v) coordinates, (b) Image transformed to (x, y, z) coordinates, (c) Image formed directly in (x, y, z) coordinates.

more focused image due to its small bandwidth approximation. This is consistent with our past experience from ISAR and ASAR algorithms. To show the time savings that we gain by using the image-domain approach, the total computation times of the frequency-aperture algorithm and the fast algorithm are compared in Table 1. The timings are divided into the ray-tracing time and the ray-summation time. As it can be seen from the table, the ray-tracing time of 9 minutes is the same for both approaches. Ray summation takes over 160 hours for the frequency-aperture approach and is the dominant portion of the

	Ray Tracing Time	Ray Summation Time	Total Time
Frequency-Aperture Approach	9 minutes	161 hours	161 hours
Fast Algorithm	9 minutes	6 minutes	15 minutes

Table 1. ACSAR simulation time for Slicy on an IBM RS6000/590 workstation.

total simulation time. The fast approach reduces the ray summation time to only 6 minutes.

In addition to large savings in simulation time, it is also possible to circumvent the image distortion effect due to the coordinate transformation by using the image-domain formulation. This is accomplished by generating the ACSAR image directly in the platform (x, y, z) coordinates in (12) instead of the (R, u, v) coordinates. To find the correct (x_i, y_i, z_i) position for a multi-bounce ray, we move along the direction opposite to the vector from the last hit point to the receiver. The amount of the shift is given by the cumulative trip of the ray. This has been discussed earlier in the image interpretation context in Sec. 2.1. In this manner, the image in the platform coordinate is updated one ray at a time using the 3-D ray-spread function in the (x, y, z) coordinate system, thereby eliminating the need to perform the transformation in (5). Fig. 8(c) shows the result of generating the image directly in the (x, y, z) coordinates. We observe that all the features are now much more focused than those in Fig. 8(b).

To summarize, we have demonstrated the feasibility to simulate AC-SAR imagery using the SBR technique very rapidly. This is achieved by a combination of the image-domain formulation and an FFT-based fast algorithm. Furthermore, we have shown that it is possible to form the image in the platform coordinates directly by using this approach. This eliminates the need to perform the required coordinate transformation which can defocus the features in the image.

4. A SPARSE REPRESENTATION OF ACSAR IMAGERY

4.1 Point Radiator Model of ACSAR Imagery

In simulating the ACSAR image of the platform using SBR, tens of thousands of rays are shot onto the platform. Yet, as we can see from the resulting data, the ACSAR images are in fact quite sparse. This is because the rays interfere with each other to give rise to strong coherent scattering over a small, localized area on the platform. Hence, it may be possible to accurately represent the ACSAR image by a finite set of point "radiation centers" on the platform. This concept is similar to the scattering center representation in radar scattering problems [10,11]. We shall adopt a point radiator model which has the same form of (12a) to parameterize the ACSAR image

$$\text{ACSAR}(x, y, z) = \sum_{\substack{n \text{ radiation} \\ \text{centers}}} A_n \cdot h(x - x_n, y - y_n, z - z_n) \qquad (15)$$

where $h(x, y, z)$ is given in (12b) and A_n is the strength of the point radiator located at (x_n, y_n, z_n). The remaining problem is to determine (A_n, x_n, y_n, z_n) to find a radiation representation for the image.

4.2 Extraction Using CLEAN

To perform the extraction process in (15), we apply the image-processing algorithm CLEAN. CLEAN is a well-known extraction algorithm first developed in radio astronomy [12], and has been successfully applied for scattering center extraction [10]. It is a robust technique that successively picks out the highest point in the image and removes its point-spread function (assumed to be the ray-spread function in our case) from the image. At the nth iteration of CLEAN, if the strength of the point scatterer is A_n, the 3-D residual image can be written as

$$[3 - \text{D Residual Image}]_{n+1} = [3 - \text{D Residual Image}]_n \\ - [A_n \cdot h(x - x_n, y - y_n, z - z_n)] \qquad (16)$$

The above iteration process continues until the highest point in the residual image falls below to a user-defined threshold. Once we extract
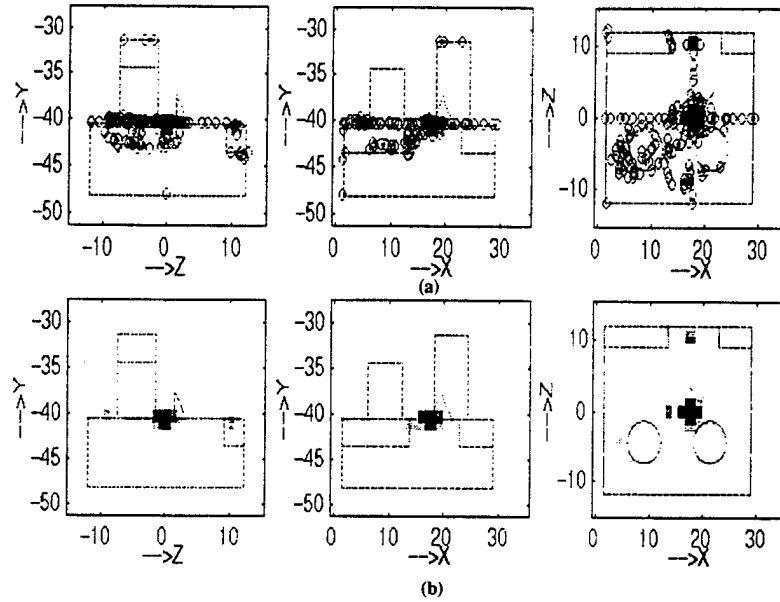
Figure 9. (a) The locations of the 150 extracted radiation centers, (b) 2-D projected ACSAR images reconstructed by using the extracted radiation centers.

the radiation centers from the image, we can reconstruct the multi-frequency and multi-spatial data by the formula:

$$E_s(k, y, z) = \sum_{\substack{n \text{ radiation} \\ \text{centers}}} A_n \cdot e^{-jk \cdot R_n} \cdot e^{-ju_n \cdot y} \cdot e^{-jv_n \cdot z} \qquad (17)$$

where (R_n, u_n, v_n) are related to (x_n, y_n, z_n) through the transformation described earlier.

We apply the CLEAN extraction algorithm to the 'Slicy' example. We extract a total of 150 point radiators from the 3-D ACSAR image shown in Fig. 8(c). The locations of the extracted radiation centers are projected on three different 2-D planes and are shown as small circles in Fig. 9(a). As it can be seen from the figures, most of the radiation centers are located on the platform at $y = -40\text{m}$. The remainders are located on the top of tall cylinder and around the step region. We then reconstruct the ACSAR image using the radiation centers and they are shown in Fig. 9(b). We use the same dynamic range of 35dB when
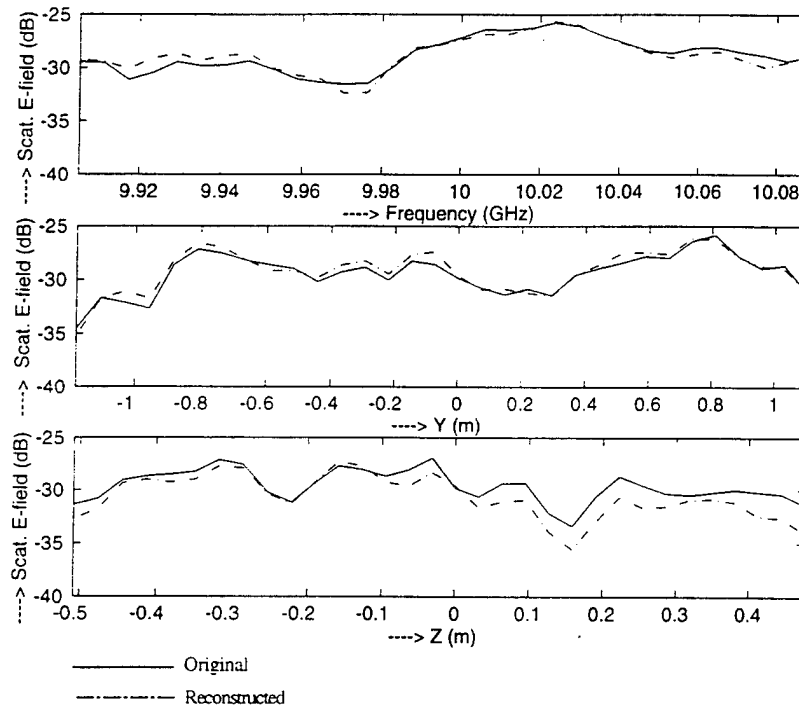
Figure 10. Comparison of the original and the reconstructed field patterns. (a) Frequency sweep at (35, 0, 0). (b) Spatial comparison at 10 GHz along (35. y, 0). (c) Spatial comparison at 10 GHz along (35, 0. z).

plotting the images. By comparing the reconstructed ACSAR images to the reference image in Fig. 8(c), we see that the reconstruction is good. The rms error between the original and the reconstructed ACSAR images is calculated to be less than 0.1%. Next, we reconstruct the frequency and the spatial data by using the formula in (17). The original (solid) and the reconstructed (dashed) patterns are shown in Fig. 10. In Fig. 10(a), the frequency sweep comparison is made at the center point of the receiver. In Fig. 10(b) and 10(c), the spatial variation comparisons are made at the 10 GHz center frequency along the y-axis and along the z-axis, respectively. We observe a fairly good agreement for the frequency-spatial reconstruction by using the radiation center model. Therefore, we can represent complex coupling
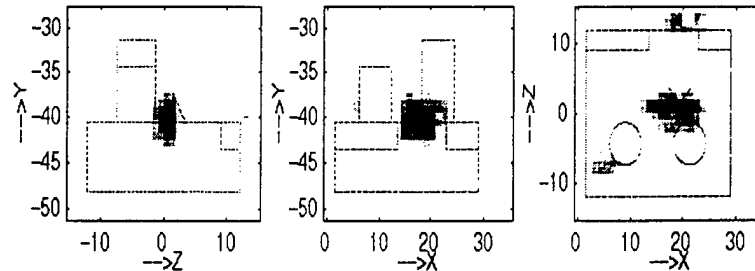
Figure 11. 2-D projected ACSAR images based on frequency-aperture data, formed by first parameterizing the (R, u, v) image using CLEAN and reconstructing the image in the (x, y, z) platform coordinates.

data between antennas on a platform by using only a small set of point radiators. Such sparse data representation may be useful for data compression and system simulation applications.

4.3. Eliminating Coordinate Transform Distortion Using CLEAN

We now describe a method that takes advantage of the CLEAN algorithm to eliminate the image distortion resulting from the (R, u, v) - to- (x, y, z) coordinate transformation in the frequency-aperture image formation algorithm described in Sec. 2. In Sec. 3.3, we have already shown that this can be accomplished by using the image-domain formulation. However, the approach is only applicable when coupled to the SBR simulation. When data from measurement or other types of computational electromagnetics simulators are used, we must adopt a different strategy. Our approach is to first parameterize the image in the (R, u, v) coordinate system using the CLEAN algorithm. Once the image is parameterized by radiation centers located at (R_n, u_n, v_n), we use (5) to find the corresponding (x_n, y_n, z_n) location of each radiation center in the platform coordinate. Then, the construction of the image in the platform coordinate is carried out using (15). Note that the main advantage of this approach is that the point-spread response in the final platform image is well-controlled. Consequently, the distorted point-spread response in the (x, y, z) coordinates is avoided in the platform image.

As an example, we apply this methodology to the ACSAR image in Fig. 7(a) by extracting a total of 150 radiation centers. After transforming these radiation centers into the platform coordinates, we form the ACSAR image directly in the (x, y, z) coordinates. The result is shown in Fig. 11. By comparing the new images to the images in Fig. 7(b), we observe that the mechanisms are much better focused using this approach. It is therefore the preferred step to generate the final platform image using the general frequency-aperture algorithm.

5. CONCLUSION

The ACSAR (antenna coupling synthetic aperture radar) imaging algorithm has been introduced to map platform scattering locations in antenna coupling scenarios. It is shown that under the single-bounce and small-bandwidth approximations, a Fourier transform relationship exists between the multi-frequency, multi-spatial coupling data and the 3-D locations of antenna-platform interaction. Hence, by 3-D inverse-Fourier transforming the coupling data, it is possible to image the scattering locations on the platform. This concept has been demonstrated by using the computed frequency-spatial data from the SBR technique. However, the algorithm is general and can be applied to other simulation data or even measurements. Furthermore, we have presented a fast ACSAR imaging algorithm that is specifically tailored to the SBR technique. By taking advantage of the ray tracing information within the SBR engine, we have demonstrated that a direct image-domain formation is possible without resorting to multi-frequency, multi-spatial calculations. The image-domain formation algorithm can be further accelerated by the application of the FFT algorithm. The fast algorithm has been shown to reduce the total simulation time from hundreds of hours to minutes without significant loss of fidelity. Finally, we have presented a method to extract a sparse point-radiator model to represent ACSAR imagery. This is accomplished by parameterizing the ACSAR image with a set of point radiators on the platform using the CLEAN algorithm. Once such a sparse set of radiation centers have been extracted, it is possible to reconstruct the 3-D ACSAR image and the 3-D frequency-spatial data very rapidly with good fidelity.

ACKNOWLEDGMENT

REFERENCES

1. Mensa, D. L., *High Resolution Radar Imaging,* Artech House, Dedham, MA, 1981.
2. Chen, C. C., and H. C. Andrews, "Target motion induced radar imaging," *IEEE Transactions on Aerospace and Electronic Systems,* Vol. AES-16. 2-14, Jan. 1980.
3. Ozdemir, C., R. Bhalla, L. C. Trintinalia, and H. Ling, "ASAR-Antenna synthetic aperture radar (ASAR) imaging," accepted for publication in *IEEE Trans. Antennas Propagat.,* June 1998.
4. Ling, H., R. Chou, and S. W. Lee, "Shooting and bouncing rays: calculating the RCS of an arbitrary shaped cavity," *IEEE Trans. Antennas Propagat.,* Vol. AP-37, 194-205, Feb. 1989.
5. Baldauf, J., S. W. Lee, L. Lin, S. K. Jeng, S. M. Scarborough, and C. L. Yu, "High frequency scattering from trihedral corner reflectors and other benchmark targets: SBR versus experiment," *IEEE Trans. Antennas Propagat.,* Vol. AP-39, 345-1351, Sept. 1991.
6. Lee, S. W., "Users manual for APATCH," version 1.0, DEMACO, Inc., Champaign, IL. Oct. 1992.
7. Bhalla, R., and H. Ling, "Image-domain ray-tube integration formula for the shooting and bouncing ray technique," *Radio Sci.,* Vol. 30, 1435-1444, Oct.-Sept. 1995.
8. Ozdemir, C., R. Bhalla, and H. Ling, "Fast ASAR image formation using the shooting and bouncing ray technique," *IEEE Antennas Propagat. Soc. Int. Symp.* Vol. 4, 2605-2608, July 1997, Montreal, Canada.
9. Sullivan, T. D., "A technique of convolving unequally spaced samples using fast Fourier transforms," Sandia National Laboratories, SAND89-0077, Jan. 1990.
10. Bhalla, R., and H. Ling, "Three-dimensional scattering center extraction using the shooting and bouncing ray technique," *IEEE Trans. Antennas Propagat.* Vol. AP-44, 1445-1453, Nov. 1996.

11. Bhalla, R., J. Moore, and H. Ling, "A global scattering center representation of complex targets using the shooting and bouncing ray technique," *IEEE Trans. Antennas Propagat.* Vol. AP–45, 1850–1856, Dec. 1997.

12. Segalovitz, A., and B. D. Frieden, "A 'CLEAN'-type deconvolution algorithm," *Astron. Astrophys.*, Vol. 36, 543–556, Apr. 1988.

Caner Ozdemir was born in Edremit, Turkey on March 29, 1971. He received the B.S.E.E. degree, in 1992, from the Middle-East Technical University (METU), Ankara, Turkey, and the M.S. and Ph.D. degrees in Electrical Engineering from the University of Texas, at Austin in 1995 and 1998, respectively. From 1992 to 1993, he worked as a project engineer at the Electronic Warfare office of the Turkish Military Electronics Industries (ASELSAN), Ankara, Turkey. From 1995 to 1998, he worked as a research assistant at the University of Texas, at Austin. He is currently with Allied Signals, Columbia, MD. His primary research interests are radar signal processing, electromagnetic scattering and computational electromagnetics.

Hao Ling was born in Taichung, Taiwan, on September 26, 1959. He received the B.S. degrees in electrical engineering and physics from the Massachusetts Institute of Technology, in 1982, and the M.S. and Ph.D. degrees in electrical engineering from the University of Illinois at Urbana-Champaign, in 1983 and 1986, respectively. He joined the faculty of the University of Texas at Austin in September 1986 and is currently a Professor in the Department of Electrical and Computer Engineering and holder of the Chevron Centennial Fellowship in Engineering. In 1982, he was associated with the IBM Thomas J. Watson Research Center, Yorktown Heights, NY, where he conducted low temperature experiments in the Josephson Program. While in graduate school at the University of Illinois, he held a research assistantship in the Electromagnetics Laboratory as well as a Schlumberger Fellowship. He participated in the Summer Visiting Faculty Program in 1987 at the Lawrence Livermore National Laboratory. In 1990, he was an Air Force Summer Fellow at the Rome Air Development Center, Hanscom Air Force Base. His research interests in electromagnetic scattering include radar cross section prediction and backscattered signature analysis for scattering mechanism interpretation and target identification applications. Dr. Ling is a recipient of the National Science Foundation Presidential Young Investigator Award in 1987 and the NASA Certificate of Appreciation in 1991.

ADAPTIVE ISAR IMAGE CONSTRUCTION FROM

UNEVENLY UNDERSAMPLED DATA

Yuanxun Wang and Hao Ling

Department of Electrical and Computer Engineering
The University of Texas at Austin
Austin, Texas 78712-1084

ABSTRACT

An adaptive approach is proposed to construct ISAR images from unevenly undersampled data in the angular domain. The algorithm uses an adaptive scattering feature extraction engine in place of the Fourier transform in the image construction procedure. The algorithm entails searching and extracting out individual target scattering features one at a time in an iterative fashion. Therefore the strong interference between different target scattering features can be reduced. After all the main features are extracted, they can be displayed in the same image plane without the aliasing effect in the final ISAR image. The algorithm is verified by constructing the ISAR image from the simulated point scatterer data as well as the chamber measurement data of the scaled VFY-218 airplane.

I. Introduction

Inverse Synthetic Aperture Radar (ISAR) imaging is a well-known tool for pinpointing target scattering features for signature diagnostic and target identification purposes. Constructing an ISAR image requires data collection in both the frequency and angular dimensions. If the data are evenly sampled and the sampling rate is dense enough, an ISAR image can be obtained by using a two-dimensional Fourier transform algorithm [1]. In this paper, we address the case when the angular data are unevenly undersampled. This scenario may arise in real-world data collection when the target is fast maneuvering with respect to the radar pulse repetition interval so that the angular look on the target by the radar is not dense enough to satisfy the Nyquist sampling rate. This will cause serious aliasing error in the cross range dimension if the regular Fourier transform is used. We propose an algorithm to overcome the aliasing effect in the cross range dimension and construct ISAR images from undersampled data. This algorithm can also be easily extended to deal with undersampling in both the frequency and angular domains.

The algorithm uses an adaptive scattering feature extraction engine in place of the Fourier transform in the image construction process. The original concept of adaptive feature extraction was proposed in [2,3]. It has been applied to ISAR image processing in the joint time-frequency space for resonant scattering mechanism extraction [4], target motion compensation [5] and Doppler interference removal [6]. In contrast to the Fourier transform where the signal is projected to all the image domain bases simultaneously, the adaptive algorithm searches and extracts the individual target scattering features one at a time in an iterative fashion. When applied to the present problem, the severe aliasing error caused by the interference between different target scattering features can be

avoided. Therefore, after all the main features are extracted, they can be displayed in the image plane without the aliasing effect in the final ISAR image. This paper is organized as follows. In Sec. II, we describe the adaptive feature extraction algorithm based on a point scatterer model. In Sec. III, we verify the algorithm by using simulated data consisting of point scatterers. In Sec. IV, the algorithm is further tested using the chamber measurement data of the model VFY-218 airplane [7]. It is found that a reasonable ISAR image can be constructed from seriously undersampled data. Finally, discussions on the limitation of the algorithm and some conclusions are given in Sec. V.

II. Adaptive Feature Extraction (AFE) Algorithm

In standard ISAR image construction, the target is assumed to be a collection of point scattering centers. Under the small-angle approximation, the scattered field from the target observed versus frequency and angle can be written as:

$$E(f,\theta) = \sum_{i=1}^{N} O(x_i, y_i) e^{-2jkx_i\cos\theta - 2jky_i\sin\theta} \cong \sum_{i=1}^{N} O(x_i, y_i) e^{-2jkx_i - 2jk_c\theta y_i} \quad (1)$$

where $O(x_i, y_i)$ is the amplitude of the ith scattering center, k is the free space wave number and k_c corresponds to the wave number at the center frequency. x_i and y_i denote the down range and cross range dimensions, respectively. We shall assume that the sampling in frequency is evenly spaced and dense enough to satisfy the Nyquist criterion. This is a reasonable assumption since the frequency parameter is completely controlled by the radar. Thus the range profile versus angle data can be generated from the frequency-aspect data by applying a 1-D Fourier transform (which can be implemented

using the FFT algorithm) along the frequency dimension. We shall denote the result as $R(x, \theta)$:

$$R(x, \theta) = \sum_{i=1}^{N} O(x_i, y_i) S_x(x - x_i) e^{-2jk_c y_i} \qquad (2)$$

In the above expression, $S_x(x-x_i)$ is the point spread function due to the finite-length frequency domain data. For example, for unwindowed frequency data the point spread function in down range is given by:

$$S_x = \Delta k \cdot \text{sinc}[\frac{\Delta k}{2}(x - x_i)] \cdot \exp(-j2k_c x_i) \qquad (3)$$

where Δk is the frequency bandwidth. Similarly, the cross range information can also be obtained from angular data via a 1-D Fourier transform of $R(x, \theta)$ along the angular dimension. The resulting image $I(x, y)$ is:

$$I(x, y) = \int R(x, \theta) e^{2jk_c y \theta} d\theta = \sum_{i=1}^{N} O(x_i, y_i) S_x(x - x_i) \int e^{2jk_c \theta (y - y_i)} d\theta \qquad (4a)$$

$$= \sum_{i=1}^{N} O(x_i, y_i) S_x(x - x_i) S_y(y - y_i)$$

where

$$S_y(y - y_i) = \int e^{2jk_c \theta (y - y_i)} d\theta \qquad (4b)$$

is the cross-range point spread function due to the finite-length angular domain data. In the ideal case, the target rotates at a constant velocity so that the observation angle is proportional to the dwell time and is sampled evenly. Thus the integral in (4b) can be calculated using an FFT algorithm. However, if the data are not evenly sampled in angle, the integration must be carried out numerically in place of the FFT algorithm. We shall

now turn our attention to the undersampling issue. If the data are sampled densely enough so that the numerical integration can be carried out accurately, the integration result S_y should be a well localized function with its peak at y_i while rapidly decaying away from the peak, similar to the point spread function S_x. Under this condition, the resulting image $I(x, y)$ will be a clean image with good indication of the amplitudes and positions of the target point scattering features. However, when the data are undersampled, the numerical integration in (4b) will result in large aliasing error that shows up as high sidelobes in S_y. Consequently, the constructed image will contain strong interference between the scattering features. This effect can be interpreted as the loss of orthogonality of the Fourier bases under the undersampled condition. For the scattering signal from a given target, the Nyquist sampling criterion requires the maximum interval between two consecutive angles be smaller than $\pi/k_c y_{max}$ where y_{max} is the maximum cross range dimension of the target. When this criterion is met, the sidelobe noise is outside the target region, and (4) gives the correct image of the target. Otherwise, the sidelobe noise will overlap with the target features, thus causing aliasing and corrupting the image.

In the proposed approach, we use an adaptive feature extraction algorithm in place of the Fourier processing. To avoid the sidelobe interference between different image bases, an iterative procedure is employed. Instead of projecting the signal onto all the exponential bases simultaneously, we search out the strongest point scattering feature in the cross-range domain and remove it from the original signal. Then the search is repeated for the remainder signal and the point scattering features are extracted one at a time until the energy of the residue signal is smaller than a preset threshold. The search

procedure is carried out by calculating the integral in (4b) for all the points in cross range but saving only the maximum value and position, i.e.,

$$[B_p, y_p] = \max_{y_p}[I_p(x, y)] \tag{5}$$

where p denotes the pth stage of the iterative procedure. The remainder signal is produced by subtracting out the pth feature:

$$R_{p+1}(x, \theta) = R_p(x, \theta) - B_p e^{-2jk_c y_p 6} \tag{6}$$

The convergence of the above procedure is guaranteed and the mathematical proof is given in [2]. The advantage of such an iterative procedure is that each time we extract out the strongest feature, we also eliminate its interference on the other features. It should be noted that unevenly sampling is a prerequisite to ensure that there is no ambiguity in the strongest features, since evenly undersampled data will result in multiple positions of the strongest features. After all the features are extracted out, we can construct an ISAR image using the amplitudes and positions of the point scatterers.

III. Test Results Using Simulated Data

To verify the algorithm, we first simulate scattering data using 11 point scattering centers with different amplitudes and positions. The radar center frequency is assumed to be 10.4 GHz and the bandwidth is 1 GHz. The total angular observation aperture is 5°. The frequency sampling is fixed at 256 points. The sampling in the angular domain is varied to compare the performance of the algorithm. Shown in Fig.1(a) is the ISAR image constructed using the Fourier transform from 128 evenly sampled points in the angular domain. No aliasing error occurs in the image because the angular sampling satisfies the

Nyquist rate. However, if the same 128 points are not evenly sampled within this fixed angular range, the sampling no longer satisfies the Nyquist rate because some of the intervals between two consecutive angles is greater than $\pi/k_c y_{max}$. Fig.1(b) is the ISAR image constructed using the Fourier transform from 128 randomly sampled angular data points. The aliasing effect can be clearly seen from Fig.1(b). It behaves like sidelobe noise smearing across the cross range dimension. The aliasing error gets more severe when fewer sampled points are used. This is illustrated in Fig. 2(a), which is the image obtained using the Fourier transform from 64 randomly sampled points in the angular domain. We next apply the AFE algorithm to the same set of undersampled data. The resulting image is plotted in Fig.2(b). Comparing Fig. 2(b) with the reference image in Fig. 1(a), we can see that the aliasing error is removed and the amplitudes and positions of all the scattering center features are well restored in the image through AFE. The performance of the AFE is further demonstrated when the angular sampling is lowered to 32 random points. The ISAR image constructed using the Fourier transform and the AFE algorithm are plotted respectively in Figs. 3(a) and 3(b). We observe that AFE is still able to remove the aliasing error in the image and restores all the point scattering features while the image obtained using the Fourier transform is badly overwhelmed by aliasing error.

IV. Test Results Using Measurement Data

To examine the applicability of the algorithm on real target scattering data, we reconstruct the radar image of a model (1:30 scale) VFY-218 airplane using undersampled chamber measurement data [7]. The original measurement data consist of

201 samples in a 40-degree azimuth aperture, and 401 samples in frequency from 8 GHz to 16 GHz. To construct an ISAR image, we first polar-reformat the frequency-aspect data to the (K_x, K_y) space, since the observation angular window involved is too large to use the small-angle approximation in (1). (However, for full-size targets the required angular swath is typically small enough so that polar reformatting is not very important.) The reformatted data consist of 401 samples in K_x and 438 samples in K_y. For the observation azimuth aperture from 110 degrees to 150 degrees, the ISAR image is first generated by FFT to the X-Y plane and is shown with the airplane overlay in Fig. 4. The point scattering features can clearly be seen. Next we test our algorithm by generating an undersampled data set in K_y. This is approximately the same as undersampling in angle. (Again, for full size targets, this approximation gets better.) Note that the original measurement data set is oversampled. We can downsample K_y by at most 12 times without violating the Nyquist sampling rate, which means at least 36 points must be evenly sampled in K_y. The test is conducted as follows. First we randomly choose 24 out of the 438 points (in this example, at [1, 27, 30, 36, 77, 79, 110, 143, 169, 199, 211, 260, 272, 280, 289, 320, 329, 333, 367, 378, 390, 420, 438]). Note that the maximum sampling interval is 49 points which is much larger than the Nyquist sampling of every 12 points. Serious aliasing occur if the regular Fourier transform algorithm is used, as shown by the ISAR image displayed in Fig. 5(a). All the features are overlapped with sidelobe noise so that no point scattering features on the airplane can be distinguished anymore. Next, we apply the AFE algorithm for each range cell of the image. The image is reconstructed and shown in Fig. 5(b). Comparing Fig. 5(b) with Fig. 4, we can see the main features of the airplane in Fig. 4 are all well reconstructed in Fig. 5(b). We do

observe some noisy spots outside the target at the lower dynamic ranges in Fig. 5(b). This low-level noise occurs at about 25dB down from the key features and presents a dynamic range limitation of the present AFE algorithm. We also notice that the weak dispersive cloud over the right wing of the airplane due to the exhaust duct in Fig. 4 does not appear fully in Fig. 5(b). The possible reason is that the algorithm assumes a point-scatterer basis, so dispersive returns may not be well reconstructed. The same test has been done for another set of observation angles. This time the radar observation angle is in the front of the airplane from 10 degrees to 50 degrees. The original ISAR image for this angle is plotted in Fig. 6. The images reconstructed from the undersampled data using the Fourier processing and the AFE are plotted respectively in Figs. 7(a) and 7(b). Again we observe a good reconstruction of the key scattering features in Fig. 7(b).

V. Conclusions and Discussions

An adaptive feature extraction algorithm has been proposed in place of regular Fourier processing in ISAR image construction from unevenly undersampled data. Based on a point scattering model of the target, the Nyquist sampling criterion could be overcome using this adaptive algorithm. The algorithm has been successfully tested using both simulated data and chamber measurement data. The images reconstructed from unevenly undersampled data agree very well with the original image without aliasing error. The algorithm has also been tested on measured data from in-flight targets with good success.

Three remarks are in order. First, although we have focused on the angular undersampling issue, the AFE algorithm can be easily extended to two dimensions to

process undersampled data in both the frequency and angular domains. Second, we expect the performance of the AFE algorithm to be strongly dependent on how well the model used reflects the real physical phenomenon. In this paper, the point scatterer model is assumed for AFE, which is a coarse approximation of real target scattering. It is also possible to apply AFE based on more sophisticated models such as point scatterers with frequency dependence. In that case, the basis functions in AFE can be extended to include a broader dictionary. The tradeoff is expected to be better performance at the expense of algorithm complexity. Third, as we have observed, the dynamic range the AFE algorithm can achieve is limited. The reason is that the manner in which the scattering features are selected in the algorithm is not without error. Both the amplitude and position of the strongest basis are in fact contaminated by sidelobes of the other weaker bases. Possible ways to improve the dynamic range, such as incorporating a relaxation procedure to modify the previously found scattering features [8], are currently being investigated.

References

[1] D. A. Ausherman, A. Kozma, J. L. Walker, H. M. Jones and E. C. Poggio, "Developments in radar imaging," *IEEE Trans. Aerospace Electronic Sys.*, vol. AES-20, pp. 363-400, July 1984.

[2] S. Qian and D. Chen, "Signal representation using adaptive normalized Gaussian functions," *Signal Processing*, vol. 36, pp. 1-11, Mar. 1994.

[3] S. G. Mallat and Z. Zhang, "Matching pursuits with time-frequency dictionaries," *IEEE Trans. Signal Processing*, vol. SP-41, pp. 3397-3415, Dec. 1993.

[4] L. C. Trintinalia and H. Ling, "Joint time-frequency ISAR using adaptive processing," *IEEE Trans. Antennas Propagat.*, vol. AP-45, pp. 221-227, Feb. 1997.

[5] Y. Wang, H. Ling and V. C. Chen, "ISAR motion compensation via adaptive joint time-frequency techniques," *IEEE Trans. Aerospace Electronic Sys.*, vol. AES-34, pp. 670-677, Apr. 1998.

[6] Y. Wang, H. Ling, and V. C. Chen, "Application of adaptive joint time-frequency processing to ISAR image enhancement and Doppler feature extraction for targets with rotating parts," *SPIE Proceedings on Radar Processing, Technology, and Application* , vol.3462, San Diego, CA, July 1998.

[7] H. T. G. Wang, M. L. Sanders and A. Woo, "Radar cross section measurement data of the VFY 218 configuration," Tech. Rept. NAWCWPNS TM-7621, Naval Air Warfare Center, China Lake, CA, Jan. 1994.

[8] J. Li and P. Stoica, "Efficient mixed-spectrum estimation with applications to target feature extraction," *IEEE Trans. Signal Processing*, vol. SP-44, pp. 281-295, Feb. 1996.
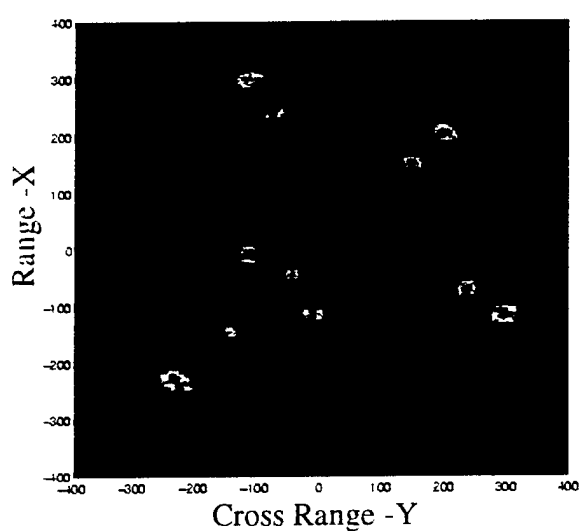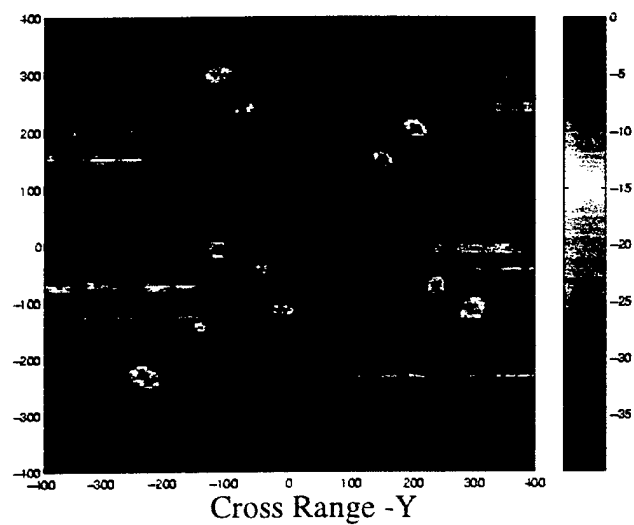
Fig.1. (a) Simulated ISAR image from 128 points evenly sampled in the angular domain using Fourier transform. (b) Simulated ISAR image from 128 points randomly sampled in the angular domain using Fourier transform.
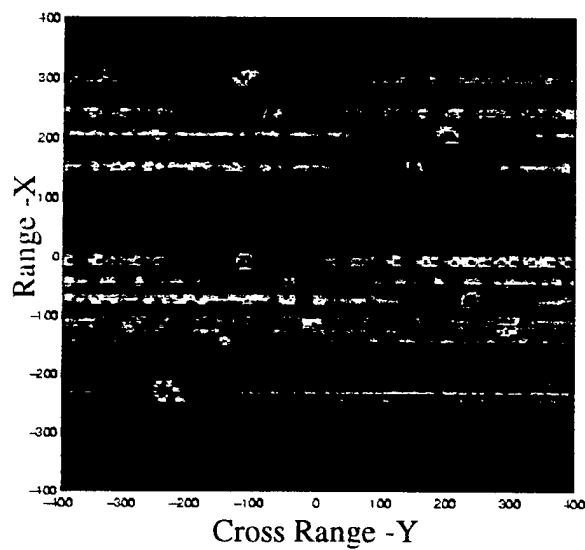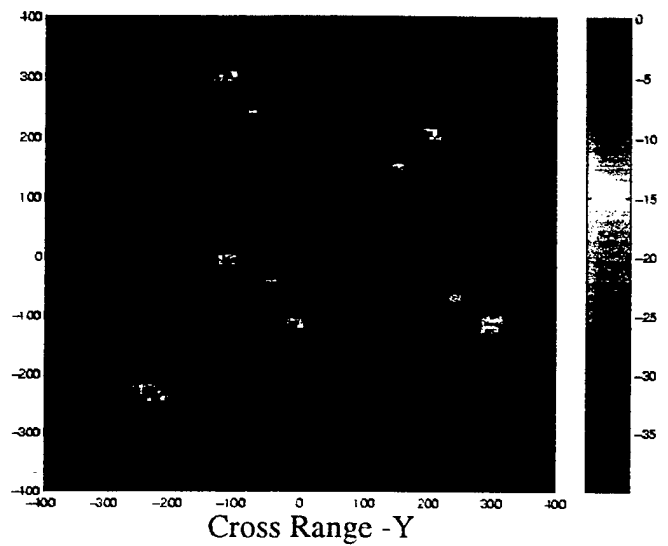
Fig.2. (a) Simulated ISAR image from 64 points randomly sampled in the angular
domain using Fourier transform. (b)Simulated ISAR image from 64 points
randomly sampled in the angular domain using the AFE algorithm.
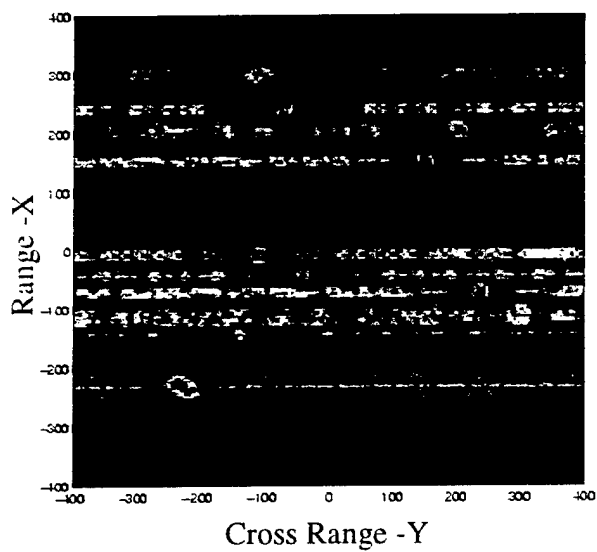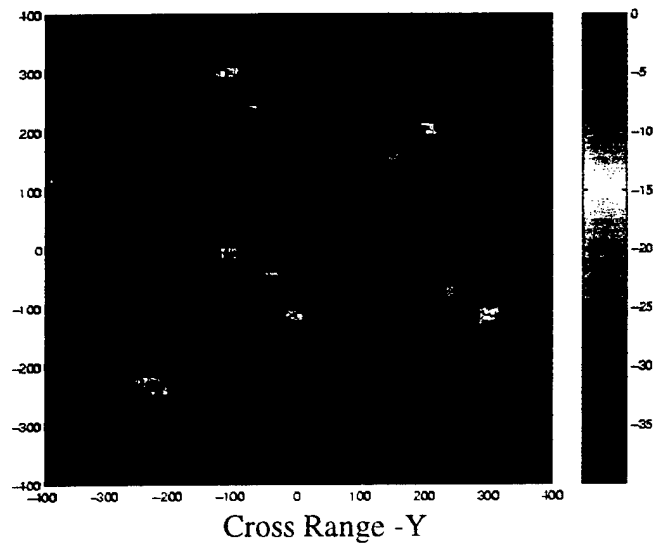
Fig.3. (a) Simulated ISAR image from 32 points randomly sampled in the angular domain using Fourier transform. (b)Simulated ISAR image from 32 points randomly sampled in the angular domain using the AFE algorithm.
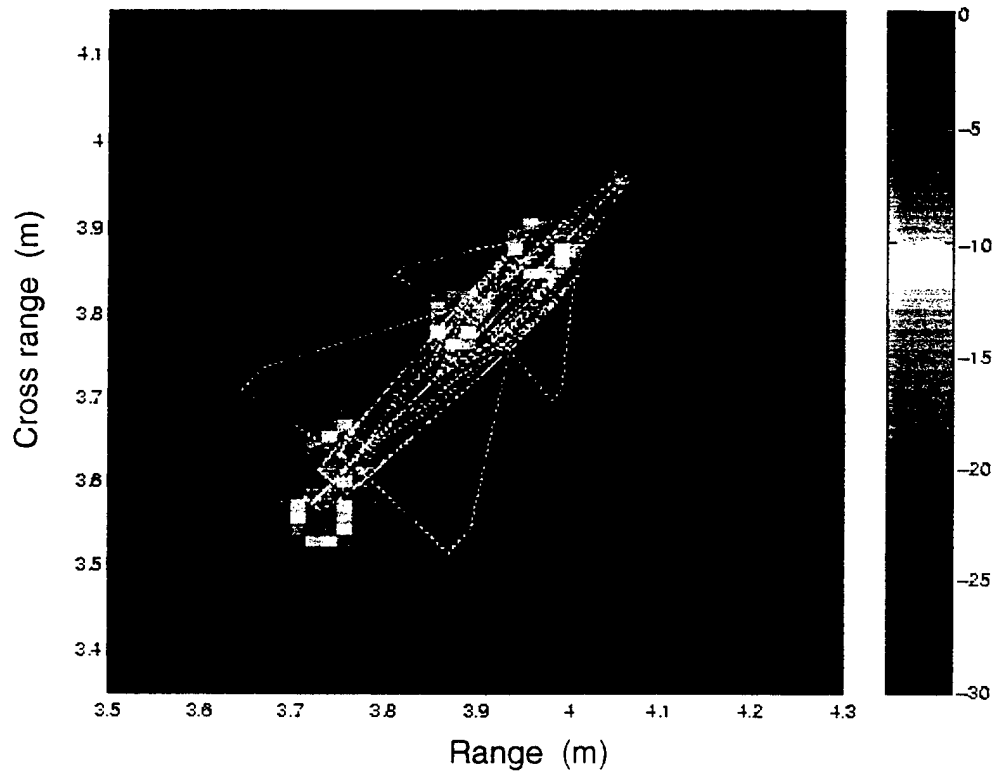
Fig.4 The ISAR image constructed at 130 degree azimuth from the original data using FFT .
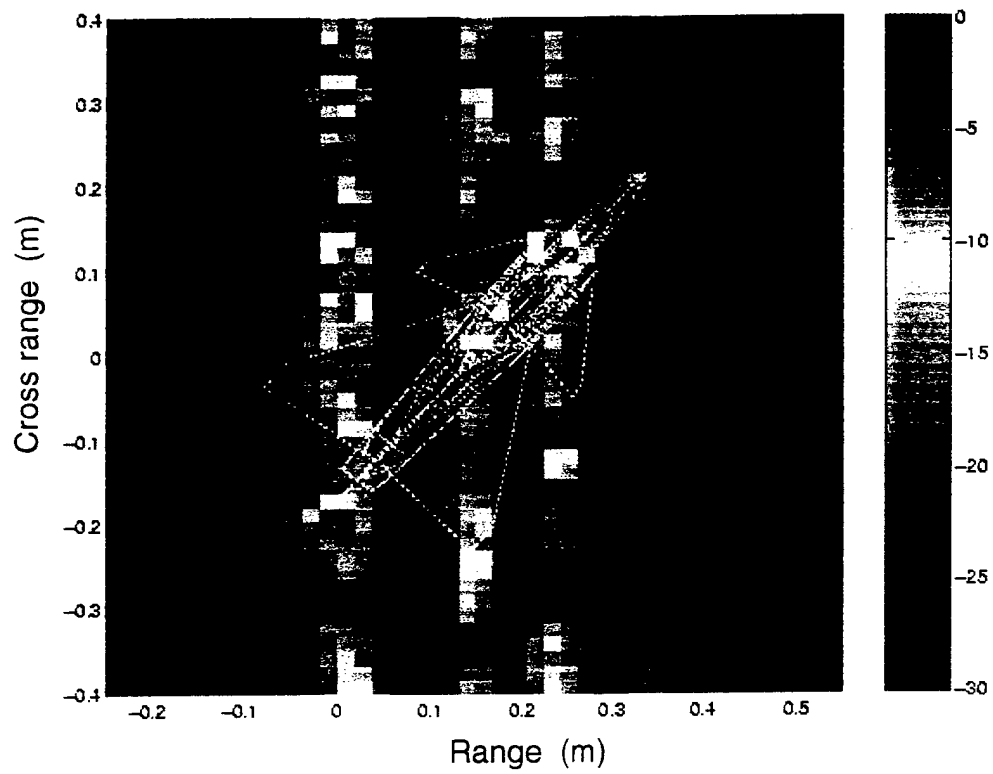
Fig.5(a) The ISAR image constructed at 130 degree azimuth from randomly undersampled data using Fourier transform.
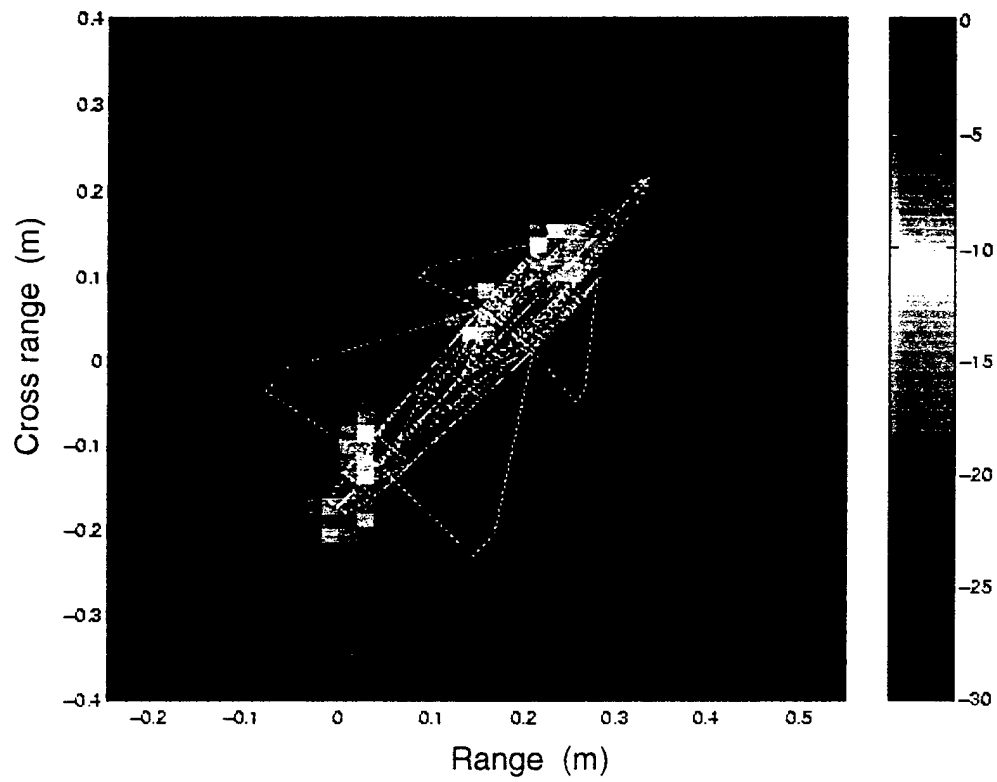
Fig.5(b) The ISAR image constructed at 130 degree azimuth from
randomly undersampled data using the AFE algorithm.
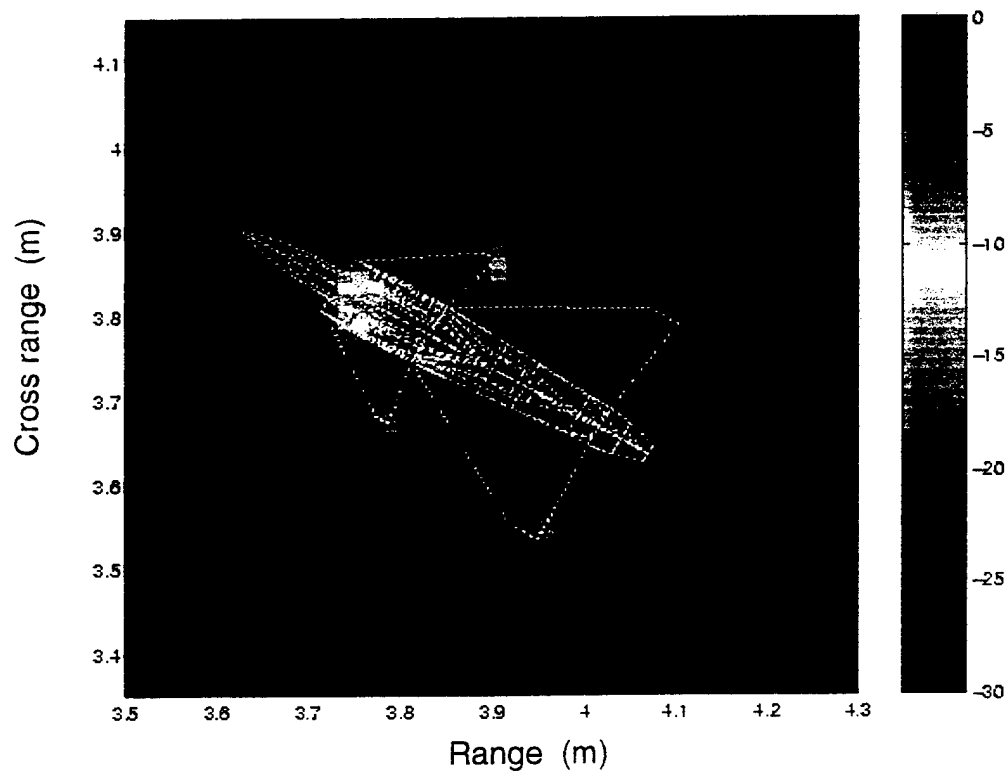
Fig.6 The ISAR image constructed at 30 degree azimuth from the original data using FFT .
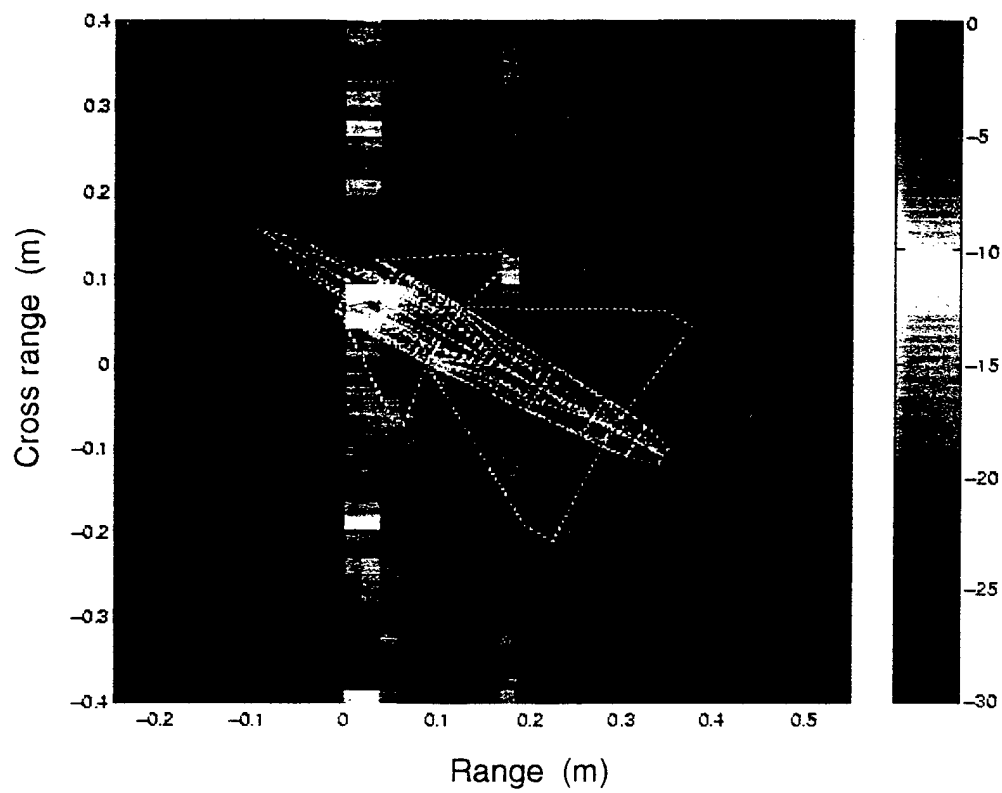
Fig.7(a) The ISAR image constructed at 30 degree azimuth from randomly
undersampled data using Fourier transform.
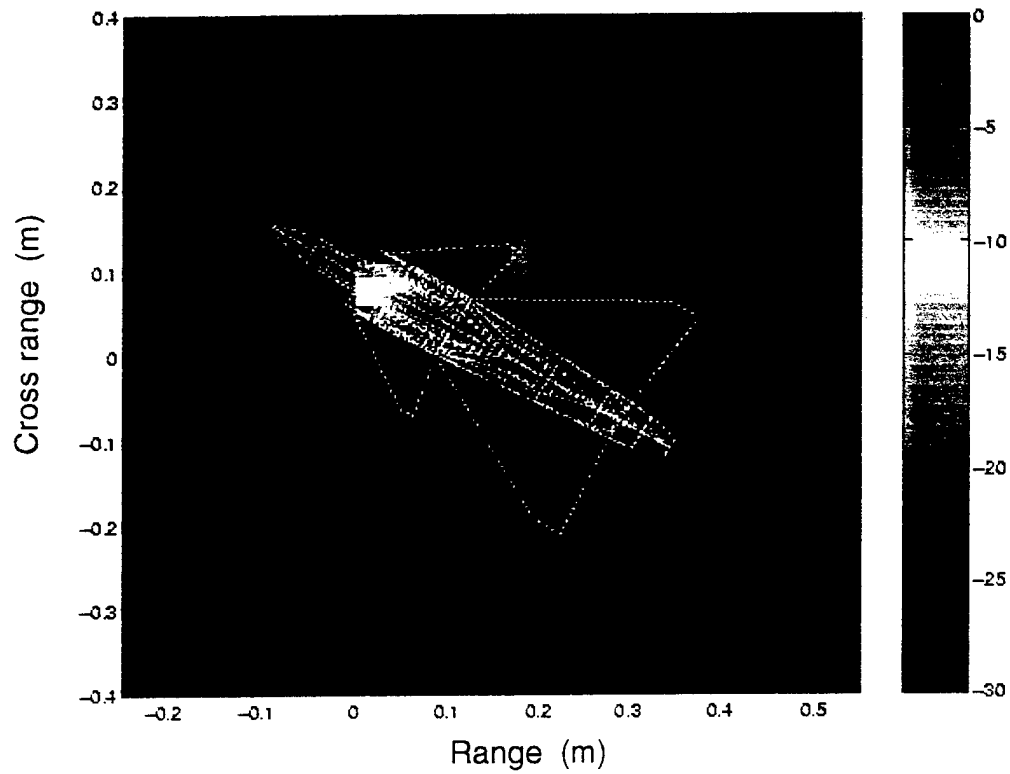
Fig.7(b) The ISAR image constructed at 30 degree azimuth from randomly
undersampled data using the AFE algorithm.

Determining the Equivalent Impedance Boundary Condition for

Corrugated Coatings Based on the Genetic Algorithm

Tao Su and Hao Ling
Department of Electrical and Computer Engineering
The University of Texas at Austin
Austin, TX 78712

Abstract

A methodology based on the genetic algorithm (GA) is proposed to determine the equivalent impedance boundary condition (IBC) for corrugated material coating structures. In this approach, rigorous solutions of the reflection coefficients at a number of incident angles are first calculated using a periodic method of moments (MoM) solver. The IBC model is used to predict the reflection coefficients at the same observation angles. The model coefficients are then optimized using GA so that the difference between the approximated and the MoM-predicted reflection coefficients is minimized. The genetic algorithm proves efficient in obtaining an optimal IBC model. The resulting IBC model can be readily incorporated into an existing computational electromagnetics code to assess the performance of the corrugated coating when mounted on complex platforms.

I. Introduction

It is well known that the impedance boundary condition (IBC) approximation is an efficient way to model complex structures such as material coatings and sub-skinline features [1-3]. It replaces the original volumetric structure with a surface impedance so that the problem dimension is reduced by one. Thus, large savings in computational resources can be achieved in the analysis of the original problem. However, to determine a simple IBC for an arbitrary structure that is valid over a wide range of incident angles, polarizations and frequencies is a non-trivial task. In this paper, we set out to develop a methodology to determine the equivalent IBC model for a corrugated coating structure backed by a conducting surface (see Fig. 1). The corrugation of the surface is assumed to be periodic in one dimension along the x-axis. Of interest is an IBC model that is valid over a large range of incident angles in both the θ and ϕ directions. Our objective is to establish a robust methodology such that the resulting IBC model can be used in place of the actual coating structure in subsequent analysis and design involving complex platforms.

The problem at hand is difficult since the scattering characteristics of the corrugated surface is strongly dependent on polarization and incident angle. The standard IBC used for flat coatings accounts for neither the aniostropic nor the angular behavior of the scattering characteristics of the corrugated surface. Some improved impedance boundary conditions have been proposed in the literature, including the tensor impedance boundary condition (TIBC) [1] and the generalized impedance boundary condition (GIBC) [2],[4]. TIBC usually works only for a very limited range of incident angles. GIBC improves the accuracy of the IBC model by including higher order derivatives of the fields on the

surface. However, it cannot be easily implemented in existing MoM solvers since it requires further reformulation in the integral equation. A resistive boundary condition (RBC) has been reported that works well over large incident angles for 2-D planar periodic surfaces [5]. However, it is limited to surfaces with very small periods. Furthermore, the choice for the position of the equivalent impedance surface is not obvious for the corrugated structure.

Our proposed approach to this problem is based on the genetic algorithm (GA). First, we compute the reflection coefficients from the corrugated surface over a number of incident angles and polarizations using a periodic method of moments (MoM) solver [6]. The resulting reflection coefficients constitute our reference data base. Next, a simple periodic IBC model is proposed. from which we can derive an expression for the reflection coefficients. In the GA step, we optimize the model coefficients so that the difference between the IBC-predicted and the MoM-predicted reflection coefficients is minimized. GA searches the entire parameter space in a way similar to natural evolution and arrives, after many generations, at the best parameters for the model.

This paper is organized as follows. In Section II, the MoM solution of the problem, the IBC model formulation and the GA optimization are discussed as the steps of the IBC determination. Numerical results are provided in Section III to verify the effectiveness of the approach in a number of corrugated geometries. A 3-D scattering example is also given to demonstrate the utility of the resulting IBC model.

II. Methodology for Determining the Optimal IBC Model

In this section, we describe the proposed methodology for determining the equivalent IBC of a corrugated coating using the genetic algorithm. In the first step, the reflection coefficients from the coating are computed using the MoM at multiple incident angles to serve as the reference data of the model. The MoM solution for the corrugated coating structure in Fig. 1 has been formulated earlier in [6]. The formulation entails dividing one cell of the grating into different homogeneous regions according to the material layers as shown in Fig. 2 (a). Boundary integral equations are first obtained for each region. Field continuity at region interfaces and periodic boundary conditions at cell boundaries are then enforced. The fields in the top half-space are expanded into a sum of Floquet harmonics and are matched to the fields in the lower region so that the reflection coefficients can be found.

In the next step, a periodic IBC model is proposed, from which we can derive an expression for the reflection coefficients. In the final step, the optimal parameters for the IBC model are obtained by minimizing the mean squared error between the two sets of reflection coefficients based on the genetic algorithm. These steps are described in detail below.

A. Periodic IBC model

The equivalent IBC relating the tangential electric and magnetic fields for a planar coated surface can be written as [1]:

$$\begin{bmatrix} E_z \\ E_x \end{bmatrix} = \begin{bmatrix} Z_{zz} & Z_{zx} \\ Z_{xz} & Z_{xx} \end{bmatrix} \begin{bmatrix} H_z \\ H_x \end{bmatrix} \tag{1}$$

We shall adopt this model for the corrugated problem due to its simplicity and usefulness for our applications. The model parameters will then be optimized to emulate the

properties of the exact structure. Note that since the corrugated surface exhibits anisotropic scattering characteristics, the equivalent IBC must also in general be anisotropic. Therefore, the cross impedance terms Z_{xx} and Z_{zz} are kept in our formulation to assess their importance. The boundary impedance Z_{zz}, Z_{zx}, Z_{xz}, and Z_{xx} are in general functions of incident angle and spatial position. For the IBC model to be useful for subsequent electromagnetic analysis, however, it is much preferable to model the boundary impedances as functions of spatial position only. We cannot prove theoretically the existence of such a model for an arbitrary corrugated structure. Instead, the applicability and limitation of this approach will be explored numerically in Section III.

In our IBC model, the periodic grating structure with period p as shown in Fig. 2 (a) is replaced by an equivalent impedance boundary condition which also has a period p, as illustrated in Fig. 2 (b). Each surface impedance term can be expanded into a Fourier series. Since the cross impedance terms Z_{zz} and Z_{xx} are usually very small, we shall treat them as constants and only expand the impedances Z_{zx} and Z_{xz} as

$$Z_{zx} = \sum_{n=-\infty}^{\infty} a_n e^{-j\frac{2\pi}{p}nx} , \qquad Z_{xz} = \sum_{n=-\infty}^{\infty} b_n e^{-j\frac{2\pi}{p}nx} . \tag{2}$$

Therefore, to fully describe the IBC model, we must determine the Fourier series coefficients $\{a_n\}$ and $\{b_n\}$.

B. Solution to the forward problem of scattering by the IBC model

Next, we derive the reflection coefficients resulting from the plane wave scattering from the IBC model given above. Under plane wave incidence where

$$k_{x0}^i = k_0 \sin\theta \sin\phi , \qquad k_{y0}^i = -k_0 \cos\theta \quad \text{and} \quad k_{z0}^i = k_0 \sin\theta \cos\phi ,$$

each component of the tangential electric and magnetic fields at the impedance surface can be expanded into a sum of Floquet harmonics [7]. For example, the tangential electric field in the z direction is expanded as

$$E_z = E_z^i e^{-jk_{x0}x} + \sum_{n=-\infty}^{\infty} E_{zn}^r e^{-jk_{xn}x} \tag{3}$$

where

$$k_{xn} = k_{x0} + n\frac{2\pi}{p}$$

is the propagation constant of the nth order harmonic along the x-direction. This Floquet harmonic is a reflected wave with propagation constants $(k_{xn},\ k_{yn}^r,\ k_z)$, where

$k_{yn}^r = \sqrt{k_0^2 - k_z^2 - k_{xn}^2}$ with the square root taken as positive real or negative imaginary. The superscripts i and r denote respectively the incident and reflected field throughout this paper. The harmonic term $e^{j\omega t}e^{-jk_z z}$ is suppressed in (3) and y is set to zero at the impedance surface for convenience. Assuming that the coefficients of the higher order Floquet harmonics are negligible, and applying this to other tangential field components, we get

$$F = F^i e^{-jk_{x0}x} + \sum_{n=-N}^{N} F_n^r e^{-jk_{xn}x} \tag{4}$$

where F can be E_z, H_z, E_x or H_x, and N is a positive integer. Substituting (2) and (4) into (1), and matching the coefficients of the exponential terms, we obtain a set of equations relating E_{zn}, H_{xn} and H_{zn}

$$E_z^i \delta_{n0} + E_{zn}^r = Z_{zz}H_{zn}^r + \sum_{m=-N}^{N} a_{n-m}H_{xm}^r + a_n H_x^i + Z_{zz}H_z^i \delta_{n0} \tag{5}$$

for $n = -N$ to N. δ_{n0} is the Kronecker delta. This set of equations can be written in matrix form as

$$E_z^i \mathbf{u}_N + \mathbf{E}_z^r = Z_{zz} \mathbf{H}_z^r + \mathbf{A} \mathbf{H}_x^r + H_x^i \mathbf{a} + Z_{zz} H_z^i \mathbf{u}_N \tag{6}$$

where

$$\mathbf{E}_z^r = \begin{bmatrix} E_{z,-N}^r & \cdots & E_{z0}^r & \cdots & E_{z,N}^r \end{bmatrix}^{\mathrm{T}},$$

$$\mathbf{H}_z^r = \begin{bmatrix} H_{z,-N}^r & \cdots & H_{z0}^r & \cdots & H_{z,N}^r \end{bmatrix}^{\mathrm{T}},$$

$$\mathbf{H}_x^r = \begin{bmatrix} H_{x,-N}^r & \cdots & H_{x0}^r & \cdots & H_{x,N}^r \end{bmatrix}^{\mathrm{T}},$$

$$\mathbf{A} = \begin{bmatrix} a_0 & \cdots & a_{-N} & \cdots & a_{-2N} \\ \vdots & \ddots & \vdots & \ddots & \vdots \\ a_N & \cdots & a_0 & \cdots & a_{-N} \\ \vdots & \ddots & \vdots & \ddots & \vdots \\ a_{2N} & \cdots & a_N & \cdots & a_0 \end{bmatrix}, \qquad \mathbf{a} = \begin{bmatrix} a_{-N} \\ \vdots \\ a_0 \\ \vdots \\ a_N \end{bmatrix}$$

and

$$\mathbf{u}_N = \begin{bmatrix} u_{-N} & \cdots & u_0 & \cdots & u_N \end{bmatrix}^{\mathrm{T}}, \qquad u_n = \delta_{n0}.$$

Following the same steps, we also arrive at the relationship for E_{xn}, H_{xn} and H_{zn}

$$\mathbf{B} \mathbf{H}_z^r = \mathbf{E}_x^r - Z_{xx} \mathbf{H}_x^r + E_x^i \mathbf{u}_N - Z_{xx} H_x^i \mathbf{u}_N - H_z^i \mathbf{b} \tag{7}$$

where

$$\mathbf{B} = \begin{bmatrix} b_0 & \cdots & b_{-N} & \cdots & b_{-2N} \\ \vdots & \ddots & \vdots & \ddots & \vdots \\ b_N & \cdots & b_0 & \cdots & b_{-N} \\ \vdots & \ddots & \vdots & \ddots & \vdots \\ b_{2N} & \cdots & b_N & \cdots & b_0 \end{bmatrix}, \qquad \mathbf{b} = \begin{bmatrix} b_{-N} \\ \vdots \\ b_0 \\ \vdots \\ b_N \end{bmatrix}$$

For a plane wave, the tangential components of the fields in the x-direction E_x, H_x can be expressed in terms of E_z and H_z as:

$$\begin{bmatrix} \mathbf{E}_x^r \\ \mathbf{H}_x^r \end{bmatrix} = [\mathbf{T}] \begin{bmatrix} \mathbf{E}_z^r \\ \mathbf{H}_z^r \end{bmatrix}, \quad \text{and} \quad \begin{bmatrix} E_x^i \\ H_x^i \end{bmatrix} = [\mathbf{T}^i] \begin{bmatrix} E_z^i \\ H_z^i \end{bmatrix} \tag{8}$$

where

$$\mathbf{T} = \begin{bmatrix} -\dfrac{k_{x,-N}k_z}{k_t^2} & 0 & -\dfrac{k_{y,-N}^r k_0}{k_t^2}\eta_0 & 0 \\ & \ddots & & \ddots \\ 0 & -\dfrac{k_{xN}k_z}{k_t^2} & 0 & -\dfrac{k_{yN}^r k_0}{k_t^2}\eta_0 \\ \dfrac{k_{y,-N}^r k_0}{k_t^2 \eta_0} & 0 & -\dfrac{k_{x,-N}k_z}{k_t^2} & 0 \\ & \ddots & & \ddots \\ 0 & \dfrac{k_{yN}^r k_0}{k_t^2 \eta_0} & 0 & -\dfrac{k_{xN}k_z}{k_t^2} \end{bmatrix}$$

and

$$\mathbf{T}^i = \begin{bmatrix} -\dfrac{k_{x0}k_z}{k_t^2} & -\dfrac{k_{y0}^i k_0}{k_t^2}\eta_0 \\ \dfrac{k_{y0}^i k_0}{\eta_0 k_t^2} & -\dfrac{k_{x0}k_z}{k_t^2} \end{bmatrix}, \qquad (k_t = \sqrt{k_0^2 - k_z^2})$$

Combine (6), (7) and (8), the matrix relationship between the incident and reflected fields is written as

$$\begin{bmatrix} \mathbf{E}_z^r \\ \mathbf{H}_z^r \end{bmatrix} = \left(\begin{bmatrix} \mathbf{I} & -Z_{xx}\mathbf{I} \\ 0 & \mathbf{B} \end{bmatrix} - \begin{bmatrix} 0 & \mathbf{A} \\ \mathbf{I} & -Z_{zz}\mathbf{I} \end{bmatrix}[\mathbf{T}] \right)^{-1} \left(\begin{bmatrix} 0 & \mathbf{a} \\ \mathbf{u}_N & -Z_{zz}\mathbf{u}_N \end{bmatrix}[\mathbf{T}^i] + \begin{bmatrix} -\mathbf{u}_N & Z_{xx}\mathbf{u}_N \\ 0 & \mathbf{b} \end{bmatrix} \right) \begin{bmatrix} E_z^i \\ H_z^i \end{bmatrix}$$

$$\tag{9}$$

In (9), the z components of the scattered field can be directly related to those of the incident field. We can therefore define the reflection coefficients for the different polarizations as:

$$R_n^{TM-TM} = \left.\frac{E_{zn}^r}{E_z^i}\right|_{H_z^i=0} \quad , \qquad R_n^{TM-TE} = \left.-\frac{\eta_0 H_{zn}^r}{E_z^i}\right|_{H_z^i=0} \qquad .$$

$$R_n^{TE-TE} = \left.-\frac{H_{zn}^r}{H_z^i}\right|_{E_z^i=0} \quad , \qquad R_n^{TE-TM} = \left.\frac{E_{zn}^r}{\eta_0 H_z^i}\right|_{E_z^i=0} \qquad (10)$$

To summarize, the reflection coefficients from the IBC model can be calculated by using (9) and (10) if a_n and b_n are given. This relationship is utilized by the genetic algorithm to calculate the reflection coefficients for a given sample of $\{a_n\}$ and $\{b_n\}$ and compare them with the reference data obtained from the MoM solution to optimize the model parameters.

Two comments are in order. First, although the reflection coefficients are derived for the TE_z/TM_z polarizations, they can be easily transformed to the more conventional vertical(V) / horizontal(H) polarizations with respect to the surface. Second, we have assumed the position of the IBC surface is at $y = 0$ in the above formulation. However, if the IBC surface is at the position $y = -d$ (as shown in Fig. 2(b)), a factor of e^{-j2k_yd} should be multiplied to each of the reflection coefficients to arrive at the correct answer. It is well known that in general layered coating problems, there is not a preferred position for the impedance surface. The solution can sometimes be improved by applying the IBC at a position other than a natural interface in the structure [4]. Therefore, by including the position of the IBC surface as an additional tuning parameter in our IBC model, we can further improve the accuracy of the model.

C. Genetic algorithm to determine the optimal IBC parameters

In the genetic algorithm, the parameters to be optimized are first encoded into binary form. A set of the encoded parameters is known as a chromosome. The basic idea of GA is to generate a pool of chromosomes, discard the bad ones, keep the best ones and let them evolve to produce better chromosomes. The evaluation of each chromosome is performed by a cost function which, in this case, is chosen to be the mean squared error between the MoM computed reflection coefficients and those solved using (9) and (10) with the $(Z_{zz}, a_n, b_n, Z_{xx}, d)$ parameters decoded from the corresponding chromosome. Chromosomes in the pool are ranked according to the cost function. The best ones are selected in pairs to act as parents of the next generation. Reproduction of children chromosomes is based on specific rules of heredity and mutation. The process of selection and reproduction is repeated until a set of satisfactory parameters is found or the generation limit is reached. The flow chart of the genetic algorithms is shown in Fig. 3. Detailed discussion of the genetic algorithms can be found in [8].

In the IBC model for the corrugated coating, the parameters to be optimized are the coefficients of the Fourier expansion a_n and b_n, the cross impedances Z_{zz}, Z_{xx} and the position of the impedance surface d. Each of the parameters a_n, b_n, Z_{zz} and Z_{xx} consists of a real part and an imaginary part. We assume a symmetric structure so that $a_n=a_{-n}$, $b_n=b_{-n}$. For an approximation truncated to the Nth order, the total number of real numbers is $4N+9$. The number of bits contained in each parameter B is adjustable. If B is too large, the convergence of GA will be slow. If B is too small, the accuracy of the calculation will suffer. In the examples given in this paper, we choose B = 8 to be efficient in both speed and accuracy. In order to encode the unknown parameters into binary form, the minimum and maximum possible values of each parameter are required. For example, the values

for the real and imaginary parts of the Fourier series a_n and b_n are estimated to be in the range from $-3\eta_0$ to $3\eta_0$, which is found to be reasonable in the numerical examples. Thus the 8-bit binary 00000000 denotes $-3\eta_0$ and 11111111 represents $3\eta_0$. Z_{zz} and Z_{xx} are relatively small and their real and imaginary parts vary from $-0.1\eta_0$ to $0.1\eta_0$. The distance d is limited between the upper and lower boundaries of the coating so that the resulting IBC model will not cause any ambiguity in its applications.

In the beginning of the genetic algorithm, a number of chromosomes are randomly generated. Each chromosome is decoded into parameters Z_{zz}, a_n, b_n, Z_{xx} and d. The reflection coefficients are then computed using (9) and (10). The cost function gives the mean squared error between these reflection coefficients and their corresponding MoM solution:

$$Cost = \sum_{\theta,\phi} \sum_{P_1,P_2} \left| R^{P_1-P_2} - R_0^{P_1-P_2} \right|^2$$

where R_0 denotes the MoM solution of the reflection coefficients at a specific observation angle (θ, ϕ) and P_1, P_2 is the polarization TE_z / TM_z (or V / H). The fitness value of each chromosome is given by

$$f(C_i) = c_1 - c_2 Cost(C_i)$$

where c_1 and c_2 are constants and C_i is the ith chromosome in the population. This fitness value is used in ranking the chromosomes and selecting of parents for the next generation [8-11]. There are several standard ways of selection. In this paper, the roulette wheel selection, in which the probability of each chromosome to be selected is proportional to its fitness value, is used.

After two chromosomes are selected, they mate to generate children. This is realized by the process of crossover, in which a break point is randomly chosen in the chromosomes and the two chromosomes are switched at that point. Mutation is imposed at this point so that new genes appear in the next generation. The mutation rate, which is the portion of bits to be randomly changed, is also an important parameter in GA. Experiments show that a mutation rate of 5-8% is often efficient in the calculation.

The process of evaluation, selection and reproduction is repeated until a desired mean squared error is achieved or a maximum generation is reached. For a population of 400 chromosomes, the 0th order IBC (ie. $N = 0$) takes 10-20 generations to converge to the optimum while the 2nd order IBC takes 200-400 generations.

III. Numerical Examples

In this section, some examples are presented to demonstrate the effectiveness of the method. The first example is a deep, triangular grooved grating with relatively small period. The geometry of one cell of the grating is shown in Fig. 4 (a) where the period $p = 0.067\lambda_0$ and $h_1 = 0.22\ \lambda_0$, $h_2 = 0.017\ \lambda_0$. The coating material is MagRAM with material constants $\varepsilon_r = 14.35 - j0.28$ and $\mu_r = 1.525 - j1.347$ at the frequency of 10 GHz. 17 observation angles are selected which include normal incidence and the combination of $\theta = 20°, 40°, 60°, 80°$ and $\phi = 0°, 30°, 60°, 90°$. In this example, we set Z_{xx} and Z_{zz} in (1) to zero and $N = 0$ in (4) to make the model comparable with TIBC. The co-polarization reflection coefficients for the H-pol and V-pol incidence are plotted in Figs. 5(a) and 5(b), respectively, and the H-V cross-polarization reflection coefficients are plotted in Fig. 5(c). In the figures, the x axis is divided into sections of different incident angle θ.

which varies from 5 to 85 degrees in steps of 10 degrees. In each of the θ section, the grating angle ϕ varies from 0 to 90 degrees. The matching of the reflection coefficients between the GA approach and MoM solution is good at most incident angles, even near grazing incidence. The value of d is found to be $0.027\lambda_0$ from the tip of the groove, or $0.21\lambda_0$ above the ground plane,. The TIBC result is also generated by using the reflection coefficient at normal incidence to derive the equivalent boundary condition. The impedance surface is placed at the plane of the conductor backing. It can be seen that the TIBC results deviate significantly from the reference solution away from normal incidence. With the same complexity of the boundary condition, GA achieves a much better matching because more observation points are used in the modeling and because of the additional degree of freedom in the position of the IBC surface.

Next, we compare the IBC approximations with and without the cross impedance terms Z_{xx} and Z_{zz}. The structure is a rectangular groove as shown in Fig. 4 (b) with a period $p = 0.17\lambda_0$ and a groove depth of $h_1 = h_2 = 0.042\lambda_0$. The material constants are $\varepsilon_r = 8.3\text{-}j2.4$ and $\mu_r = 2\text{-}j0.9$ at 10 GHz. The same observation points are used as in the previous example. The 0th order ($N = 0$) IBC is determined and the comparison between the reflection coefficients is illustrated in Fig. 6. With the cross impedance included, the accuracy of the approximation is improved.

In the third example, the IBC of different orders are obtained for the structure shown in Fig. 4 (b) where $p = 0.42\ \lambda_0$, $h_1 = 0.25\ \lambda_0$ and $h_2 = 0.17\ \lambda_0$. The coating material is the same as that in example 2 but the period is much larger and the groove is deeper. The reflection coefficients predicted by the 0th order and 2nd order model are plotted in Fig. 7. While the approximation by the 0th order model is fairly satisfactory, the 2nd order

model further improves the result and the matching is better at most incident angles. The price of the improvement is the computation time. For the 0th order modeling, it takes only a few minutes for the GA to converge while the 2nd order IBC takes more than 1 hour on an SGI O2 workstation (R10000/155MHz). Another consequence as the order of the model is increased is that the resulting IBC will show more spatial variation. This implies that when the IBC model is utilized in subsequent analysis using numerical electromagnetics solvers, the impedance surface must be divided more finely to faithfully describe the IBC. This will lead to a higher computation cost. Thus the higher order model is not recommended unless the 0th order one is intolerable or the period is large compared to the wavelength. Generally speaking, the IBC model can be improved by increasing the model order, whether or not the cross impedance terms exist. But with the cross impedance terms, the required model order is usually smaller than that without them.

We further investigate a structure with a period larger than half a wavelength, which results in higher order Floquet mode reflection at some incident angles. The rectangular groove shown in Fig. 4(b) has a period $p = 0.85\lambda_0$ and $h_1 = h_2 = 0.42 \lambda_0$. The material constant are $\varepsilon_r = 10.5\text{-}j2.2$ and $\mu_r = 2\text{-}j0.3$. The 0th and 1st order reflection coefficients are plotted in Figs. 8(a) and 8(b), respectively. It is shown that the Floquet modes are also well characterized.

In the final example, we investigate the limitation of the IBC model. We consider a triangular groove shown in Fig. 4(a) with $p = 0.33 \lambda_0$ and $h_1 = h_2 = 0.08\lambda_0$. The optimal IBC model is found using the genetic algorithm for different coating materials. A second order IBC model with cross impedance terms is used and the optimal model parameters

are determined by running GA to convergence. After the model is found, the root mean squared (RMS) error of the IBC-predicted reflection coefficients over the selected angles are computed. Fig. 9 shows the RMS error of the optimal IBC model as a function of ε_r' and ε_r'', which are the real and imaginary parts of the coating relative permittivity ε_r. μ_r is set to 1 for all the coatings. We observe that the IBC model works best for high contrast, high loss materials. For low contrast or low loss materials, the model error can be large. This behavior is very similar to conventional IBC models for planar coatings.

We now apply our derived IBC model to a 3D scattering problem. Consider the corner reflector as shown in Fig. 10. The monostatic radar cross section (RCS) is calculated for both the uncoated reflector and that coated with the MagRAM structure described in example 1. The groove of the coating is either parallel or perpendicular to the incident direction. Both cases are computed for comparison. Note that the solution for such a structure is very complicated if we try to use the exact MoM formulation. Instead, we use the 0th order impedance boundary condition obtained from example 1 to replace the corrugated absorber. We assume that the size of the plate remain the same after the IBC replacement. The RCS is computed using FISC [12], which is a 3D MoM code based on the fast multipole method [13]. Comparisons of the RCS at several elevation angles are shown in Fig. 11 for both the H- and V-polarizations. The result shows the effect of coating, which lowers the overall RCS level for both polarizations. We further observe that a 30 dB RCS reduction can be achieved for both polarizations over the range of elevation angles from 20 to 75 degrees if the grating is oriented parallel to the incident wave.

IV. Conclusions

In this paper, an impedance boundary condition model is derived based on the genetic algorithm to approximate arbitrary corrugated coating structures in scattering problems. The periodic structure is replaced by a periodic IBC on a virtual surface. The boundary impedance and the position of the surface are optimized by matching the reflection coefficients to the rigorous numerical solution at a number of incident angles. Similar to traditional IBC models, this approach is most effective when the coating material is high-loss and of high contrast. The resulting IBC model generated by this algorithm can be incorporated into an existing computational electromagnetics code to assess the performance of the corrugated coating when mounted on complex platforms.

Compared with other IBC approaches, the method described above has several advantages. First, the boundary impedance is assumed to be anisotropic so that the same model can be applied to oblique incidence from any arbitrary angles. Second, it is possible to build in spatial variation of the boundary impedance by adjusting the number of terms used in the Fourier series expansion. By using more terms, the IBC model can be made more accurate. In addition, the position of the impedance surface can also be optimized. By solving for the best position of the impedance surface as one of the model parameters, the accuracy of the model can be improved.

Numerical experiments show that the IBC approximation can be improved if some of the parameters of the genetic algorithm are carefully chosen. These parameters include the incident angles at which the rigorous solution is obtained, the range of each model parameter and the mutation rate, etc. The genetic algorithm can also be accelerated with carefully chosen parameters and a well designed cost function.

Acknowledgement

References

[1] D. J. Hoppe and Y. Rahmat-Samii, *Impedance Boundary Conditions in Electromagnetics*, Bristol: Taylor & Francis, 1995.

[2] T. B. A. Senior and J. L. Volakis, *Approximate Boundary Conditions in Electromagnetics*, London: Institution of Electrical Engineering, 1995.

[3] G. Pelosi and P. Y. Ufimtsev, "The impedance-boundary condition." *IEEE Antennas Propagat. Mag.*, vol. 38, pp. 31-34, Feb. 1996.

[4] T. B. A. Senior and J. L. Volakis, "Derivation and application of a class of generalized boundary conditions," *IEEE Trans. Antennas Propagat.*, vol. 37, pp. 1566-1572, Dec. 1989.

[5] K. W. Whites, R. Mittra, "Equivalent boundary-condition model for lossy planar periodic structures at low frequencies," *IEEE Trans. Antennas Propagat.*, vol. 44, pp. 1617-1629, Dec. 1996.

[6] J. Moore, H. Ling and C. S. Liang, "The scattering and absorption characteristics of material-coated periodic grating under oblique incidence," *IEEE Trans. Antennas Propagat.*, vol. 41, pp. 1281-1288, Sept. 1993.

[7] R. Petit, Editor, *Electromagnetic Theory of Gratings*, New York: Springer-Verlag, 1980.

[8] L. Davis, *Handbook of Genetic Algorithms*, New York: Van Nostrand Reinhold, 1991.

[9] R. L. Haupt, "An introduction to genetic algorithms for electromagnetics," *IEEE Antennas Propagat. Mag.*, vol. 37, pp. 7-15, Apr. 1995.

[10] D. S. Weile and E. Michielssen, "Genetic algorithm optimization applied to electromagnetics: a review," *IEEE Trans. Antennas Propagat.*, vol. 45, pp. 343-353, Mar. 1997.

[11] G. Winter, J. Periaux, M. Galan and P.Cuesta, *Genetic Algorithms in Engineering and Computer Science*, New York: Wiley, 1995.

[12] *User's Manual for FISC (Fast Illinois Solver Code)*, Center of Computational Electromagnetics, Univ. of Illinois, Champaign, IL, and DEMACO, Inc., Champaign, IL, Jan. 1997.

[13] J. M. Song and W. C. Chew, "Fast multipole method solution using parametric geometry," *Microwave Opt. Tech. Lett.*, vol. 7, pp. 760-765, Nov. 1994.
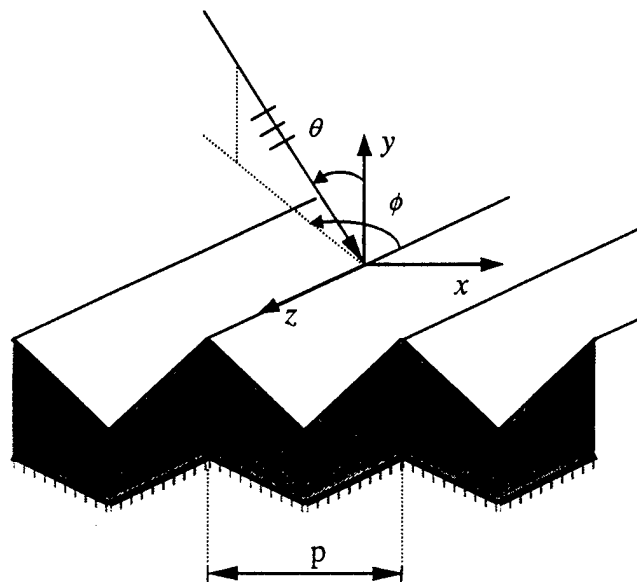
Fig. 1. Scattering from a corrugated coating structure backed by a conducting surface

(a) Original structure   (b) IBC Approximation
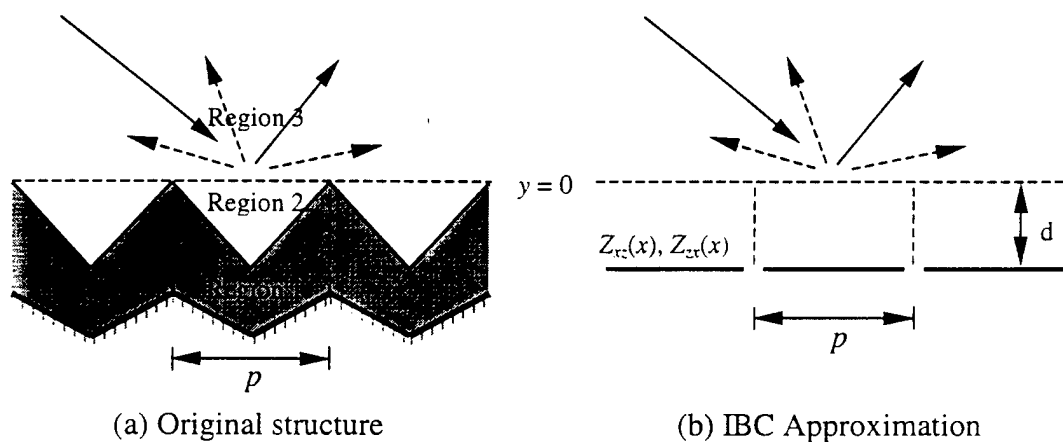
Fig. 2. Equivalent impedance boundary problem

Fig. 3. Flow chart of the genetic algorithm

(a) triangular groove　　　　　　(b) rectangular groove
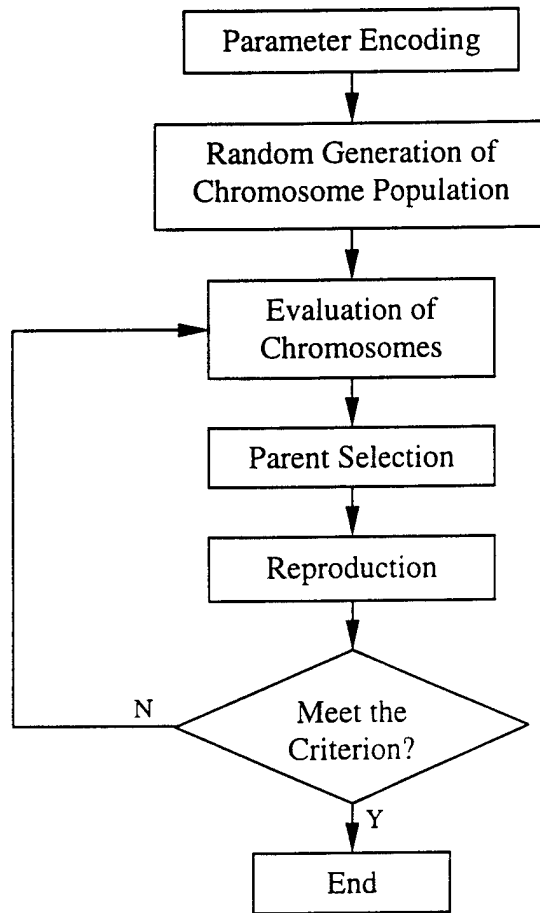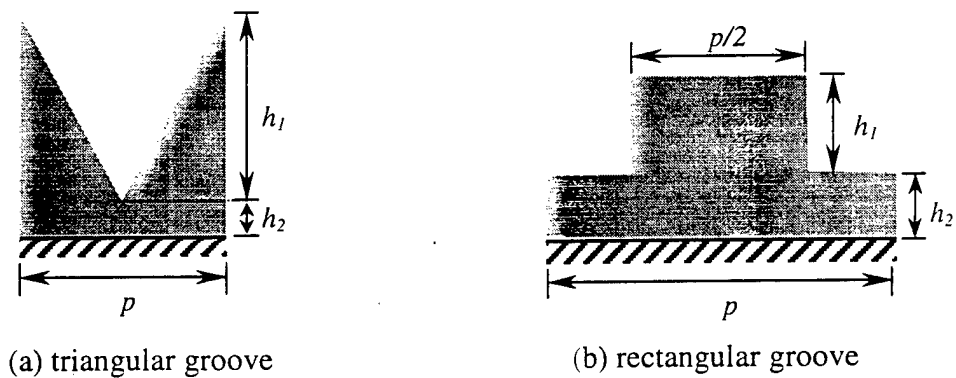
Fig. 4. Grating geometry for the examples
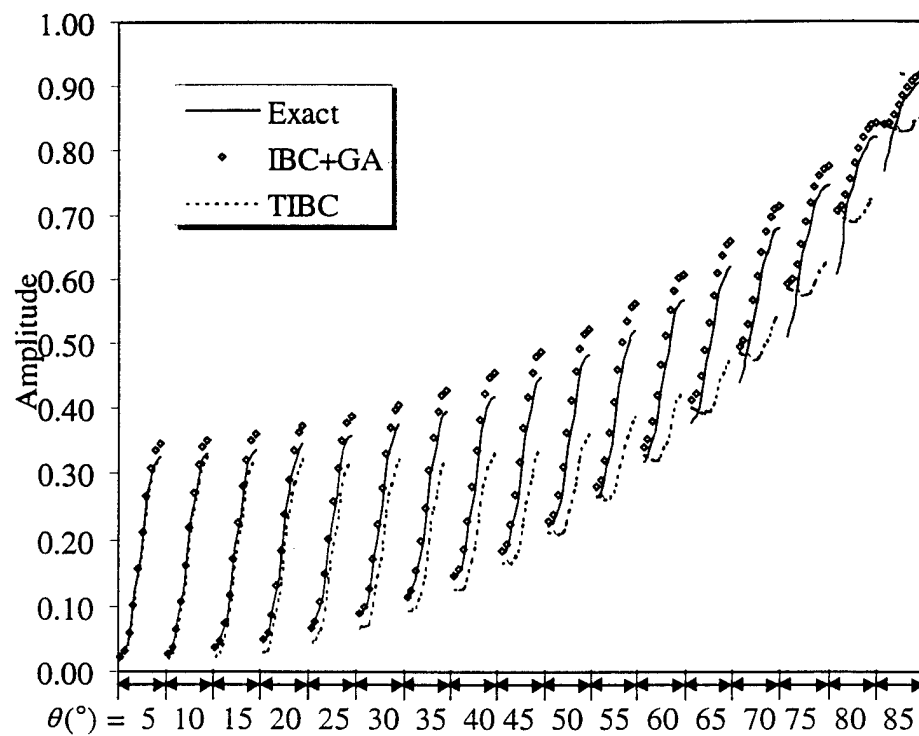
(a) H-polarization
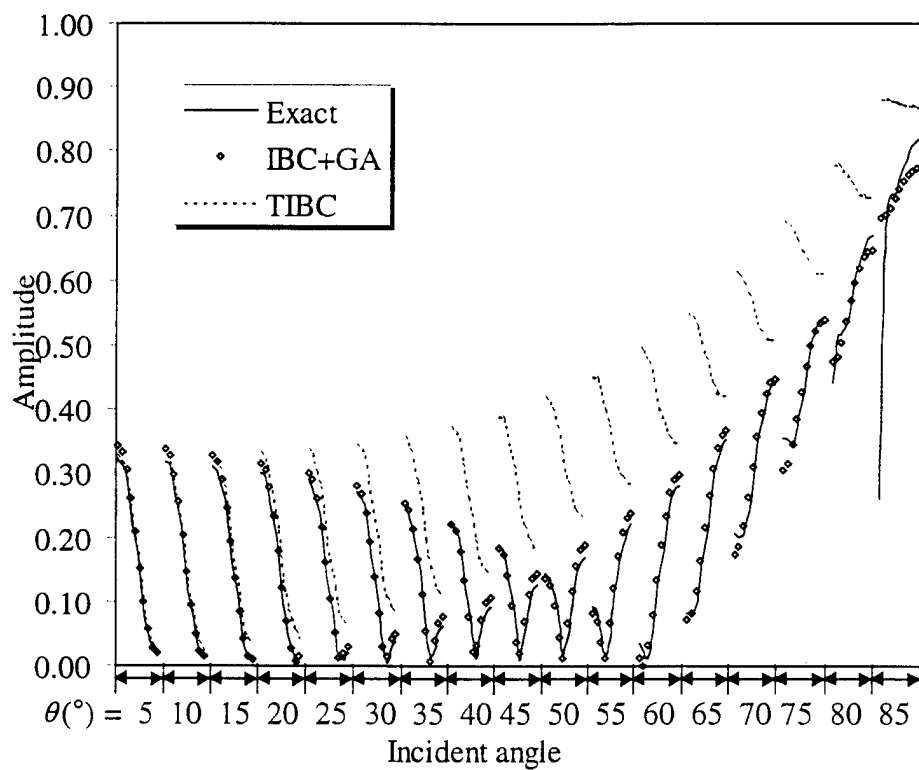
(b) V-polarization
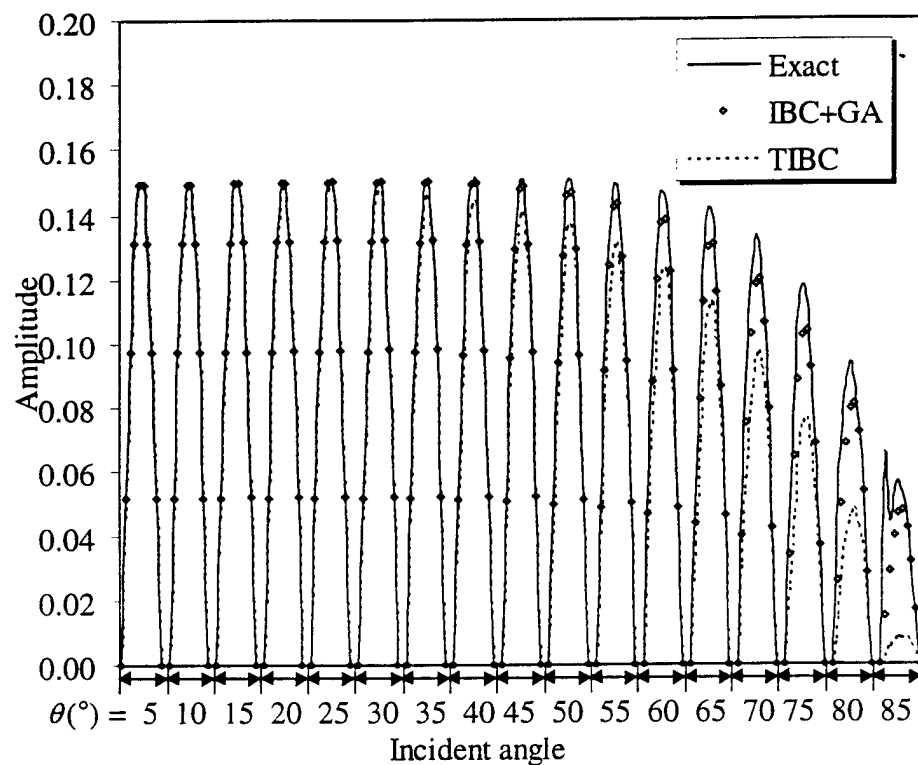
(c) H-V cross-polarization

Fig. 5. Comparison of reflection coefficients versus angle among (i) the exact MOM result, (ii) the IBC derived from GA and (iii) the TIBC result

(a) H-polarization
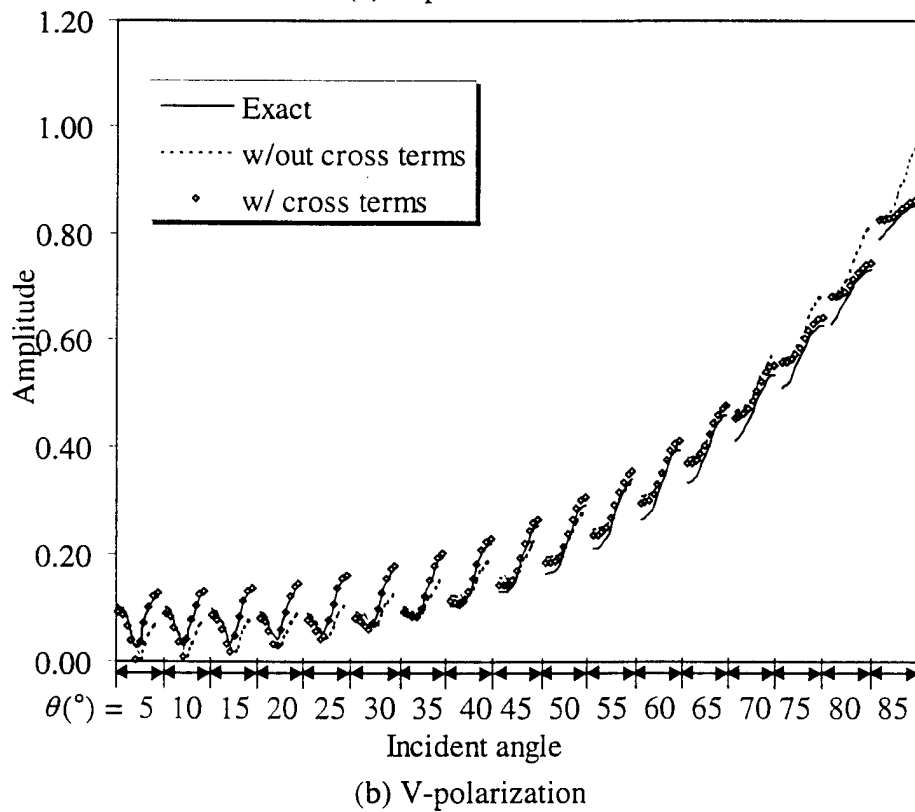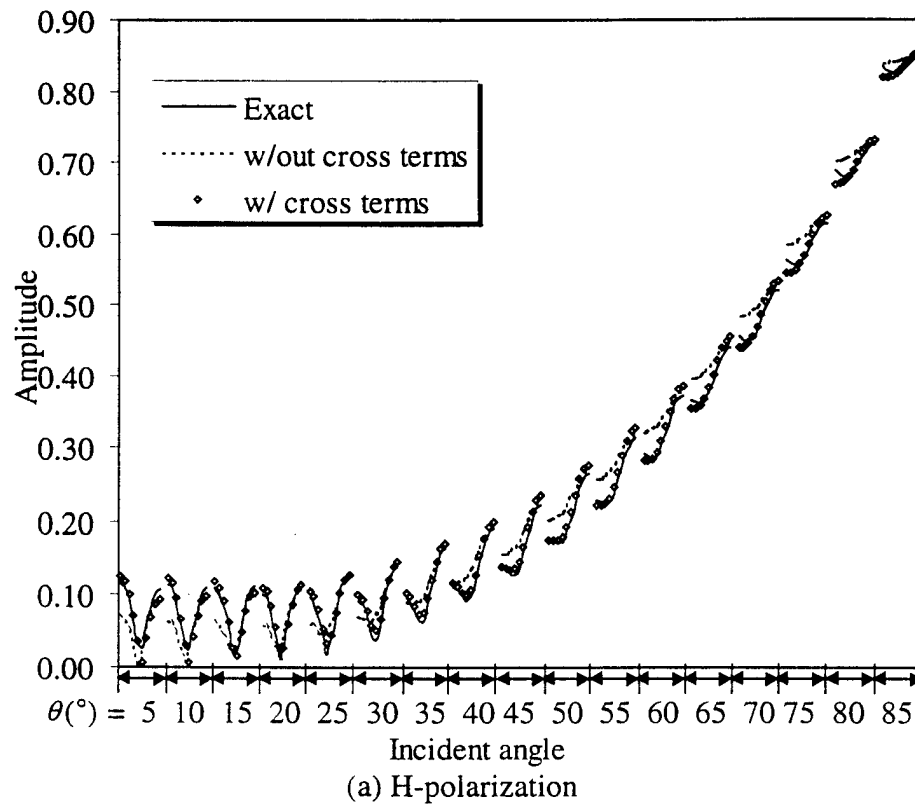
(b) V-polarization

Fig. 6. Effect of incorporating the cross impedance terms in the IBC model generated from GA
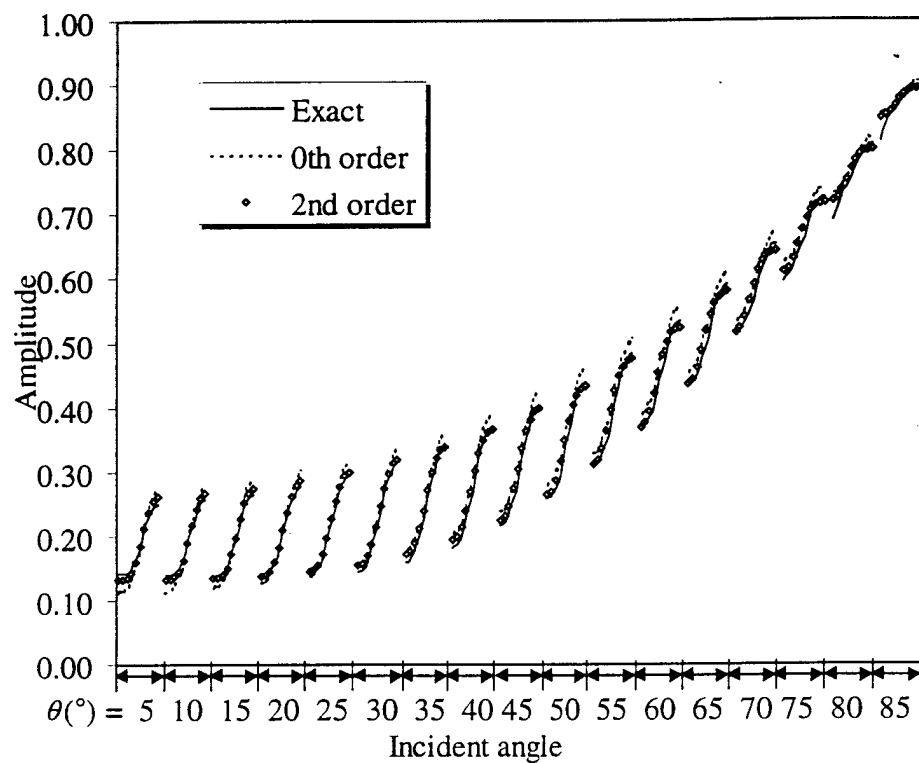
(a) Amplitude, H-polarization
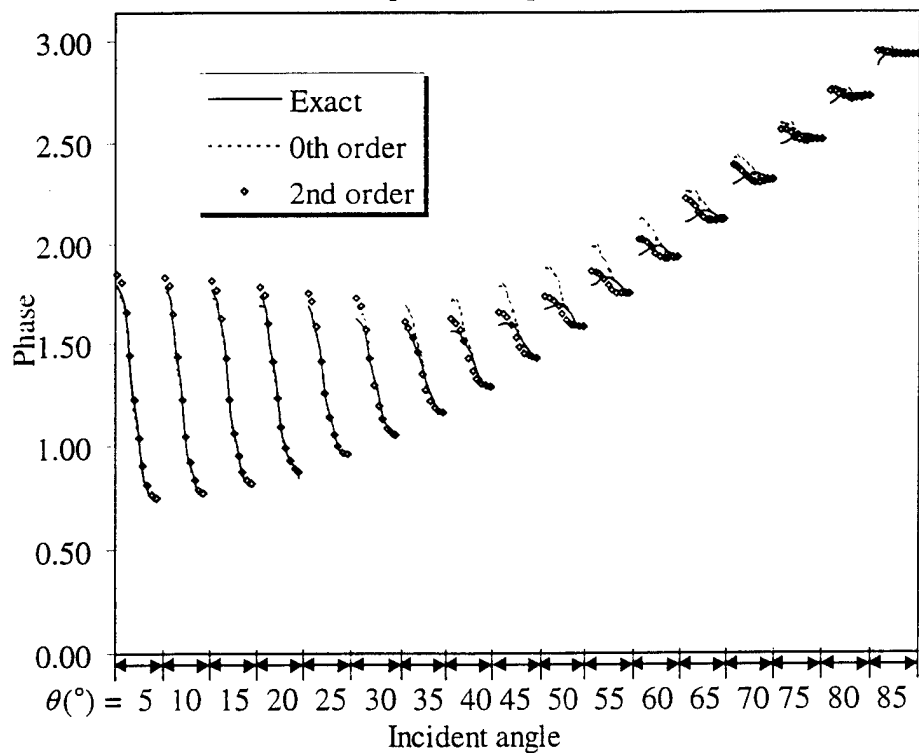
(b) Phase, H-polarization

Fig. 7. Effect of increasing the model order in the IBC model generated from GA
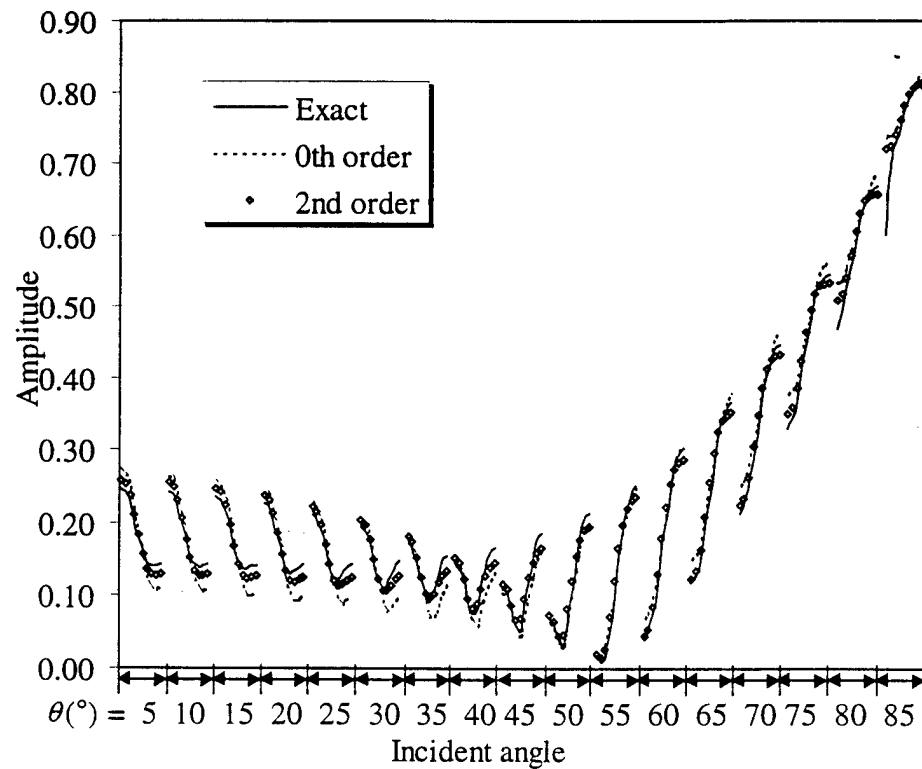
Fig. 7 (c) Amplitude, V-polarization
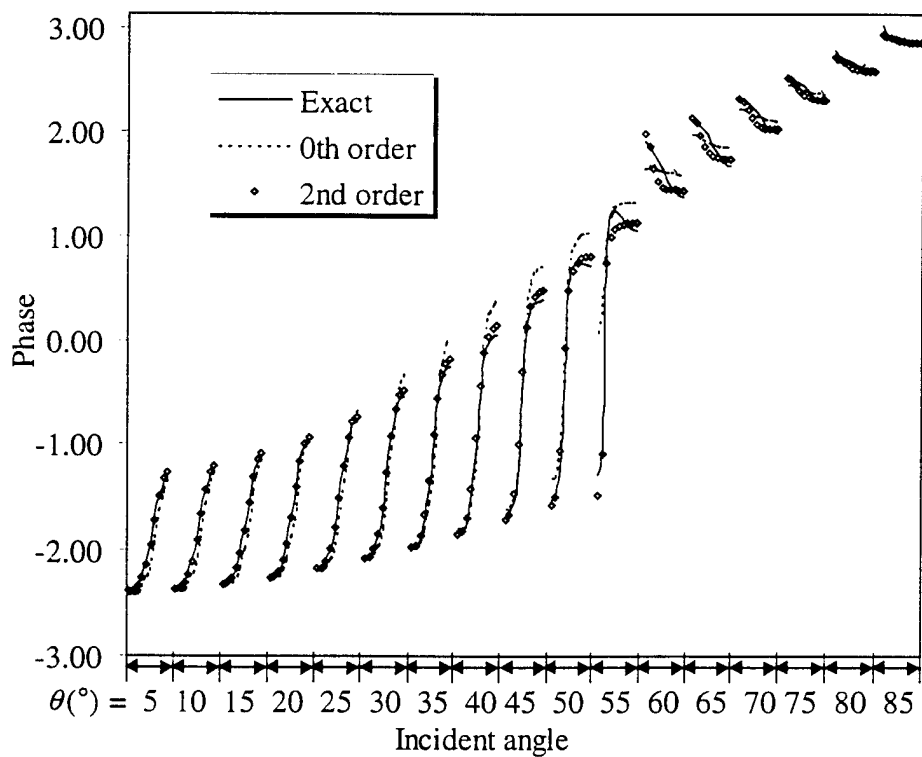
Fig. 7 (d) Phase, V-polarization
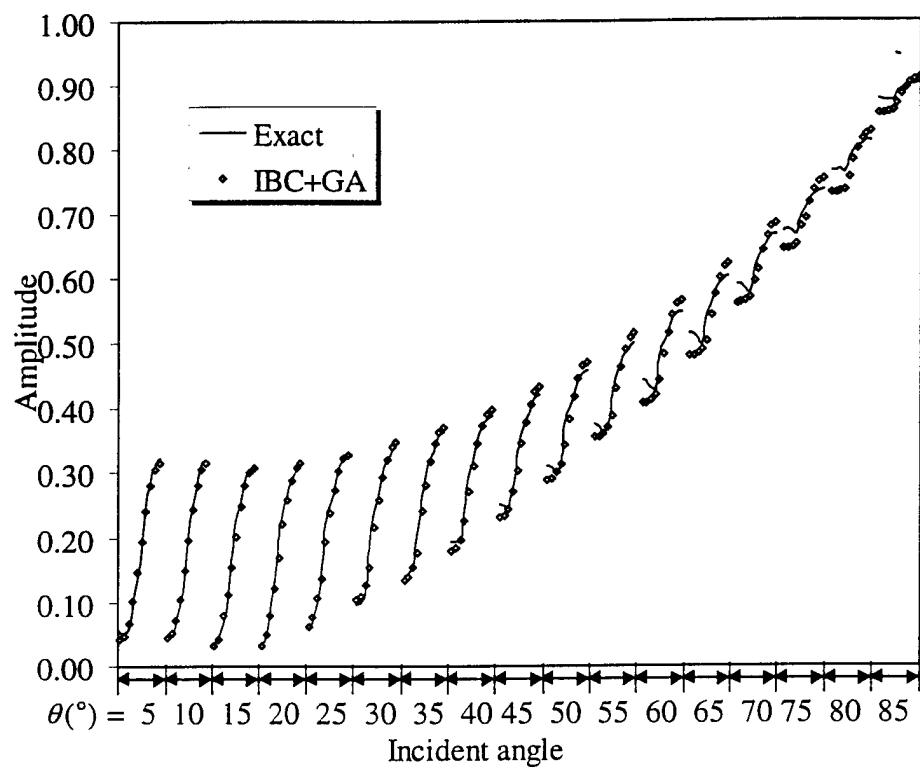
Fig. 8 (a) 0th order, H-pol
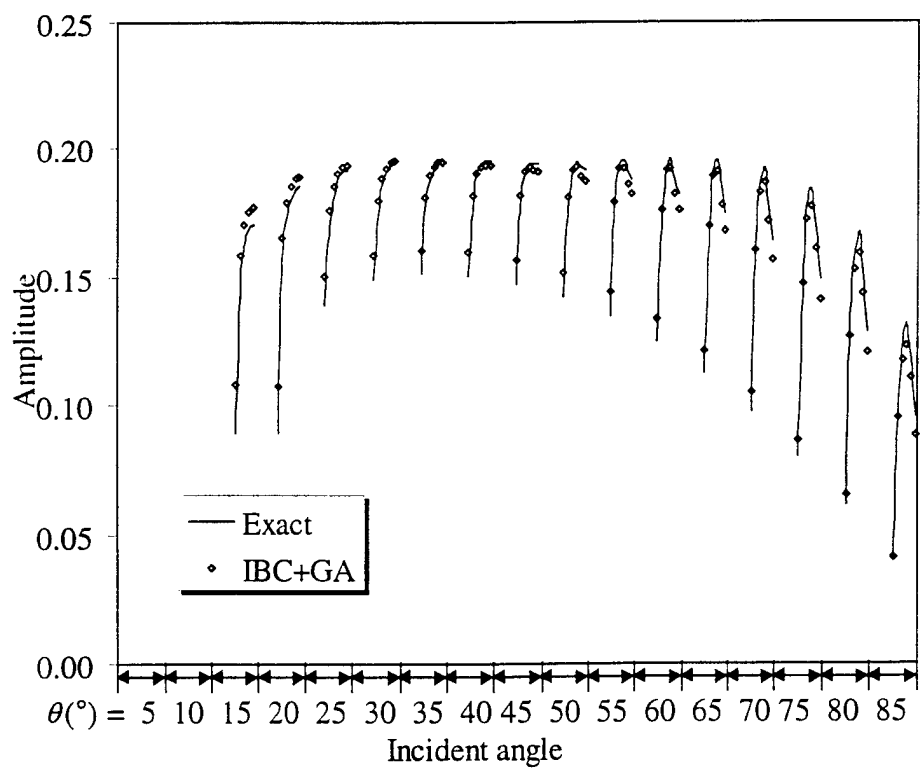
Fig. 8 (b) 1st order, H-pol
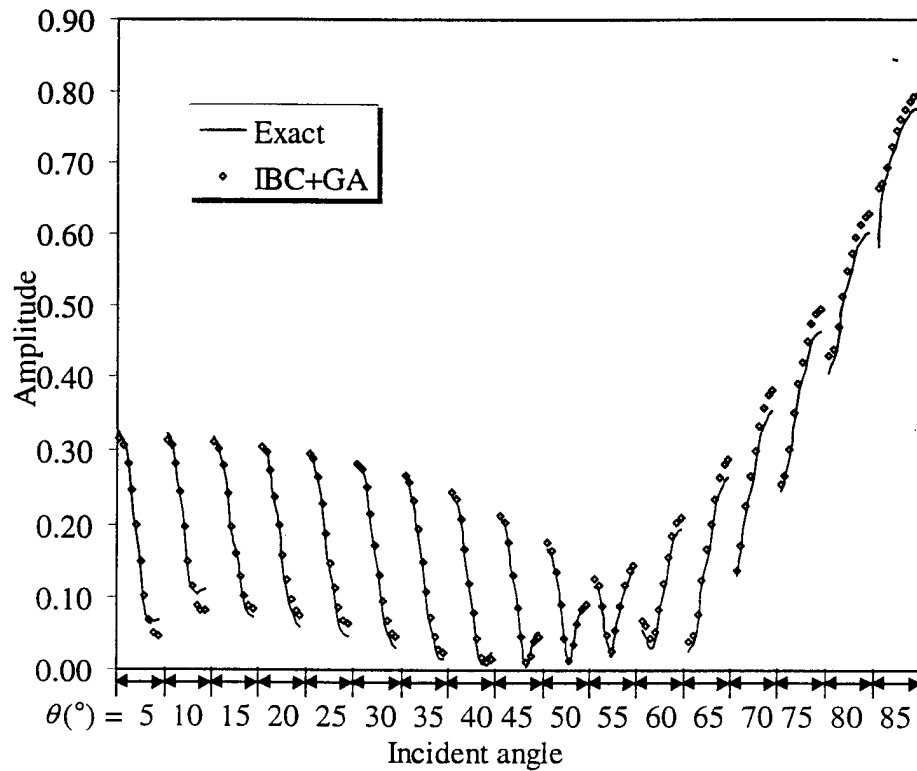
Fig. 8 (c) 0th order, V-pol
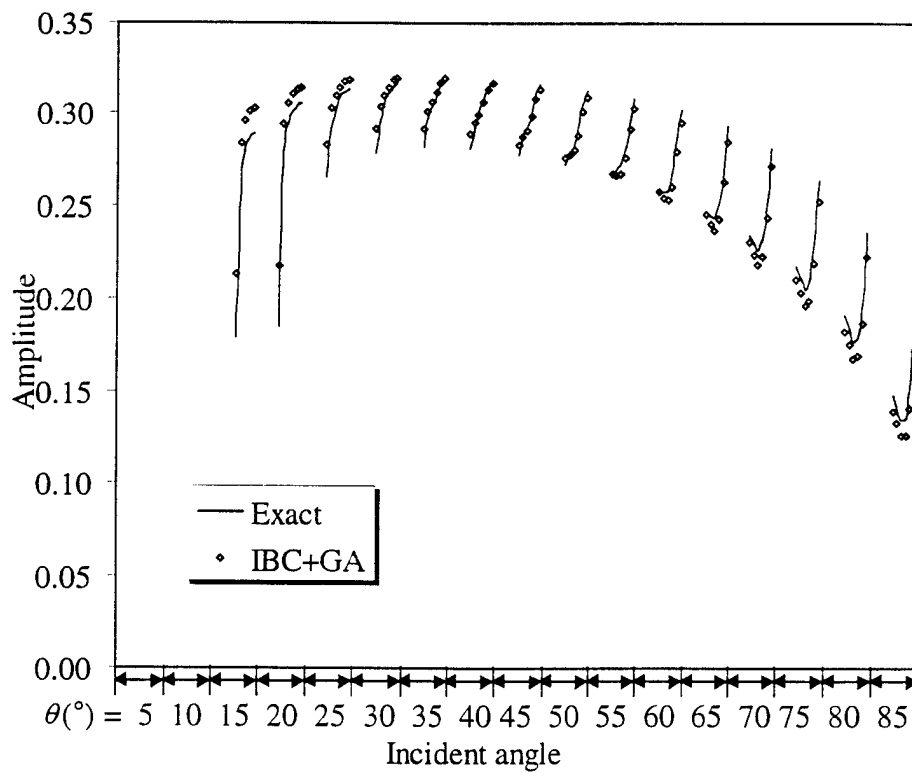
(d) 1st order, V-pol

Fig. 8 Higher order reflection coefficients simulated by the IBC model
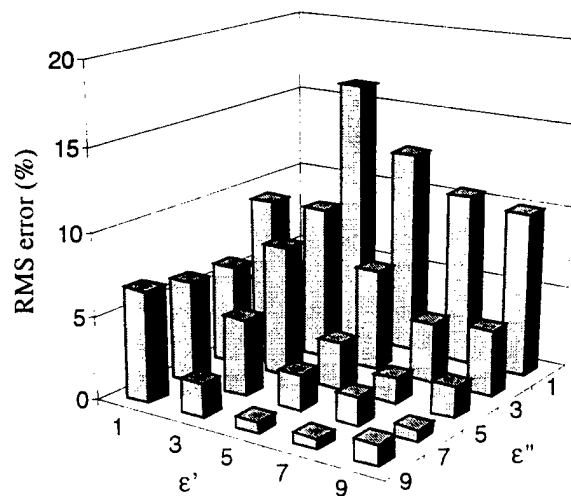
Fig. 9. Error of the IBC model as a function of material constant $\varepsilon = \varepsilon' - j\,\varepsilon''$
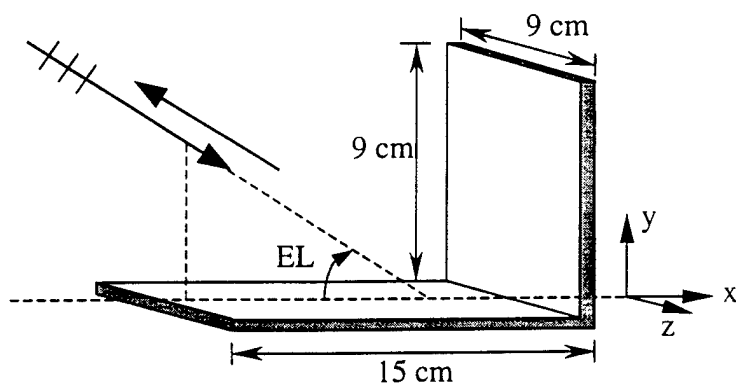
Fig. 10. Geometry of the corner reflector

(a) H-polarization

(b) V-polarization
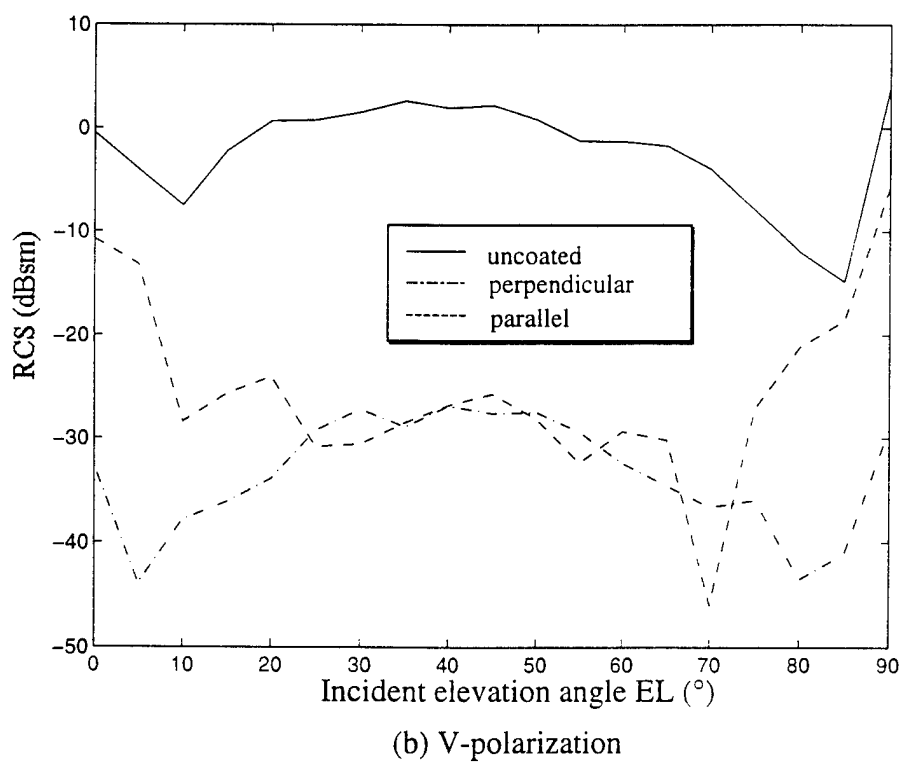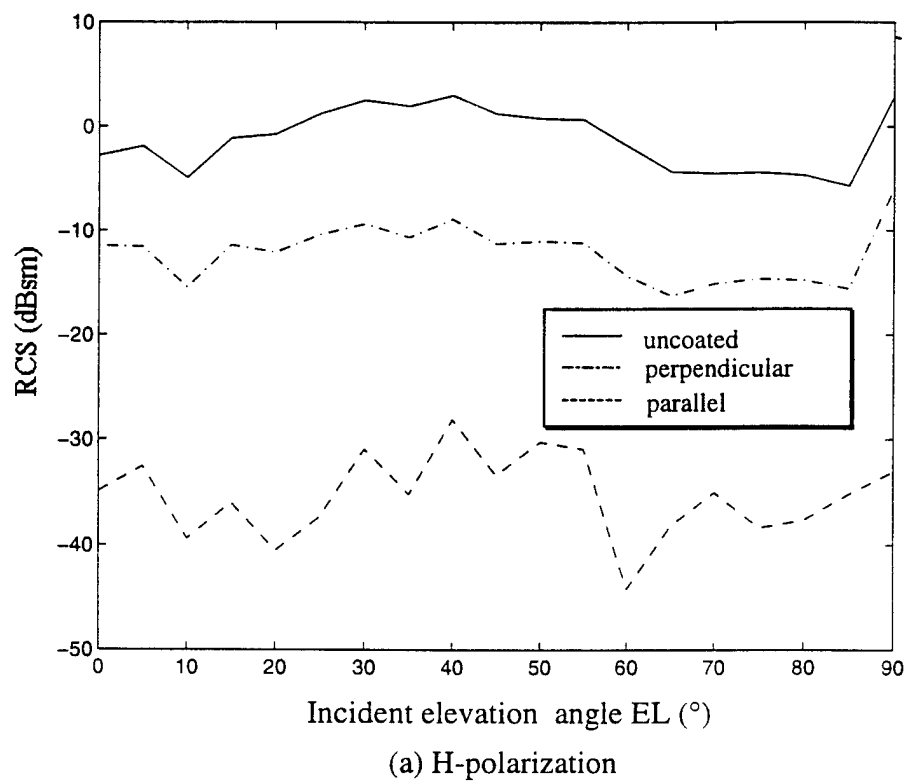
Fig. 11. RCS of the corner reflector (f = 10 GHz)

EFFICIENT RADAR SIGNATURE PREDICTION USING
A FREQUENCY-ASPECT INTERPOLATION TECHNIQUE
BASED ON ADAPTIVE FEATURE EXTRACTION

Yuanxun Wang and Hao Ling

Department of Electrical and Computer Engineering
The University of Texas at Austin
Austin, Texas 78712-1084

ABSTRACT

A radar cross section (RCS) interpolation technique in both frequency and aspect is proposed for the efficient prediction of radar signatures from computational electromagnetics data. Our approach is based on a multiple-arrival model for the induced current on the target. The model parameters are determined by an adaptive feature extraction (AFE) algorithm, which uses an iterative search-and-extract procedure to find the individual model features. Random frequency and aspect sampling is used to circumvent the ambiguity in selecting the features. Numerical examples are presented to test the interpolation algorithm. It is found that sufficient accuracy in the predicted radar features can be achieved even when the original computed data is sampled at 5:1 below the Nyquist criterion in either frequency or aspect. The algorithm is also applied to efficiently predict the radar image of the benchmark VFY218 airplane at UHF band with good results.

I. Introduction

Accurate prediction of the radar scattering from complex targets requires solving the electromagnetic boundary-value problem using numerical methods. This is a computationally intensive task when targets of large electrical sizes are involved. Recently, fast iterative solvers have emerged based on the fast multipole method [1,2]. These solvers have much lower computational complexity than traditional approaches. However, for frequency-aspect radar cross section (RCS) calculations, the solver has to be executed repeatedly for each angle and each frequency. To generate RCS data with as few electromagnetic computation points as possible, a number of model-based interpolation or extrapolation approaches have been developed to date [3-10]. In this work, we address the problem of RCS interpolation in frequency and aspect based on a multiple-arrival model in conjunction with an adaptive feature extraction (AFE) algorithm.

Model-based techniques are based on the assumption that all the unknown samples to be interpolated obey the same reduced-order model as the known samples, from which the model coefficients can be determined. The key in the success of a model-based interpolation algorithm is a good model of the physical observable to be interpolated. The most commonly used model is the rational function model, which is applicable in the low frequency region. Here, we consider a multiple-arrival model for the induced current. This model is motivated by the well-known behaviors of scattering mechanisms at high frequencies [11], and has been applied previously to the extrapolation of RCS in the frequency and angular domains with good success [8-10].

To obtain the model parameters from the computed data, we adopt an algorithm termed adaptive feature extraction (AFE). AFE can be considered as a generalization of the CLEAN algorithm [12], and is similar to the adaptive joint time-frequency technique [13-15] and the matching pursuit algorithm [16] in the iterative manner it performs the parameterization. We have previously applied it to construct the inverse synthetic aperture radar (ISAR) image from radar measurement data that was undersampled in the aspect dimension [17]. The essential idea of the AFE algorithm is to search and extract out individual scattering features from the data set one at a time. During each iteration the strongest feature is identified and removed from the original data. The procedure is then iterated until the data is well parameterized by the feature set. In this manner, the interference between different scattering features, which is significant for undersampled data, can be largely avoided. Since the features in our model are exponential functions of frequency and aspect, we use random sampling during the collection of the original computation data in order to avoid the ambiguity in selecting the strongest feature. This approach is similar to the random array concept that uses highly thinned but randomly spaced elements to avoid grating lobes [18].

This paper is organized as follows. In Sec. 2, we introduce the multiple-arrival model for the current and the AFE algorithm to develop a one-dimensional (1-D) frequency interpolation scheme. A numerical example is given to verify our approach and show that the Nyquist sampling criterion can be overcome with the extra information provided by the model-based approach. In Sec. 3, the

interpolation algorithm is extended for 2-D frequency-aspect interpolation. Some numerical examples are given to illustrate the performance of the algorithm. The algorithm is also applied to efficiently predict the ISAR image of the benchmark VFY218 airplane at UHF band. Finally, some discussions and conclusions on the interpolation algorithm are given Sec. 4.

II.   1-D Frequency Interpolation

2.1. Multiple-Arrival Model and AFE Interpolation Algorithm. Before presenting our interpolation algorithm, we shall briefly discuss the sampling criterion for frequency response in electromagnetic scattering problems. Nyquist sampling theorem states that if the sampling rate is higher than the highest Fourier component of a signal, the signal can be perfectly reconstructed by interpolation with the *sinc* function. In the context of electromagnetic scattering, this means that the frequency sampling interval for the scattered far field should be less than $1/(\tau_{max})$, where τ_{max} corresponds to the total extent of the time-domain response. Strictly speaking, due to the finite frequency bandwidth of the data, the actual time extent of the signal does not have finite support and a perfect reconstruction is not guaranteed. However, an approximate Nyquist criterion can usually be defined in practice for the sampling density in frequency.

To overcome the Nyquist sampling limitation, extra information must be provided by an *a priori* model based on the scattering physics. We utilize a multiple time-of-arrival model of the induced current:

$$J(f) = \sum_p B_p \exp(- j2\pi f t_p) \tag{1}$$

The essential idea of this model is illustrated in Fig.1. It assumes that the current on the target surface is induced by various incident wave mechanisms that arise from the direct incident field as well as the multiply scattered fields from other parts of the target. Each incident mechanism has amplitude B_p, which is assumed to be frequency independent, and a time-of-arrival t_p. Thus each basis function in (1) is an exponential function with linear phase in frequency. This is what we shall also refer to as a "feature" in the data. This model has been found to work well in modeling the scattering mechanisms of complex targets [8-10]. It should be noted that the induced current instead of the scattered far field is chosen for the interpolation. This is because the scattered field in general requires a much higher model order to parameterize. Furthermore, each current element usually contains more localized interactions in time than the total scattered field and therefore has a looser Nyquist sampling criterion. The price we pay is that the interpolation needs to be performed for all the current elements on the target.

If the original frequency sampling is dense enough, the basis functions in (1) are orthogonal and the model parameters B_p and t_p can be determined using the Fourier transform. However, when the data is undersampled, the basis functions are no longer orthogonal. To avoid the interference between the non-orthogonal bases, we use the iterative AFE procedure instead of the Fourier transform to carry out the parameterization. To find parameters B_p and t_p, we first project the sampled frequency response onto the complex conjugate of the model bases for all possible values of t. We then select as the best basis the one with the

maximum projection value B_p and the corresponding time-of-arrival parameter t_p. This is denoted by the following equation:

$$B_p = \max_{t=t_p} \langle J_p(f), \exp(j2\pi ft) \rangle \tag{2}$$

where the subscript p denotes it is at the pth stage of the iterative procedure and the inner product is defined as:

$$\langle a(f), b(f) \rangle = \frac{1}{N} \sum_{i=1}^{N} a(f_i) b(f_i) \tag{3}$$

Once the strongest feature is found, a remainder signal is generated by subtracting out that feature:

$$J_{p+1}(f_i) = J_p(f_i) - B_p \exp(-j2\pi f_i t_p) \tag{4}$$

The above process is iterated to extract out as many features as needed to sufficiently parameterize the signal, i.e., until the remainder signal reaches a preset threshold. Note that since the stronger features are extracted out before we begin the search for the weaker features in the iteration process, the interference from the stronger features on the weaker features is reduced significantly.

An additional problem exists due to the undersampling of the exponential bases used in our model. As an example, if $J(f)$ consists of a single exponential function $exp(-j2\pi ft_0)$, we expect the inner product in (2) to give the strongest peak at $t_p = t_0$ with amplitude $B_p = 1$. However, if the frequency sampling is uniform with sampling interval δf, the strongest peak will occur not only at $t_p = t_0$ but also at $t_p = t_0 + 2n\pi/\delta f$. These periodic lobes cause ambiguity in determining the true time-of-arrivals. To overcome this problem, we utilize random sampling to weaken the repeated lobes. The idea is similar to random arrays where random

element spacing is used to circumvent the antenna grating lobe problem in designing highly thinned arrays [18]. The random sampling in frequency can be easily realized in the present problem without computational penalty. We choose the frequency sampling points f_i based on a uniform probability distribution in the frequency band of interest. Then once the current is parameterized at each point on the scatterer using AFE, the interpolated current function at any frequency within the band can be calculated using equation (1). Finally, the far field at the denser frequency sampling can be obtained by integrating the induced current over the target.

2.2. Numerical Example. To verify the above frequency interpolation scheme, we consider the scattering from a two-dimensional structure consisting of three circular cylinders as an example. The structure is shown in Fig. 2. The reference RCS is computed at 71 points from 0.3 GHz to 0.65 GHz using the method of moments. The result is shown as the solid line in Fig. 3(a). The spiky behavior of the frequency response indicates that the scattered field is sampled very close to the Nyquist rate. For comparison, we use the values at 18 equally spaced points and carry out a current-based interpolation using simple spline fitting. The result is shown as the dash-dotted line in Fig. 3(a). Deviations between the two results can be seen. Next, we use the AFE algorithm to carry out the interpolation. Instead of 18 equally spaced points, we randomly select 18 points from the original 71 points. The interpolated result is plotted as the dashed line in Fig. 3(b), which agrees with the reference calculation much better than the current-domain spline interpolation. This contrast is further demonstrated when we

Fourier transform the complex frequency responses into the range profiles displayed in Fig. 4. In the reference range profile, the first two strong peaks in range are the direct scattering from the two cylinders on the left. Those smaller peaks further down range represent the multiple scattering due to the interactions among the cylinders. We can see that most of the features from the AFE interpolation coincide with the reference result in Fig. 4(b), while the current-domain spline interpolation gives strong artifacts among the real scattering features in Fig. 4(a). The only peaks correctly predicted by the current spline are the two direct reflection peaks off the two left cylinders. This is because the current elements contributing to those two peaks contain only the physical optics component. Since each current element has only a single time-of-arrival, the Nyquist sampling criterion is very loose for these elements. This is why the current at these positions can be easily interpolated even with the spline function. Over the rest of the target, this is clearly not the case.

III. 2-D Frequency-Aspect Interpolation

3.1. 2-D AFE Interpolation Algorithm. We now extend the above 1-D frequency interpolation algorithm to 2-D frequency-aspect interpolation. Note that for iterative electromagnetic solvers, the solver has to be executed for each new aspect angle, just as in the frequency dimension. We again utilize the multiple-arrival model for the induced current shown in Fig. 1, except we consider how the current varies as a function of both the frequency and the direction of the incident wave. We shall denote the down range direction with respect to the incident wave

as x and the direction perpendicular to x, or the cross range direction, as y. The first scattering point on the target due to the pth scattering mechanism is represented by (x_p, y_p). l_p represents the path length from the first scattering point to the observation point S. It is zero for the direct incident wave. Next, we make a key assumption about the induced current at S as the angle of the incident wave is varied from the nominal direction (solid arrows) by an amount θ shown by the dashed arrows in Fig. 1. We assume that the intermediate interaction path l_p for the pth scattering mechanism remains unchanged as the incident angle is varied. This approximation was first introduced for ray optical fields [19], and has been applied in model-based angular extrapolation by us previously with good success [9]. Using this assumption, we arrive at a 2-D version of the multiple-arrival model for the current at a point S on the target:

$$J(f,\theta) = \sum_p B_p \exp\left[-j \frac{2\pi f}{c}(x_p \cos\theta + y_p \sin\theta + l_p) \right]$$

(5)

Under further assumption of small observation angles, (5) can be approximately written as:

$$J(f,\theta) \approx \sum_p B_p \exp\left[-j \frac{2\pi f}{c}((x_p + l_p)\cos\theta + y_p \sin\theta) \right]$$

$$= \sum_p B_p \exp\left[-j \frac{2\pi f}{c}(r_p \cos\theta + y_p \sin\theta) \right]$$

(6)

Note that (6) reduces to (1) for $\theta = 0$, $r_p = ct_p$, as expected. In contrast to (1), the basis functions in (6) are two-dimensional exponential functions of frequency and angle. Therefore we modify the AFE algorithm in Sec. 2 by replacing (2) by:

$$B_p = \max_{r=r_p, y=y_p} \left\langle J_p(f,\theta), \exp[j\frac{2\pi f}{c}(r\cos\theta + y\sin\theta)] \right\rangle \qquad . \quad (7)$$

By searching out the parameters B_p, r_p and y_p, the AFE technique is thus extended for 2-D interpolation in both the frequency and angular domains.

To summarize, our goal for the 2-D interpolation algorithm is to efficiently generate dense frequency-aspect RCS data from a small number of data points calculated using a fast iterative solver. The steps are first to select a number of randomly distributed sample points within the frequency and angular band of interest and solve the scattering problem for those points. Second, the induced current is interpolated to a denser sampling grid based on the reduced-order model generated from AFE processing. Third, the current is integrated to generate the scattered far field and the RCS. In the following numerical tests, we go one step further by generating the 2-D ISAR image of the target from the interpolated frequency-aspect data using standard ISAR processing. This is done to facilitate better physical interpretation of the results.

3.2. *Numerical Example.* To test the frequency-aspect interpolation algorithm, we consider a 2-D cylinder-plate structure shown in Fig. 5. The diameter of the cylinder is 4.2 m and the length of the plate is 20 m. The origin of the cylinder and the center of the plate are separated by 6.2 m. The frequency band of interest is from 0.3 GHz to 0.65 GHz. Fig. 6 shows the reference ISAR image generated from 71x 81=5751 computed points in the frequency-aspect plane. The image has a dynamic range of 40 dB. In this structure, strong multiple scattering mechanisms between the cylinder and the plate dominate the backscattering. We can clearly see in the image the features corresponding to the direct scattering

from the cylinder and the edge points of the plate, as well as the other range-delayed features corresponding to the multiple scattering mechanisms. (The detailed description of the different mechanisms can be found in [19].) For comparison, we collect 15x15=225 equally spaced sampling points in frequency-aspect and use 2-D splines to interpolate the current. Fig. 7 plots the resulting ISAR image from the spline-interpolated frequency-aspect data. In this image, only the direct scattering features (the cylinder and the edge points of the plate) are correctly predicted in position while all the higher-order scattering features are completely wrong.

Next we construct the ISAR image using the AFE algorithm. We choose 50 points randomly from the original 5751 points and use AFE to interpolate the frequency-aspect data to the dense sampling grid. The resulting ISAR image is plotted in Fig. 8(a). We repeat this process using AFE interpolation for 100, 200 and 400 input points, and the resulting images are shown in Figs. 8(b), 8(c) and 8(d), respectively. From this series of images, we can see that the strong scattering features are quite stable throughout while the weak features begin to converge as the number of input points is increased. Nearly all of the features of the interpolated image agree well with those in the reference image from the brute-force calculation. We do notice that the very weak features are underpredicted in the interpolated result. This is mainly caused by the termination threshold in the parameterization process and some signal energy is lost. In this example, the parameterization is stopped when the maximum magnitude of the remainder signal is less than 10% of the incident magnetic field

strength. Another possible cause for the noise in the low dynamical ranges is that the AFE algorithm itself leads to biased estimates on the position and amplitude of the scattering features. This bias becomes more severe for the weaker features.

Plotted in Fig. 9 is the correlation index between the images generated using AFE and the reference image versus different number of input points used in the interpolation. To properly reflect the contribution of the weaker features to the correlation index, we use the dB-scaled images in computing the correlation index (a constant offset is added to the images to avoid negative numbers in decibel). Fig. 9 shows that the 200-point mark is the turning point of the curve, after which the image quality does not improve further. This is consistent with the visual sensation in Fig. 8. From this example, we believe a good rule-of-thumb limit that can be handled by the AFE interpolation algorithm is about 5:1 undersampling in both the frequency and aspect dimensions. This criterion is established based on a very challenging target containing strong multiple scattering.

3.3. Application of AFE Interpolation to VFY218 Benchmark. The interpolation algorithm is next applied to predict the ISAR image of the benchmark VFY218 airplane [20]. The fuselage length of the airplane is 15.33 meters and the maximum width measured from the wing tips is 8.90 meters. To generate its ISAR image at a center frequency of 400 MHz with bandwidth 267 MHz, we use the fast solver FISC [21] on a Pentium II 450MHz computer. The total number of sampling points must be at least 40 frequency points by 40 aspect points within the 40-degree aperture to satisfy the Nyquist sampling criterion. The resulting

range and cross range resolution is about half a meter. Since the calculation for one single frequency-aspect point takes about 3 hours (with about 80,000 unknowns in the moment equation), the total computation time would be 200 days if we use brute-force calculation to generate the data. Based on the 5:1 undersampling criterion derived in the previous example, we only compute the scattering problem at 62 randomly sampled points and use the AFE interpolation scheme to interpolate the data to all 40x40=1600 points. The computation time is about 8 days. The resulting ISAR image at the 130-degree (from nose-on) look angle is plotted in Fig. 10. For comparison, Fig. 11 shows the ISAR image constructed from the chamber measurement data for the same look angle. The target outline is overlaid on the measurement image. The measurement was carried out at the US Navy China Lake facility on a 1:30 scaled model at the frequency band of 8 to 16 GHz [20]. Comparing Fig. 10 to Fig. 11, we find that all the features in the measurement image are well predicted in the simulated image from using FISC and interpolation. The correlation index (on a dB scale) is 88.2 % between the two images. The sources of discrepancy in this case include measurement error, computation error from FISC, differences between the actual model used in the measurement and the CAD model used in the FISC calculation, and error from the interpolation algorithm. There is also an additional error in the measured image due to the ISAR formation procedure [22]. For the wide 40-degree observation aperture in the measurement, the scattered field data is collected on a polar grid in k-space and polar reformatting must be performed to generate a focused ISAR image with FFT. This process introduces additional

error and results in a more diffused resolution cell. The predicted image, on the other hand, is generated directly on a rectangular grid with rectangular boundary in k-space using the parameterized current model and completely circumvents the polar reformatting step.

As a second case study, the predicted image (generated using 62 FISC-computed points and AFE interpolation) for another look angle at 30 degrees from nose-on is shown in Fig. 12. Two measurement images are shown in Figs. 13 and 14. Fig. 13 is from the measured data when the airplane engine inlet ducts are untreated and Fig. 14 is from the measured data when absorber material is inserted into the inlet. Since the CAD model used to carry out the simulation has sealed engine inlets, the cloud over the right wing in Fig. 13 due to the inlet return is not predicted in Fig. 12. However, the other features agree quite well. The more diffused spot sizes in the measured image are due to the polar-reformatting operation, as discussed earlier. Fig. 12 also agrees well with Fig. 14, although the inlet contribution is not completely removed from the measurement in the latter case. Furthermore, there appears to be more measurement noise in Fig.14.

IV. Summary and Discussions

A current-domain AFE interpolation technique has been developed to generate densely sampled frequency-aspect RCS data from a sparse set of computed data. The induced current on the target is modeled by a multiple-arrival model and the AFE procedure is applied to extract the model parameters. Random sampling of the original data is used to avoid the ambiguity problem

associated with the exponential model basis. Numerical results have been generated to test this approach. Lastly, the algorithm has been applied in conjunction with a fast electromagnetic solver to predict the high-fidelity ISAR image of the benchmark VFY218 airplane at UHF band. The resulting images agree well with chamber measurement data.

The AFE approach is found to be stable and robust. Sufficient accuracy in the predicted image features can be achieved even when the original computed data is sampled at 5:1 below the Nyquist criterion in either frequency or aspect. This limit was established based on a target containing very strong multiple scattering. Therefore, the expected time savings in using this approach is about 25:1 in comparison to the brute-force computation. The AFE algorithm does involve exhaustive search and must be carried out for every current element on the target. However, the time consumed in the interpolation is still relatively insignificant when compared to the electromagnetic computation time.

The possible sources of error in the overall interpolation procedure include imperfection of the multiple-arrival model for the current and errors in the AFE procedure. The former includes our assumption about the frequency independence of the model coefficients as well as the small-angle approximations used to derive the model in the angular dimension. Errors in the AFE procedure can occur when there are too many features in the data or when the undersampling is too severe. The interference from the weaker features affects the determination of the strong features in the projection process. These biased estimates of the strong features, when propagated to the later stage of the iteration process, prevent the accurate

extraction of the very weak features. This error source limits the dynamic range of the final interpolated data.

Reference

[1]   R. Coifman, V. Rokhlin, and S. Wandzura, "The fast multiplole method for the wave equation : a pedestrian prescription," *IEEE Trans. Antennas Propagat. Mag.*, Vol. 35, No. 3, pp. 7-12, June 1993.

[2]   J. Song, C. C. Lu and W. C. Chew, "Multilevel fast multipole algorithm for electromagnetic scattering by large complex objects," *IEEE Trans. Antennas Propagat.*, vol. AP-45, pp. 1488-1493, Oct. 1997.

[3]   G. J. Burke, E. K. Miller, S. Chakrabarti and K. Demarest, "Using model-based parameter estimation to increase the efficiency of computing electromagnetic transfer functions," *IEEE Trans. Magnetics*, vol. 25, pp. 2807-2809, July 1989.

[4]   K. Kottapalli, T. K. Sarkar, Y. Hua, E. K. Miller, and G. L. Burke, "Accurate computation of wide-band response of electromagnetic systems utilizing narrow-band information," *IEEE Trans. Microwave Theory Tech.*, vol. MTT-39, pp. 682-687, Apr. 1991.

[5] Z. Altman and R. Mittra, "Combining an extrapolation technique with the method of moments for solving large scattering problems involving bodies of revolution," *IEEE Trans. Antennas Propagat.*, vol. AP-44, pp. 548-553, Apr. 1996.

[6] E. K. Miller, "Model-based parameter estimation in electromagnetics: part I. background and theoretical development," *IEEE Antennas Propagat. Mag.*, vol.40, No.1, pp.42-52, Feb. 1998.

[7] C. J. Reddy, M. D. Deshpande, C. R. Cockrell and F. B. Beck, " Fast RCS computation over a frequency band using method of moments in conjunction with asymptotic waveform evaluation technique," *IEEE Trans. Antennas Propagat.*, vol. AP-46, pp. 1229-1233, Aug. 1998.

[8] Y. Wang, H. Ling, J. Song and W. C. Chew, "A frequency extrapolation algorithm for FISC," *IEEE Trans. Antennas Propagat.*, vol. AP-45, pp. 1891-1893, Dec. 1997.

[9] Y. Wang and H. Ling, "A model-based angular extrapolation technique for iterative method-of-moment solvers," *Microwave Opt. Tech. Lett.*, Vol.20, No.4, pp. 229-233, Feb. 1999.

[10] Y. Wang and H. Ling, "Radar signature prediction using moment method codes via a frequency extrapolation technique," accepted for publication in *IEEE Trans. Antennas Propagat.*, Mar. 1999.

[11] R. Bhalla, J. Moore and H. Ling, "A global scattering center representation of complex targets using the shooting and bouncing ray technique," *IEEE Trans. Antennas Propagat.*, Vol. AP-45, pp. 1850-1856, Dec. 1997.

[20] H. T. G. Wang, M. L. Sanders and A. Woo, "Radar cross section measurement data of the VFY 218 configuration," *Tech. Rept. NAWCWPNS TM-7621*, Naval Air Warfare Center, China Lake, CA, Jan. 1994.

[21] *User's Manual for FISC (Fast Illinois Solver Code)*, Center for Computational Electromagnetics, Univ. of Illinois and DEMACO, Inc., Champaign, IL, Jan. 1997.

[22] A. Ausherman, A. Kozma, J. L. Waker, H. M. Jones and E. C. Poggio, "Developments in radar imaging," *IEEE Trans. Aerospace Electron. Syst.*, vol. 20, pp. 363-400, Apr. 1984.
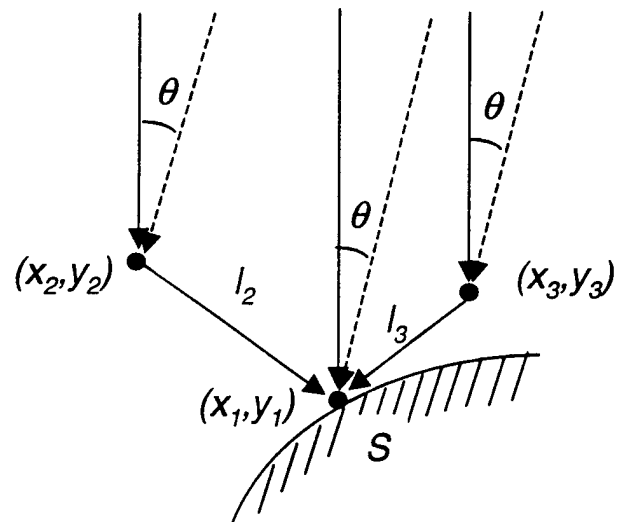
Fig. 1 The multiple arrival model for the induced current.
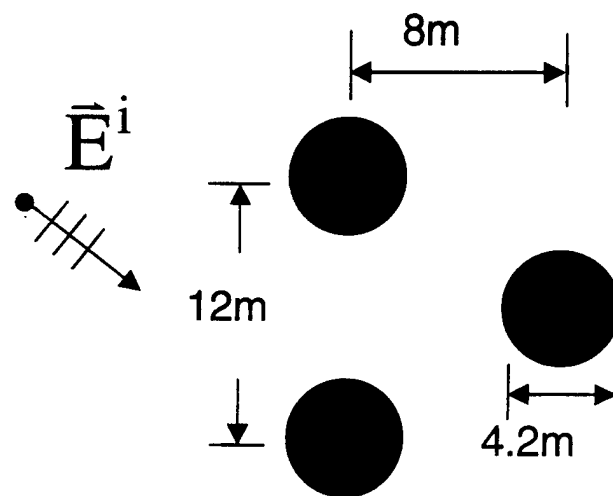
Fig.2 Geometry of the three-cylinder target.
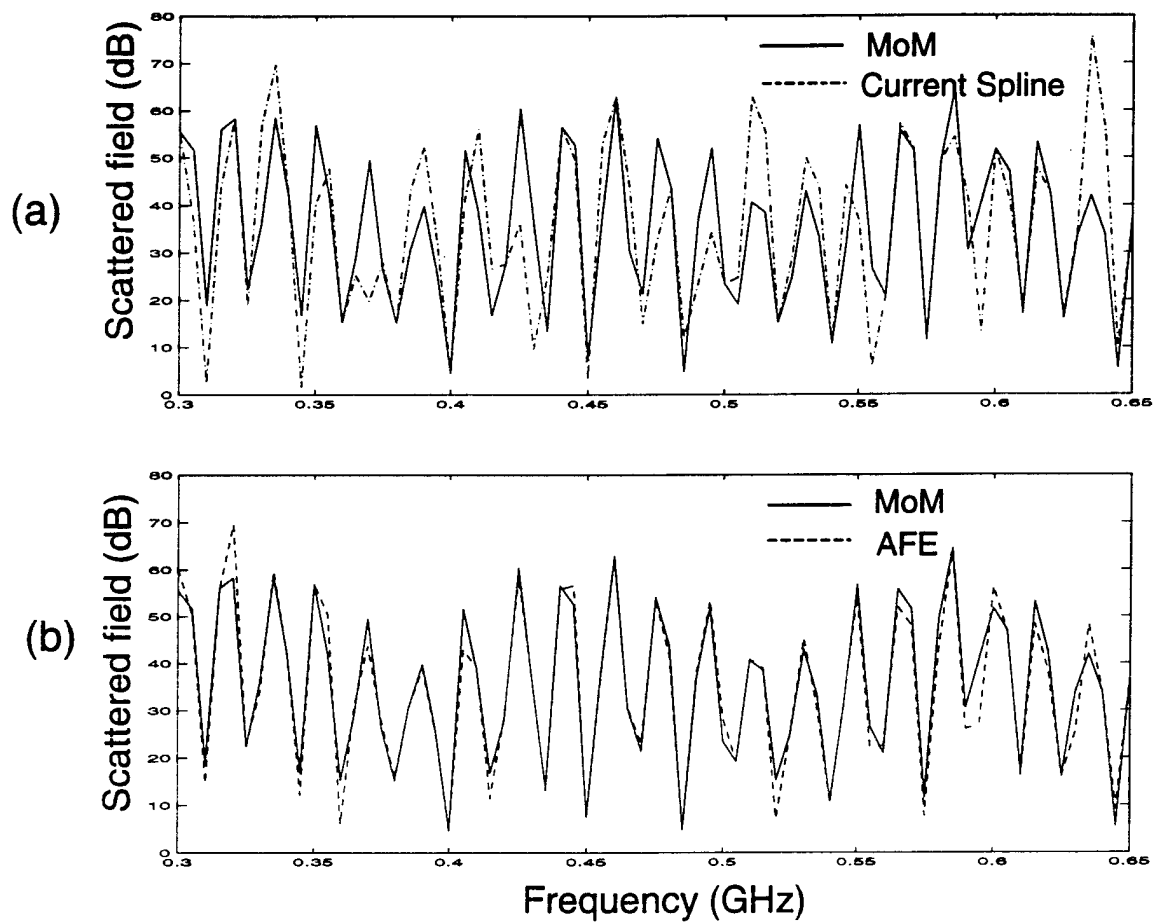
Fig.3 RCS versus. frequency plots. (a)current domain spline (dash-
dotted line) vs. MoM (solid line). (b) AFE interpolation (dash
line) vs. MoM (solid line).
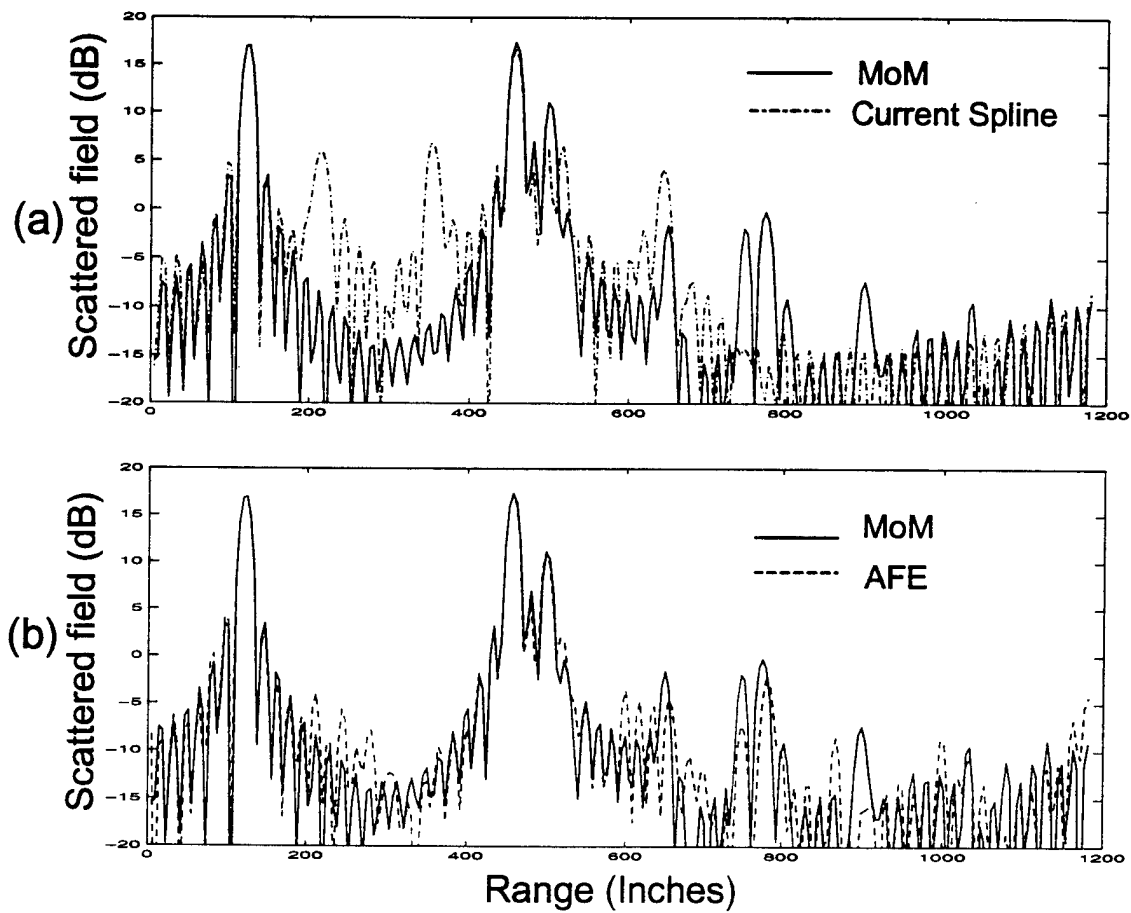
Fig.4 Range profile comparison. (a)current domain spline (dash-dotted line) vs. MoM (solid line). (b) AFE interpolation (dash line) vs. MoM (solid line).
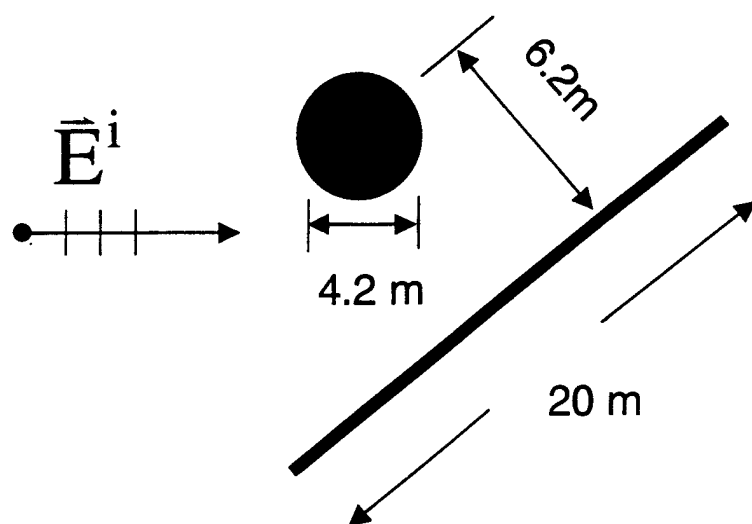
Fig.5 Geometry of the cylinder-plate target.
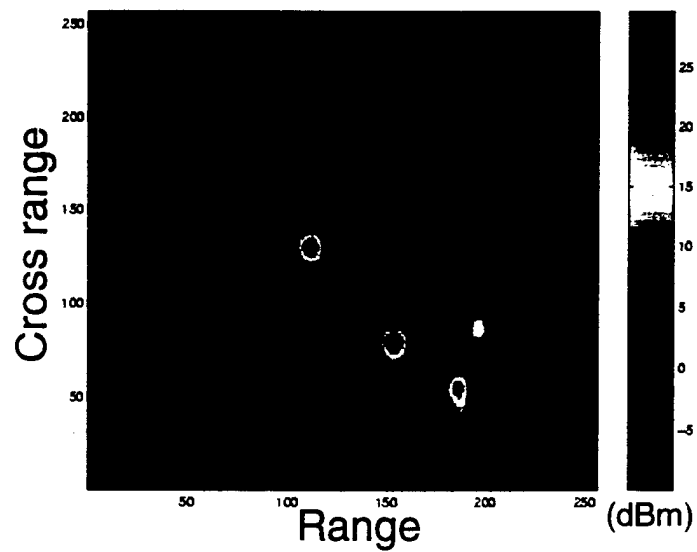
Fig.6 Referenced ISAR image generated using brute-force MoM
calculations at 71x81=5751 points.
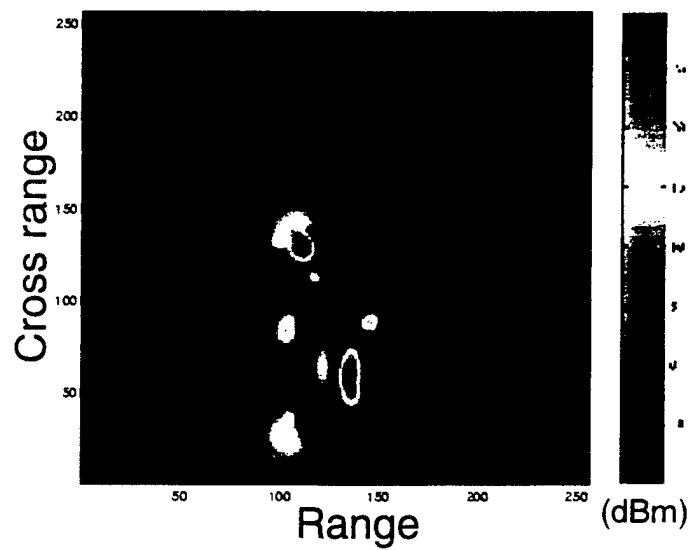
Fig.7 ISAR image generated from interpolated results using
current-domain 2-D spline with 15x15=225 calculated
points.
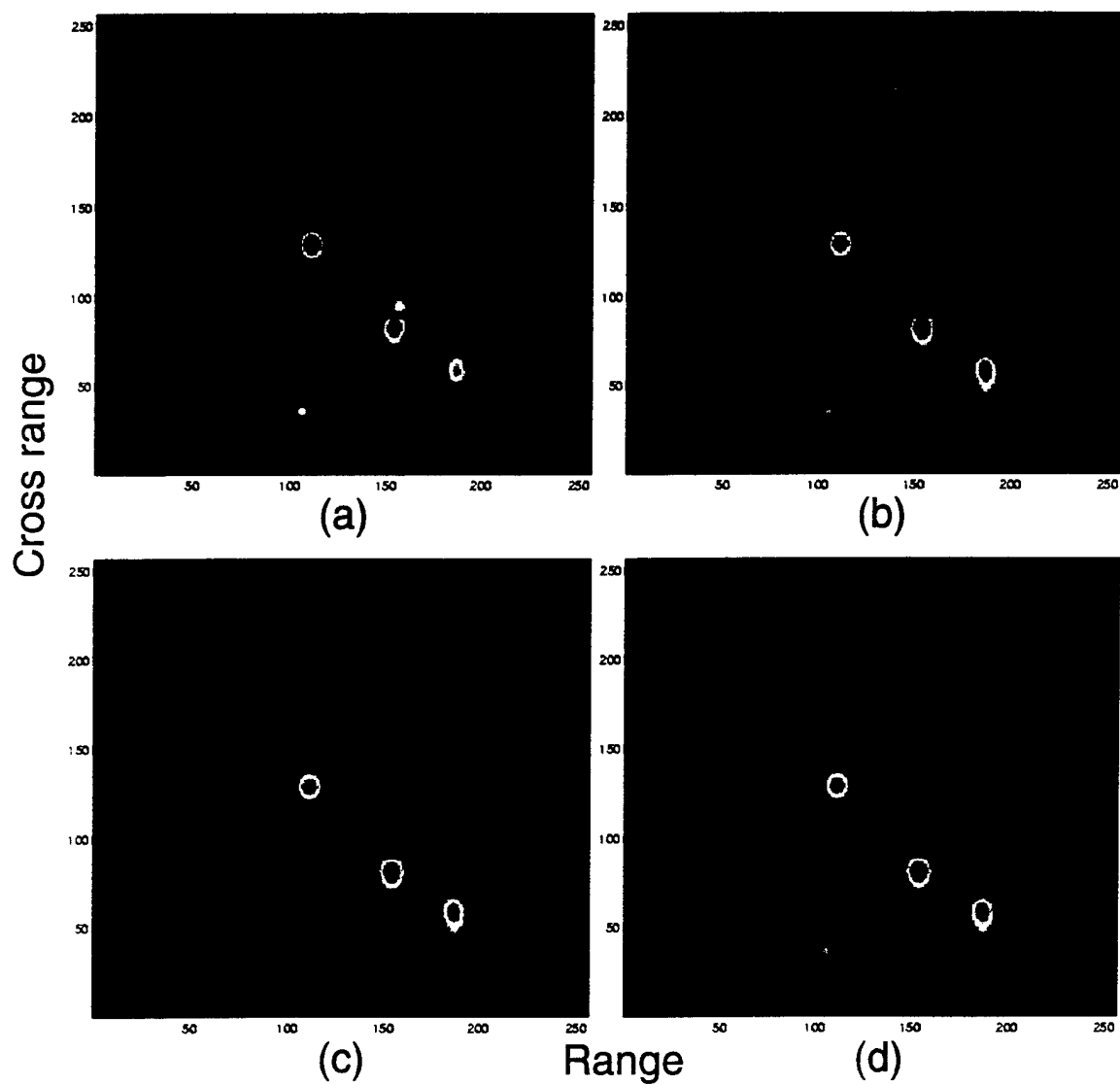
Fig.8 ISAR image interpolated using AFE from (a) 50 calculated
points (b) 100 calculated points (c) 200 calculated points (d) 400
calculated points.
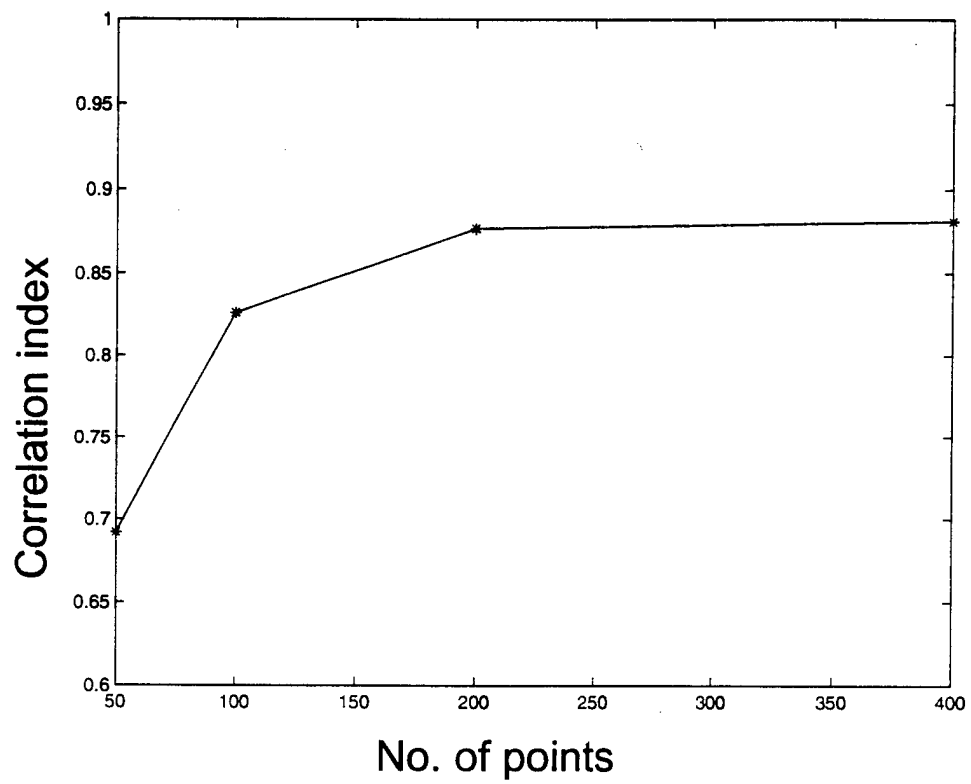
Fig.9 Image correlation index between the interpolated result and the
reference result versus the number of points used for interpolation.
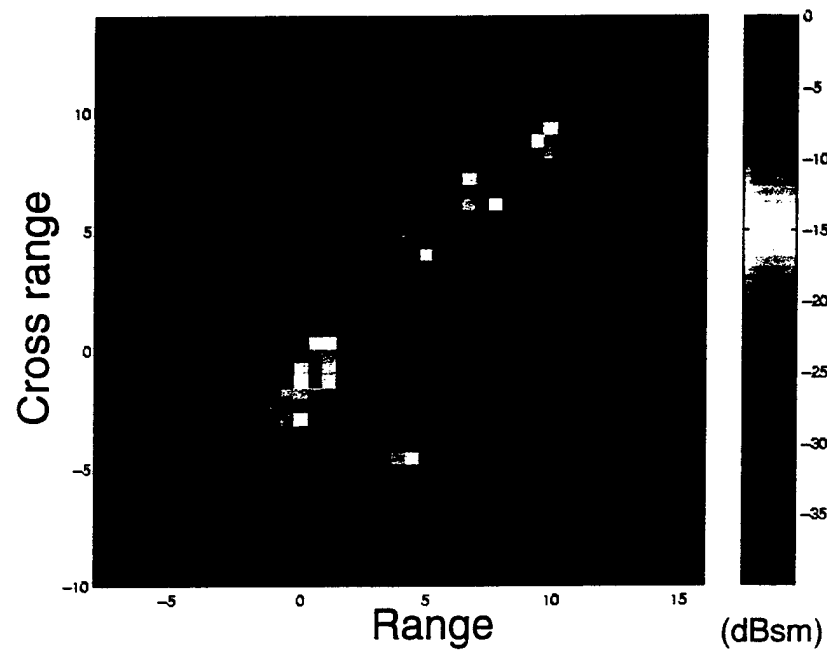
Fig.10 ISAR image of VFY-218 at 130 degrees from nose-on generated from interpolated result using AFE with 62 FISC-computed points.
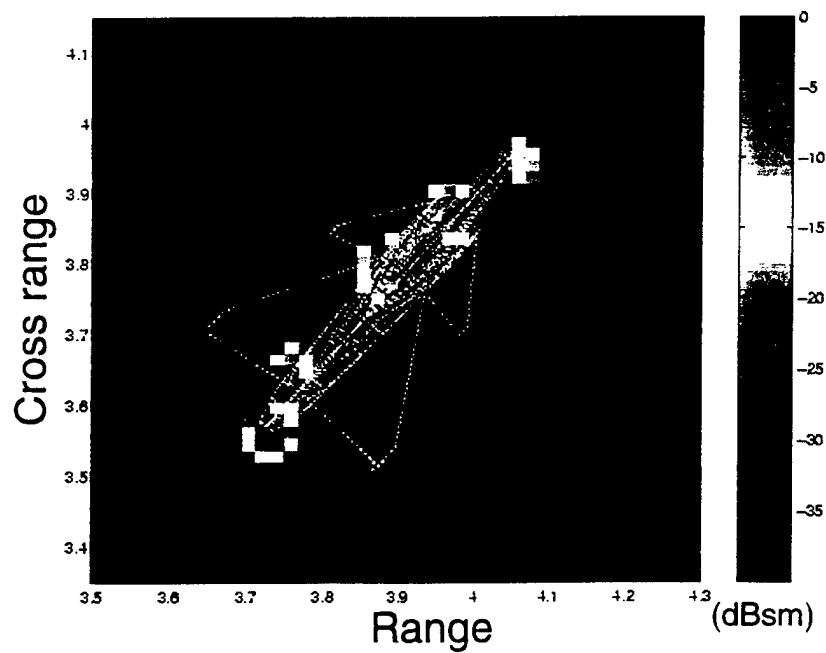
Fig.11 ISAR image of VFY-218 at 130 degrees from nose-on generated from chamber measurement data.
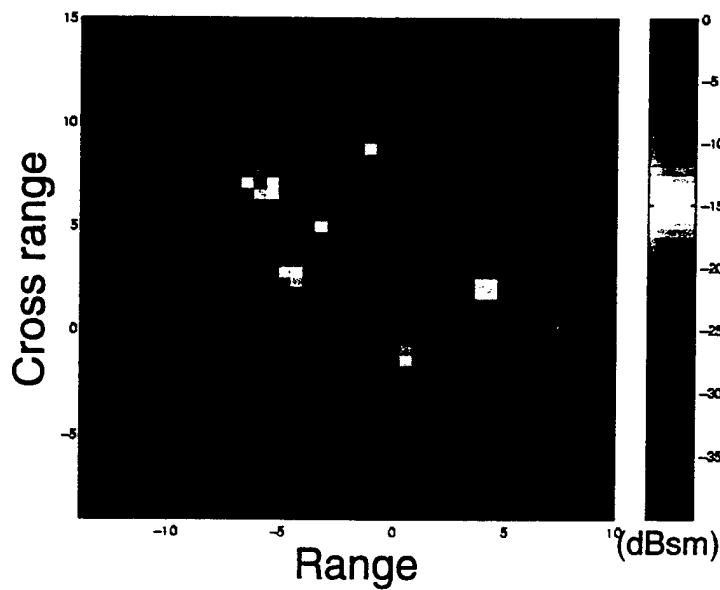
Fig.12 ISAR image of VFY-218 at 30 degrees from nose-on
generated from interpolated results using AFE with 62
FISC-computed points. The CAD model used in the
computation has sealed engine inlets.
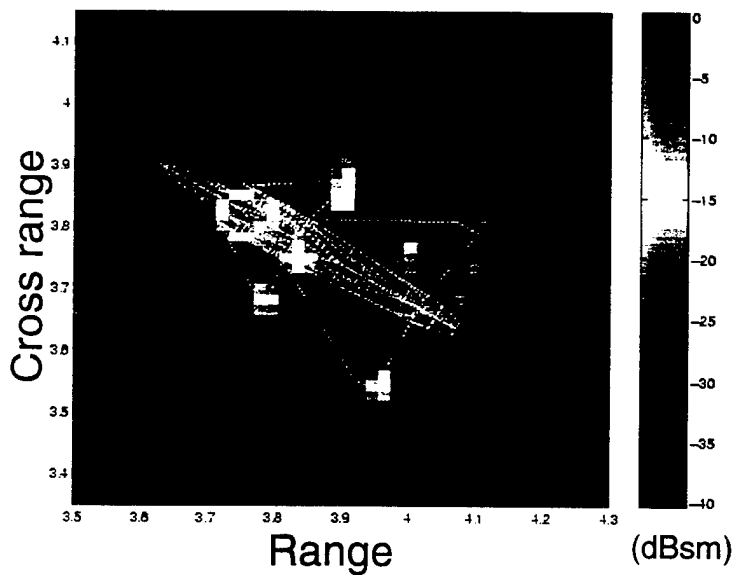
Fig.13 ISAR image of the VFY218 at 30 degrees
from nose-on generated from chamber
measurement data. The measured model
has open, untreated engine inlets.
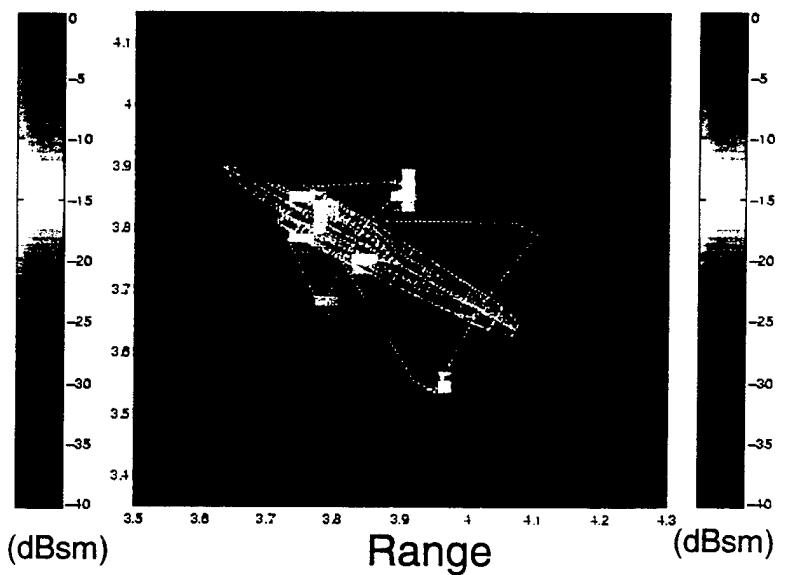
Fig.14 ISAR image of VFY-218 at 30 degrees
from nose-on generated from chamber
measurement data. The measured model
has absorber material placed in the inlets.

A Frequency-Aspect Extrapolation Algorithm for ISAR Image Simulation Based on Two-Dimensional ESPRIT

Yuanxun Wang and Hao Ling

Department of Electrical and Computer Engineering

The University of Texas at Austin

Austin, Texas 78712-1084

Abstract

A frequency-aspect extrapolation algorithm is proposed to accelerate ISAR image simulation using fast multipole solvers. A 2-D multiple-arrival model based on high-frequency physics is proposed to parameterize the induced currents on the target. A 2-D ESPRIT algorithm is developed to estimate the model parameters from a limited number of computed data samples in frequency and aspect. The model is then extrapolated to other frequencies and aspects to arrive at broadband, wide-angle RCS data for ISAR image construction. This algorithm is tested using a canonical cylinder-plate structure to evaluate its performance. The ISAR image of the benchmark VFY-218 airplane at UHF band is then predicted using the fast multipole solver FISC and the 2-D extrapolation algorithm. The resulting image compares favorably with that obtained from chamber measurement data.

Key words: ISAR Image Simulation, Frequency-Aspect Extrapolation, 2-D ESPRIT, Fast Multipole Solver

I. INTRODUCTION

Inverse synthetic aperture radar (ISAR) imaging is an important tool for radar signature diagnostic and target identification [1,2]. In order to simulate the ISAR image of a target, it is necessary to solve the electromagnetic scattering problem at multiple frequencies and angles. Then by performing a two-dimensional (2-D) Fourier transform on the resulting frequency-aspect radar cross section (RCS) data, a 2-D ISAR image of the target can be constructed. In this work, we consider ISAR image simulation of complex targets using a full-wave numerical technique. The focus of our attention is the class of iterative solvers based on the fast multipole method [3,4]. These solvers have much lower computational complexity than traditional moment method for scattering problems at a single frequency and a single observation angle. For multiple frequency-aspect RCS calculations, however, the solver has to be executed repeatedly for each angle and frequency.

To reduce the computation burden incurred by multiple frequency-aspect calculations, the concept of model-based parameter estimation can be applied to populate the required data set from a sparse set of computed data [5-12]. In particular, we have recently developed a 1-D frequency extrapolation algorithm [10,12] and a 1-D angular extrapolation algorithm [11] to predict the high-frequency RCS of complex targets. Our approach is based on modeling the induced current on the target using a multiple-arrival model that closely resembles the ray-optical behavior at high frequencies. The model coefficients are determined by the superresolution algorithm ESPRIT (Estimation of Parameters via Rotation Invariance Technique) [13, 14]. In this paper, we extend our algorithm to two dimensions to carry out simultaneous frequency-aspect extrapolation.

We begin by proposing a 2-D multiple-arrival model in the frequency-aspect domain. Next, we implement a 2-D ESPRIT algorithm [15, 16] to estimate the model coefficients from a limited number of frequency-aspect current data computed using a fast multipole solver. Once the model is determined, the currents, and subsequently the RCS, at other frequencies and aspects can thus be computed.

This paper is organized as follows. In Section II, we examine the frequency and angular dependency of the current phase and propose a multiple-arrival model in the frequency-aspect domain. In Section III, a 2-D ESPRIT algorithm is developed and applied to estimate the time-of-arrival and cross range parameters in the frequency-aspect model from a few calculated frequency-aspect samples. In Section IV, the extrapolation algorithm is tested on a canonical 2-D cylinder-plate structure. The result is compared against both the exact result and that obtained by using the well-known bistatic approximation in angle [12,17,18]. The extrapolated results are also generated as a function of the number of calculated samples to investigate the convergence of the algorithm. Finally, we apply the algorithm to extrapolate the RCS and generate a 2-D ISAR image of the VFY-218 airplane at UHF band. The extrapolated result is compared against the image obtained from chamber measurement data [19]. Conclusions are given in Section V.

II. 2-D MODEL FOR FREQUENCY-ASPECT EXTRAPOLATION

We shall first formulate a physical model for the current induced on the surface of a target due to an incident wave. The induced current at any point is in general the result of multiply incident waves from both the direct excitation and multiple scattering from

other parts of the target. Therefore, we postulate that the induced current can be written as a sum of multiply incident waves, each with a different travel paths, as shown in Fig. 1. If we denote the down range direction with respect to the incident wave as x and the cross range direction as y, the current at S as a function of frequency f can be written as

$$J(f,S) = \sum_{k=1}^{K} A_k e^{-j\frac{2\pi f}{c}d_k} \qquad , d_k = x_k + l_k \qquad (1)$$

where K is the number of incident waves arriving at S and c is the speed of light in free space. In the above definition of the path length d_k, we let (x_k, y_k) be the first hit point on the target due to the incident wave, and l_k be the total intermediate path length of the multiple scattering mechanism from the first hit point to point S. A_k is the amplitude coefficient for each mechanism and is assumed to be frequency independent. Among the three mechanisms illustrated in Fig.1, mechanism 1 is the direct incident wave from the source. Therefore, $l_1=0$ and (x_1, y_1) corresponds to point S. Mechanisms 2 and 3 are respectively a once-scattered and a twice-scattered wave before arriving at S. At high frequencies, this model is expected to be quite sparse. i.e., only a few terms are needed to adequately describe the scattering physics at an arbitrary point S on the target surface. This 1-D model was used to achieve frequency extrapolation at a fixed aspect angle in our earlier work [10,12].

Angular dependency can also be incorporated in the above model. We assume that all the intermediate scattering points and the amplitude coefficient for each mechanism remain fixed as the incident angle is varied, as illustrated in Fig.1. This assumption was found to be fairly accurate for ray-optical fields under small angular variation [20]. We have also applied it to achieve angular extrapolation at a fixed

frequency for iterative moment solvers [11]. When we combine the aspect behavior with the frequency model in (1), we arrive at the following model for the current as a function of both frequency and incident angle:

$$J(f,\theta,S) = \sum_{k=1}^{K} A_k e^{-j\frac{2\pi f}{c}(x_{ki}\cos\theta + y_{ki}\sin\theta + l_{ki})} \tag{2}$$

Equation (2) contains three unknowns in the phase function of each mechanism. Next we use the small-angle approximation $\cos\theta \approx 1$ to arrive at an expression with two unknowns in the phase:

$$J(f,\theta,S) \approx \sum_{k=1}^{K} A_k e^{-j\frac{2\pi f}{c}(d_{ki}\cos\theta + y_{ki}\sin\theta)} = \sum_{k=1}^{K} A_k e^{-j(k_x d_{ki} + k_y y_{ki})} \tag{3}$$

where $k_x = 2\pi f \cos\theta / c$ and $k_y = 2\pi f \sin\theta / c$. Note that equation (3) can be further approximated to completely decouple the frequency and aspect variable:

$$J(f,\theta,S) = \sum_{k=1}^{K} A_k e^{-j\frac{2\pi f_c}{c} y_{ki}\theta} e^{-j\frac{2\pi f}{c} d_{ki}} \tag{4}$$

if we use $\sin\theta \approx \theta$ and replace the frequency variable in the first exponential by the center frequency f_c. Equation (4) then reduces to equation (3b) in [11] when only aspect variation is considered. For the 2-D extrapolation in this work, we choose to use the model in (3) since it is more accurate when the aspect range is large. Equation (3) is in the form of a sum-of-exponential model, with linear phase dependence with respect to both k_x and k_y. Consequently, the 2-D superresolution algorithm ESPRIT [17] can be applied to equally spaced k_x and k_y data samples. Next, we shall describe the implementation of the 2-D ESPRIT algorithm to estimate the unknown parameters in the model.

III. TWO-DIMENSIONAL ESPRIT ALGORITHM

In [16], a 2-D ESPRIT algorithm was developed for estimating the direction-of-arrival in 2-D antenna array problems. Here, we shall show that with some minor modifications, it can be applied to estimate the parameters A_k, d_k and y_k in equation (3). First, we assume that the parameters are to be estimated from known current values solved at M x N equally spaced samples in the k_x - k_y plane, where M is the number of samples in k_x and N is the number of samples in k_y. These M x N samples are similar to the elements of a 2-D antenna array described in [16]. We define:

$$p_k = e^{-j\Delta k_x d_k}, \quad q_k = e^{-j\Delta k_y y_k} \tag{5}$$

where Δk_x and Δk_y are the sampling intervals in k_x and k_y, respectively. If we shift the origin of the variables k_x and k_y to zero, we can rewrite equation (3) into a form similar to equation (9) of [16]:

$$z_{il} = \sum_{k=1}^{K} s_k p_k^{i-1} q_k^{l-1} + n_{il}, \quad i = 1,2,.....,M, \quad l = 1,2,.....,N \tag{6}$$

where z_{il} is the current at the ith k_x value and the lth k_y value. s_k is the modified amplitude coefficient for the kth mechanism to account for the origin shift. n_{il} is assumed to be white Gaussian noise, which in our case is used to model the numerical error in the current computation. Since ESPRIT postulates such a sum-of-exponential model with additive white noise, an averaging procedure has to be performed to smooth out the noise to obtain the correct estimate of the covariance matrix. In [16], the averaging is performed naturally in the time domain. However, for the problem at hand, the time

dimension does not exist and has to be synthesized. This can be accomplished via a sub-array processing technique. As shown in Fig. 2, a sub-array size is chosen to be half of the original array. Then shifting the sub-array one data sample at a time in either k_x or k_y will result in a new sub-array, which can be considered as the array at a new time index. If we assume M and N are even numbers, the total number of sub-arrays that can be generated in this manner is $(\frac{M}{2}+1)(\frac{N}{2}+1)$. The signal vectors $\mathbf{z}(t)$, $\mathbf{s}(t)$ and $\mathbf{n}(t)$ are defined as the reshaped column vectors of the tth sub-array as follows:

$$z(t) = [z_{11}(t) \cdots z_{1L}(t) \cdots z_{l1}(t) \cdots z_{lL}(t)]^T \tag{7}$$

$$s(t) = [s_1(t) \quad s_2(t) \cdots s_K(t)]^T \tag{8}$$

$$n(t) = [n_{11}(t) \cdots n_{1L}(t) \cdots n_{l1}(t) \cdots n_{lL}(t)]^T \tag{9}$$

In the above expressions, $I = \dfrac{M}{2}$ and $L = \dfrac{N}{2}$, which are the maximum row and column indices of each sub-array. The array covariance matrix can thus be defined exactly like formula (15) in [16]. Following the procedures in [16], we estimate the parameters p_k and q_k. The time-of-arrival parameter d_k and the cross-range parameter y_k are obtained using:

$$d_k = \frac{1}{\Delta k_x}\angle p_k, \qquad y_k = \frac{1}{\Delta k_y}\angle q_k \tag{10}$$

Finally, the amplitude coefficient A_k can be generated by solving equation (3) via a least squares procedure. Noted that the maximum order number K permitted by the algorithm is:

$$K \leq \min[(\tfrac{M}{2}-1)\tfrac{N}{2}, (\tfrac{N}{2}-1)\tfrac{M}{2}]-1 \tag{11}$$

For the scattering problems we have examined, K is usually chosen to be 3 or 4. The minimum number of frequency and angular samples can then be selected to satisfy the above criterion.

After the coefficients A_k, d_k and y_k are estimated, we assume equation (3) also holds for other frequencies and aspects. Therefore, the induced current can be extrapolated to other k_x and k_y values of interest. An ISAR image is then generated using standard Fourier processing of the k_x-k_y data. To summarize, the extrapolation procedure is carried out by first selecting a number of densely sampled points in a limited frequency-aspect range and solving the scattering problems at these points. Usually the computed frequencies are chosen close to the low frequency end and the aspect angles are centered about the central angle of interest. Second, the 2-D ESPRIT algorithm is applied to estimate the model parameters of the current at each point on the target surface. Third, the induced current is extrapolated to a wider k_x and k_y range based on the model coefficients generated from 2-D ESPRIT processing. Finally, the current is integrated to generate the scattered far field as a function of frequency and aspect and the results are used to generate the desired ISAR image.

IV. NUMERICAL RESULTS

To validate the frequency-aspect extrapolation algorithm, we first consider a 2-D cylinder-plate structure shown in Fig. 3. The diameter of the cylinder is 4.2 m and the length of the plate is 20 m. The origin of the cylinder and the center of the plate are separated by 6.2 m. The frequency band of interest is from 0.3 GHz to 0.65 GHz and the observation angle is from 25° to 65°. Fig. 4 shows the reference ISAR image generated

from 71x 81=5751 computed points in the frequency-aspect plane. The image has a dynamic range of 40 dB. In this structure, strong multiple scattering mechanisms between the cylinder and the plate dominate the backscattering. We can see in the image the features corresponding to the direct scattering from the cylinder (labeled as (i)), the front edge point of the plate (ii), and the shadow boundary cast on the plate by the cylinder (iii). Additionally, there are other range-delayed features corresponding to the multiple scattering mechanisms. For comparison, we calculate the current at 71 frequency samples for one aspect angle, and use the well-known bistatic approximation [17, 18] to extrapolate the RCS to other aspect angles. Fig. 5 plots the resulting ISAR image from the extrapolated frequency-aspect data using the bistatic approximation. In this image, only the direct scattering features ((i) and (ii)) are correctly predicted while the higher-order scattering features are poorly predicted in either position or amplitude. This is because the bistatic approximation is based on physical optics, in which the current is assumed to be excited by only the direct incident wave.

We next construct the ISAR image using the 2-D frequency-aspect extrapolation algorithm. We choose 8 x 8 points at the low frequency end and about the central angle of the original 71x 81 points. After the time-of-arrival and cross-range parameters are extracted by using 2-D ESPRIT, the induced currents and scattered far fields are extrapolated to the k_x-k_y aperture of the original samples. In this manner, the ISAR image can be generated directly by a 2-D FFT of the k_x-k_y data without the polar reformatting operation [2]. The resulting ISAR image is plotted in Fig. 6(a). As we can see, most of the features are predicted in the correct position. However, some of the weaker features are highly defocused. We repeat this process using 2-D ESPRIT

extrapolation for 9 x 9, 10 x 10 and 11 x 11 input points. The resulting images are shown in Figs. 6(b), 6(c) and 6(d), respectively. From this series of images, we see that the strong scattering features are quite stable throughout while the weaker features begin to converge as the number of input points is increased. We find that the correlation indices between the extrapolated images and the reference image are respectively 0.72, 0.80, 0.82 and 0.88. This shows a steady improvement as the number of input points is increased. For the case of 11 x 11 input points, nearly all of the features in the extrapolated image agree well with those in the reference image from the brute-force calculation. This corresponds to a 7:1 extrapolation ratio in each dimension.

Next, we use the 2-D extrapolation algorithm to simulate the ISAR image of the benchmark VFY-218 airplane. The simulation is carried out using the multi-level fast multipole code FISC [21] on a Pentium II 450 MHz PC. The total computation time would take about 200 days if a brute-force calculation is carried out over the required 41x41 frequency-aspect samples (to achieve 0.5 meter resolution in range and cross range). Based on the 7:1 criterion found above, the actual computation is only carried out for 6 x 6 = 36 points from 267 MHz to 297 MHz in frequency and 127° to 132° in aspect. The total computation time is 40 hours. Note that the time savings over the brute-force calculation is even greater than the $(41/6)^2$ ratio. This is because these 36 points are chosen at the low end of the frequency band, and take far less time to compute than those at the high frequency end. The induced current and far fields are then extrapolated to a k_x-k_y grid from 267 MHz to 533 MHz in frequency and from 110° to 140° in aspect. The resulting ISAR image of the airplane at 130° is shown in Fig. 7. Fig. 8 shows the ISAR image constructed from chamber measurement data at the same look angle [19].

Comparing these two images, we observe that nearly all of the key features in the measurement image are predicted in the simulated image from using FISC and the 2-D extrapolation algorithm. As expected, the image in Fig. 7 is much cleaner than the previously predicted image shown in Fig. 11 of [12], which was simulated from the 1-D frequency extrapolation procedure in combination with the bistatic approximation. The improvement is due to the fact that the multiple scattering mechanisms are correctly incorporated in both dimensions in our new model. There still exist some low dynamic range noises in the predicted image, which can be improved with more computed points.

V. CONCLUSIONS

A 2-D frequency-aspect extrapolation algorithm has been developed to accelerate ISAR image simulation using fast multipole solvers. A 2-D multiple-arrival model consistent with high-frequency scattering physics was proposed to model the induced currents on the target. A 2-D ESPRIT algorithm was developed to estimate the model parameters from a limited number of computed data samples in frequency and aspect. The model was then extrapolated to other frequencies and aspects to arrive at broadband, wide-angle RCS data for ISAR image construction. This algorithm has been tested using a canonical cylinder-plate structure to evaluate its performance. It was found that a 7:1 extrapolation ratio in each dimension can been achieved. Furthermore, the input data samples can be chosen in the low frequency range for greater computational payoff. Lastly, the ISAR image of the benchmark VFY-218 airplane at UHF band has been predicted using the fast multipole solver FISC and the 2-D extrapolation algorithm. The resulting image compared favorably with that obtained from chamber measurement data.

The computation time savings over the brute-force calculation was about two orders of magnitude.

Acknowledgments

Reference

[1]. C. C. Chen and H. C. Andrews, "Target motion induced radar imaging," *IEEE Transactions on Aerospace Electronic Systems,* vol. AES-16, pp. 2-14, Jan. 1980.

[2]. A. Ausherman, A. Kozma, J. L. Waker, H. M. Jones and E. C. Poggio, "Developments in radar imaging," *IEEE Trans. Aerospace Electron. Syst.,* vol. 20, pp. 363-400, Apr. 1984.

[3]. R. Coifman, V. Rokhlin, and S. Wandzura, "The fast multiplole method for the wave equation : a pedestrian prescription." *IEEE Trans. Antennas Propagat. Mag.,* vol. 35, pp. 7-12, June 1993.

[4]. J. Song, C. C. Lu and W. C. Chew, "Multilevel fast multipole algorithm for electromagnetic scattering by large complex objects," *IEEE Trans. Antennas Propagat.,* vol. AP-45, pp. 1488-1493, Oct. 1997.

[5]. G. J. Burke, E. K. Miller, S. Chakrabarti and K. Demarest, "Using model-based parameter estimation to increase the efficiency of computing electromagnetic transfer functions," *IEEE Trans. Magnetics.* vol. 25, pp. 2807-2809, July 1989.

[6]. K. Kottapalli, T. K. Sarkar, Y. Hua, E. K. Miller, and G. L. Burke, "Accurate computation of wide-band response of electromagnetic systems utilizing narrow-band information," *IEEE Trans. Microwave Theory Tech.*, vol. MTT-39, pp. 682-687, Apr. 1991.

[7]. Z. Altman and R. Mittra, "Combining an extrapolation technique with the method of moments for solving large scattering problems involving bodies of revolution," *IEEE Trans. Antennas Propagat.*, vol. AP-44, pp. 548-553, Apr. 1996.

[8]. E. K. Miller, "Model-based parameter estimation in electromagnetics: part I. background and theoretical development," *IEEE Antennas Propagat. Mag.*, vol. 40, pp. 42-52, Feb. 1998.

[9]. C. J. Reddy, M. D. Deshpande, C. R. Cockrell and F. B. Beck, "Fast RCS computation over a frequency band using method of moments in conjunction with asymptotic waveform evaluation technique," *IEEE Trans. Antennas Propagat.*, vol. AP-46, pp. 1229-1233, Aug. 1998.

[10]. Y. Wang, H. Ling, J. Song and W. C. Chew, "A frequency extrapolation algorithm for FISC," *IEEE Trans. Antennas Propagat.*, vol. AP-45, pp. 1891-1893, Dec. 1997.

[11]. Y. Wang and H. Ling, "A model-based angular extrapolation technique for iterative method-of-moment solvers," *Microwave Opt. Tech. Lett.*, vol. 20, pp. 229-233, Feb. 1999.

[12]. Y. Wang and H. Ling, "Radar signature prediction using moment method codes via a frequency extrapolation technique," *IEEE Trans. Antennas Propagat.*, vol. AP-47, pp. 1008-1015, June 1999.

[13]. R. Roy, A. Paulraj, and T. Kailath, "ESPRIT - a subspace rotation approach to estimation of parameters of cisoids in noise," *IEEE Trans. Acoust. Speech Signal Processing,* vol. ASSP-34, pp. 1340-1342, Oct. 1986.

[14]. R. Roy and T. Kailath, "ESPRIT - estimation of signal parameters via rotation invariance techniques," *IEEE Trans. Acoust. Speech Signal Processing,* vol.37, pp. 984-995, July 1989.

[15]. J. Li and R. T. Compton, Jr., "Angle and polarization estimation using ESPRIT with a polarization sensitive array," *IEEE Trans. Antennas Propagat.,* vol. AP-39, pp. 1376-1383, Sept. 1991.

[16]. J. Li and R. T. Compton, Jr., "Two-dimensional angle and polarization estimation using the ESPRIT algorithm," *IEEE Trans. Antennas Propagat.,* vol. AP-40, pp. 550-555, May. 1992.

[17]. R. Bhalla and H. Ling, "ISAR image formation using bistatic data computed from the shooting and bouncing ray technique," *J. Electromag. Waves Appl.,* vol. 7, pp. 1271-1287, Sept. 1993.

[18]. J. F. Shaffer, B.A. Cooper, K. W. Hom, R. C. Baucke and N. A. Talcott, Jr., "A review of bistatic k-space imaging for electromagnetic prediction codes for scattering and antennas," *IEEE Antennas Propagat. Mag.,* vol. 39, pp. 21-29, Oct. 1997.

[19]. H. T. G. Wang, M. L. Sanders and A. Woo, "Radar cross section measurement data of the VFY 218 configuration," *Tech. Rept. NAWCWPNS TM-7621,* Naval Air Warfare Center, China Lake, CA, Jan. 1994.

[20]. R. Bhalla, H. Ling and H. Nussbaum, "Multi-aspect range profile extrapolation for the shooting and bouncing ray technique," *J. Electromag. Waves Applications*, vol. 10, pp. 249-268, Feb. 1996.

[21]. *User's Manual for FISC (Fast Illinois Solver Code)*, Center for Computational Electromagnetics, Univ. of Illinois and DEMACO, Inc., Champaign, IL, Jan. 1997.
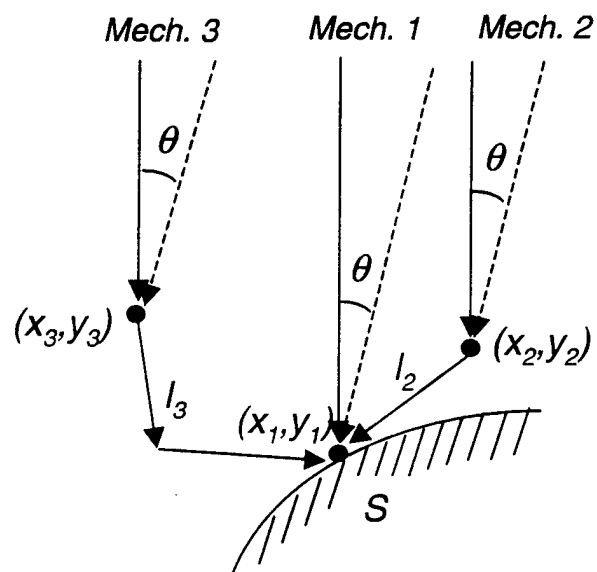
Fig. 1. Multiple-arrival model for the induced current.
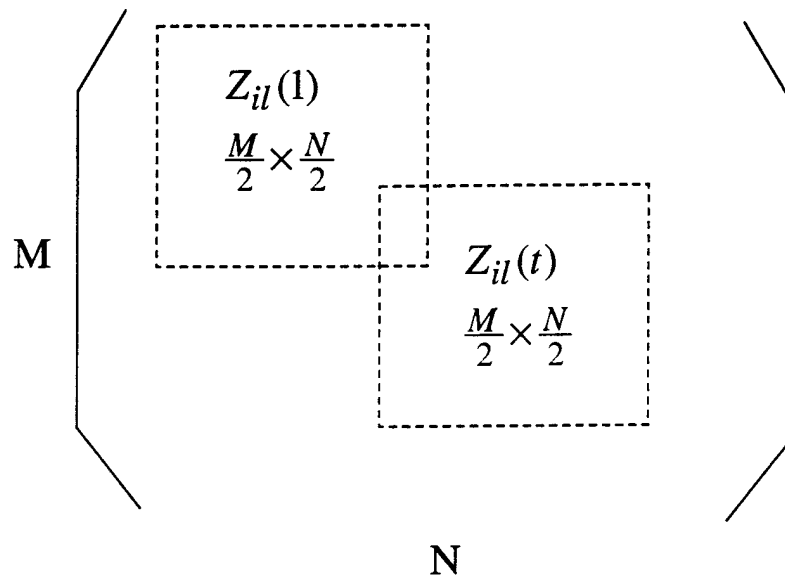
Fig. 2. Sub-array processing.
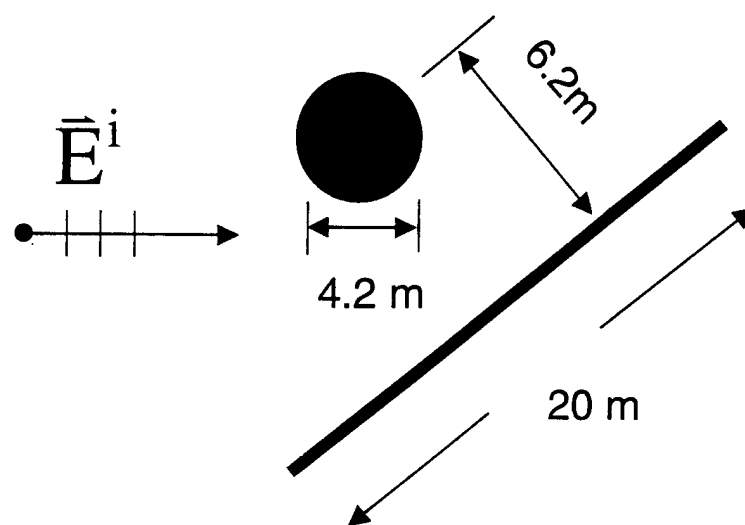
Fig. 3. Geometry of the cylinder-plate target.
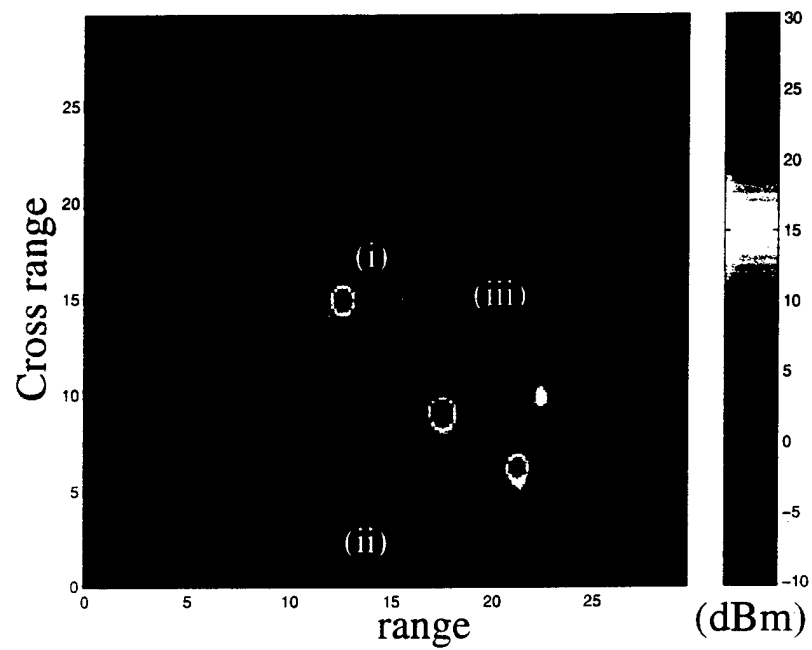
Fig. 4. Reference ISAR image generated using the brute-force
MoM calculations at 71x81=5751 points.
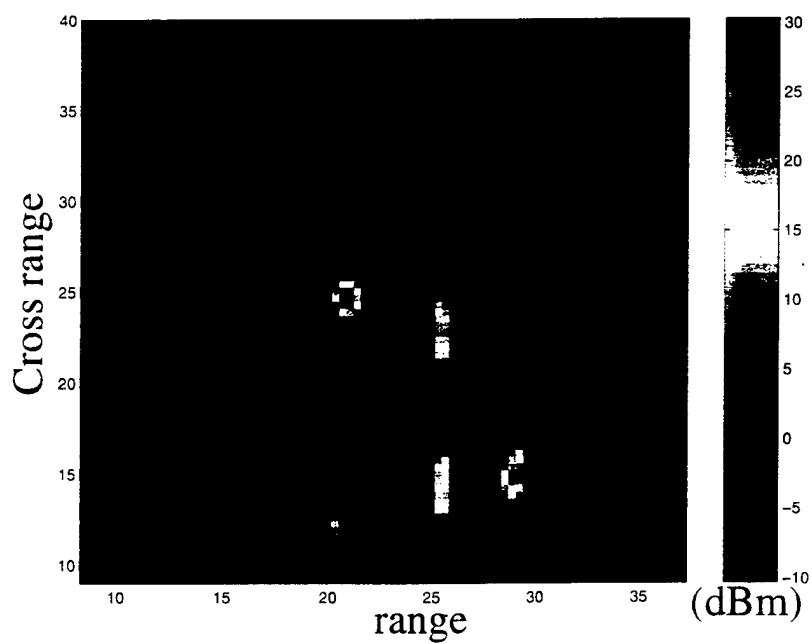
Fig. 5. ISAR image generated from 71 calculated frequency
points and the bistatic approximation.
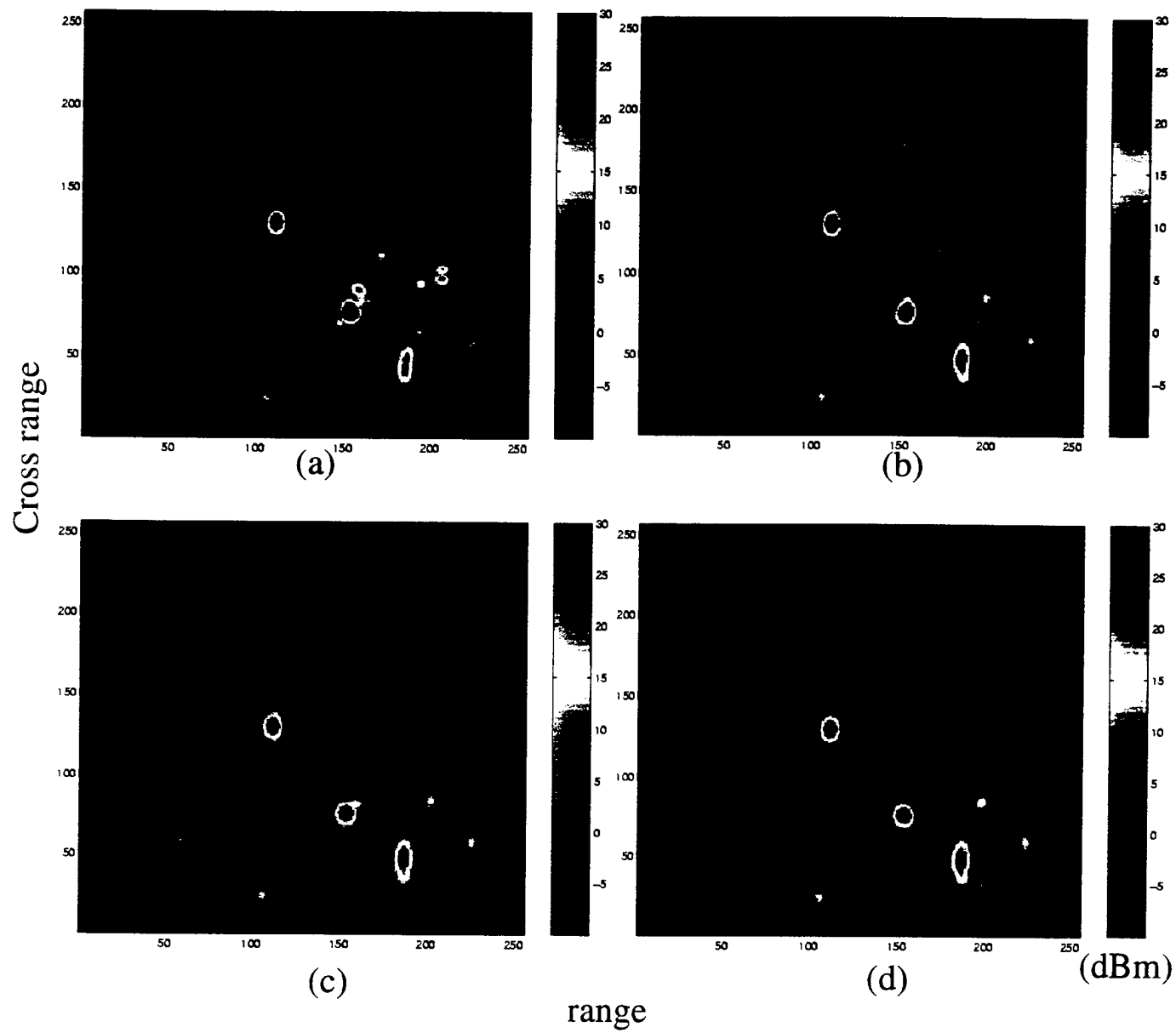
Fig. 6. ISAR images generated from the 2-D extrapolation algorithm
using: (a) 8 x 8 calculated points, (b) 9 x 9 calculated points,
(c) 10 x 10 calculated points, (d) 11 x 11 calculated points.
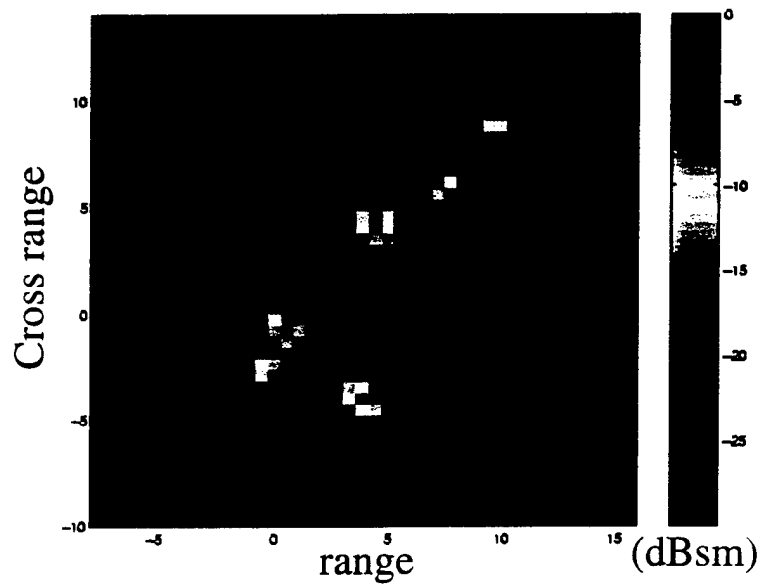
Fig. 7. ISAR image of the VFY-218 at 130 degrees from nose-on
generated from the extrapolated result using 2-D ESPRIT
with 36 FISC-computed points.
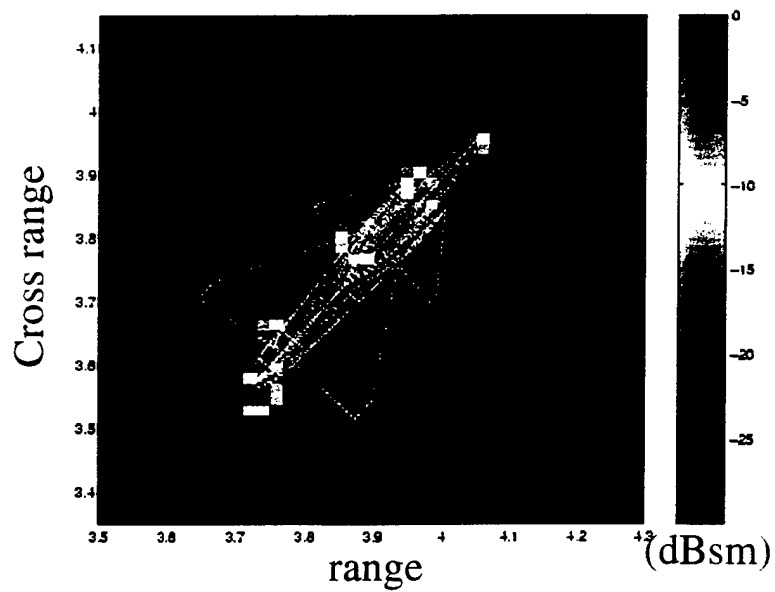
Fig. 8. ISAR image of the VFY-218 at 130 degrees from nose-on
generated from chamber measurement data [19].

A Frequency Extrapolation Technique for Computing Antenna-Platform Radiation Problems

Tao Su, Yuanxun Wang and Hao Ling

Department of Electrical and Computer Engineering
The University of Texas at Austin
Austin, TX 78712

Abstract

A frequency extrapolation technique is proposed to obtain the broad band radiation patterns of antenna-platform radiation problems. A frequency-dependent time-of-arrival model is applied to the induced current computed at low frequencies. The model parameters are estimated by applying the ESPRIT superresolution algorithm to the computed data. A pre-multiplication scheme in conjunction with the complex time-of-arrival estimation from ESPRIT is used to determine the additional frequency-dependent factors in the model. The current at high frequencies is then extrapolated based on the model and the radiated field is computed using the extrapolated current. The algorithm is applied to several 2D and 3D antenna-platform radiation problems. The extrapolated radiation patterns are found to be in good agreement with those generated by brute force computation. Since the current required for the extrapolation is only computed at lower frequencies, large savings in computation time and memory can be achieved.

I. Introduction

The numerical solution of electromagnetic scattering and radiation problems from complex structures is usually very computer intensive in time and memory, especially at high frequencies. In the standard method of moments (MoM), for example, the computation complexity scales as f^6 where f is the frequency. Even for fast solvers such as the fast multipole method [1,2], the frequency scaling is still between f^2 and f^3. Thus it is desirable to obtain the broad band response from the computation results at only a few frequencies. This can be accomplished by fitting the computed frequency response to a reduced-order model and extracting the model parameters from the data. Approaches based on model-based parameter estimation have been studied extensively and applied to many aspects in electromagnetic computation [3-11]. The appropriate reduced-order models to parameterize the physical observables are different depending on the frequency region of interest. In the low frequency range, the rational function model is widely used, while in the high frequency range, the time-of-arrival model is the preferred choice in characterizing the ray-optical behaviors of fields and currents.

In this paper, we address the model-based frequency extrapolation of antenna-platform radiation problems. It is well known that the radiation patterns of antennas are strongly affected by the mounting platform. Since the simulation of such radiation problems is very costly to generate as a function of frequency, we set out to extrapolate the high frequency response from computed data at lower frequencies. Our approach entails fitting the computed current at low frequencies to a time-of-arrival model and estimating the model parameters by the superresolution algorithm ESPRIT [12]. Previously, this approach has been applied to radar signature prediction with good

success [10]. In that work, the coefficients of the time-of-arrival model were assumed to be frequency independent. In the radiation problem, the primary radiation from the antenna is usually frequency dependent. Furthermore, when there exist higher-order multiple interactions on the platform, the amplitude of each mechanism is in general also frequency dependent [13-17]. Thus a more accurate model is needed to parameterize the current. Here we generalize the extrapolation algorithm by using a frequency-dependent time-of-arrival model. To extract the additional frequency dependence in this model, we adopt an approach similar to the one proposed in [15], which was developed to effectively extract the frequency dependency of the scattering mechanisms in measured backscattered data. Our results show that the radiation pattern can be accurately extrapolated based on the frequency dependent model.

This paper is organized as follows. Section II describes the frequency-dependent time-of-arrival model and the procedure to determine the model parameters. Section III gives a numerical example of the extrapolation algorithm using simulated data. The performance of the algorithm in the presence of noise is investigated and the errors in the estimation of model parameters are quantified. In Section IV we apply the algorithm to extrapolate the induced current in antenna-platform radiation problems. The radiation patterns predicted at high frequencies are compared against the reference MoM computation in both 2D and 3D platforms. Conclusions are given in Section V.

II. Frequency Dependent Model and Determination of Model Parameters

We postulate that the current induced on a complex platform due to illumination from a primary source can be well described by a time-of-arrival model at high frequencies.

The different time-of-arrival terms correspond to the different incident wave mechanisms from both the direct antenna radiation and higher-order scattering from other parts of the platform, as illustrated in Fig. 1. Therefore, the current at an arbitrary point P on the platform can be expressed as:

$$J(\omega) = \sum_n a_n e^{-j\omega t_n} \tag{1}$$

where t_n is the arrival time of the nth incident wave and a_n is its amplitude. In [10], a_n was assumed to be independent of frequency. However, in the antenna-platform radiation problem, the primary radiation from the antenna is in general frequency dependent. For instance, the radiation strength of a dipole antenna is proportional to the ω (or $\omega^{1/2}$ for a line source in 2D problems). Furthermore, for complex platforms, the incident waves to a specific current element can come from the scattered fields from other parts of the platform. These secondary incident fields are also frequency dependent. For canonical shapes, their exact frequency dependencies are predicted by the geometrical theory of diffraction (GTD), and are in the form of ω^α where α is the frequency factor. For example, the strength of the scattered field from corner diffraction has a frequency dependency of ω^{-1}, and that from edge diffraction has a frequency dependency of $\omega^{-1/2}$. Therefore, the time-of-arrival model can be improved by incorporating the frequency factor:

$$J(\omega) = \sum_n a_n \omega^{\alpha_n} e^{-j\omega t_n} \tag{2}$$

where α_n is the frequency factor for each incident wave. Compared with (1), this model is better matched to the actual physics of the radiation and scattering mechanisms.

Since we are attempting to extrapolate the frequency response to a much broader range, the accurate estimation of the frequency factors is critical. A small error in α will result in dramatic difference in amplitude at frequencies in the extrapolated region. However, the existing superresolution algorithms based on eigenspace decomposition (e.g. ESPRIT and MUSIC) apply only to signals in the form of (1). For instance, the ESPRIT algorithm [12] estimates (a_n, t_n) from uniformly sampled current data from ω_1 to ω_M based on the data model:

$$J(\omega_m) = \sum_n a_n e^{-j\omega_m t_n} + n(\omega_m), \qquad \omega_m = \omega_1, \omega_2, \cdots, \omega_M \qquad (3)$$

where n denotes additive Gaussian white noise. This model can be easily extended to estimate complex time-of-arrivals via analytic continuation. If we separate the real and imaginary part of t_n, the resulting model can be written as

$$J(\omega) = \sum_n a_n e^{\omega \operatorname{Im}(\tilde{t}_n)} e^{-j\omega \operatorname{Re}(\tilde{t}_n)} \qquad (4)$$

where the tilda symbol is used to indicate a complex number. This is the well-known complex exponential model and has been used to approximately model the frequency dependence in a_n [13]. Comparing (4) to the frequency-dependent time-of-arrival model (2), we find that the only difference between the two is the frequency dependency, which is in the form of ω^α in (2) and $e^{\omega \operatorname{Im}(\tilde{t}_n)}$ in (4). For a narrow band signal, (4) is usually a good approximation of (2), and can be simply used to model the frequency dependence within this band. However, in order to achieve accurate extrapolation results, the complex exponential model is a poor choice since it is not properly matched to the underlying physics.

To better determine the frequency factor α_n, we adopt an approach similar to the one proposed in [15] based on a pre-multiplication concept. We multiply the data by an assumed frequency factor $\omega^{-\alpha_m}$. The data model then becomes

$$\hat{J}(\omega) = \omega^{-\alpha_m} J(\omega) = \sum_n a_n \omega^{(\alpha_n - \alpha_m)} e^{-j\omega t_n} \tag{5}$$

Next, we apply ESPRIT and the complex exponential model on $\hat{J}(\omega)$ to estimate the real and imaginary parts of $\tilde{t}_n$. Note that if the frequency dependence of the pre-multiplier is exactly matched to that of a particular mechanism, the resulting exponential term will have no frequency dependence. Consequently, the estimated complex time-of-arrival term will have a zero imaginary part. Therefore, by repeatedly pre-multiplying the signal using different values of α_m and observing the imaginary parts of the resulting $\tilde{t}_n$, we can detect the correct frequency dependence α_n whenever $Im(\tilde{t}_n)$ goes to zero. The implicit assumption of this approach is that the mismatched terms will not significantly distort the estimation of $Im(\tilde{t}_n)$ of the matched term. This is usually true when the arrival times $Re(\tilde{t}_n)$ are well separated. When two or more of the arrival times are very close to each other, this algorithm becomes less accurate due to the interference between the exponential terms. The imaginary part of $\tilde{t}_n$ may not vanish even when the corresponding frequency factor is matched by the pre-multiplication. Quantitative evaluation of the resulting error will be discussed in detail in the next section. Once α_n and t_n are estimated, the amplitude a_n can be easily found by the standard least squares procedure.

III. Algorithm Testing and Error Estimation Using Simulated Data

To test the extrapolation algorithm, we consider the signal

$$J(\omega) = (1 + 0.4j)\omega^{-1/2}e^{-j2.8\omega} + (4.3 - 2.2j)\omega^{1/2}e^{-j1.3\omega} + n, \qquad \omega = 5, 6, \ldots, 35 \qquad (6)$$

where n is additive Gaussian white noise. The signal-to-noise ratio (SNR) is set to 10 dB. We now use a two-term time-of-arrival model to extrapolate the signal based on its first 10 samples. The actual signal is plotted as the solid line in Fig. 2. The extrapolation results of three different models are plotted. The frequency independent model, which is plotted in dashed dot, is obtained by the model in (1) with real time-of-arrival t_n determined by ESPRIT. This model matches badly with the original curve, even in the sampled region. The complex exponential model, plotted in dashed line, uses the model in (4) with complex $\tilde{t}_n$. The resulting curve is in good agreement with the actual signal within the sampled region, but not in the extrapolated region. This indicates that although the model (4) can be a very good approximation to the actual signal in the sampled region, it cannot be used to accurately extrapolate the signal because it does not have the correct frequency dependency. The frequency-dependent time-of-arrival model, which is plotted in dots, matches the best with the original signal in both the sampled region and the extrapolated region. Its parameters are estimated using the method described in Sec. II.

To show the detail workings of the pre-multiplier procedure, the imaginary parts of $\tilde{t}_n$ corresponding to the two terms in (6) are plotted as functions of α_m in Figs. 3(a) and 3(b) at the SNR levels of ∞ and 10 dB, respectively. The two curves cross zero at the corresponding frequency factor of -0.5 and 0.5. It can be observed that the shapes of the curves change when the SNR is decreased, especially for the term with smaller power ($\alpha_n = -0.5$). However, the positions of the zero-crossing points vary only weakly as the SNR is decreased.

Next, we examine the error performance of the extrapolation algorithm through numerical simulation. Among the three sets of model parameters a_n, α_n and t_n, the time-of-arrival t_n is directly estimated by the ESPRIT algorithm. When frequency dependent mechanisms are present in the signal, the estimation error in t_n is expected to be larger due to the interference between the exponential terms, especially when two or more arrival times are very close to each other. In this example, we estimate the arrival times in a simulated signal consisting of two frequency dependent exponential terms using ESPRIT. As a comparison, we also determine the arrival times in a two-term frequency independent signal. In both signals, the power of the stronger term is five times that of the weaker term. For the frequency dependent signal, the two frequency factors are set to 0.5 and -0.5 for the stronger and weaker terms, respectively. The test is performed 1000 times subject to random noise. In Fig. 4(a), the root mean squared (RMS) error on the time-of-arrival estimate of the weaker term is plotted as a function of the separation between the two arrival times and for different SNR conditions. The dashed lines are the estimation errors from the frequency independent signal, while the solid lines are the errors from the frequency dependent signal. Both axes are calibrated in terms of the Fourier resolution, which is the reciprocal of the available data bandwidth. It is shown that the arrival time error is larger for the frequency dependent signal, especially when the SNR is high. However, the degradation is not too severe overall. Good estimation (with error less than 0.1 Fourier bin) is still achievable for signal separation well within one Fourier bin.

The RMS error of estimating the frequency factor α_n of the weaker signal is plotted in Fig. 4(b) for the frequency dependent signals used in the above test. We observe that the

error decreases as the separation between the exponential terms increases and as the SNR increases, similar to the trends in Fig. 4(a). When the two arrival times are close, the interaction between the two terms results in error on the estimation of α_n and the error is strongly affected by the noise level. We can further decrease the error by imposing the constraint that the frequency factors are integer multiples of 1/2, as dictated by GTD. This is implemented when we deal with actual electromagnetic data in the next section.

Finally we look at the extrapolation error of the entire frequency-dependent time-of-arrival model. An extrapolation ratio of 3 to 1 is used in the example, i.e. the frequency response is extrapolated to three times the original bandwidth. The percentage RMS error is plotted in Fig. 4(c). When the separation between the two terms is large, the extrapolation error behaves similar to the errors of t_n and α_n. When the two terms become too close in time, we note that the error curves actually reach a maximum and then drop off. This is because below this point, the two exponential terms are too close to be resolved within the extrapolation region of interest. For larger extrapolation bandwidth, the position of the peak should move toward zero.

IV. Numerical Results

We now apply the frequency extrapolation technique to computation data from antenna-platform radiation problems. In the first example, a two-dimensional structure shown in Fig. 5 is considered. The platform is 14m in length and 3m in height. The antenna is a horizontal line source placed at 5m above the platform. The induced current on the platform is computed from 0.1 to 0.5 GHz at 21 frequency points using 2D MoM. The current is extrapolated to 1.3 GHz and radiated field is then computed based on the

extrapolated current. Both the frequency-independent and frequency-dependent time-of-arrival models are used to perform the extrapolation, and the resulting radiated fields at the observation angle of $\theta = 40°$ are plotted in Figs. 6(a) and 6(b), respectively. Also plotted is the reference MoM results obtained via brute force computation. The primary radiation of the dipole antenna is not included in the plots so that we can better observe the secondary radiation from the platform. It is obvious that the frequency dependency in the field response is not captured by the frequency-independent time-of-arrival model, while the field predicted by the frequency dependent model is in good agreement with the computed result. The time domain response corresponding to Fig. 6(b) is plotted in Fig. 6(c). It is shown that the time-domain peaks are well characterized by the extrapolated field. Finally, the radiation patterns obtained through brute force MoM computation and frequency extrapolation are plotted as functions of frequency and observation angles in Figs. 7(a) and 7(b), respectively. Very good agreement is observed between the two figures. For a quantitative comparison, the correlation index between the two figures is computed using the definition

$$R = \frac{\iint E_1^{*}(f,\theta)E_2(f,\theta)dfd\theta}{\frac{1}{2}\iint (|E_1(f,\theta)|^2 + |E_2(f,\theta)|^2)dfd\theta} \tag{7}$$

where E_1 and E_2 are the radiated fields in linear scale obtained by extrapolation and MoM computation, respectively. The correlation index between the two figures is 0.9992 in the sampled region and 0.9857 in the extrapolated region. As expected, the correlation is lower in the extrapolated region. However, the drop off is relatively small.

Next, we look at a 3D platform shown in Fig. 8. The antenna is a horizontal dipole oriented in the x direction. The induced current is computed from 0.1 to 0.36 GHz at 13

frequencies and extrapolated to 0.7GHz. The computation is carried out using FISC [18], which is a 3D MoM code based on the fast multipole method. The extrapolated frequency and time domain responses at the observation angle $\phi_{el} = 30°$, $\phi_{az} = -60°$ are plotted in Figs. 9(a) and 9(b), respectively. Also plotted for comparison are the reference responses computed by FISC via brute force. The major radiation features are captured in both domains by the extrapolation. In the time domain response, we observe that the amplitudes of some of the weaker peaks are not correctly predicted by the extrapolation, although their arrival times are estimated quite accurately. We believe this is due to the estimation error of α_n in the current parameterization, as we expect larger errors in the frequency factors for the weaker time-of-arrival terms. Figs. 10(a) and 10(b) show the reference and extrapolated radiation patterns as functions of frequency and azimuth angle when the elevation angle is fixed at 50°. Good qualitative agreement is observed. The correlation index between the two figures is found to be 0.9980 in the sampled region and 0.9742 in the extrapolated region, respectively. This result is a little worse than the 2D example because the noise level of the FISC-computed current is higher than that of the 2D MoM code. As was shown in the last section, the extrapolation performance is affected by the SNR in the computed data. The computation time of the brute force reference results is about 50 hours on a PentiumII 400MHz PC, while the total computation time to carry out the EM computation in the sampled region and the extrapolation process is 7 hours.

V. Conclusions

In this paper, the frequency-dependent time-of-arrival model has been applied to extrapolate the induced current and radiation pattern in antenna-platform radiation problems. The model parameters are estimated by applying the ESPRIT superresolution algorithm to the computed data. A pre-multiplication scheme in conjunction with the complex time-of-arrival estimation from ESPRIT is used to determine the additional frequency-dependent factors. The performance of the algorithm in the presence of noise has been evaluated based on simulated data and errors in the estimation of model parameters have been quantified. Our results show that the method is quite robust. The algorithm has been applied to extrapolate the induced currents and radiation patterns in both 2D and 3D antenna-platform radiation problems. The radiation patterns computed from the extrapolated currents have been found to be in good agreement with those generated by brute force computation.

Although the determination of model parameters is more complicated, the frequency dependent model show significant performance improvement over the frequency independent model. This is due to the improved modeling of the scattering physics. Since the current required for the extrapolation is only computed at lower frequencies, large savings in computation time and memory can be achieved.

References:

[1] R. Coifman, V. Rokhlin and S. Wandzura, "The fast multipole method for the wave equation: a pedestrian prscription," *IEEE Antennas Propagat. Mag.*, vol. 35, pp.7-12, June 993.

[2] J. Song, C. C. Lu and W. C. Chew, "Multilevel fast multipole algorithm for electromagnetic scattering by large complex objects," *IEEE Trans. Antennas Propagat.*, vol. 45, no. 10, pp. 1488-1493, Oct. 1997.

[3] E. K. Miller, "Model-based parameter estimation in electromagnetics: part I. background and theoretical development," *Applied Computational Electromagnetics Society Newsletter*, vol. 10, no. 3, Nov. 1995.

[4] E. K. Miller, "Model-based parameter estimation in electromagnetics: part II. applications to EM observables," *Applied Computational Electromagnetics Society Newsletter*, vol. 11, no. 2, pp. 35-56, Feb. 1996.

[5] E. K. Miller, "Model-based parameter estimation in electromagnetics: part III. Application to EM integral equations," *Applied Computational Electromagnetics Society Newsletter*, vol. 10, no. 3, pp. 9-29, Nov. 1995.

[6] K. Kottapalli, T. K. Sarkar, Y. Hua, E. K. Miller, G. J. Burke, "Accurate computation of wide-band response of electromagnetic systems utilizing narrow-band information," *IEEE Trans. Microwave Theory Tech.*, vol. 39, pp. 682-687, Apr. 1991.

[7] R. S. Adve and T. K. Sarkar, "Generation of accurate broadvand information from narrowband data using the Cauchy method," *Microwave Opt. Tech Lett.*, vol. 6, no. 10, Aug. 1993.

[8]   Z. Altman and R. Mittra, "Combining an extrapolation technique with the method of moments for solving large scattering problems involving bodies of revolution," *IEEE Trans. Antennas Propagat.*, vol. 44 pp. 548-553, Apr. 1996.

[9]   C. J. Reddy, M. D. Deshpande, C. R. Cockrell and F. B. Beck, "Fast RCS computation over a frequency band using method of moments in conjunction with asymptotic waveform evaluation technique," *IEEE Trans. Antennas Propagat.*, vol. 46, no. 8, pp. 1229-1233, Aug. 1998.

[10] Y. Wang and H. Ling, "Radar signature prediction using moment method codes via a frequency extrapolation technique," *IEEE Trans. Antennas Propagat.*, vol. 47, pp.1008-1015, June 1999.

[11] T. Su, Y. Wang and H. Ling, "Model-based frequency extrapolation of antenna radiation characteristics on complex platforms", *Proceedings of the 15th Annual Symposium of the Applied Computational Electromagnetics Society*, Monterey, pp. 272-277, Mar. 1999.

[12] R. Roy, A. Paulraj and T. Kailath, "ESPRIT – A subspace rotation approach to estimation of parameters of cisoids in moise." *IEEE Trans. Acoust., Speech, Signal Processing*, vol. ASSP-34, pp.1340-1342, Oct. 1986.

[13] M. P. Hurst and R. Mittra, "Scattering center analysis via Prony's method," *IEEE Trans. Antennas Propagat.*, vol. AP-35, pp. 986-988, Aug. 1987.

[14] R. Carriere and R. L. Moses, "High resolution radar target modeling using a modified Prony estimator," *IEEE Trans. Antennas Propagat.*, vol. 40, pp. 13-18, Jan. 1992.

[15] A. Moghaddar, Y. Ogawa, E. K. Walton, "Estimating the time-delay and frequency decay parameter of scattering components using a modified MUSIC algorithm," *IEEE Trans. Antennas Propagat.*, vol. 42, pp. 1412-1418, Oct. 1994.

[16] L. C. Potter, D. Chiang, R. Carriere and M. J. Gerry, "A GTD-based parametric model for radar scattering," *IEEE Trans. Antennas Propagat.*, vol. 43, pp. 1058-1067, Oct. 1995.

[17] K. M. Cuomo, J. E. Piou and J. T. Mayhan, "Ultrawide-band coherent processing," *IEEE Trans. Antennas Propagat.*, vol. 47, pp. 1094-1107, June 1999.

[18] *User's Manual for FISC (Fast Illinois Solver Code)*, Center for Computational Electromagnetics, University of Illinois at Urbana-Champaign and DEMACO, Inc., IL, Jan. 1997.
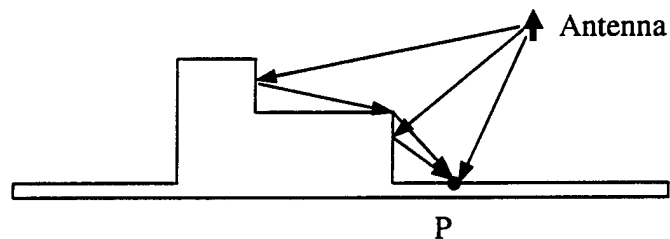
Fig. 1. Time-of-arrival model for the induced current at point P accounts for the direct incident radiation from the antenna and the multiple scattered waves from other parts of the platform.
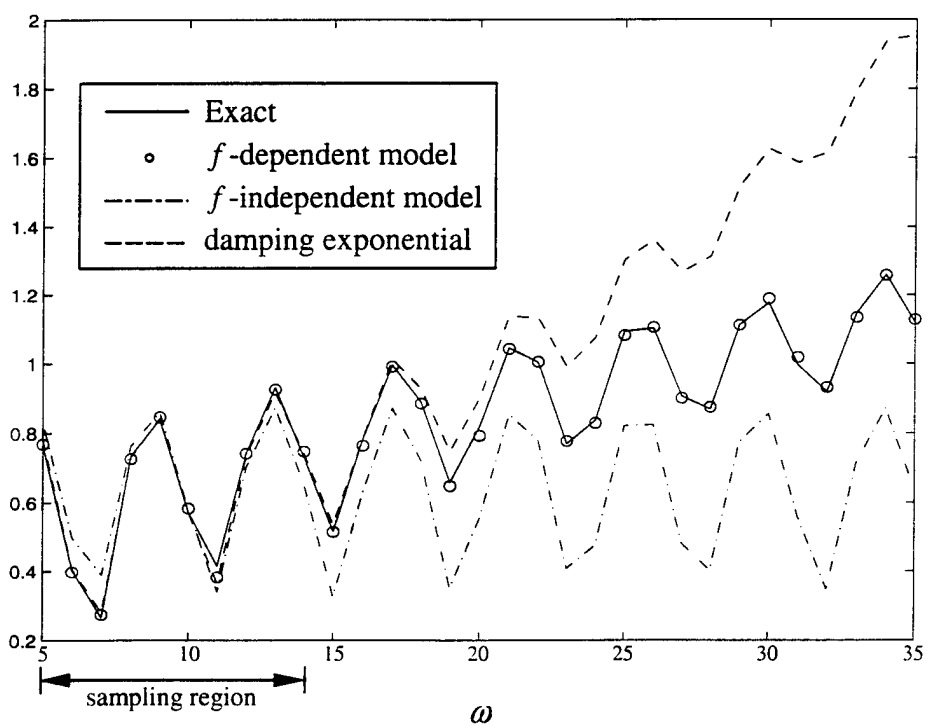
Fig. 2. Extrapolation of a simulated signal using different models.

(a) SNR = ∞   (b) SNR = 10dB
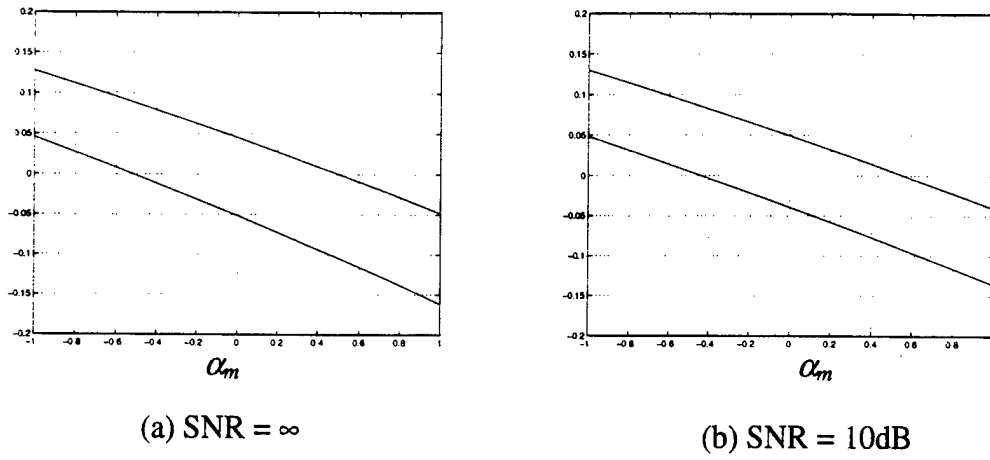
Fig. 3. Variation of $\text{Im}(t_n)$ as a function of the pre-multiplication factor α_m for the simulated signal at two different SNR levels.
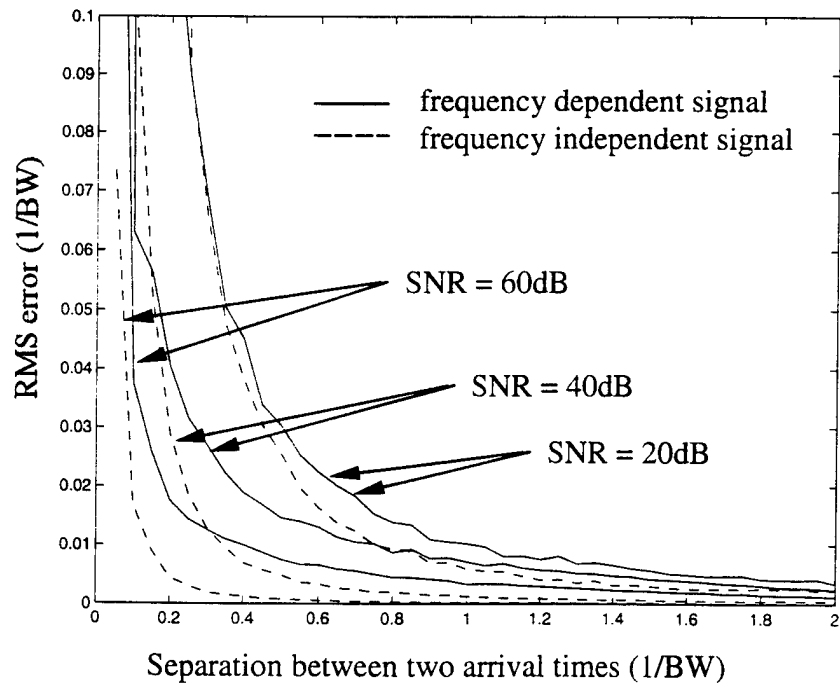
Fig. 4(a) RMS error in estimating the time-of-arrival t_n using ESPRIT.
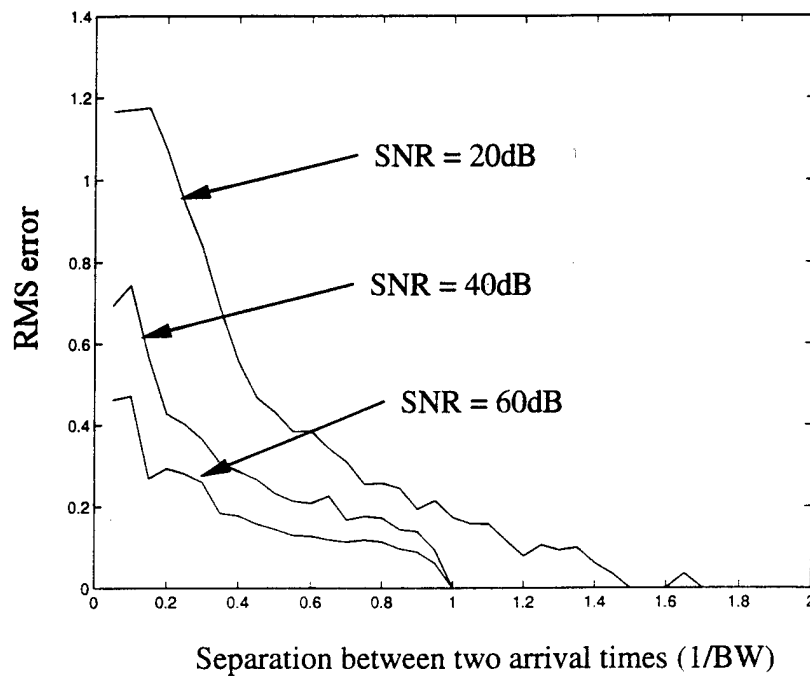
(b) RMS error in estimating the frequency factor α_n.
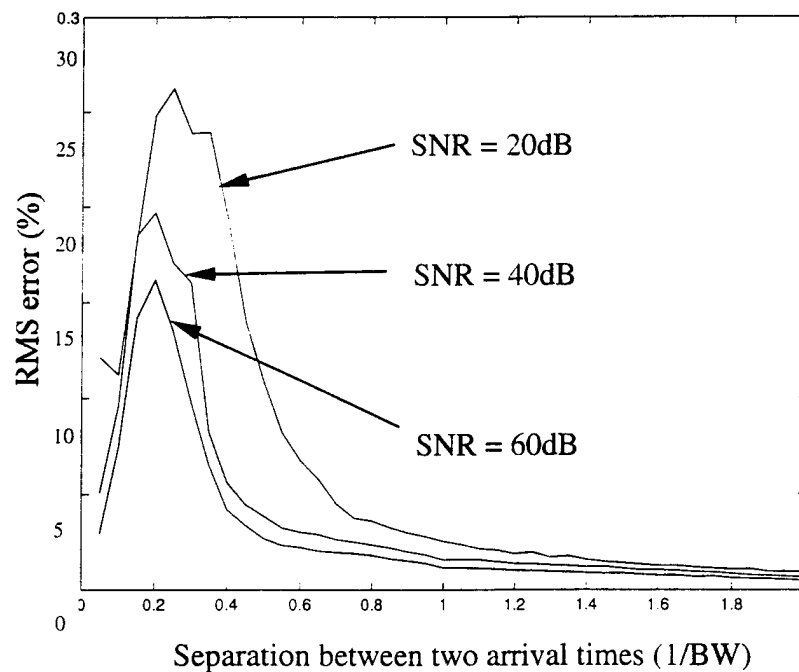
(c) Percentage RMS error of the extrapolated signal at the extrapolation ratio of 3:1.

Fig. 4. Error performance of the extrapolation algorithm as a function of the separation between two arrival times at different SNR levels.
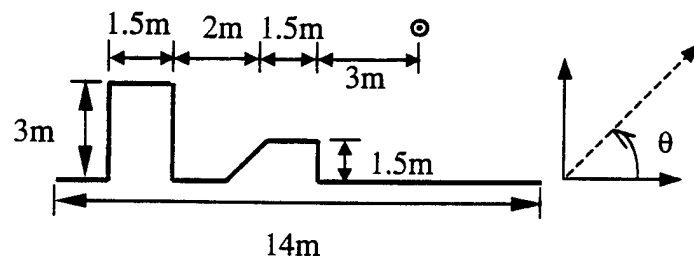
Fig. 5. 2D platform geometry
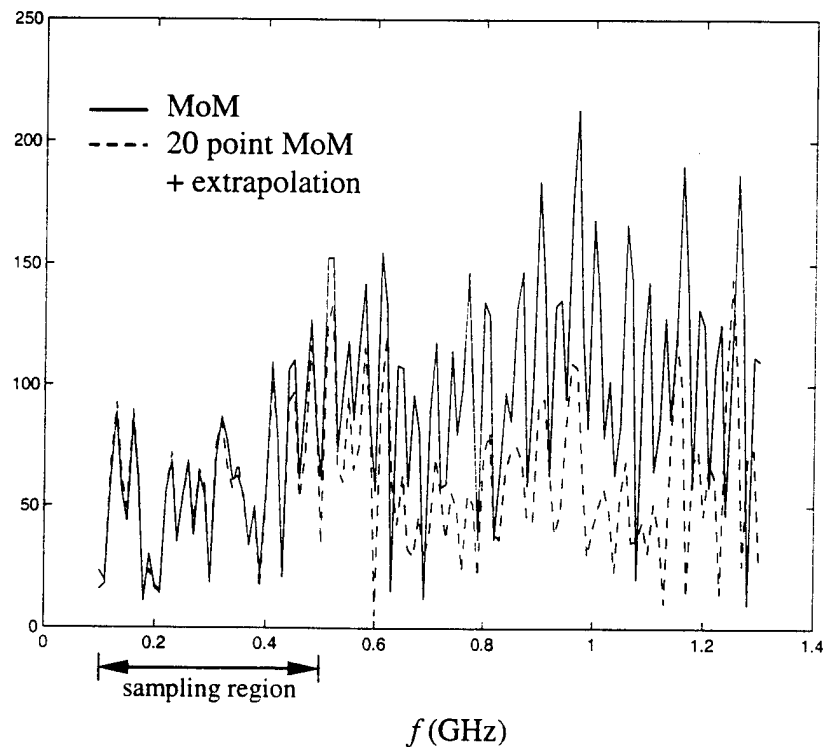
Fig. 6(a) Frequency response predicted by the frequency-independent time-of-arrival model at $\theta = 40°$.
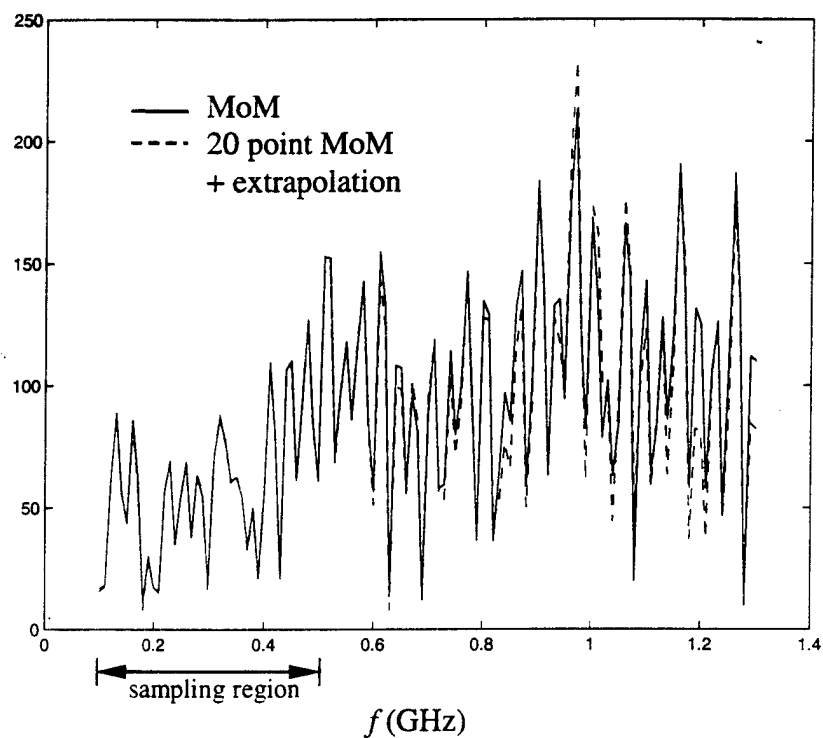
(b) Frequency response predicted by the frequency dependent model at $\theta = 40°$.
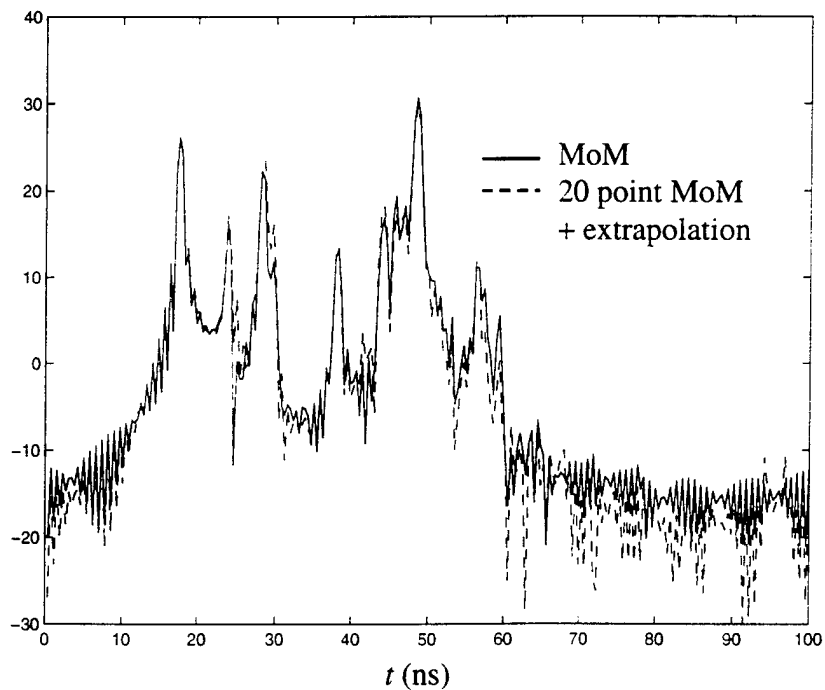
(c) Time domain response predicted by the frequency dependent model.

Fig. 6. Frequency extrapolation example for the 2D platform.
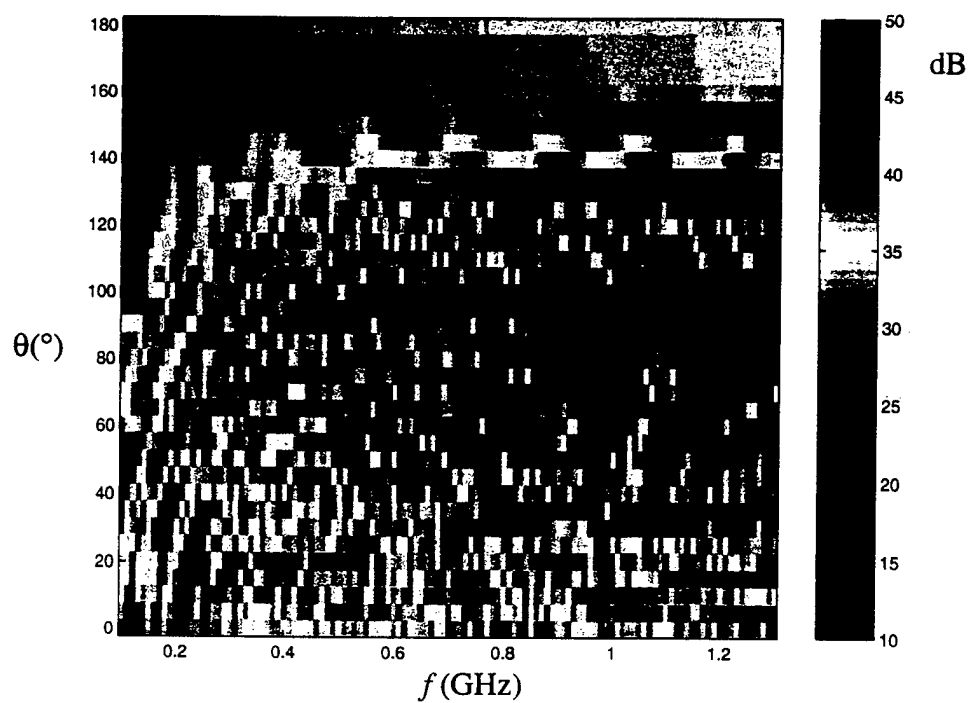
(a) Computed by MoM
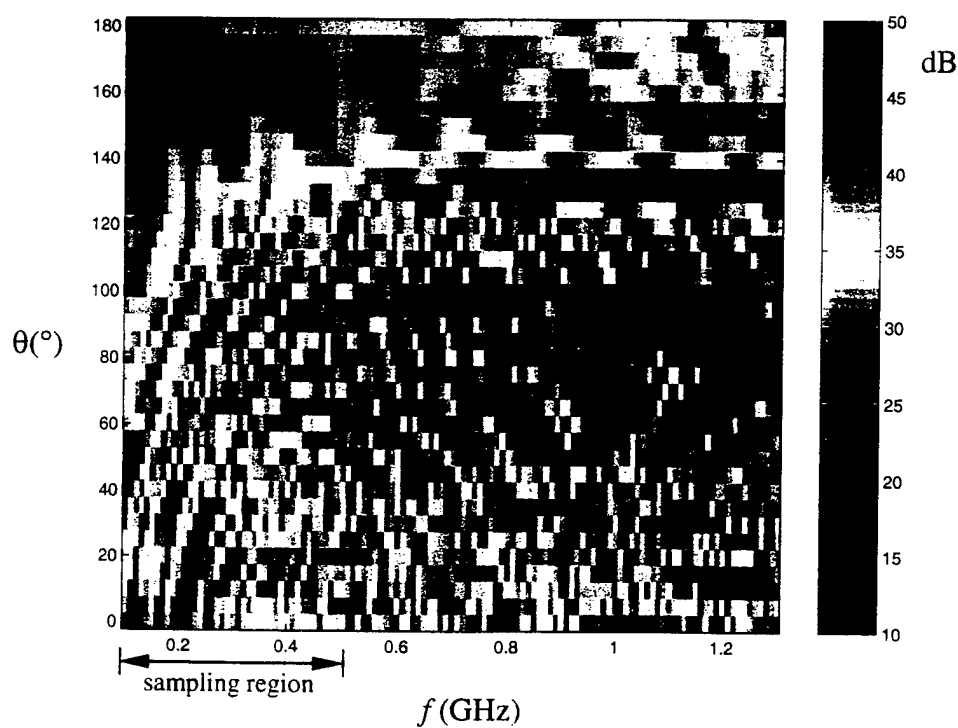
(b) Computed through extrapolation

Fig. 7. Comparison of the radiated field generated from brute force MoM computation and frequency extrapolation as a function of frequency and observation angle.
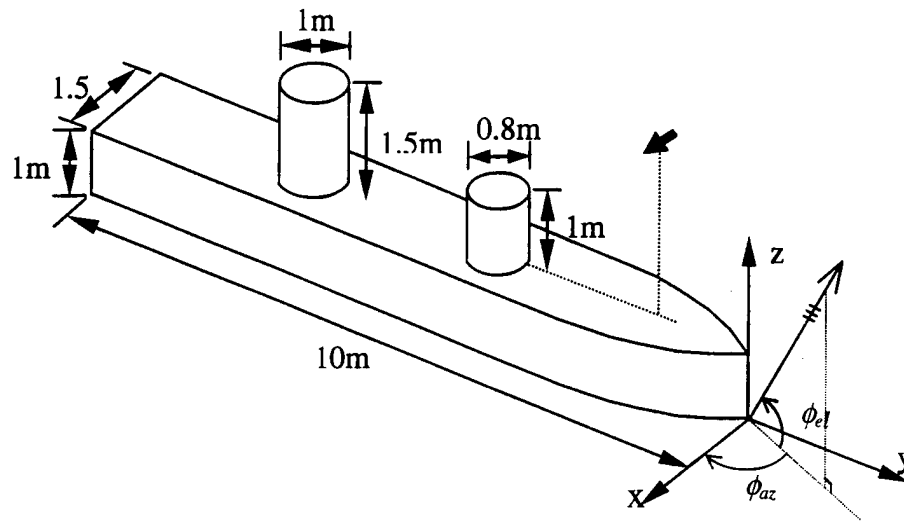
Fig. 8. 3D platform geometry
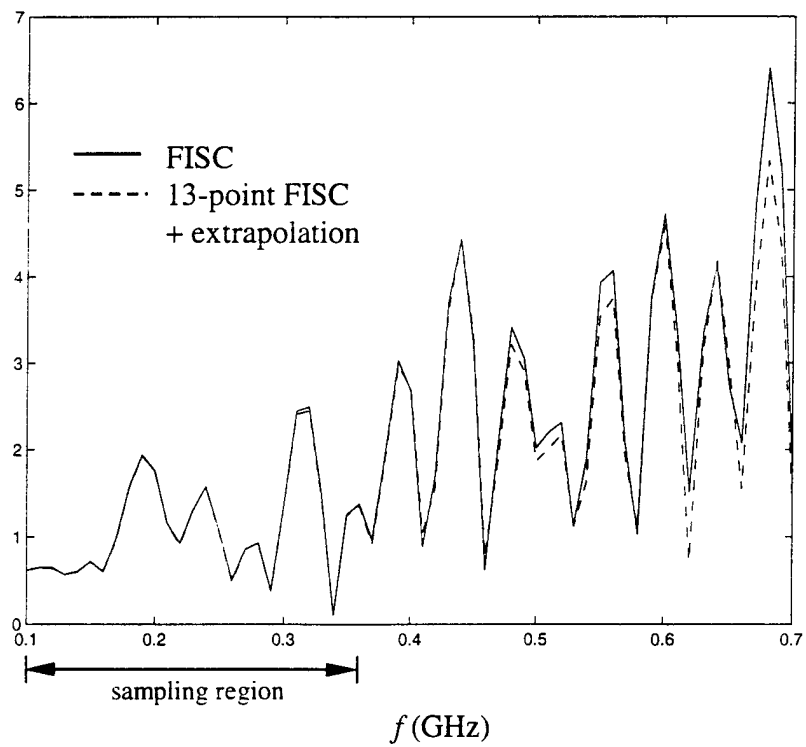
Fig 9. (a) Frequency response predicted by the frequency dependent
model at $\phi_{el} = 30°$, $\phi_{az} = -60°$.
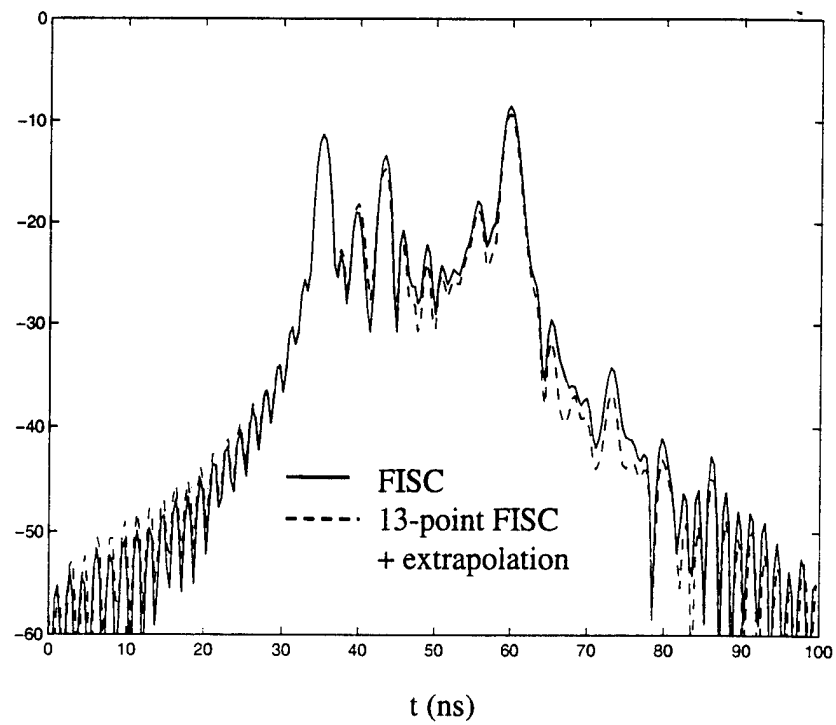
(b) Time domain response predicted by the frequency dependent model.

Fig. 9. Frequency extrapolation example for the 3D platform.
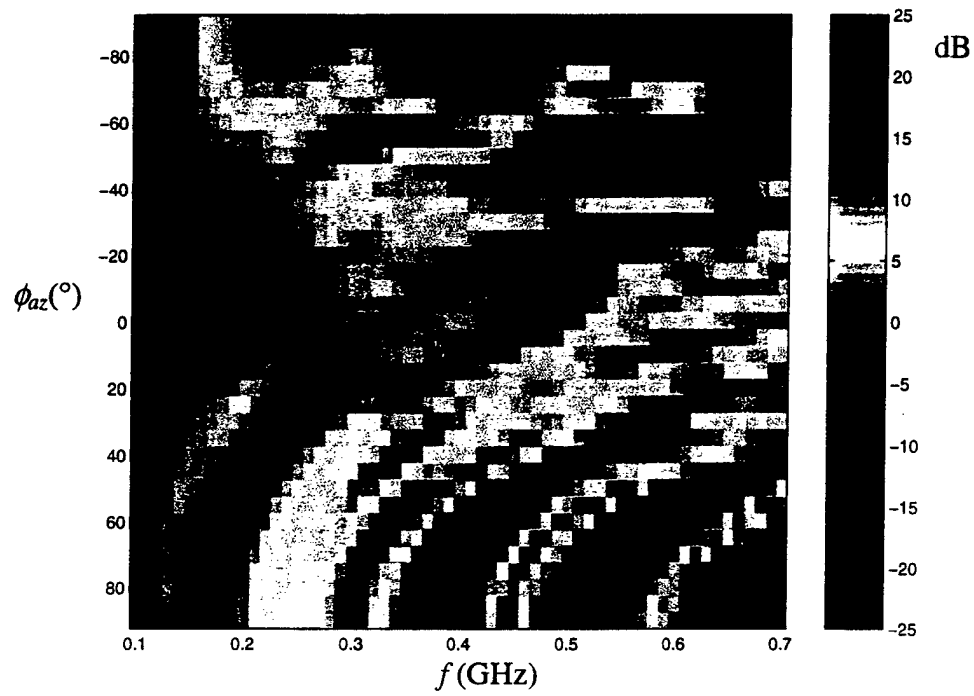
(a) Computed by FISC
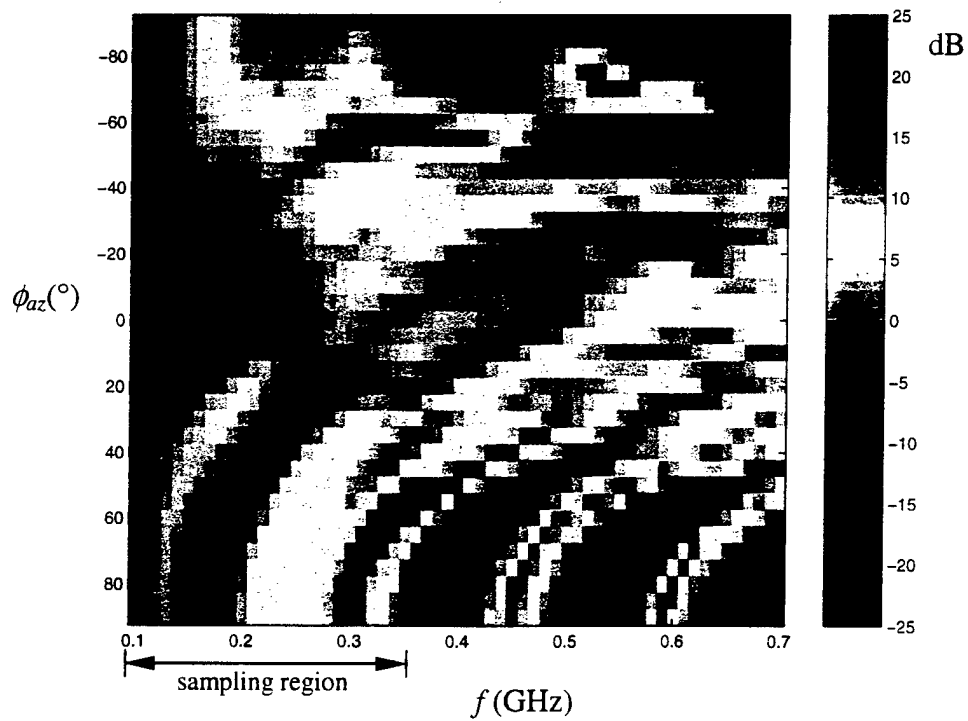
(b) Computed through extrapolation

Fig. 10. Comparison of the radiated field generated from brute force FISC computation and frequency extrapolation as a function of frequency and azimuth angle at the elevation angle of $\phi_{el} = 50°$.

AN EFFICIENT PRECONDITIONER FOR ELECTROMAGNETIC INTEGRAL EQUATIONS USING PRE-DEFINED WAVELET PACKET BASIS

Hai Deng and Hao Ling

Department of Electrical and Computer Engineering

The University of Texas at Austin

Austin, TX 78712-1084

ABSTRACT — An approximate-inverse preconditioner based on the pre-defined wavelet packet (PWP) basis is proposed for the fast iterative solution of electromagnetic integral equations. The PWP basis is designed to achieve a sparse representation of the moment matrix and the preconditioner is constructed by inverting the block-diagonal approximation of the PWP-based moment matrix and transforming the results into the space domain. Numerical results show that the PWP preconditioner is effective in accelerating the convergence rate of iterative solution to moment equations. It is also demonstrated that by properly designing the block-diagonal matrix and computing the matrix elements, the total computational complexity and memory costs for the preconditioner can be kept to $O(N\log N)$, making it applicable for the multilevel fast multipole method.

Index Terms — Computational Electromagnetics, Preconditioning, Wavelet Packet Basis.

I. Introduction

Iterative algorithms are commonly used to solve large-scale moment equations resulting from electromagnetic integral equations. The computational cost of iterative solution is proportional to both the moment matrix-vector multiplication operation and

the number of iterations required for a convergent solution. The multilevel fast multipole method (MLFMM) has been developed to reduce the time complexity and memory of the dense matrix-vector multiplication operation from $O(N^2)$ to $O(NlogN)$ [1-3]. However, the total solution time remains dependent on the number of iterations required to achieve an accurate solution. If the scatterer contains near-resonant structures such as deep cavities, the moment matrix is not well conditioned and the convergence rate of the iterative solution can become very slow [4, 5]. In these cases, a preconditioning matrix [**P**] is desired to accelerate the convergence rate. We consider a left-preconditioning system:

$$[\mathbf{P}][\mathbf{Z}]\,\mathbf{J} = [\mathbf{P}]\,\mathbf{E} \tag{1}$$

where [**Z**] is the moment matrix, **J** is the unknown induced current vector and **E** is the excitation vector. To achieve the best preconditioning, [**P**] should be as close to the inverse of [**Z**] as possible. Hence, [**P**] is called an approximate-inverse preconditioner. In this work, we set out to construct an approximate-inverse preconditioner [**P**] that satisfies the following conditions:

(a)   [**P**] is an accurate approximation to $[\mathbf{Z}]^{-1}$ to be an effective preconditioner.

(b)   The total computational complexity and memory requirement to construct the preconditioner are of $O(NlogN)$.

(c)   The total computational complexity and memory requirement to implement the preconditioning operation in (1) are of $O(NlogN)$.

Conditions (b) and (c) are set to keep the complexity of the preconditioning on par with that of the MLFMM, making our preconditioner applicable for the MLFMM. The traditional preconditioning methods, such as incomplete LU factorization (ILU),

Frobenius-norm-based approximate inverse and polynomial preconditioners could be effective [6, 7]. But they are computationally too complicated to meet conditions (b) and (c). In [5], an approximate-inverse preconditioner was constructed by inverting a block-banded form of the original moment matrix. Low complexity was maintained by choosing a bandwidth that is independent of problem size.

Our approach to the problem is to derive an effective preconditioner meeting conditions (a)-(c) based on the wavelet packet basis [8]. With the conventional subsectional basis, [Z] in (1) is dense, making it difficult to find an effective approximate-inverse preconditioner. However, if we can transform the moment equation to a new basis to make the transformed moment matrix sparse and diagonal dominant, it will be much easier to find an effective preconditioner. We have recently proposed the Pre-defined Wavelet Packet (PWP) basis for the efficient representation of moment matrices [9, 10]. The PWP basis was designed to match the oscillatory nature of the Green's kernel in the integral equation. Numerical results showed that the PWP-transformed moment matrices are strongly diagonal dominant, and have about $O(N\log N)$ non-zero elements for large-scale problems. In this paper, we shall demonstrate that an effective approximate-inverse preconditioner in the space domain can be derived from the PWP basis with no more than $O(N\log N)$ computational or memory cost. It is worthwhile to point out that there have been some recent works on using the conventional wavelet transform to precondition linear systems for iterative solutions [11-14]. However, the requirements for computational cost and memory are at least $O(N^2)$ to implement the wavelet transform and the preconditioning operation. In this work, we

overcome the $O(N^2)$ complexity and memory bottlenecks by computing the PWP preconditioner directly from the PWP basis functions [10].

This paper is organized as follows. In Section II, we give a brief review of the PWP basis and its representation of the moment matrices. In Section III, we describe the design and construction of our approximate-inverse preconditioner in the space domain from the sparse PWP-based moment matrix. We show that the total cost for the construction and preconditioning operation can be kept under $O(N\log N)$. Numerical results are presented in Section IV. Finally we draw some conclusions in Section V.

II. PWP Basis and Its Representation of Moment Equations

Wavelet packet basis is a set of orthonormal functions derived from the shift and dilation of a basic wavelet function, and can be considered as a generalization of the conventional wavelet basis [15]. From the point of view of function space decomposition, the wavelet packet basis space is generated from the decomposition of both the scaling function space and the corresponding wavelet function space. Let us assume that $\psi(x)$ is the wavelet packet basis function with the finest spatial resolution available for signal representation. Using the "two-scale equations," we can express the wavelet packet basis functions in the next scale as [16]:

$$\psi_0^1(n) = \sum_k \psi(k)h(2n-k)$$

$$\psi_1^1(n) = \sum_k \psi(k)g(2n-k)$$

(2)

where $\{h(k)\}$ and $\{g(k)\}$ are the impulse responses of two quadrature filters H (low-pass) and G (high-pass), respectively. The functions in the next scale become coarser in spatial resolution and finer in spectral resolution after the filtering and down-sampling in (2).

The same procedure can be applied recursively to the outputs of (2) into subsequent scales. Conversely, the decomposition results in (2) can also be used to reconstruct the original sequence by using another pair of quadrature filters P and Q, which are the mirror filters of H and G, respectively. This reconstruction procedure can be expressed as:

$$\psi(x) = \sum_k p(x-2k)\psi_0^1(k) + \sum_k q(x-2k)\psi_1^1(k) \qquad (3)$$

where {p(k)} and {q(k)} are the impulse responses of P (low-pass) and Q (high-pass), respectively. The functions become finer in spatial resolution and coarser in spectral resolution through filtering and up-sampling in (3).

A complete and orthogonal wavelet packet basis can be generated from a spectral decomposition tree that starts from an initial mother function $\psi(x)$ with the finest spatial resolution by using recursive two-channel filtering and down-sampling in (2). It can be shown that the decomposed functions at the outermost branches of the tree satisfy orthogonality and completeness for any decomposition trees, and thus constitute a wavelet packet basis set [17]. In this context, the conventional wavelet transform (CWT) basis can be considered as a special case of the wavelet packet basis when the decomposition tree grows along only the lowest frequency branch. However, we have shown in [18] that the structure of the CWT tree is not optimal for representing the moment matrix from electrodynamic integral equations. Instead, we have proposed a special wavelet packet tree for electrodynamic problems [9, 10]. This class of wavelet packet bases, which we term the pre-defined wavelet packet (PWP) basis, has a spectral decomposition tree that zooms in along the free-space wave number k_0. The motivation for this tree structure is to ensure that the basis is well-matched to the oscillatory nature

of the Green's function kernel in the integral equation. Figs. 1(a) and 1(b) show respectively the conventional wavelet decomposition tree and the PWP decomposition tree for N=32. In the PWP tree, the center frequency of its deepest branch is as close as possible to k_0. Detailed discussion on the construction of the PWP basis can be found in [10].

Once the PWP basis is defined, it is straightforward to transform the original moment equation into the new basis representation as follows:

$$[\widetilde{\mathbf{Z}}]\widetilde{\mathbf{J}} = \widetilde{\mathbf{E}} \tag{4}$$

where
$$[\widetilde{\mathbf{Z}}] = [\mathbf{M}]^{T}[\mathbf{Z}][\mathbf{M}] \tag{5}$$

$$\widetilde{\mathbf{J}} = [\mathbf{M}]^{T}\mathbf{J} \tag{6}$$

$$\widetilde{\mathbf{E}} = [\mathbf{M}]^{T}\mathbf{E} \tag{7}$$

$[\mathbf{M}]^{T}$ denotes the transpose of $[\mathbf{M}]$, and is the PWP transformation matrix. It changes the original expansion/testing functions from the standard subsectional bases into the PWP bases. Note that $[\mathbf{M}]^{T}$ is equal to $[\mathbf{M}]^{-1}$ since $[\mathbf{M}]$ is an orthonormal transformation. $[\widetilde{\mathbf{Z}}]$, $\widetilde{\mathbf{J}}$, and $\widetilde{\mathbf{E}}$ are the moment matrix, induced current, and excitation vector represented in the PWP basis, respectively. Our numerical results from [10] showed that the transformed moment matrix under the PWP basis is very sparse. In particular the number of above-threshold elements in the transformed moment matrix grows at a rate of $O(N^{1.3})$ for small-sized problems, and approaches $O(N\log N)$ for large-scale problems. Furthermore, the significant elements in $[\widetilde{\mathbf{Z}}]$ are located mainly along the diagonal or near-diagonal positions. Unfortunately, the exact locations of the significant elements are difficult to predict. Consequently, the complexity of the algorithm in solving the complete moment equation is still hampered by an N^2 computational bottleneck, since

every element of the matrix must be computed to determine whether it is small enough to be discarded. However, for the proposed preconditioning application in this paper, we shall show in the next section that an effective approximate-inverse preconditioner can be constructed by computing only those elements within the diagonal blocks.

III. PWP-Based Approximate-Inverse Preconditioner in the Space Domain

We will first outline our approach to constructing the PWP-based preconditioner. Since the PWP transformed moment matrix $[\tilde{Z}]$ is very sparse and diagonal dominant, we approximate $[\tilde{Z}]$ by a block-diagonal matrix $[\tilde{Z}_{bd}]$ that consists of the near-diagonal terms of $[\tilde{Z}]$. The approximate-inverse preconditioner $[P]$ defined in (1) is then constructed by inverting the block-diagonal matrix $[\tilde{Z}_{bd}]$ and transforming the resulting matrix back to the space domain:

$$[P] = [M] \, [\tilde{Z}_{bd}]^{-1} \, [M]^{T} \tag{8}$$

Therefore, the preconditioned moment equation becomes:

$$[M] \, [\tilde{Z}_{bd}]^{-1} \, [M]^{T} [Z] \, J = [M] \, [\tilde{Z}_{bd}]^{-1} \, [M]^{T} E \tag{9}$$

The inverse of the block diagonal matrix $[\tilde{Z}_{bd}]$ is simply the inverse of its individual diagonal blocks, and the inverted matrix $[\tilde{Z}_{bd}]^{-1}$ remains block diagonal. By properly choosing the block sizes of $[\tilde{Z}_{bd}]$, we can limit the computational cost of the inversion while maintaining the effectiveness of the preconditioner.

The actual implementation of the preconditioner will now be considered. If we solve equation (9) using an iterative algorithm such as the conjugate gradient method, the complexity of each iteration is proportional to that of the product between the matrix $[M]$, $[\tilde{Z}_{bd}]^{-1}$, $[M]^{T}$ or $[Z]$ and a vector. The product $[Z]$ and a vector can be implemented

using the MLFMM algorithm with $O(N\log N)$ complexity and memory requirement. Because the PWP transformation matrix $[\mathbf{M}]^T$ has about $O(N\log N)$ non-zero elements, the multiplication of $[\mathbf{M}]^T$ or $[\mathbf{M}]$ with a vector is also of $O(N\log N)$ in complexity. Therefore, if we can limit both the number of non-zero elements in $[\widetilde{\mathbf{Z}}_{bd}]^{-1}$ and the complexity of constructing $[\widetilde{\mathbf{Z}}_{bd}]^{-1}$ to $O(N\log N)$, the total cost per iteration in (9) will remain at $O(N\log N)$.

Our design of the block-diagonal matrix $[\widetilde{\mathbf{Z}}_{bd}]$ is shown in Fig. 2. The blocks are designed so as to capture the most significant elements in the PWP-transformed moment matrix $[\widetilde{\mathbf{Z}}]$. The block-diagonal matrix consists of the following: (i) a block centered about the spectral frequency k_0 with block size M_1, (ii) a set of diagonal blocks in the remaining upper-left region with block size M_2, and (iii) a set of diagonal blocks in the lower-right region with block size M_3. The number of diagonal blocks with size M_2 is $[(N/2 - M_1)/ M_2]$, and that with size M_3 is $[(N/2)/ M_3]$. The block from (i) is usually the densest part of $[\widetilde{\mathbf{Z}}]$, since its elements correspond to the interactions between PWP bases with the longest spatial extent and spectral frequency close to k_0. They tend to have the strongest interaction with each other. The blocks from (iii), on the other hand, are nearly diagonal, since their elements correspond to the interactions between PWP bases with the highest spectral frequency and the shortest spatial extent. Therefore, we generally choose block sizes with $M_1 > M_2 > M_3$. Furthermore, as N is increased we keep the sizes M_2 and M_3 fixed, but let M_1 grow slightly with problem size at a rate of $N^{1/3}$ to capture even more of the dominant elements in $[\widetilde{\mathbf{Z}}]$. This growth rate is chosen to ensure that the cost of inverting the block remains bounded by N, as the cost of the inversion is proportional to the cube of the matrix dimension. The inverse of $[\widetilde{\mathbf{Z}}_{bd}]$ is equivalent to the inverse of

each of the blocks of [$\widetilde{Z}_{bd}$] in Fig. 2. Therefore, under our construct, the total computational complexity to invert [$\widetilde{Z}_{bd}$] is proportional to N and the resulting number of nonzero elements in [$\widetilde{Z}_{bd}$]$^{-1}$ is also proportional to N.

Next, we discuss the computation of the required elements in [$\widetilde{Z}_{bd}$]. Each element $\widetilde{Z}$(m, n) of the matrix [$\widetilde{Z}$] can be directly expressed as [10]:

$$\widetilde{Z}(m,n) = \sum_i \sum_j \psi_m(i) G(i,j) \psi_n(j) \tag{10}$$

where G(i, j) is the free space Green's function, i and j represent the indices of the discretization grid in the space domain, and ψ_k is the k-th PWP basis function. It can be seen from (10) that the computational complexity for each matrix element is proportional to the product of the spatial supports of the two corresponding basis functions. The support of a PWP basis function is related to the depth of the branch in the PWP decomposition tree. Let us assume that the basis functions corresponding to branches in the first stage of the PWP decomposition tree have spatial support L (i.e., the order of the wavelet filter). The complexity for computing a diagonal (or near-diagonal) element is then L^2. The support of a PWP basis function doubles if it corresponds to the branches on the next deeper stage in the decomposition tree [10, 16]. Therefore, the spatial support of the basis functions generated from the tree branches at stage k is $2^{k-1}L$, and the complexity to compute an element from basis functions in the same stage is $(2^{k-1}L)^2$. Since the maximum possible depth of the wavelet decomposition tree is $K_{max} = \log_2 N$, the cost for computing an element using bases from this maximum depth would then be N^2. However, as we shall discuss in the next section, the best preconditioning performance is often achieved using a tree with depth much less than the maximum possible depth. Similar observation has also been reported in [11]. Therefore, if we impose that the

maximum depth index of the PWP decomposition trees is a small number K, the number of operations needed to compute an element in $[\tilde{Z}_{bd}]$ will be between L^2 and $4^{K-1}L^2$. With $O(N)$ elements in $[\tilde{Z}_{bd}]$, the total complexity to compute the matrix $[\tilde{Z}_{bd}]$ is about $O(N)$ operations.

To summarize, we have designed a preconditioner based on the block-diagonal approximation of the PWP-transformed moment matrix. The steps to construct and carry out the preconditioning operation entail: (i) computing the elements in the diagonal blocks of $[\tilde{Z}_{bd}]$ one term at a time using (10), (ii) inverting $[\tilde{Z}_{bd}]$ one block at a time to arrive at its inverse $[\tilde{Z}_{bd}]^{-1}$, and (iii) carrying out the preconditioning operation by a successive set of sparse matrix-vector multiplication operations in (9). It is shown that the computational complexity of the each of the three steps can be limited to within $O(N\log N)$ operations, thus making the proposed preconditioner compatible with the MLFMM in solving moment equations.

IV. Numerical Results

Two two-dimensional targets, an open-ended inlet and a bent structure shown in Fig. 3, are chosen to test our PWP preconditioner. With a large depth-to-opening ratio (l/m), the moment matrices from the scatterers are ill-conditioned, and the convergence rate is slow if an iterative solver is used to solve the systems. For the inlet structure, if the thickness parameter t is equal to zero, the electric field integral equation (EFIE) is use to construct the moment equation. Otherwise, the combined field integral equation (CFIE) is used. For the bent structure, EFIE is always used to find the solution. The discretization of the structure is chosen to be fixed at 0.1 wavelength while the electrical

size of the structure is varied. In all cases the incident plane wave is E-polarized and makes an angle of 45° with respect to the inlet opening.

Fig. 4 is the moment matrix $[\tilde{\mathbf{Z}}]$ represented by the PWP basis for the inlet structure with dimensions $l{:}m{:}t{=}15{:}1{:}1$ and N=256. It is shown in logarithmic scale without any thresholding. We find that the most significant elements in the transformed matrix match the patterns we chose for the PWP preconditioner in Fig. 2. The densest portion of the matrix is located in the upper left region, with the strongest elements near the k_0 spectral position. The wavelet filter used to generate the PWP basis functions is Daubechies filter with order 16 (with 7 vanishing moments).

We use both the conjugate-gradient squared (CGS) method and the biconjugate gradient stabilized (BiCGSTAB) method. Both of them are effective iterative solvers for linear equations with nonsymmetric coefficient matrix [19]. CGS is used in most of the cases in this work since it converges faster than BiCGSTAB. However, we use the BiCGSTAB to compare the detailed convergence rates of the different preconditioners, as the convergence behavior of the CGS is not very smooth. In the application of the iterative solvers, the initial current guess is $\mathbf{J}_0{=}0$, and the stopping criterion used is when the relative residual error $\|r_n\|/\|r_0\| \leq 10^{-6}$, where $r_n = \mathbf{E}{-}[\mathbf{Z}]\mathbf{J}_n$ and $r_0 = \mathbf{E}$.

We first examine how the iteration number changes as the electrical size of the scatterer is increased in the following three cases:

Case 1: The scatterer is the inlet structure shown in Fig. 3(a) with $t = 0$ and $l{:}m{=}15{:}1$. The moment equation is formulated with the EFIE. For the PWP preconditioner, we choose $M_2{=}32$, $M_3{=}1$, and M_1 grows at a rate of $\sqrt[3]{N}$ starting from 32 at N=128.

Case 2: The scatterer is the inlet structure with $l{:}m{:}t{=}15{:}1{:}1$. The moment equation is formulated with the CFIE. The PWP preconditioner is constructed the same way as that in Case 1.

Case 3: The scatterer is the bent structure shown in Figure 3(b) with $l{:}m{=}12{:}1$. The EFIE is used, and the parameters for the PWP preconditioner are chosen as: $M_2{=} M_3{=} 32$, and M_1 grows at a rate of $\sqrt[3]{N}$ starting from 32 at N=128.

The iteration numbers required versus problem sizes are shown in Figs. 5(a)-(c) for Cases 1-3, respectively. We increase the problem size by proportionally increasing the electrical size of the scatterer while keeping the discretization interval fixed at 0.1 wavelength. The results for the moment equation without any preconditioning and that with the PWP preconditioner are plotted. For comparison, we also show the results from a simple block-diagonal preconditioner in the space domain. It is constructed by inverting the block-diagonal form of the original space-domain moment matrix. The block sizes are uniform and the total number of non-zero elements is kept the same as that used in the PWP preconditioner. We find that the iteration number grows very rapidly with the problem size if no preconditioning is applied. With the PWP preconditioners applied, the iteration numbers are significantly reduced and they increase much more slowly with problem size. Furthermore, the PWP preconditioner performs better than the equivalent space domain preconditioner. This is because the PWP preconditioner captures more of the energy in the original moment matrix. Note that the CFIE results shown in Fig. 5(b) have smaller iteration numbers than the results from the EFIE cases shown in Figs. 5(a) and 5(c). However, the effectiveness of the PWP preconditioner is still apparent. In Fig. 5(c), we also plot the results using the

conventional wavelet transform (CWT) basis instead of the PWP basis. The CWT preconditioner is constructed in exactly the same way as the PWP preconditioner, except the approximate matrix is formed from the elements of the CWT transformed moment matrix rather than the PWP transformed one. We observe that the PWP preconditioner outperforms the CWT preconditioner since the PWP basis can more efficiently represent the moment matrix. Although not shown, similar comparisons between the PWP and CWT preconditioners are also found for Cases 1 and 2.

Figs. 6(a)-(c) show the convergence behaviors for a fixed problem size (N=512) for Cases 1-3, respectively. The BiCGSTAB algorithm is used as the iterative solver. In each figure, the residual error is plotted as a function of the number of iterations for the moment equation without any preconditioning, with the space domain and/or the CWT preconditioner, and with the PWP preconditioner. We observe that, with the PWP preconditioning, the relative residue decreases the fastest. In addition, the convergence behaviors are more stable. Similar convergence behaviors are found for larger problem sizes.

Next, we investigate the effect of the depth index K in the wavelet tree on the resulting PWP preconditioner. For a scattering problem with a problem size of N, the maximum depth index for the PWP decomposition tree is (log_2N). However, this does not necessarily lead to the best preconditioning performance. Fig. 7 plots the required iteration number versus the depth index K used in constructing the PWP preconditioner for N=1024. The results show that the curves flatten considerably after K=5, implying that there is not much to be gained beyond this depth in the wavelet tree. The reason for this phenomenon is because although the maximum-depth PWP tree generates the

sparsest transformed moment matrix [10], the long PWP basis functions resulting from that tree shift some of the energy into the non-diagonal blocks, making the preconditioning results worse. For the problem sizes we have studied from 128 to 4096, the optimal PWP tree depths are usually between 3 and 6. Since the computational cost of constructing the preconditioner is proportional to the maximum depth of the PWP decomposition tree, we should not go beyond this depth when constructing the PWP preconditioner.

Finally, we examine the computational cost of the PWP preconditioner. Fig. 8 shows the CPU running time required to generate the PWP preconditioning matrix $[\tilde{\mathbf{Z}}_{bd}]$ for Case 1 versus problem size N. The direct element computation in equation (10) is carried out and the PWP tree depth K is increased slightly from 3 to 6 as the problem size is changed from 128 to 4096. Fig. 9 shows the CPU running time needed to implement the multiple matrix-vector products required for the carrying out the PWP preconditioning in (9). We exclude the time needed for the first moment matrix and vector product in (9), as that operation can be done via the MLFMM. We find that the CPU running time grows at rate close to $O(\mathrm{N log N})$ in the both cases. This is consistent with the estimates given in Section III and meets the objectives we have set forth for the preconditioner.

V. Conclusions

A preconditioner for the moment equation based on the pre-defined wavelet packet basis has been proposed in this paper. Due to the vanishing moments of wavelet

basis functions, the PWP-based moment matrix is sparse and diagonally concentrated. Consequently, an approximate-inverse preconditioner can be more easily designed and constructed than that based on the original space-domain moment matrix. The PWP preconditioner is constructed by inverting a block-diagonal form of the PWP-based moment matrix and transforming the resulting matrix back into the space domain. It has been shown that the complexity for the construction and preconditioning operation can be kept under $O(N\log N)$ in both computational cost and memory requirement. Our numerical results showed that the iteration numbers for the PWP-preconditioned moment equations are significantly smaller and grow at a lower rate than those without preconditioning or preconditioned using a space-domain preconditioner. In addition, the PWP preconditioner also performed better than the equivalent preconditioner derived from the conventional wavelet basis. Application of this concept to three-dimensional (3-D) problems is currently under investigation, with the goal of combining the preconditioner with the 3-D MLFMM to obtain solutions of large-scale problems.

Finally, although we have chosen the block-diagonal matrix as the underlying structure of our approximate-inverse preconditioner, we have found that a block-banded matrix [5] or a thresheld transformed matrix [11, 20] gave better preconditioning results than the block-diagonal form. However, the inverses of those matrices are dense, resulting in $O(N^2)$ computational bottlenecks for implementing the matrix-vector product in the preconditioning step. A worthwhile topic is to find a more effective approximate matrix in the PWP basis domain than the block-diagonal one, while preserving the $O(N\log N)$ total computational cost and memory requirement.

Acknowledgement

References

[1] R. Coifman, V. Rokhlin and S. Wandzura, "The fast multipole method for the wave equation: a pedestrian prescription," *IEEE Antennas Propagat. Mag.,* vol. 35, no. 3, pp. 7-12, June 1993.

[2] J. M. Song and W. C. Chew, "Fast multipole method solution using parametric geometry," *Microwave Opt. Tech. Lett.,* vol. 7, pp. 760-765, Nov. 1994.

[3] J. M. Song, C. C. Lu and W. C. Chew, "Multi-level fast-multipole algorithm for electromagnetic scattering for large complex objects," *IEEE Trans. Antennas Propagat.,* vol. 45, pp. 1488-1493, Oct. 1997.

[4] C. C. Lu and W. C. Chew, "A near-resonance decoupling approach (NRDA) for scattering solution of 3D near-resonant structures," *IEEE Trans. Antennas Propagat.,* vol. 45, pp. 808-811, Feb. 1997.

[5] C. H. Ahn., W. C. Chew, J. C. Zhao and E. Michielssen, "Approximate inverse preconditioner for near resonant scattering problems," Research Report, Univ. of Illinois, Apr. 1998

[6] R. Barrett, M. Berry, T. F. Chan, J. Demmel, J. Donato, J. Dongarra, V. Eijkhout, R. Pozo, C. Romine and H. van der Vorst, *Templates for the Solutions of Linear Systems: Building Blocks for Iterative Methods,* SIAM, Philadelphia, 1994.

[7] A. M. Bruaset, *A Survey of Preconditioned Iterative Methods,* John Wiley & Sons, New York, 1995.

[8] H. Deng and H. Ling, "Preconditioning of electromagnetic integral equations for iterative solvers using pre-defined wavelet packet basis," *Electronics Lett.,* vol. 35, pp. 1144-1146, July 1999.

[9] H. Deng and H. Ling, "Efficient representation of moment matrix using pre-defined wavelet packet basis," *Electronics Lett.,* vol. 34, pp. 176-177, Mar. 1998.

[10] H. Deng and H. Ling, "On a class of pre-defined wavelet packet basis for efficient representation of electromagnetic integral equations," to appear in *IEEE Trans. Antennas Propagat.,* Nov. 1999.

[11] T. F. Chan, W. P. Tang and W. L. Wan, "Wavelet sparse approximate inverse preconditioners," *BIT,* vol. 37, pp. 644-660, Sept. 1997.

[12] F. Canning and J. Scholl, "Diagonal preconditioners for the EFIE using a wavelet basis," *IEEE Trans. Antennas Propagat.,* vol. 44, pp.1239-1246, Sept. 1996.

[13] W. L. Golik and D. S. Wang, "Fast wavelet packet algorithm for the combined field integral equation," in *Proc. 13th Annu. Rev. Progress in Applied Comput. Electromagnetics,* Monterey, CA, Mar. 1997.

[14] A. Cohen and R. Mason, "Wavelet methods for second order elliptic problems, preconditioning and adaptivity," preprint, Universit Pierre et Marie Curie, 1998.

[15] C. K. Chui, *An Introduction to Wavelets,* New York: Academic, 1992.

[16] I. Daubechies, *Ten Lectures on Wavelets,* CBMS-NSF Series Applied Math., SIAM, 1991.

[17] M. V. Wickerhauser, *Adapted Wavelet Analysis from Theory to Software,* Wellesley, MA: A. K. Peters, 1994.

[18] H. Deng and H. Ling, "Fast solution of electromagnetic integral equations using adaptive wavelet packet transform," *IEEE Trans. Antennas Propagat.,* vol. 47, pp. 674-682, Apr. 1999.

[19] R. Weiss, *Parameter-Free Iterative Linear Solvers,* Berlin: Akademie Verlag GmbH, 1996.

[20] M. J. Grote and T. Huckle, "Parallel preconditioning with sparse approximate inverses," *SIAM J. Sci. Comput.,* vol. 18, no.3, pp. 838-853, May 1997.
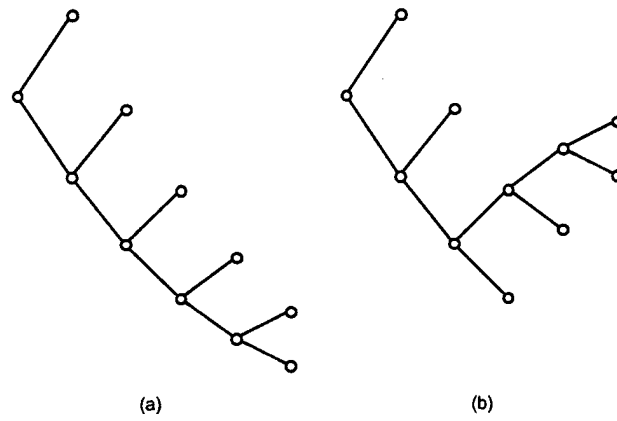
Figure 1. (a) Conventional wavelet decomposition tree;
(b) Pre-defined Wavelet Packet (PWP) decomposition tree.
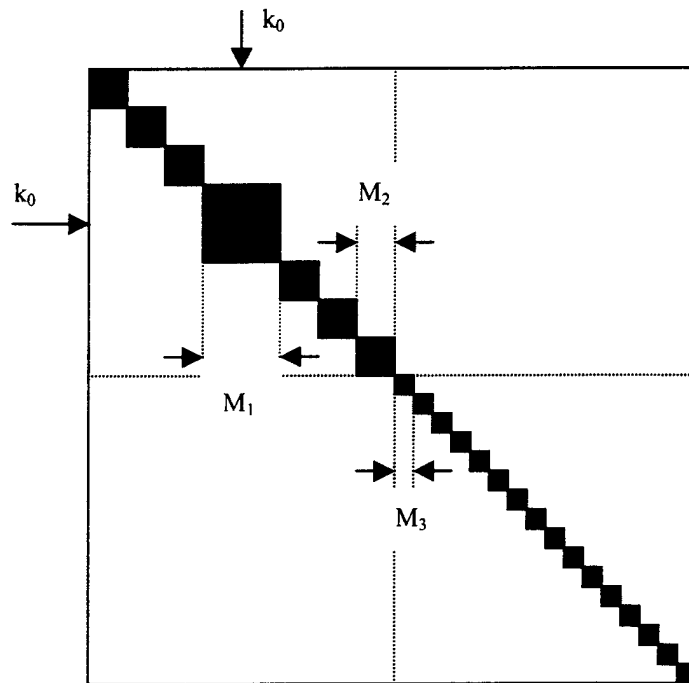
Figure 2. The pattern used to construct $[\widetilde{Z}_{bd}]$ from $[\widetilde{Z}]$.
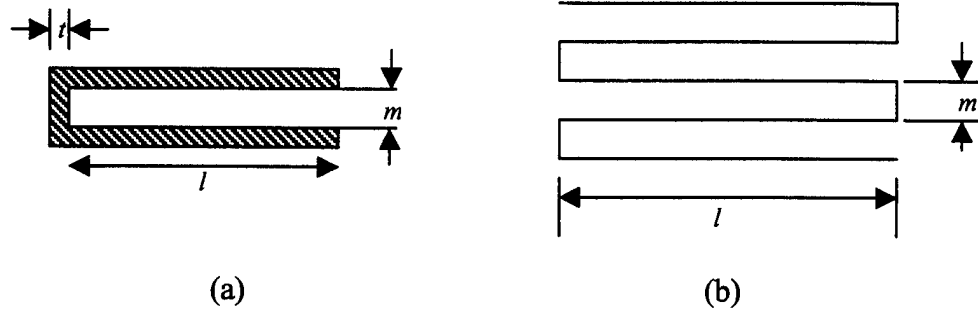
Figure 3. The test scatterers: (a) an open-ended inlet, and (b) a bent structure.
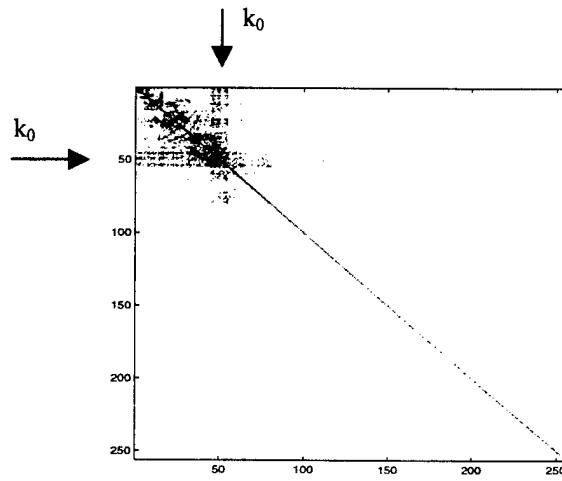
Figure 4. The moment matrix represented by PWP basis, $[\widetilde{\mathbf{Z}}]$, for the inlet with N=256 (in logarithmic scale)
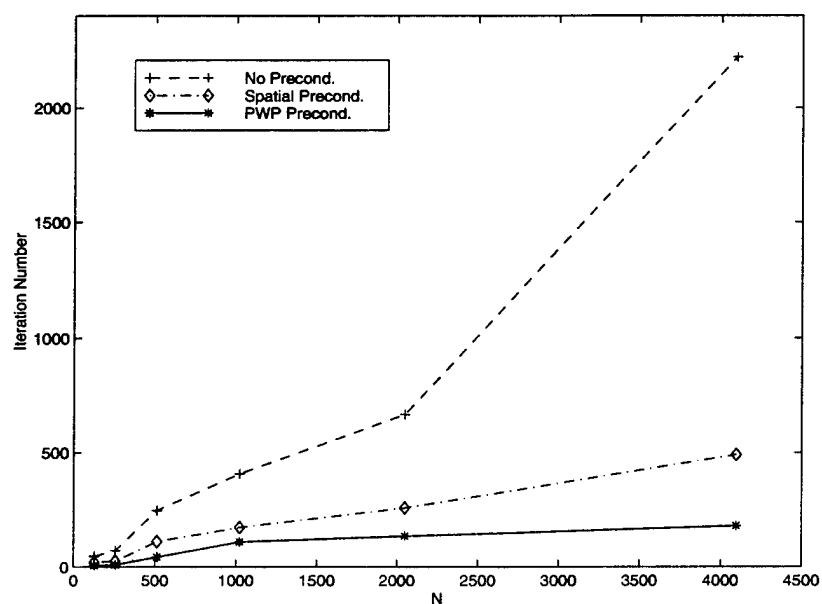
(a)
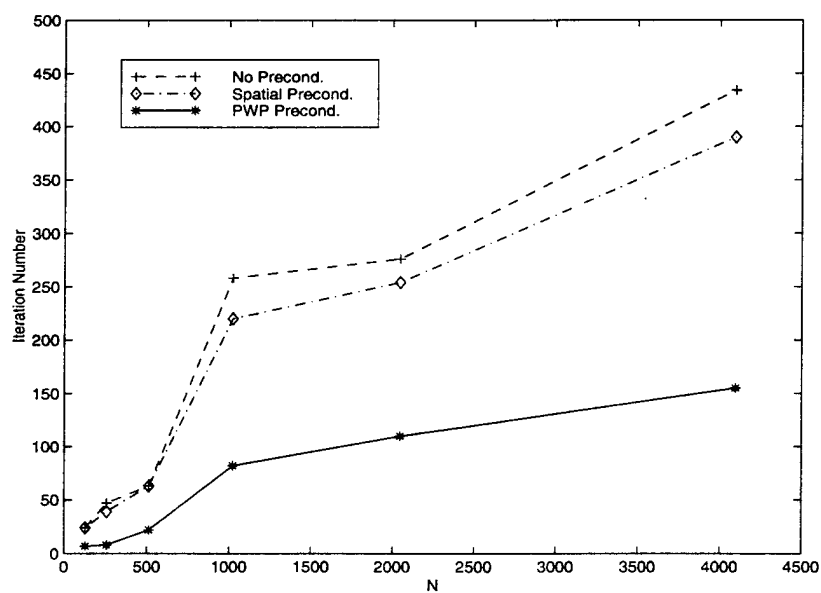
(b)
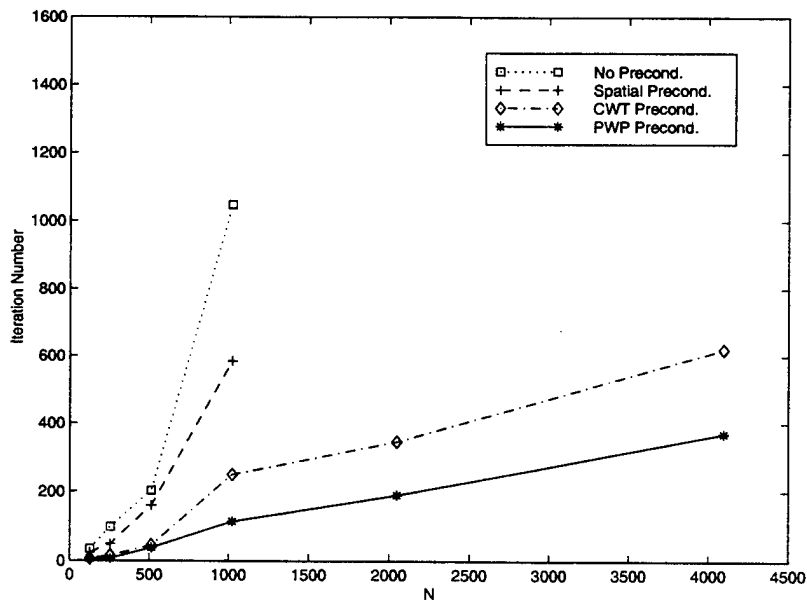
(c)

Figure 5. Iteration numbers vs. problem sizes for solving moment
equations with different preconditioning methods for the scattering
structures in (a) Case 1, (b) Case 2, and (c) Case 3. The problem sizes
are increased by proportionally increasing the scatterer sizes.
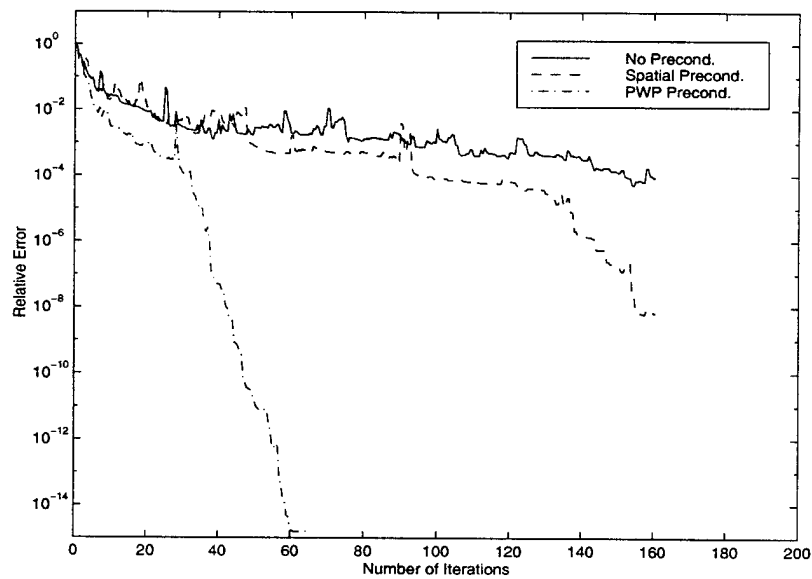
(a)
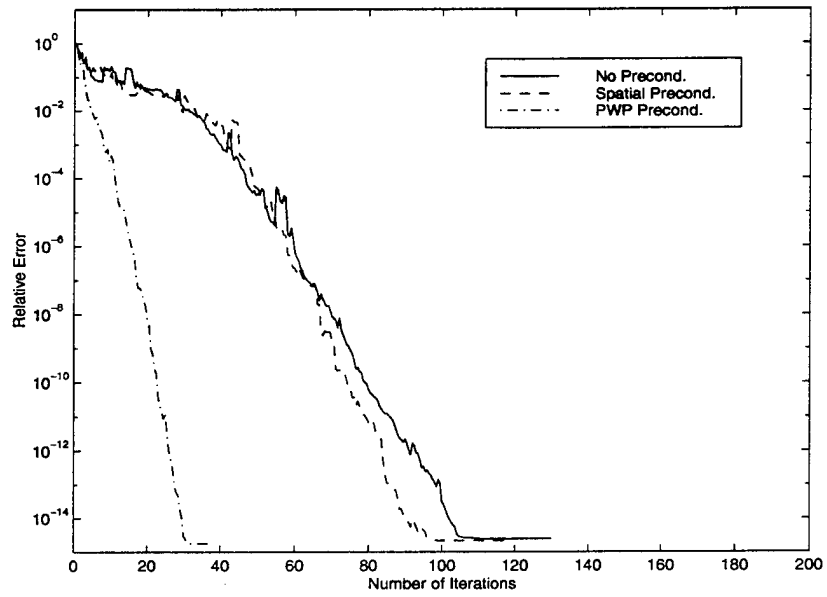
(b)
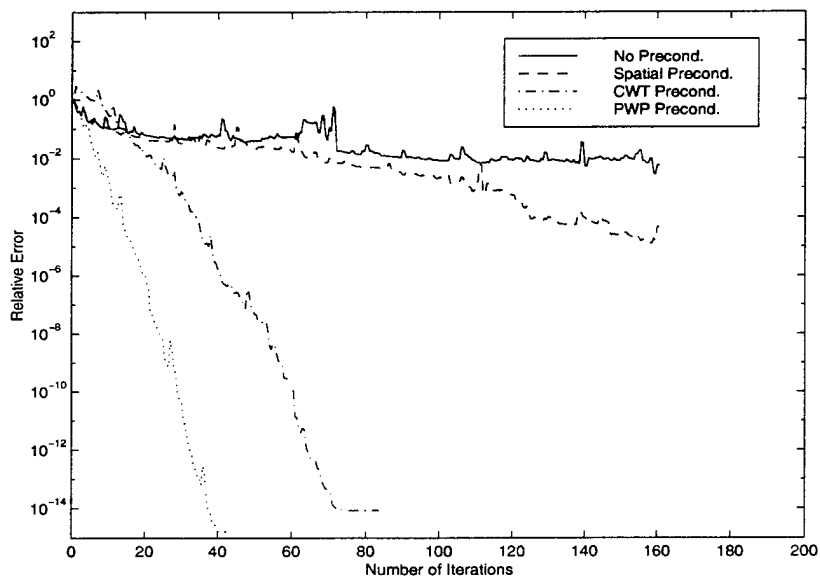
(c)

Figure 6. Convergence behaviors of the preconditioned systems
versus iteration numbers for PWP and other preconditioning methods in
(a) Case 1, (b) Case 2, and (c) Case 3 with N=512.
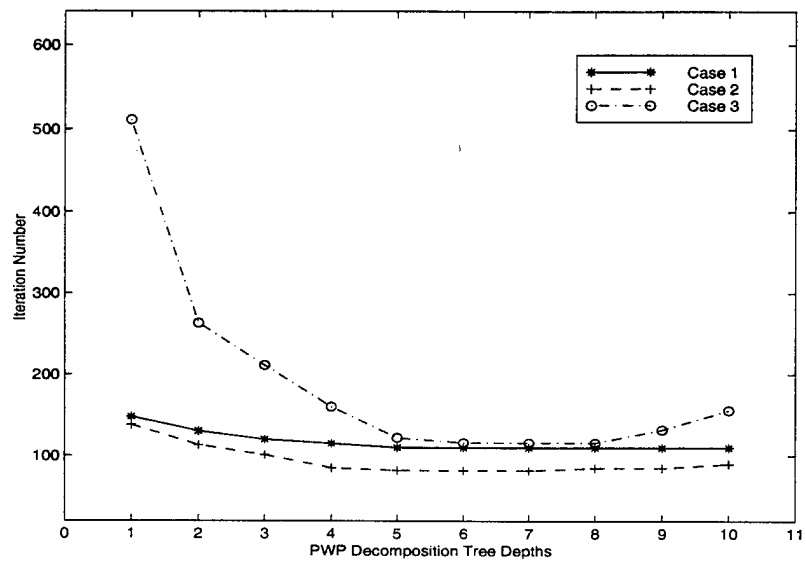
Figure 7. Effect of the PWP decomposition level on
iteration number for Cases 1-3 using the PWP preconditioner
with N=1024.
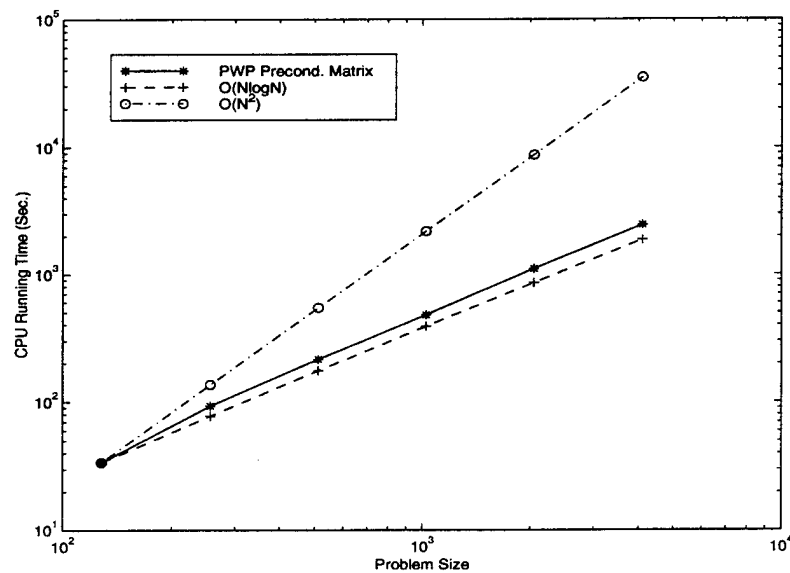
Figure 8. CPU running time vs. problem size for forming the PWP matrix [$\widetilde{Z}_{bd}$] using (10) for Case 1.
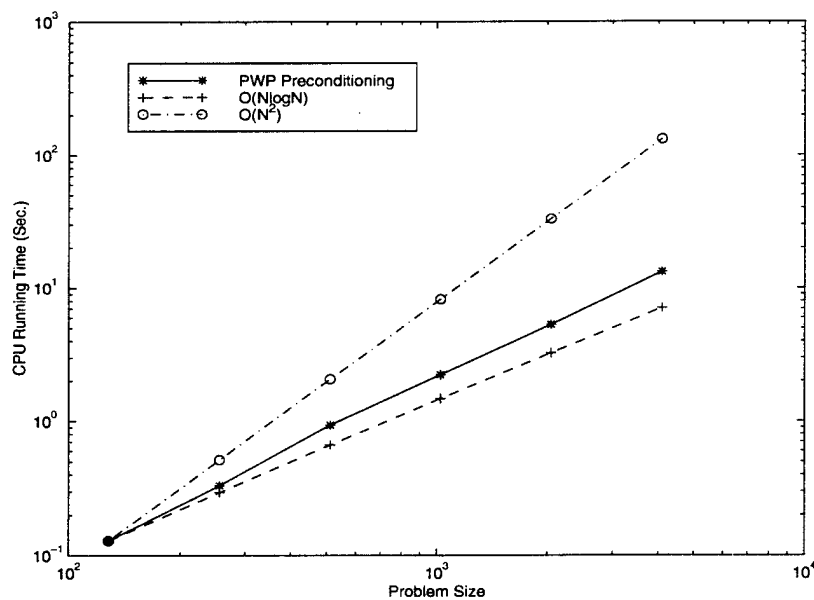
Figure 9. CPU running time vs. problem size for implementing multiple matrix-vector products in (9) for the PWP preconditioning in Case 1.
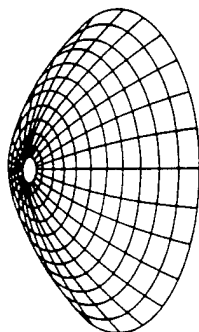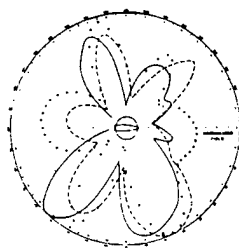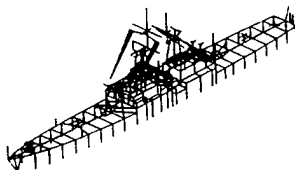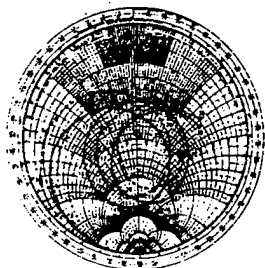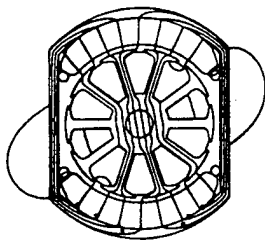
15th Annual Review of Progress in

APPLIED

COMPUTATIONAL

ELECTROMAGNETICS

at the

Naval Postgraduate School

Monterey, CA

March 15-20, 1999

CONFERENCE PROCEEDINGS

Model-Based Frequency Extrapolation of Antenna Radiation Characteristics on Complex Platforms

Tao Su, Yuanxun Wang and Hao Ling
Department of Electrical and Computer Engineering
The University of Texas at Austin
Austin, TX 78712

I. Introduction

In antenna design and analysis, the mounting platform can have a significant effect on the antenna radiation characteristics. However, rigorous solution of the radiation problem over a complex platform is very time consuming, and the computation complexity increases dramatically as the frequency increases. In this paper, we present a model-based frequency extrapolation technique with which the radiated field over a broad band of frequencies can be obtained using the rigorously computed results at low frequencies.

Our approach entails three steps. First, the induced current on the platform surface is computed at low frequencies using the method of moments (MoM). Second, we apply the time-of-arrival model to the current on each basis element on the surface. The model coefficients are obtained using super-resolution algorithm ESPRIT [1]. Finally, the induced current at higher frequencies is computed using the model and the radiation characteristics are calculated. This approach is similar to that present in [2] and [3] for radar signature extrapolation. Our results show that when the frequencies and the discretization of the platform are properly chosen, the radiated field at higher frequencies can be extrapolated with only moderate computational cost.

II. Extrapolation Methodology

As the first step of the extrapolation process, the induced current on the target is computed at a small set of points at low frequencies. Once the current over the surface is computed at low frequencies, we apply the time-of-arrival model to each of the current element. In this model, we assume that the total current is induced by different scattering mechanisms, as shown in Fig. 1. Each of the incident mechanism has a distinct arrival time, so that the current can be written as

$$J(\omega) = \sum_{n=1}^{N} a_n e^{-j\omega t_n} \tag{1}$$

where ω is the angular frequency, N is the total number of incident mechanisms and t_n is the arrival time of the nth incident mechanism.

Since the incident mechanisms correspond to scattering from different parts of the target, the maximum difference in t_n is related to the size of the target. Thus the sampling rate in the frequency domain should be high enough to distinguish these time events from all parts of the target. Based on this consideration, we approximately constraint the sampling rate in frequency to

272

$$\Delta f < c / D \qquad \qquad (2)$$

where c is the speed of light and D is the maximum dimension of the target.

The model coefficients a_n and t_n are obtained using the superresolution algorithm ESPRIT, which is based on the model that the signal consists of a sum of exponential and additive white noise. Given a sequence with M samples, the algorithm can estimate the number of exponential N and determines the amplitude and period of each exponential term. The basic requirement in the number of samples is $M > 2N + 1$. Once the model parameters are found, the induced current at higher frequencies can be computed using (1). The radiated field is then easily obtained from the extrapolated current.

III. Results

As an example, we consider a 2-D structure as shown in Fig. 2 (a). We are interested in the radiation pattern over a frequency band from 0.15 to 0.45 GHz. To obtain the data for the extrapolation, we compute the induced current at 10 frequencies from 0.15 to 0.24 GHz. Then we use the ESPRIT algorithm to obtain the model coefficients for each current element and compute the radiated field based on the model. Fig. 2(a) shows the radiated field of a horizontally polarized line source as a function of frequency at an elevation angle of 40°. The dashed curve is obtained from the model-based extrapolation while the solid curve is the reference brute-force solution. We observe that the extrapolation algorithm correctly predicts the peaks and null positions in frequency, indicating a good estimate on the times-of-arrival. Fig. 2(b) is the time domain response obtained via an inverse Fourier transform of the frequency data. The first large peak corresponds to the specular scattering from the flat surface and the second large peak is due to the scattering from the step region.

We notice from Fig. 2(a) that the model-predicted field matches well with the reference field at the first 10 frequencies, but drops below the computed field as frequency goes higher. This is because the intensity of the field radiated by the line source is proportional to the square root of the frequency. We can overcome this by compensating this effect before doing the extrapolation. Thus the time-of-arrival model becomes

$$J(\omega) = \left(\sum_{n=1}^{N} a_n e^{-j\omega t_n} \right) \sqrt{\omega} \qquad \qquad (3)$$

where $\sqrt{\omega}$ should be replaced by ω for 3-D situations. After the compensation, the extrapolation result is further improved, as shown by the frequency and time responses in Figs. 3(a) and 3(b).

Finally we look at the radiation problem of the 3-D platform in Fig. 4(a). The source is a horizontally polarized dipole. The solver used is FISC [4], which is a 3D MoM code based on the fast multipole method. Similar to the 2-D case, we use the computed current at 10 frequencies from 0.15 to 0.24 GHz to extrapolate the data to 0.45 GHz. The extrapolated radiation field as a function of frequency at the elevation angle of 40° is shown in Fig. 4(b) as the dashed curve. The reference brute-force solution is plotted as the solid curve. The major features of the radiated field are well characterized by the extrapolation algorithm.

273

IV. Conclusion and Discussion

As we have seen from the results, the frequency extrapolation technique is an efficient way of obtaining the radiation pattern over a broad band of frequencies. Computation time is reduced dramatically since the current is rigorously solved only at low frequencies. We improved the result by compensating the frequency factor of the source in the time-of-arrival model. This indicates that a wrong frequency dependence in the model may result in errors in the model coefficients. In addition to the frequency factor of the source, the frequency dependence of different scattering components of each current element could be different, due to different scattering physics. Further incorporation of these effects should further enhance the accuracy of the extrapolation.

References

[1]   R. Roy, A. Paulraj and T. Kailath, "ESPRIT – a subspace rotation approach to estimation of parameters of cisoids in noise," *IEEE Trans. Acoust., Speech, Signal Processing*, vol. ASSP-34, pp. 1340-1342, Oct. 1986.

[2]   Y. Wang, H. Ling J. Song and W. C. Chew, "A frequency extrapolation algorithm for FISC," *IEEE Trans. Antennas Propagat.*, vol. 45, pp. 1891-1893, Dec. 1997.

[3]   Y.Wang and H. Ling, "Radar signature prediction using moment method codes via a frequency extrapolation technique," submitted to *IEEE Trans. Antennas Propagat.*, Feb. 1998.

[4]   *User's Manual for FISC (Fast Illinois Solver Code)*, Center of Computational Electromagnetics, Univ. of Illinois, Champaign, IL, and DEMACO, Inc., Champaign, IL, Jan. 1997.
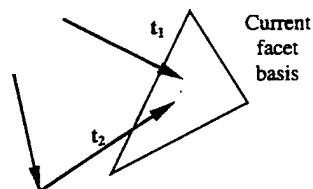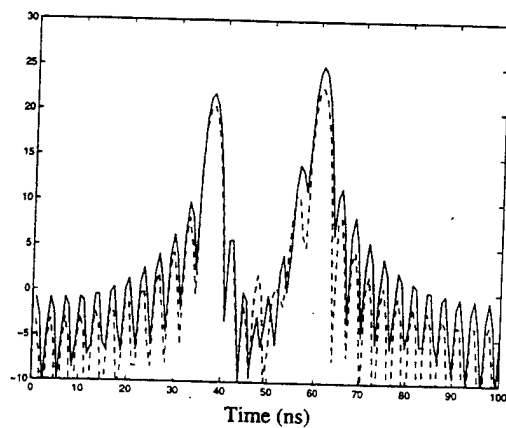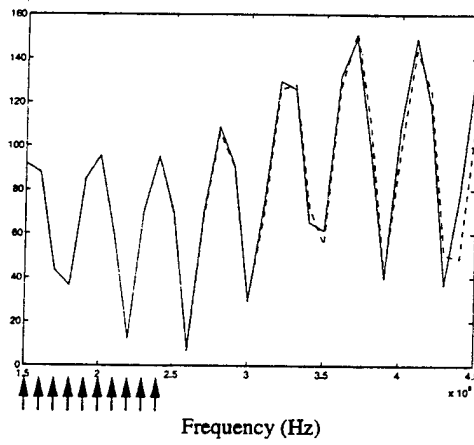
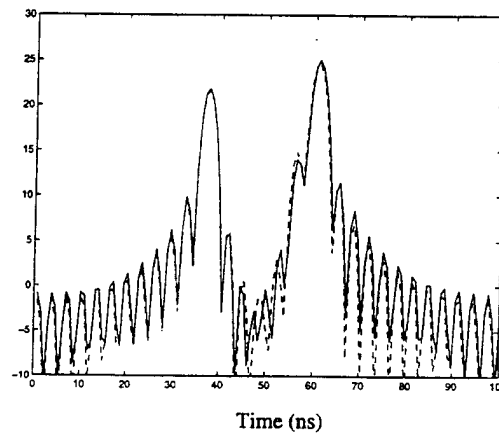Fig. 1. Time-of-arrival model
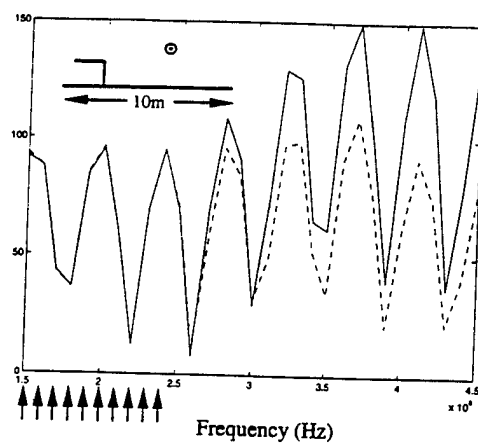
(a) Frequency response

(b) Time domain response

Fig. 2. Frequency extrapolation for 2-D problem (H-Pol). ——— MoM,
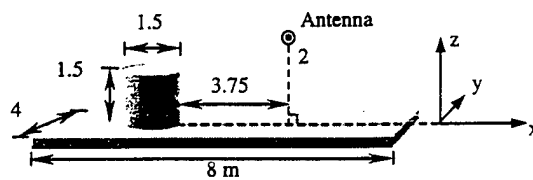-------- 10 point MoM + extrapolation

275

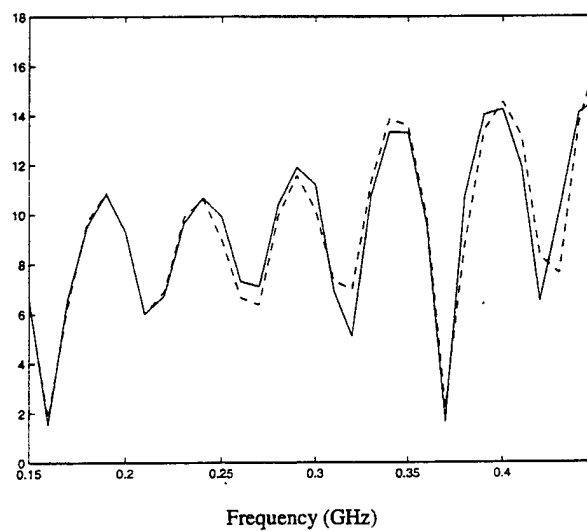(a) Frequency response

Time (ns)

(b) time domain response

Fig. 3. Frequency compensated extrapolation (H-pol). ——— MoM,
-------- 10 point MoM + extrapolation

276

(a) Geometry of the 3-D platform

Frequency (GHz)

(b) Frequency response

Fig. 4. Frequency extrapolation for 3-D radiation. ——— FISC
-------- FISC at 10 point + extrapolation

277

IEEE Antennas and Propagation Society International Symposium 1999

Renaissance Orlando Resort
July 11-16, 1999
Orlando, Florida

VOLUME ONE

Frequency Extrapolation and Model-Based Parameterization of Antenna-Platform Radiation from CEM Data

Tao Su*, Yuanxun Wang and Hao Ling
Department of Electrical and Computer Engineering
The University of Texas at Austin
Austin, TX 78712-1084

I. Introduction

The numerical characterization of antenna radiation in the presence of a large, complex platform is usually very time consuming. The problem is further compounded when the radiation pattern is desired over a broad frequency band. In this paper, we present a frequency extrapolation technique for the antenna radiation problem to obtain the radiated field over a wide band of frequencies from a limited set of frequency calculations. Our approach is similar to our previous work on radar signature extrapolation [1]. Given a CAD model of the platform, the induced current on the surface is first computed using a computational electromagnetics (CEM) simulator at a set of low frequencies. A time-of-arrival model is then applied to each current element and the super-resolution algorithm ESPRIT [2] is used to calculate the model coefficients. The frequency response of the current is extrapolated based on this model and the radiated field is obtained over a wide band of frequencies. The CEM simulator used in our work is the multi-level fast multipole solver FISC [3].

As a follow-up to the frequency extrapolation algorithm, we also set out to extract a sparse point-radiator model of the antenna radiation pattern in the presence of the platform. We assume the total radiation over some extended frequency and aspect window can be approximated by the radiation from a set of radiation centers. The location and amplitude of the radiation centers are determined by using a matching pursuit algorithm [4]. To speed up the parameterization time, we estimate the location of the radiation centers by utilizing a Fourier-based ASAR (Antenna Synthetic Aperture Radar) algorithm [5] we have developed previously. The resulting sparse point-radiation center model can be used for real-time reconstruction of complex radiation patterns. In addition, it can be used to pinpoint cause-and-effect in antenna-platform interaction.

II. Frequency Extrapolation

An example of the antenna-platform problem is shown in Fig. 1. The antenna is assumed to be a horizontal dipole. We first compute the induced current at a number of low frequency points using FISC based on the CAD model of the platform. We assume that the total current is induced by different scattering

mechanisms where each of the incident mechanism has a distinct arrival time [1]. Also taking into account the fact that the amplitude of the radiated field from a dipole source is proportional to the frequency, a current element can be described by the following model:

$$J(\omega) = \omega \sum_{n=1}^{N} a_n e^{-j\omega t_n}$$ (1)

where ω is the angular frequency, N is the total number of incident mechanisms, and a_n and t_n are the amplitude and arrival time of the nth incident mechanism, respectively. The model coefficients a_n and t_n are obtained by parameterizing the computed currents using ESPRIT, which is based on the model that the signal consists of a sum of exponential and additive white noise. Once the model parameters are found, the induced current at higher frequencies can be computed using (1). The radiated field is then easily obtained from the extrapolated current.

In the example, the induced current is computed from 0.15 to 0.24 GHz at an interval of 0.01 GHz. The current is then extrapolated and the radiated field is computed. The extrapolation result is compared with the brute-force reference data, which is also computed by FISC over the frequency band from 0.15 to 0.45 GHz at $\theta = 50°$ and $\phi = 0°$, as shown in Fig. 2(a). The corresponding time domain response is plotted in Fig. 2(b). The matching between the two is good in both the frequency and time domain, demonstrating the effectiveness of the extrapolation algorithm.

III. Model-Based Parameterization

Next, we set out to find a sparse model to represent the radiated field from the antenna-platform configuration. We assume that the radiated field can be approximated by the radiation of a set of point radiators, each having a frequency-aspect behavior described by:

$$E^z(k, \theta, \phi) = Ae^{-jkr_0}e^{jk(x_0 \sin\theta \cos\phi + y_0 \sin\theta \sin\phi + z_0 \cos\theta)} = Ae^{-jkr_0}e^{j(k_x x_0 + k_y y_0 + k_z z_0)}$$ (2)

where k is the wave number, (x_0, y_0, z_0) is the location of the radiation center. The origin of the above basis is illustrated in Fig. 3. The matching pursuit algorithm is applied to extract the point radiators one at a time. To speed up the extraction time of the matching pursuit algorithm, we estimate the location of the radiation centers by utilizing the Fourier-based ASAR algorithm. We inverse Fourier transform the radiated field with respect to the frequency and angles to generate an ASAR image. The point with the highest intensity is first located in the ASAR image and its amplitude and coordinates serve as an estimate of the strongest radiation center. We next zoom in on the precise location of the radiation center via a fine search. We then subtract the contribution of this radiation center from the total radiated field and iterate the process until the energy in the residual signal has reached a sufficiently small level.

447

We demonstrate this concept by extracting the radiation centers from the frequency-extrapolated FISC data from 0.6 to 0.9GHz. The angular range of observation is over a 30-degree window in both azimuth and elevation. The first 10 extracted radiation centers are shown in Fig. 4, with their amplitudes represented by grayscale. We observe that the dominant platform scattering comes from the edge diffraction from the right edge of the platform and the corner structure formed by the cylinder and plate. Note that the radiation center due to the edge diffraction is slightly off the platform. This is due to the limited resolution of the matching pursuit algorithm. Once the sparse representation is generated, the radiated field can be rapidly reconstructed using the radiation centers. The original radiated field at $k_t = 0$ is plotted in Fig. 5(a) as a function of the k_x and k_y, where k_x, k_y and k_t are defined in (2). The field reconstructed from the first 10 radiation centers is shown in Fig. 5(b). The two patterns match well over both frequency and angle.

IV. Conclusions

We have applied a frequency extrapolation technique to the antenna radiation problem. The radiated field over a broad band of frequencies can be extrapolated efficiently based on the computation result at a limited number of low frequency points. In addition, a radiation center model of the platform radiation can be found by performing the matching pursuit algorithm. The model proves effective as the radiated field can be accurately reconstructed with very little computation effort.

References
[1] Y. Wang, H. Ling, J. Song and W. C. Chew, "A frequency extrapolation algorithm for FISC," *IEEE Trans. Antennas Propagat.*, vol. 45, pp. 1891-1893, Dec. 1997.
[2] R. Roy, A. Paulraj and T. Kailath, "ESPRIT – a subspace rotation approach to estimation of parameters of cisoids in noise," *IEEE Trans. Acoust., Speech, Signal Processing*, vol. ASSP-34, pp. 1340-1342, Oct. 1986.
[3] *User's Manual for FISC (Fast Illinois Solver Code)*, Center of Computational Electromagnetics, Univ. of Illinois, Champaign, IL, and DEMACO, Inc., Champaign, IL, Jan. 1997.
[4] S. G. Mallat and Z. Zhang, "Matching pursuits with time-frequency dictionaries," *IEEE Trans. Signal Processing*, vol. SP-41, pp. 3397-3415, Dec. 1993.
[5] C. Ozdemir, R. Bhalla, L. C. Trintinalia and H. Ling, "ASAR – antenna synthetic aperture radar imaging," to appear in *IEEE Trans. Antennas Propagat.*, Dec. 1998.
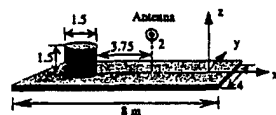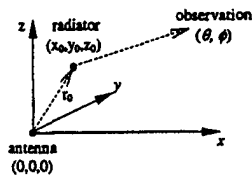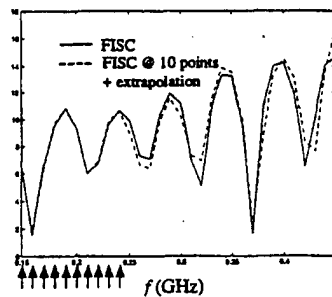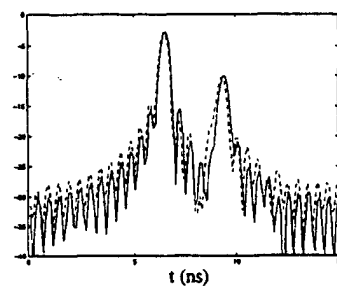
Fig. 1. Geometry of 3-D platform.

Fig. 3. Radiation center model.

— FISC

---- FISC @ 10 points
  + extrapolation

f (GHz)

(a) Frequency domain response (dB)

Fig. 4. Extracted radiation centers.

(a) Original radiated field

t (ns)

(b) Time domain response (dB)

Fig. 2. Frequency Extrapolation.
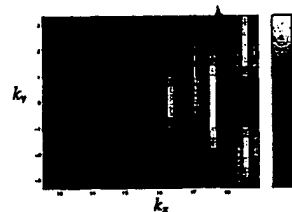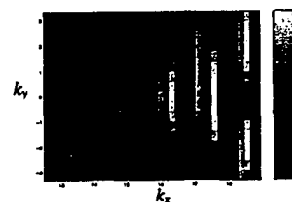
(b) Reconstructed radiated field

Fig. 5. Reconstruction of the radiated field from the radiation center model.

449

RCS INTERPOLATION IN FREQUENCY AND ANGLE USING ADAPTIVE FEATURE EXTRACTION

Yuanxun Wang* and Hao Ling
Department of Electrical and Computer Engineering
The University of Texas at Austin
Austin, Texas 78712-1084

I. Introduction

Recently, a number of iterative solvers based on fast algorithms have emerged in computational electromagnetics. These solvers have much higher computational efficiency than traditional approaches. However, for wide-band, wide-angle RCS calculations, the solver has to be executed repeatedly for each angle or frequency, which results in large computational expenses. A number of interpolation and extrapolation approaches have been developed to generate the RCS curve with as sparse a data sampling as possible [1]. In this paper, we address the interpolation problem in frequency and angle using a model-based approach. Our approach is the adaptive feature extraction (AFE) algorithm. It has been used recently by us to eliminate the aliasing effect and construct ISAR image from unevenly undersampled measurement data [2]. Unlike standard interpolation algorithms which suffers from theNyquist sampling limitation, AFE can overcome the Nyquist sampling criterion by using uneven sampling. The essential idea of the adaptive algorithm is to search and extract out individual scattering features one at a time in an iterative fashion. When applied to the present problem, the interference between different scattering features can be avoided. After all the main features are extracted, the current and the RCS on a denser grid of sampling can be interpolated by summing the contributions from all the extracted scattering features. The AFE algorithm is tested using numerical examples for both 1-D frequency interpolation and 2-D frequency-aspect interpolation.

II. 1-D Frequency Interpolation Algorithm

In simple curve fitting, if we assume that the far-field frequency response of a target is R(f) and the field at sampling frequencies f is known, the interpolated results will have the following form,

$$\hat{R}(f) = \sum_{i=1}^{N} R(f_i) \cdot W_i(f) \tag{1}$$

where N is the number of the original sampling points and W(f) is the interpolation basis functions. The interpolation will have good performance when the original function is a slowly varying function of frequency. According to the Nyquist sampling criterion, the sampling interval in the frequency domain should be less than $1/(2\tau_{max})$ to ensure good interpolation results, where τ_{max} is the

longest time delay between the different scattering mechanisms caused by the structure. The curve fitting procedure can also be carried out for the induced current at each point on the target. This has been found to have an advantage over the field-based interpolation [3], since the phase-demodulated current has much looser Nyquist sampling criterion. As a result, the number of sampling points needed to carry out the interpolation can be much less than that using a fitting scheme for the far field. However, this observation is not always true and only works for targets where the scattering mechanism is dominated by physical optics. In this work, we apply the AFE algorithm to the current to deal with the higher-order interactions in more general targets. Our approach is based on the following time-of-arrival model of the induced current

$$J(f) = \sum_p B_p \exp(-j2\pi f t_p) \qquad (2)$$

This model gives a good description of the multiple scattering physics at high frequencies [4,5]. The number of terms is left unspecified and will be determined by the algorithm. To determine the model parameters B_p and t_p, we use an iterative procedure. We first project the sampled frequency response onto the complex conjugate of the model bases in (2):

$$M_p(t) = \frac{1}{N}\sum_{i=1}^{N} J_p(f_i)\exp(j2\pi f_i t) \qquad (3)$$

where the subscript p denotes it is in the pth stage of the iterative procedure. It should be noted that the sampling f is intentionally chosen to be randomly distributed in the frequency band to avoid the ambiguity in determining the strongest feature. Then the strongest feature in this stage is decided by exhaustive search over all values of t,

$$B_p = \arg\max_{t_p}[M_p(t)] \qquad (4)$$

Once the strongest feature is found, a remainder signal is produced by subtracting out the pth feature:

$$J_{p+1}(f_i) = J_p(f_i) - B_p \exp(-j2\pi f_i t_p) \qquad (5)$$

After all the amplitude and time-of-arrival parameters are known, the interpolated current function at any frequency within the band can be calculated using formula (2). Therefore, the far field at the denser frequency sampling can be obtained by integrating the induced current.

To verify the above analysis, we use the scattering from three 2-D circular cylinders as an example. The structure is shown in Fig.1(a). The original RCS is computed at 71 points from 0.3 GHz to 0.65 GHz using the method of moments. The result is shown as the solid line in Fig.1(b). Next, we use the values at 18 equally spaced points and carry out a current-based interpolation using simple spline fitting. The result is shown as the dotted line in Fig. 1(b). Deviations between the two results can be seen. While the current-domain spline gives good prediction of the physical optics current on the target, the multiple interactions mechanisms are not well interpolated. Next, we use the AFE algorithm to carry out the interpolation. Instead of 18 equal spaced points, we select 18 points

451

randomly from the original 71 points. The result is plotted as the dashed line in Fig.1(b), which agrees with the original calculation much better than the simple spline interpolation. This comparison is further shown when we Fourier transform the frequency responses to the range profiles in Fig. 1(c). We can see that most of the features from the AFE interpolation coincide with the reference result while the current-domain spline interpolation gives strong artifacts among the real scattering features.

III. 2-D Frequency-Aspect Interpolation Algorithm

The AFE technique can be extended to 2-D interpolation in both frequency and angular domains. We replace the model in (2) by the following 2-D scattering center model [5]:

$$ J(f) = \sum_p B_p \exp\left[-j\frac{2\pi f}{c}(x_p \cos\theta + y_p \sin\theta + l_p) \right] \qquad (6) $$

where l_p represents the time delay caused by the higher order interactions. This model can be considered as an extension of the 1-D time-of-arrival model in (2). To show the payoff of the 2-D interpolation algorithm, we set out to construct an ISAR image of a cylinder-plate structure shown in Fig. 2(a). Fig. 2(b) shows the reference ISAR image generated from 71x 81 sampling points in the frequency-aspect plane. The grayscale image has a dynamic range of 40 dB. To construct the image using the AFE algorithm, we choose 200 points randomly from the original 5751 points. The ISAR image obtained using the 2-D AFE interpolation is plotted in Fig. 2(c). Most of the features of the interpolated image agree well with the brute-force calculation. The dynamic range of the interpolated result is limited by the imperfection of the 2-D model in (6) and the errors in the AFE procedure.

References

[1] E. K. Miller, "Model-based parameter estimation in electromagnetics: part I. background and theoretical development," *IEEE Antennas Propag. Mag.*, vol.40, No.1, pp.42-52, Feb. 1998.

[2] Y. Wang and H. Ling, "ISAR image formation from unevenly undersampled data using adaptive feature extraction," *1998 IEEE Antennas and Propagation Symposium Digest*, pp. 350-353, Atlanta, June 1998.

[3] J. Song, private communication.

[4] Y. Wang, H. Ling, J. Song and W. C. Chew, "A frequency extrapolation algorithm for FISC," *IEEE Trans. Antennas Propagat.*, vol. AP-45, pp. 1891-1893, Dec. 1997.

[5] Y. Wang and H. Ling, "A model-based angular extrapolation technique for iterative MoM solvers," to appear in *Microwave Opt. Tech. Lett.*, Feb. 1999.
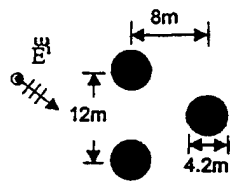
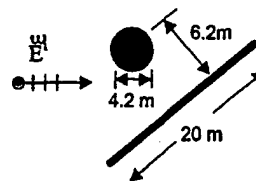Fig.1(a) Geometry of the three-cylinder target.

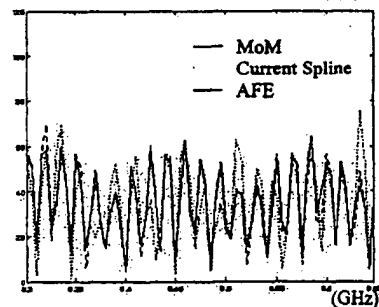Fig.2(a) Geometry of the cylinder-plate target.

Fig.1(b) RCS vs. frequency plots using current
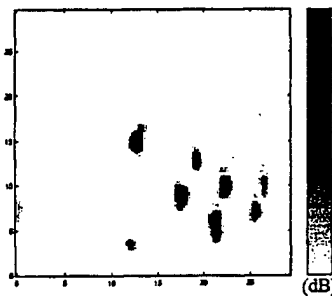domain spline and AFE interpolation.

Fig.2(b) ISAR image generated using brute
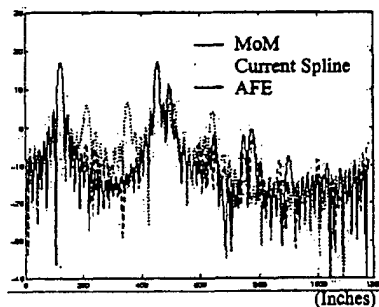force MoM calculation at 5751 points.

Fig.1(c) Range profiles generated from the
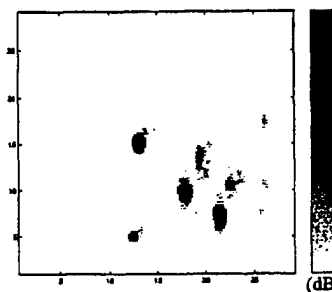interpolated results using current domain spline
and AFE.

Fig.2(c) ISAR image generated from
interpolated result using AFE with 200
calculated points.

453